THERMOMECHANICAL FATIGUE BEHAVIOR OF THE DIRECTIONALLY-SOLIDIFIED NICKEL-BASE SUPERALLOY CM247LC

A Thesis
Presented to
The Academic Faculty

by

Robert Anthony Kupkovits

In Partial Fulfillment
of the Requirements for the Degree
Master of Science in the
George W. Woodruff School of Mechanical Engineering

Georgia Institute of Technology
May 2008

THERMOMECHANICAL FATIGUE BEHAVIOR OF THE DIRECTIONALLY-SOLIDIFIED NICKEL-BASE SUPERALLOY CM247LC

Approved by:

Dr. Richard W. Neu, Advisor
George W. Woodruff School of Mechanical Engineering
Georgia Institute of Technology

Dr. David L. McDowell
George W. Woodruff School of Mechanical Engineering
Georgia Institute of Technology

Dr. W. Steven Johnson
School of Materials Science and Engineering
Georgia Institute of Technology

Date Approved: 30 March 2008

ACKNOWLEDGEMENTS

The work documented in this thesis was influenced, assisted, and to a great extent augmented, by a great number of individuals. I acknowledge this effort would not be nearly as comprehensive or thorough without their support, and I can therefore conclude that they contributed a substantial amount to the satisfaction I've derived from it.

I'd like to thank my advisor, Dr. Richard W. Neu, for his support, guidance, and encouragement throughout the course of my work. It was an honor to work with him, and his effort and expertise were essential to the completion of this project and thesis. I'd also like to thank my committee members, Dr. David McDowell and Dr. Steve Johnson, for their effort in reviewing the content of this thesis and improving the quality of work presented within it.

The support and friendship of my coworkers and close friends was most helpful. I appreciate the knowledge and experience shared by Zach Moore, Mike Hirsch, Kyle Webber, and Robert Amaro. The assistance of Matthew Schaikewitz, Noah Randolph, Robert Cooper, and Rick Brown during various phases was greatly appreciated.

I appreciate the support and encouragement from my family, and their understanding of the time commitment this work required. I'm grateful they recognized my own happiness with this work involved placing a great importance on my studies.

Without the financial support of Siemens Power Generation, this research would not have been possible. I appreciate the interaction and feedback from all the individuals at Siemens, especially Mr. Phillip Gravett and Mr. Iyer Saiganesh.

TABLE OF CONTENTS

LIST OF TABLES

Page

LIST OF FIGURES

Page

LIST OF SYMBOLS

Experimental Measures, Conditions, and Symbols:

N	Number of cycles endured: [*cycles*]
N_i	Number of cycles to crack initiation: [*cycles*]
$N/2$	Half-life cycle: [*cycles*]
N_f	Number of cycles to failure: [*cycles*]
T	Nominal test temperature: [°C]
ΔT	Temperature range: [°C]
t	Time: [*s*] or [*hr*]
t_c *or* t_{tc}	Total cycle time: [*s*]
t_{hc}	Compressive hold time: [*s*]
t_{ht}	Tensile hold time: [*s*]
t_r	Rupture time: [*s*] or [*hr*]
a_i	Crack initiation depth: [*mm*]
P_0	Stabilized maximum load: [*lbs*]
R	Load ratio
R_E	Ratio between tensile and compressive stiffness
E_T	Tensile stiffness: [*MPa*]
E_C	Compressive stiffness: [*MPa*]
$\Delta\varepsilon$	Total uniaxial strain range: $\left[\frac{mm}{mm}\right]$ or [%]

$\Delta\varepsilon_{mech}$	Mechanical strain range: $\left[\frac{mm}{mm}\right]$ or $[\%]$
$\Delta\varepsilon_{p}$	Plastic strain range: $\left[\frac{mm}{mm}\right]$ or $[\%]$
ε_t or ε_{tot}	Uniaxial total strain: $\left[\frac{mm}{mm}\right]$ or $[\%]$
ε_{el}	Uniaxial elastic strain: $\left[\frac{mm}{mm}\right]$ or $[\%]$
ε_{in}	Uniaxial inelastic strain: $\left[\frac{mm}{mm}\right]$ or $[\%]$
ε_{pl}	Local uniaxial plastic strain: $\left[\frac{mm}{mm}\right]$ or $[\%]$
ε_{th}	Thermal strain: $\left[\frac{mm}{mm}\right]$ or $[\%]$
$\dot{\varepsilon}$	Strain rate: $\left[\frac{1}{s}\right]$ or $\left[\frac{\%}{s}\right]$
ε_f	Uniaxial rupture strain: $\left[\frac{mm}{mm}\right]$ or $[\%]$
e	Nominal strain: $\left[\frac{mm}{mm}\right]$ or $[\%]$
σ	Local stress: $[MPa]$
σ_H	Hydrostatic stress: $[MPa]$
$\bar{\sigma}$	Effective stress: $[MPa]$
$\Delta\sigma$	Local uniaxial stress range: $[MPa]$
$\Delta\sigma_N / 2$	Notch net section stress amplitude: $[MPa]$
σ_m	Mean stress: $[MPa]$
$\sigma_{\max}$	Maximum uniaxial stress: $[MPa]$

S	Nominal stress: [MPa]
ΔS	Nominal uniaxial stress range: [MPa]
k_t	Theoretical elastic stress concentration factor
k_σ	Stress concentration factor
k_ε	Strain concentration factor
ρ	Notch radius: [mm]
q	Notch sensitivity
L	Length scale: [mm]
ϕ	Thermal/Mechanical phasing: [°] or [rad]
Φ_{lag}	Applied phase lag: [°] or [rad]

Material Properties and Modeling Variables:

σ_0	Endurance limit: [MPa]
ν	Poisson's Ratio
E	Elastic modulus (e.g. Young's modulus): [MPa]
σ_{UTS} *or UTS*	Ultimate tensile strength: [MPa]
σ_Y	Yield Strength (0.2% or 0.02% offset): [MPa]
α *or CTE*	Coefficient of thermal expansion: $^\circ C^{-1}$
Θ	Arrhenius Term
C_i	Generic constant used in fatigue and fatigue damage models
F or F_{ij}	Deformation gradient
J or J_{ijkl}	Jacobian matrix: [MPa]
K_{th}	Crack propagation threshold: [$MPa \cdot \sqrt{m}$]

K_{peff}	Parabolic constant: [$\mu m^2 \cdot s^{-1}$]
n	Norton's power law (secondary creep) exponent
Q	Activation energy: $\left[\frac{J}{mol}\right]$
W_A	Average strain energy density: [MPa]

Microstructural Measures and Material Descriptions:

γ	Matrix phase of a Ni-base superalloy
γ'	Precipitate phase of a Ni-base superalloy
[001]	Primary crystallographic direction
h	Oxide or γ' depleted depth: [μm] or [mm]
h_{cr}	Critical crack depth: [μm] or [mm]
$\overline{h}_f$	Critical oxide rupture thickness: [μm] or [mm]
$PDAS$	Primary dendrite arm spacing: [μm] or [mm]
$SDAS$	Secondary dendrite arm spacing: [μm] or [mm]
δ	Lattice misfit parameter
a_γ	Lattice parameter for the γ phase
$a_{\gamma'}$	Lattice parameter for the γ' phase

Fundamental Physical Constants:

δ_{ij} or **I**	Kronecker delta, identity tensor
π	Pi
R	Universal gas constant: $\left[8.31457\frac{J}{K \cdot mol}\right]$

Fatigue Analysis Variables:

σ_o	Reference Stress: [*MPa*]
b	Fatigue strength exponent
n'	Strain hardening exponent
K'	Ramberg-Osgood cyclic strength coefficient: [*MPa*]

Internal State Variables:

χ^{α}	Backstress on the α^{th} slip system: [*MPa*]
κ^{α}	Threshold stress on the α^{th} slip system: [*MPa*]
$\gamma^{(\alpha)}$	Shear strain on the α^{th} slip system

LIST OF ABBREVIATIONS

AC	Alternating current
ANN	Artificial Neural Network
ASTM	American Society for Testing and Materials
CC	Continuously Cycled
CF	Creep Fatigue
CP	Crystal Plasticity
CVP	Crystal Visco-Plasticity
DC	Direct current
DS	Directionally-Solidified
EDM	Electrical Discharge Machining
ESED	Equivalent Strain Energy Density
FCC	Face-Centered Cubic
FE or FEA	Finite Element Analysis
GB	Grain boundary
HC	Hold in Compression
HCF	High Cycle Fatigue
HT	Hold in Tension
IF	Isothermal Fatigue
ISV	Internal State Variable
IP	In-Phase
L	Longitudinal

LCF	Low Cycle Fatigue
LE	Leading Edge of Blade
LMP	Larson-Miller Parameter
LOM	Light Optical Microscope
MNM	Multiaxial Neuber Model
MPRL	Mechanical Properties Research Laboratory
NOx	Nitrous-oxide Emissions
ODS	Oxide-Dispersion Strengthened
OP	Out-of-Phase
OPL	Out-of-Phase Low Temperature
PC	Polycrystalline
PDAS	Primary Dendritic Arm Spacing
R-O	Ramberg-Osgood
RPM	Revolutions per Minute
RT	Room Temperature
SC	Single-Crystal
SDAS	Secondary Dendritic Arm Spacing
SEM	Scanning electron microscope
SSR	Slow Strain Rate
SWT	Smith-Watson-Topper
T	Transverse
TC	Thermocouple
TBC	Thermal barrier coating
TCD	Theory of Critical Distance
TE	Trailing edge of blade

TEM	Transmission electron microscope
TF	Thermal Fatigue
TIT	Turbine inlet temperature
TMF	Thermomechanical Fatigue
UMAT	User-defined Material Subroutine
UTS	Ultimate tensile strength
XRD	X-Ray Diffraction

SUMMARY

Due to the extreme operating conditions present in the combustion sections of gas turbines, designers have relied heavily on specialized engineering materials. For blades, which must retain substantial strength and resistance to fatigue, creep, and corrosion at high temperatures, directionally-solidified (DS) nickel-base superalloys have been used extensively. Complex thermomechanical loading histories makes life prediction for such components difficult and subjective. Costly product inspection and refurbishment, as well as capital expense required in turbine forced outage situations, are significant drains on the resources of turbine producers. This places a premium on accurate endurance prediction as the foundation of viable long-term service contracts with customers. In working towards that end, this work characterizes the behavior of the blade material CM247LC DS subjected to a variety of in-phase (IP) and out-of phase (OP) loading cycles in the presence of notch stress concentrations. The material response to multiaxial notch effects, highly anisotropic material behavior, time-dependent deformation, and waveform and temperature cycle characteristics is presented. The active damage mechanisms influencing crack initiation are identified through extensive microscopy as a function of these parameters.

This study consisted of an experimental phase as well as a numerical modeling phase. The first involved conducting high temperature thermomechanical fatigue (TMF) tests on both smooth and notched round-bar specimens to compile experimental results. Tests were conducted on longitudinal and transverse material grain orientations. Damage is characterized and conclusions drawn in light of fractography and microscopy. The

influences of microstructure morphology and environmental effects on crack initiation are discussed. The modeling phase utilized various finite element (FE) simulations. These included an anisotropic-elastic model to capture the purely elastic notch response, and a continuum-based crystal visco-plastic model developed specifically to compute the material response of a DS Ni-base superalloy based on microstructure and orientation dependencies. These FE simulations were performed to predict and validate experimental results, as well as identify the manifestation of damage mechanisms resulting from thermomechanical fatigue. Finally, life predictions using simple and complex analytical modeling methods are discussed for predicting component life at various stages of the design process.

CHAPTER 1. INTRODUCTION

1.1 Motivation

Land-based gas turbine engines have long been used as a significant source of power generation for utilities and independent suppliers. The system draws atmospheric air into a multi-stage compressor section, utilizing successive rows of blades to create a favorable pressure ratio for fuel mixing and combustion. Once ignited, the hot gas flow is directed by transition ducts and vanes into consecutive stages of turbine blades to maintain rotor revolutions (3000 and 3600 revolutions per minute in the 50 and 60 *Hz* markets, respectively). This powers the compressor and downstream generator connected to the transmission grid. The duty cycle, or frequency and duration of operation, varies between units depending on such factors as generation capacity, seasonal shifts in grid requirements, and sustained power consumption within the local geographical region.

Due to the operating conditions and extreme temperatures experienced in the hot section, blades must be actively cooled, and thus contain a multitude of cooling holes fed by the upstream pressure gradient. The resulting regions of stress concentration around the cooling holes are typical locations for localized micro-plasticity and thus the site of fatigue crack nucleation. Frequent fractographic studies of failed components typically reveal cracks extending both from these holes and “hot spots” resulting from severe temperature gradients [2]. Cracks such as these lead, at the very least, to premature retirement of the blades; often, unchecked complications can lead to component

liberation, foreign-object damage (FOD), or flashback (combustion instabilities) resulting in an engine shutdown trip and severe downstream damage.

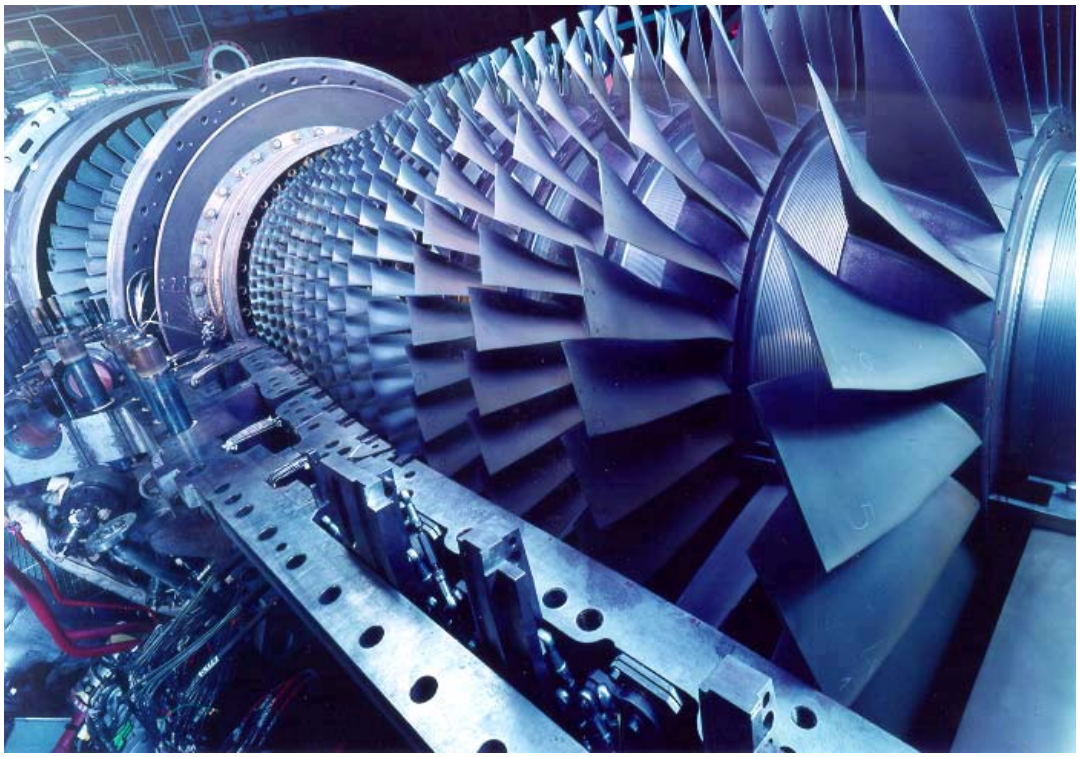

Figure 1-1: Land-based gas turbine under construction [3].

In the power generation industry, where extended unit outages (durations where the turbine is shut down and unavailable for service, due to either maintenance/standard inspection intervals or component failure) can be extremely costly, often the mere presence of a detectable crack necessitates component retirement. Accurate life-prediction methods are therefore critical in producing competitive service contracts for customer engines.

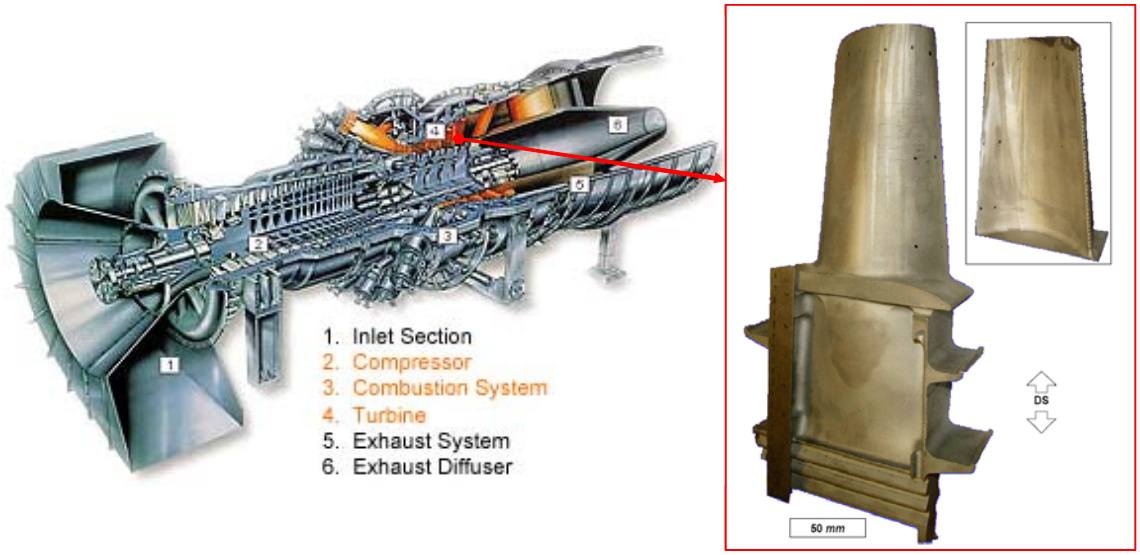

Figure 1-2: Gas turbine longitudinal layout and blade geometry [2].

Several damage mechanisms contribute to service life of gas turbine blades. During transient phases of engine startup and shutdown, there is a non-uniform temperature distribution and thermal gradients across the airfoil. This results in the blade airfoil and root being subjected to low-cycle thermomechanical fatigue due to temperature variation of the combustion gases and internally-fed air cooling. At baseload operation, centrifugal (radial) stresses induce high temperature creep-fatigue in the blades. The accumulation of inelastic creep damage at maximum operating temperatures can alter the overall fatigue resistance, material microstructure, and mechanical behavior of the alloy. In addition, exposure of the airfoil to this caustic environment leads to oxidation and degradation of the material surface. The synergistic interaction of these life-limiting factors and the critical locations where they occur often results in blades unsuitable for refurbishment. It is therefore of prime importance to predict the long-term durability and reparability of the blades.

Traditional methods to determine component life expectations have focused around isothermal low-cycle fatigue (LCF) tests. By conducting these tests near peak turbine operating temperatures, and introducing safety factors to account for complex component loading history and real geometries, a relatively accurate multi-axial stress response can be drawn for the prediction of fatigue crack initiation and growth. Frequently, data from these isothermal LCF tests is used to help predict complex deformation behavior and assess durability of components subjected to thermomechanical fatigue [4]. For simplicity, most component models assume isothermal and isotropic behavior. The three main reasons for this are:

1. High level of model complexity to predict anisotropic deformation and fracture
2. Lack of sufficient test data to fully characterize all configurations
3. Limited knowledge of deformation mechanisms which need to be incorporated into an effective and successful model

These simplified models may also fail to capture the temperature-dependent interaction between damage modes or the susceptibility of the material to particular fatigue driving forces introduced by thermomechanical cycling.

1.2 Evolution of Ni-base and DS Alloy Applications

Improvements in aspects such as compression ratio, firing temperature, and mass flow highlight continual advancements in the gas turbine industry. Substantial increases

in the thermal and aerodynamic efficiency through progressive changes in operating pressures and turbine inlet temperature (TIT) has necessitated the hot section components withstand greater exposure to high-temperature damage mechanisms. In order to achieve these higher temperatures while still maintaining acceptable NOx emission levels, higher technology materials must be utilized. As such, designers have expended great effort in the areas of both manufacturing and more accurate predictive modeling. The objectives include enhancing creep and oxidation resistance as well as improving thermodynamic reliability. This has involved the extensive use of Nickel-based superalloys, which have strengths in these areas. The application of complex mechanical loading histories and often severe thermal transients has made it difficult to predict the service life of such components, especially given the presence of stress concentrations from which a critical crack is more likely to develop.

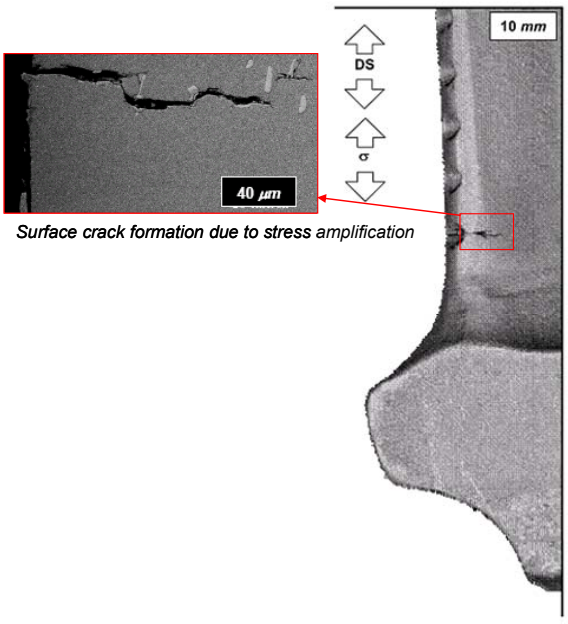

Figure 1-3: LCF crack extending from a 1^{rst} row cooling hole on a Ni-base turbine blade [2].

Combustor firing temperature was the primary driver of increased blade temperature until the introduction of forced air cooling, which effectively decoupled metal temperature from that of the combustion stream. In the 1980's, more sophisticated air cooling technologies allowed substantial increases in firing temperature. This change prompted the introduction of protective coatings to serve as an insulating thermal barrier and also to protect the underlying material from life-limiting hot corrosion. Hot corrosion and oxidation effects in this environment are dynamic and extremely malignant. As a result, the reliability and service life of these components is closely affiliated with the LCF, creep, and corrosive resistance of the material. Steam cooling of combustor components and blades was also introduced as a more efficient alternative in combined cycle applications.

Because of their tolerance of severe thermal transients and complex loading histories which may differ between field units, Ni-base superalloys are principally suited for hot flow path sections of combustion turbines. IN 738 was the industry standard blade material through the 1980's due to its corrosive resistance. As improvements led to better creep rupture and fatigue strength properties at even higher temperatures, other Ni-base superalloys began replacing IN 738 as the material of choice in the latter half of the decade.

Improvements in durability and aerodynamic performance have also been accompanied by advances in metallurgy and the manufacturing procedure. Most Ni-base superalloys consist of a dual-phase structure with matrix (γ) and strengthening precipitate (γ') phases. Extensive γ' solutioning of the materials through heat treatment resulted in enhanced yield stress at high temperatures while maintaining a relatively consistent

ductility [5]. After alloys became super-saturated with respect to γ' volume fraction, attention turned to the evolution of the casting process. Traditionally, most complex geometry turbine components used an investment (also called "lost wax") casting process, as it offered high production rates while still maintaining a surface finish that required little rework or machining. Investment casting has been found to improve creep strength resistance beyond what can be achieved by modifying the alloy's chemical composition [6]. This technique was also inexpensive by volume once the initial specialized tooling had been fabricated.

Advances in material processing have allowed the replacement of traditional conventionally-cast polycrystalline Ni-based superalloy components with specially suited alloy microstructures. Methods to control grain growth during casting have resulted in directionally-solidified and single crystal (SC) alloys. These specialized processing techniques succeed in eliminating grain boundaries transverse to the primary loading axis of the turbine blades (i.e. the radial axis of each blade, normal to its circumferential position around the rotational axis). Directional solidification provides a lower modulus in the direction of grain growth and therefore enhanced creep-rupture strength and high temperature fatigue resistance [7]. Eliminating grain boundaries along this axis also removes a prime source of fatigue crack initiation.

Directional solidification is accomplished by cooling the bottom of the molten material first, allowing grains to begin growing in a vertical fashion, as shown in Figure 1-4. Thus, DS alloys tend to be nearly transversely isotropic, with conspicuous longitudinal (L) grains typically oriented along the primary radial load axis of the blade.

The material properties for the transverse (T) orientation are thus an aggregate response from a collection of randomly oriented columnar grains.

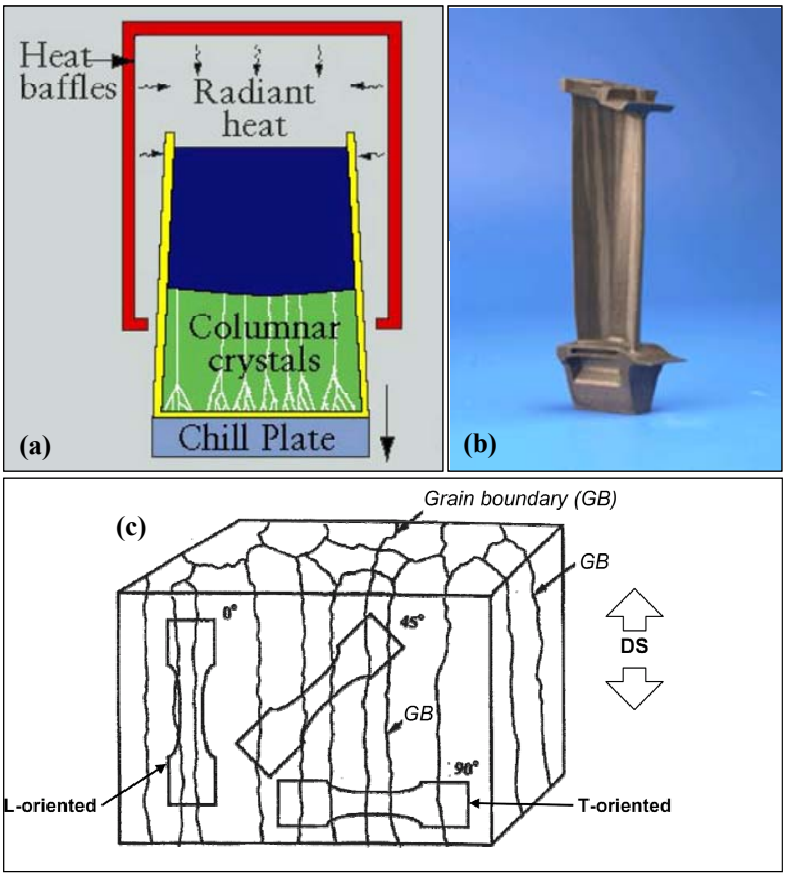

Figure 1-4: The directional-solidification process in which (a) molten material is directionally-cooled within a ceramic mold to produce a (b) DS blade. Fatigue specimens (c) can be formed from the unique orientations created in a DS casting [2, 8].

These complex casting procedures introduce additional challenges when defining and characterizing interrelated damage mechanisms and changes in the alloy microstructure which affect fatigue life [6]. Additionally, the anisotropic deformation is often difficult to predict when strongly dependent on the path history of thermal and mechanical loadings.

1.3 Research Objectives

A turbine engine's duty cycle, regardless of capacity or unit type, will invariably involve thermal transients at start-up and shut-down as well as extended periods at near peak temperature (baseload dwells) during operation. As most of the life of a typical turbine blade is spent in the initial crack formation stage, this research will have the main focus of characterizing the conditions and specific material microstructure influences associated with crack initiation for CM247LC DS under TMF loading.

More specific goals are as follows:

1.) **Conduct TMF experiments to define fatigue behavior and identify how stress concentrations and material orientation influences crack initiation.** Specimens with notches will be used to simulate geometric stress concentrations. The impact of k_t=2 and k_t=3 notches on TMF damage and fatigue life will be explored through comparison with unnotched experiments. The anisotropy associated with the orientation of crystallographic grains in directionally-solidified Ni-base superalloys also influences the driving force for crack initiation and growth. The combination of force- and displacement-controlled tests allow for any variation in the dominant damage mechanisms associated with each to be established. Post-test analysis of the fracture surfaces can identify intergranular and transgranular cracking behavior, as well as particularly susceptible sites for crack initiation.

2.) **Determine the dominant active mechanisms which develop and enhance damage during TMF and incorporate these into known methods to predict life.** Using existing data from past experiments and prior insight into material behavior from literature, mechanisms which impact life will be identified. Creep and environmental damage expected during the transients of a service engine duty cycle will be explored. These mechanisms will be quantified on the basis of cycle characteristics, such as maximum temperature T_{max}, temperature range ΔT, phase angle, and applied load. Any changes in crack initiation behavior between smooth and notched tests will be characterized. Microscopy and fractography will be used to assist in failure analysis. Results will be used to evaluate life prediction methods. This goal includes identifying microstuctural changes which may occur as a result of TMF cycling and determining the effect of these changes on the material response across the temperature range.

3.) **Characterize notch stress-strain response using FE simulations and note effects on the notch root for TMF conditions.** In conjunction with experimental observations, utilize comprehensive anisotropic-elastic and crystal visco-plastic finite element simulations to determine notch behavior. Due to material anisotropy, consistent critical locations containing either the highest effective stresses or the most significant volume of highly-stressed material can be identified. These will be notch geometry-dependant and may be offset from the notch root.

4.) **Identify the effect of microstructure morphology on the mechanical properties and thermomechanical fatigue resistance of the alloy.** As the primary strengthening mechanism, changes to the γ' precipitate phase as a result of high temperature cycling will presumably have an effect on the mechanical behavior. Experiments will define the boundaries of the γ-γ' instability and determine the effects of a rafted microstructure on the material response.

5.) **Explore life modeling approaches.** Exercise various simple and complex methods for predicting crack initiation life of the alloy under various TMF conditions. Identify the corresponding strengths and weaknesses of each model and their usefulness in design. Examine how the local notch response can be predicted and implemented under non-isothermal conditions. These steps will provide an understanding and framework for the future creation of an accurate and comprehensive life prediction model.

1.4 Overview of Thesis

This work is organized so as to outline the development process and results associated with the various experimentation and modeling stages. The general content and structure is as follows: Chapter 2 comprises a comprehensive literature review of Ni-base superalloys and their behavior under thermomechanical fatigue. CM247LC DS, its composition and structure, applications, mechanical properties, and past research on its fatigue characteristics are presented in Chapter 3. Experimental methods and testing apparatus for thermomechanical fatigue experiments are contained in Chapter 4. Chapter

5 reviews the computational finite-element modeling preliminaries, including the models, meshes and boundary conditions, and material properties used for the simulations. Thermomechanical fatigue experimental results, fracture investigation, and microscopy follow in Chapter 6. The microstructure morphology of the γ' precipitates and the associated effect on mechanical properties is reported in Chapter 7. Studies conducted on high temperature exposure and oxide growth are given in Chapter 8, along with the corresponding influence on crack initiation behavior. Chapter 9 contains an overview of constitutive and empirical TMF life prediction models for DS superalloys as well as mechanistic life modeling approaches and the preliminary correlations for the current work. Notch analysis methods used in fatigue complete this chapter. Finally, conclusions drawn from this research, and recommendations for future studies based on current observations, are presented in Chapters 10 and 11, respectively.

CHAPTER 2. BACKGROUND

To accurately predict the life of components in service, an understanding of the different mechanisms which affect the behavior of Ni-base superalloys under thermomechanical fatigue is required. Included is an overview of the typical TMF damage mechanisms prevalent in these materials, which draws heavily from accepted knowledge gained through field and laboratory testing. Subsequently, a comparative review of previous research on DS Ni-base superalloys subjected to thermomechanical loading is presented.

2.1 Damage Mechanisms Associated with Thermomechanical Fatigue of Ni-base Superalloys

Thermomechanical fatigue of Ni-base superalloys typically results in three primary damage mechanisms, which can be active to a greater or lesser extent depending on the conditions. These are fatigue, creep, and environmental degradation and their coupled effects have been investigated in great detail [2, 9-14]. A general summary is presented here.

Fatigue Damage

Cyclic inelastic strains arising are often the drivers of crack formation. Under themomechanical conditions, most efforts have focused on characterizing this mechanism through isothermal experimental data. By nature, however, the ability to effectively

characterize the drivers which differentiate TMF from isothermal LCF conditions is often quite limited. In and around stress concentrations, the stress state is highly multiaxial and the plastic zone constrained by the bulk elastic regions. This leads to considerable strain gradients, especially in the case of out-of-phase TMF cycling. Under these conditions, and especially at slow strain rates or peak temperature dwells, the application of linear stress concentration factors is insufficient to compensate for the differences between this material response and that obtained from isothermal uniaxial fatigue test data [15]. The isolation of fatigue in these cases is therefore difficult.

Classical fatigue mechanisms are prevalent at ambient or low temperatures, where cyclic deformation continually degrades material capabilities both at the macroscopic level and within the microstructure. A good example is continual slip of dislocations which leads to crack initiation within the bulk of the material. This involves the accumulation under cyclic loading of accumulated plastic strain, nominally considered under such conditions when creep and oxidation do not affect life [16]. Under typical loading conditions, the resolved plastic strain amplitude is only a fraction of the total strain amplitude due to reverse slip and work hardening normally associated with ductile single crystals. The overall inelastic strain range, however, is typically represented within the fatigue life term, given as

$$N_i^{fat} = C_{in}(\Delta\varepsilon_{in})^{d_{in}} \tag{2.1}$$

where C_{in} and d_{in} are constants. This relation works well under continuously-cycled isothermal conditions where there is little developed mean stress and sufficient inelastic

strain to model. In high-strength materials such as Ni-base superalloys, however, the plastic strain component is often virtually inert, rendering it unusable outside experimental error for fatigue life prediction techniques. In many cases, it was found that an accurate approach needed to utilize the entire strain range and include the effects of a mean stress [17]. Generally, a typical approach such as the Goodman Model would include a mean stress for the given plastic or total strain range, although the variety of simplified fatigue damage terms are too numerous to discuss here.

The stress-strain response under TMF is quite different from isothermal LCF conditions. This is congruent with the fact that the hysteresis loop shape is the result of combined fluctuations of elastic modulus, yield strength, and imposed mechanical strain with temperature. It has been shown that for equivalent loading, TMF can result in more or less material degradation than a pure isothermal LCF test, depending greatly on such factors as material microstructure, cyclic rate, *R*-ratio, and environmental factors, and maximum cyclic temperature, T_{max} [18]. They often also embody different damage and failure modes. Here, the analysis can often be broken down into a cyclic statics problem with a heat transfer component, where properties such as elastic modulus, coefficient of thermal expansion, and thermal conductivity are temperature-dependent material parameters which characterize the loading. The most important mechanical properties for this analysis are ductility and toughness, both of which strongly enhance the resistance to fatigue damage. Beyond this, failure mechanisms are also associated with inclusions, microscopic flaws at grain boundaries, and inhomogeneities in composition. As a result of these complexities, which are not accounted for within a lone fatigue damage term, a well-accepted framework for the prediction of TMF life has been elusive.

Creep-Fatigue Mechanisms

Traditional cyclic-plasticity driven fatigue cannot effectively account for all damage occurring within a TMF cycle. Viscous creep deformation contributes to the formation and propagation of microcracks, as well as the growth and rupture of intergranular cavities. These often impede the re-welding of crack surfaces which can occur upon unloading [19]. Such time-dependent mechanisms can play an important role in the inelastic strain history at high temperatures, so limiting the extent and degree to which they occur in applications is of high importance. From a design standpoint, creep deformation of less than 1% is desirable for gas turbine blade applications, as cast Ni-base superalloys often fail from brittle fracture after minimal elongation due to creep damage sustained at extreme operating temperatures [20].

Creep rupture data is usually presented in a Larson-Miller curve, a compact form which conveys an alloys performance over a wide range of temperatures and stress ranges. This is very useful in comparing the creep rupture capabilities of multiple materials. The Larson-Miller parameter, LMP, is given as

$$LMP = T(20 + \log t) \times 10^{-3} \tag{2.2}$$

where T is the temperature in Kelvin and t is the rupture time in hours.

Various studies have been conducted to characterize the impact of creep damage on the fatigue life of Ni-base superalloys. This can be done by utilizing dwells superimposed within a fatigue cycle. This tends to shorten the crack initiation life of the alloy, as shown for smooth specimens by Reger and Remy [21] and for smooth and

notched specimens by Moore [17]. Severe tensile creep in this type of cycle typically promotes failures at defects within the material, such as voids, pores, and inclusions. In additions to DS materials, this was also shown to be true for the single crystal Ni-base superalloys CMSX-2 and CMSX-4 by Okazaki [10].

Environmental Effects

Environmentally-assisted crack initiation in service run blades typically occurs in a three-stage sequence: (1) cracking of the overlay coating and the resulting environmental attack of the coating material; (2) attack of the interdiffusion zone and bulk metal by the environment; and (3) crack initiation in the base metal. Metallurgical evidence has suggested the environment plays a crucial role in this process, as environmental attack precedes crack initiation through the formation of both oxide layers and a detrimental γ'-depleted zone [11, 22]. The observance of intergranular crack formation and propagation serves as further evidence of sustained environmental damage ahead of the crack tip. This behavior is often due to preferential oxidation of the grain boundaries, which can change the fatigue fracture mode from transgranular to intergranular.

Oxidation plays a crucial role in the crack initiation behavior of Ni-base superalloys at high operating temperatures. Oxygen is the primary environmental effect which reacts with, and incidentally, changes the compositional makeup of the exposed alloy. Uniform oxidation at moderate temperatures- at or below 870°C (1600°F) has been shown not to be a major problem. At higher temperatures, attacking oxygen induces a chemical reaction with aluminum content in the alloy, resulting in the formation of a

protective Al_2O_3 layer. Generally, however, the Al content of most superalloys is insufficient to provide long-term oxidation protection and thus protective coatings are applied (see section 2.3 below).

The effect of a harsh environment on fatigue life was demonstrated on polycrystalline IN-100 by Reger et al. [23]. At 1000°C, tests conducted in a pressurized vacuum exhibited significantly increased lifetimes when compared to identical test conditions in ambient air. The severity of environmental damage was manifest in the fact that for even a small inelastic strain range, $\Delta\varepsilon_{in}$ = 0.01%, the difference in life between vacuum and ambient tests was nearly a factor of 100.

Further tests demonstrated that increasing the maximum temperature greatly increased and accelerated the environmental attack on the material. This also triggered a significant increase in observed surface cracking of the oxide layer. This effect was observed by Duquette [24] through tests on MAR-M200 in both a vacuum and air. The environment had a negligible influence on the fatigue lifetime when the isothermal test temperature was reduced from 927°C (1700°F) to 760°C (1400°F).

Environmental damage accumulation is often modeled as a measure of surface and crack tip oxidation and γ' depletion kinetics [25]. The extent of this environmental contribution to fatigue life is governed by the phasing of the thermomechanical cycle. Oxidation depletes Al and Cr near exposed surfaces (including those of the crack), which are the primary constituents of the γ' strengthening phase. The weakened γ' depleted zone is then more susceptible to crack initiation and subsequent accelerated crack growth. Oxidation and γ' depletion in Ni-base superalloys has been shown to follow a parabolic growth law [25, 26], represented by

$$h = \sqrt{K_p t} \tag{2.3}$$

where h is the average thickness of the oxide layer, t is the time of exposure measured from the instant fresh metal is subjected to the environment, and K_p is the temperature-dependent parabolic growth constant.

Oxide layers display comparatively brittle characteristics at the operating temperatures of hot section gas turbine components. In the presence of mechanical loading, the uneven thermal strain distribution and mismatch in elastic modulus across the oxide/metal interface can result in localized stresses which can fracture the layer [27]. This results in the oxide spiking and spallation mechanisms, as illustrated in Figure 2-1. Damage accrued in this way is especially prevalent in out-of-phase TMF, where oxide layers formed at the maximum temperature are cracked in the following tensile phase. Esmaeili et al. [11] demonstrated that several other factors influenced the oxidation process in the Ni-base superalloy IN 713LC under OP TMF conditions:

- Increasing the mechanical strain range impacts the general oxidation of the alloy by accelerating the growth rates of both the oxides and γ' depleted zone
- The introduction of a hold time under TMF loading enhances the oxidation process
- Oxide scale spalling and/or fracturing during cyclic loading reduces the protective effectiveness of the layer, and can change the parabolic growth kinetics to a more linear trend.

In addition, oxides at grain boundaries can generate internal residual stresses in their vicinity and in adjacent grains. Combining these mechanisms with the specific intrinsic reactivity of the microstructural composition, the corrosion and rupture kinetics of a particular material can be classified. For DS superalloys, Gordon et al. [28] demonstrated that a critical oxide rupture thickness, $\overline{h}_f$, can be correlated to the mechanical strain range through a power law trend, which can then be implemented in a physical crack initiation model for the particular material [28, 29].

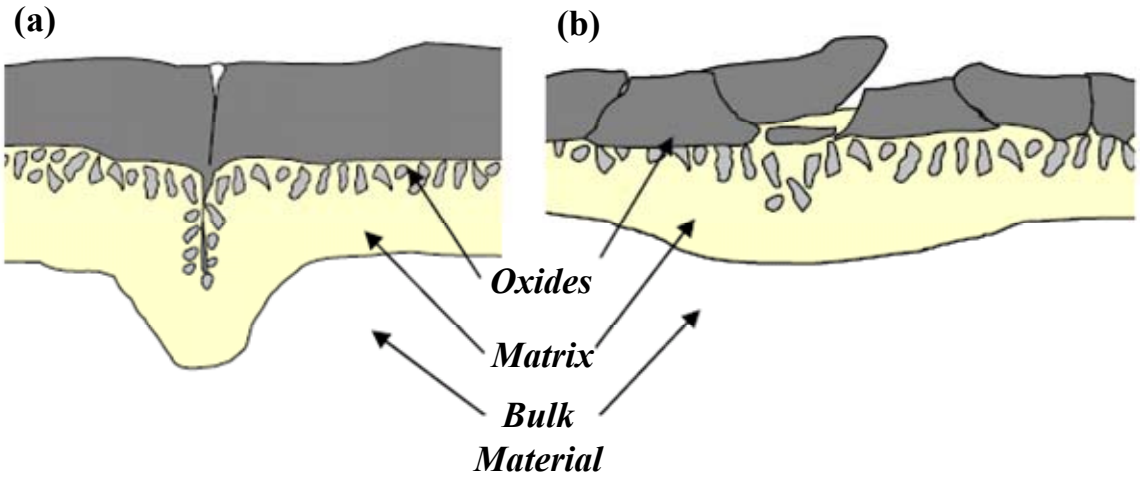

Figure 2-1: Interaction between surface oxides and mechanical loading causing (a) oxide spiking and (b) oxide spallation [2].

2.2 General Thermomechanical Fatigue Behavior of DS Ni-base Superalloys

The thermomechanical fatigue cycles occurring in gas turbine operations, and thus the duty cycle of individual fleet units, have a very strong correlation to the service life of components. Specifically, data compiled by Boyce [20] shows the number of transients (starts) per operating time has a highly deleterious effect on the life of turbine

blades. These operations result in sequences where the combustion process flow and turbine rotor rotation either have yet to initiate or are predominantly out-of-phase. These increments of the operating cycle can be most degrading to components in terms of the accrual of thermomechanical fatigue damage. This behavior can best be described by the sequences in Figure 2-2 below.

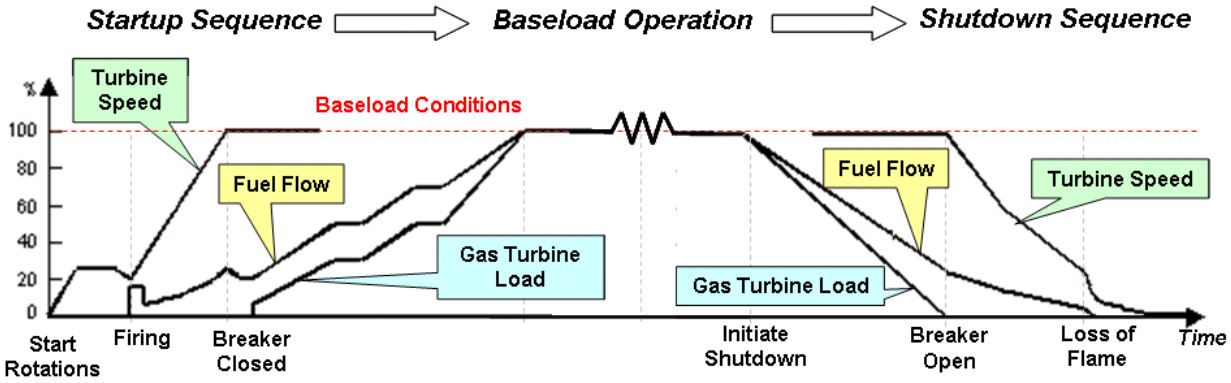

Figure 2-2: Typical gas turbine operation sequence. The breaker is only opened when the unit revolution frequency is synchronized with the electrical grid. Turbine load is synonymous with power generating capacity utilized [30].

In reality, the phasing and severity of loading experienced in service is non-linear and depends greatly on location at a sub-component scale. For laboratory testing, where simplicity is often paramount to achieve comparable and representative results, linear waveform inputs which are more severe than service conditions are often used. Independent variations which exist concurrently in both applied temperature and mechanical load during thermomechanical fatigue create a phase difference, ϕ, between the two. Several simple cycle types are shown in Figure 2-3.

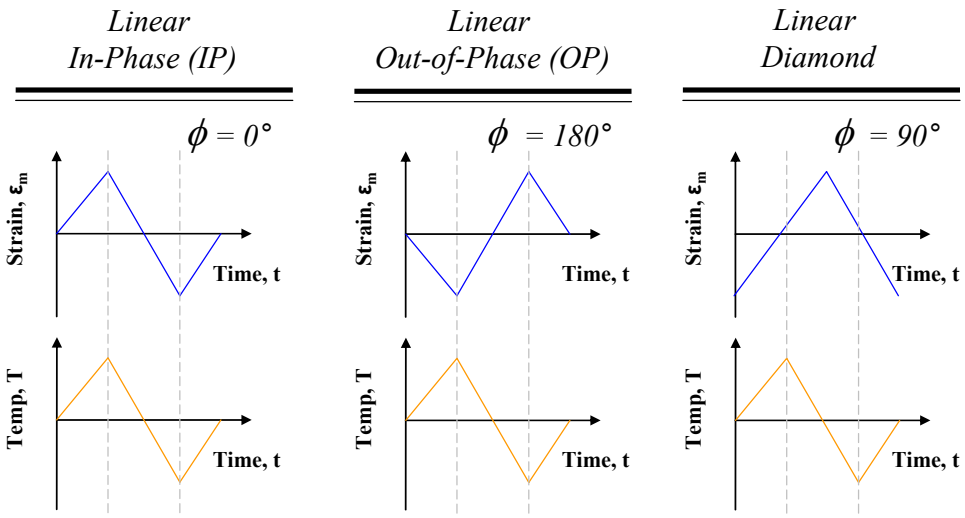

Figure 2-3: Schematics of common linear TMF laboratory cycle types

Generally, if the maximum tensile stress occurs at the peak temperature, the cycle is said to be "in-phase" and the phase angle $\phi = 0°$. Conversely, if the maximum temperature corresponds to peak compression ($\phi = 180°$), the cycle is said to be "out-of-phase". Depending further on choice of phasing, various other linear and non-linear cycle types are possible.

Damage mechanisms and TMF life characteristics can shift due to phasing. High tensile stresses at maximum temperature (IP) would tend to favor creep and the accumulation of inelastic strain at the apex of each cycle. In this case, a mean stress manifests rapidly and failure typically occurs through fatigue damage. Alternately, high tensile stresses at more moderate temperatures (OP) results in the cracking of accrued oxidation, and the acceleration of environmental damage from exposure to subsequent high temperatures. The simple linear OP waveform is approximately representative of the operating conditions of the leading edge of a turbine blade, where, during steady state operation, the surface is in compression due to thermal stresses from internal air cooling.

The surface stresses relax considerably during service at high temperature, thereby increasing the maximum tensile stresses experienced during shutdown. A diamond cycle typically results in a mixture of these two modes, with the suppression of damage due to both extreme lives resulting in significantly lengthier fatigue lives than both pure IP and OP cycling. Loche [31] presented a basic decomposition of damage mechanisms occurring during simple IP and OP mechanical strain-controlled TMF cycles, shown in Figure 2-4. This classification is not rigid, however, as a change in T_{max} will precipitate a correlative change in damage contribution.

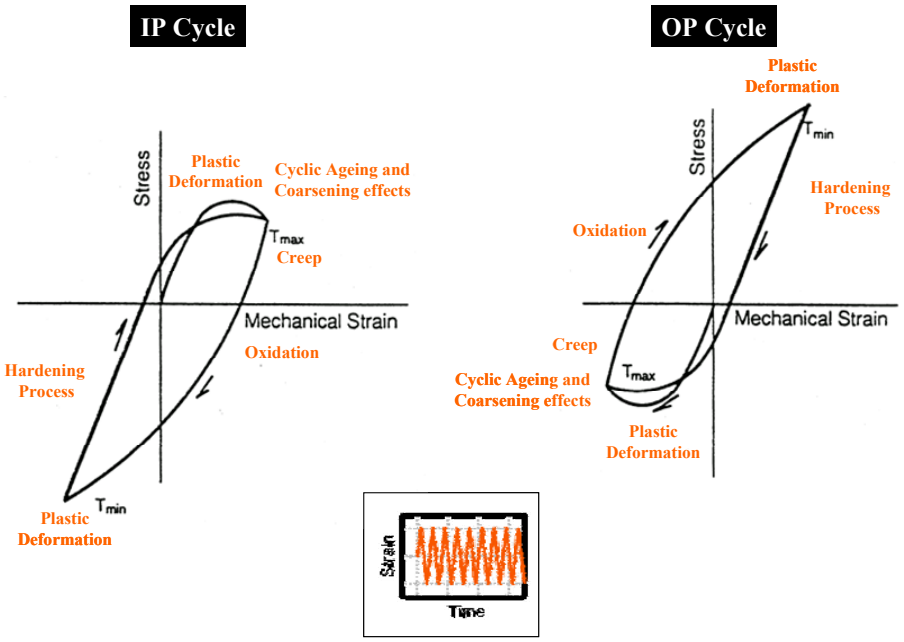

Figure 2-4: Damage mechanisms occurring in IP and OP mechanical strain-controlled TMF cycles, according to Loche [31].

Significant cyclic inelastic strains at high loads results in IP cycling being more damaging. Similarly, an analogous conclusion can be shown for low load levels, where a tensile mean stress and environmental exposure results in OP TMF having reduced fatigue resistance. Therefore, at a certain material-dependent strain level, most materials

will exhibit a crossover in predicted IP and OP fatigue lives. Accordingly, life prediction methods based on fatigue, creep, or environmental damage alone are often insufficient to accurately forecast fatigue lives. In addition, for any fully-reversed TMF strain cycle, a mean stress develops due to the disparity of the response to temperature at each extreme of the cycle.

A comprehensive assessment of the thermomechanical fatigue behavior of the Ni-base superalloy Mar-M247 was conducted by Boismier et al. [13] which exhibited the three primary damage mechanisms discussed in Section 2.1. Isothermal tests were performed in addition to in-phase and out-of-phase thermomechanical fatigue experiments in the temperature range from 500°C to 871°C. All testing utilized uniaxial smooth specimens in mechanical strain control. Results indicated that life depended on strain-temperature phasing as well as strain rate. OP tests corresponded well with isothermal tests at peak temperature, while the IP trends did not match as well due to a greater sensitivity to the applied strain range. This is demonstrated by the strain-life curves shown in Figure 2-5. The fatigue lives for in-phase tests were lower than those of out-of-phase for high strain amplitudes, but this trend was reversed for low strain amplitudes.

Post-test metallographic examination revealed the expected oxide layers and γ' depleted zones, indicating the presence of environmental damage. Crack initiation for all TMF experiments was intergranular, associated with preferentially oxidized grain boundaries at the surface. Crack propagation continued to be intergranular for IP experiments, while OP and isothermal experiments quickly deviated from the grain boundaries and grew transgranularly.

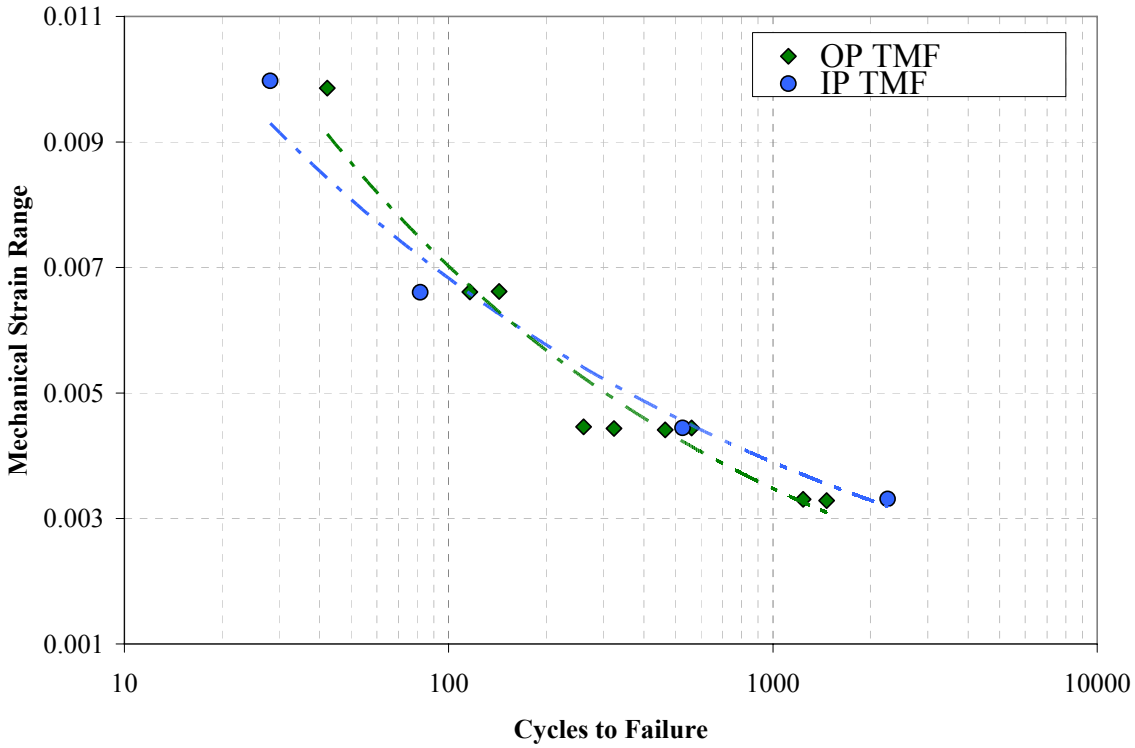

Figure 2-5: Mechanical strain range versus life for out-of-phase and in-phase TMF of MAR-M247. In all cases, R = -1 and $\dot{\varepsilon}$ =5x10^{-5} 1/s [13].

Similar results were obtained for the testing of directionally-solidified GTD-111 by Gordon [2], as shown in Figure 2-6. When crack initiation was defined by a 20% load drop, initiation lives for both IP and OP TMF samples were less than those of isothermal tests conducted at the peak temperature. Again, IP proved most damaging at high strain ranges. Cracks formed in specimens with transverse grains at least seven times sooner than their longitudinal counterparts. Increasing T_{max} reduced the fatigue life for both orientations.

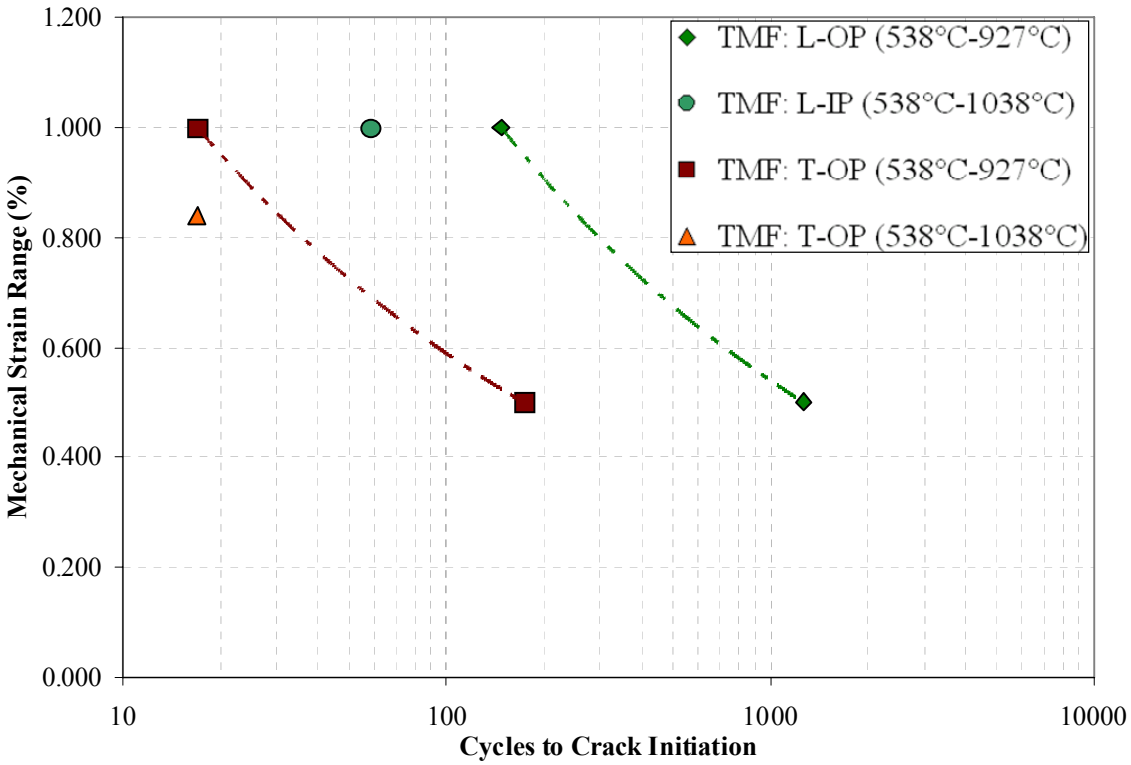

Figure 2-6: Mechanical strain range versus life for out-of-phase and in-phase TMF of DS GTD-111. In all cases, R = -1 and the cycle time was 180 s [2].

Extensive microscopy revealed the dominance of creep and fatigue for IP testing and environmental damage in OP cases. Thermal strain disparities between the oxides and metal substrate resulted in scale spallation during IP cycling and oxide spiking under OP conditions, shown in Figure 2-7. Grain boundaries at the surface for T-oriented samples provided the primary sites for crack initiation, which then propagated along grain boundaries and in the interdendritic region. In longitudinal testing, initiation was more often due to subsurface carbides or inclusions, after which cracks grew in a transgranular fashion.

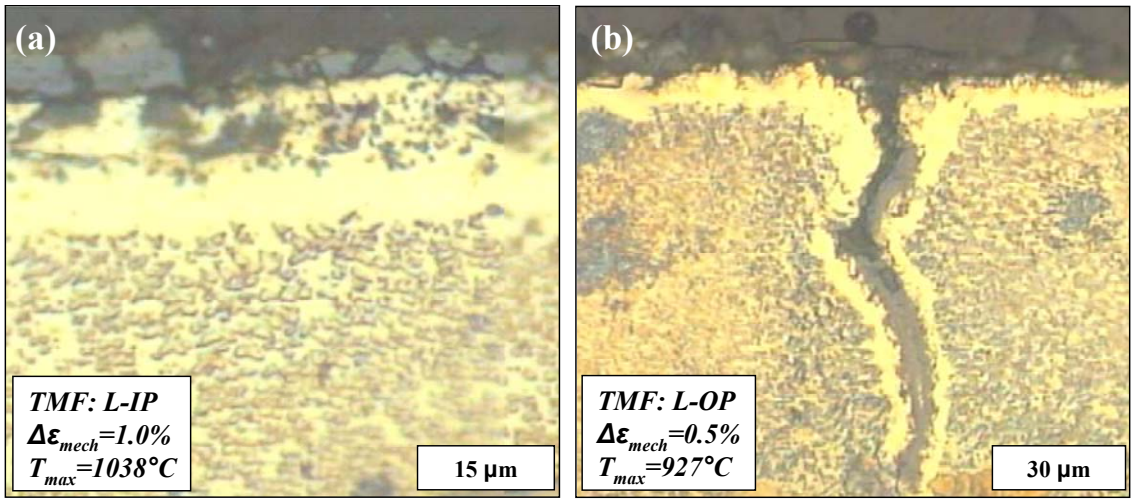

Figure 2-7: Oxide a.) spallation during IP and b.) spiking during OP TMF of DS GTD-111. In both cases, R = -1 and the cycle time was 180 *s* [2].

Embley and Russell investigated the response of two superalloys, IN 738 and polycrystalline GTD-111, to both simple linear loading cycles and more realistic "engine" cycles [32]. The "engine" cycle waveforms were considerably more complex and designed to imitate service startup and shutdown conditions at the blade leading edge and trailing edge, as shown by representations in Figure 2-8 below. It was discovered that maximum tensile stress and greatest cycle temperature were the critical parameters influencing life [32]. Crack initiation life results are shown in Figure 2-9. Due to the tensile strains generated at the lowest temperature, it was found that the linear OP cycle (TMF-OP) was the most damaging. "Engine" waveforms with holds at compressive strains induced a tensile mean stress. Of these, the cycles with the highest cycle temperatures were shown to have the shortest lives.

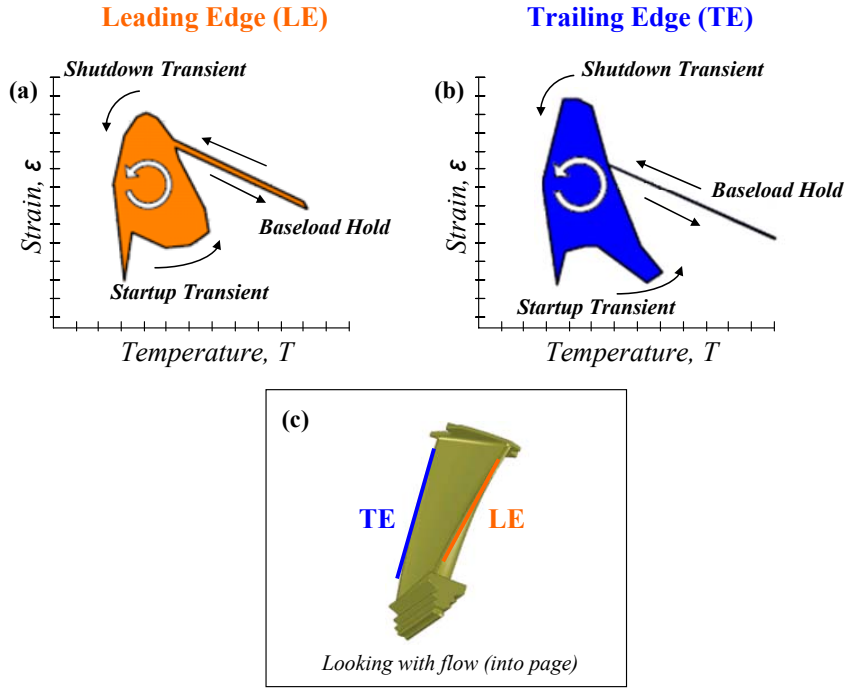

Figure 2-8: Realistic "engine" cycles for strain as a function of temperature for different engine cycle regimes at a cooling hole located (a) at the leading edge and (b) at the trailing edge. Blade orientation is shown in (c) with respect to flow [32].

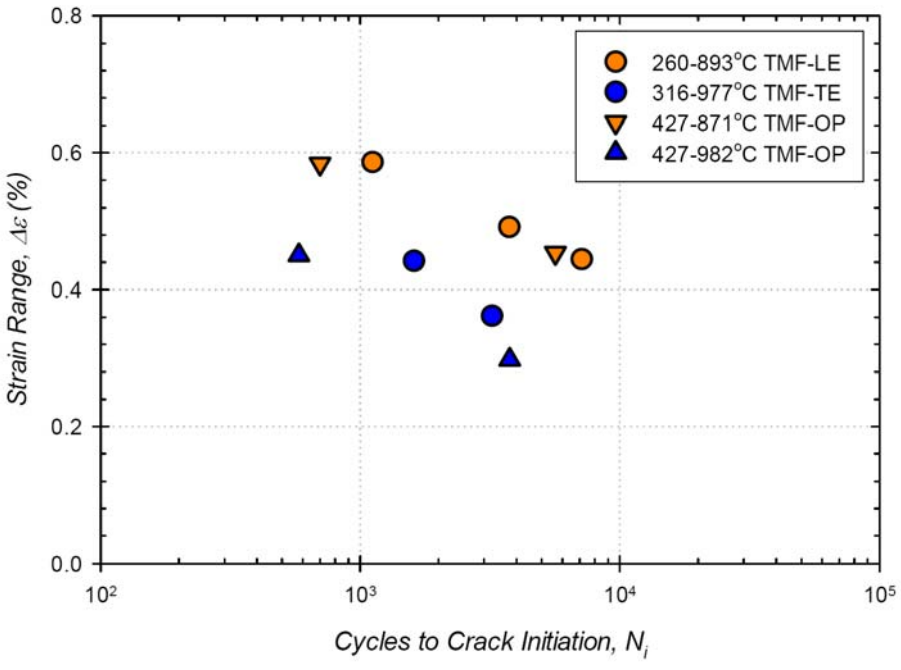

Figure 2-9: Crack initiation lives of PC GTD-111 for different TMF cycles [32].

2.3 Thermomechanical Fatigue Behavior of Coated Ni-base Superalloys

Maintaining cool metal temperatures is essential to extending the LCF life of metal parts. For actively cooled gas turbine components, such as blades, an extensive thermal gradient develops between the heated and cooled surfaces. For mechanically constrained components this often results in very high multiaxial stresses, which in some cases may even exceed those due to mechanical loading [33]. In order to maintain cool metal temperatures while simultaneously allowing for higher combustion temperatures to boost efficiency, thermal barrier coatings (TBC) are now extensively applied to hot section components in gas turbines. These coatings usually consist of two layers; an adhering metallic bond coat, which also serves to prevent atomic diffusion between the substrate and coating, and a thermally-insulating ceramic layer which serves the purpose of protecting the underlying part from oxidation and corrosion.

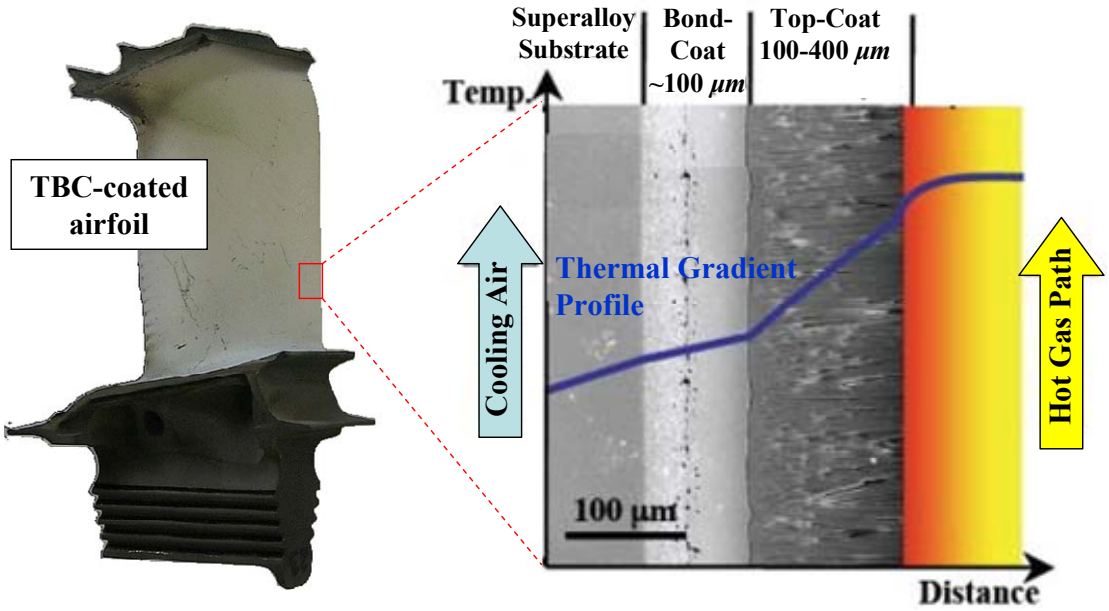

Figure 2-10: A TBC-coated Ni-base turbine blade and its associated composite cross section, showing the temperature profile through the surface [34, 35].

The bond coat composition is typically NiCoCrAlY. This coat is responsible for forming a thermally-grown stable oxide layer of alumina (Al_2O_3). This layer further protects the substrate by serving as an oxygen diffusion barrier. The ceramic topcoat is composed of yttria-stabilized zirconium (YSZ), whose low thermal conductivity at operating temperatures insulates the lower layers [36].

Several degradation modes for exist specifically for coated Ni-based superalloys. Severe thermal gradients can induce fatigue cracking and subsequent failure of the ceramic top coat through spallation, which would likely result in localized over-temperature and thermal cracking of the parent component. Both of these phenomenon are shown in Figure 2-11 below. Additionally, the bond coat contains a finite reservoir of the reactive Al and Cr scale-forming elements, and interdiffusion with the substrate can both deplete these elements and introduce other elements into the coating.

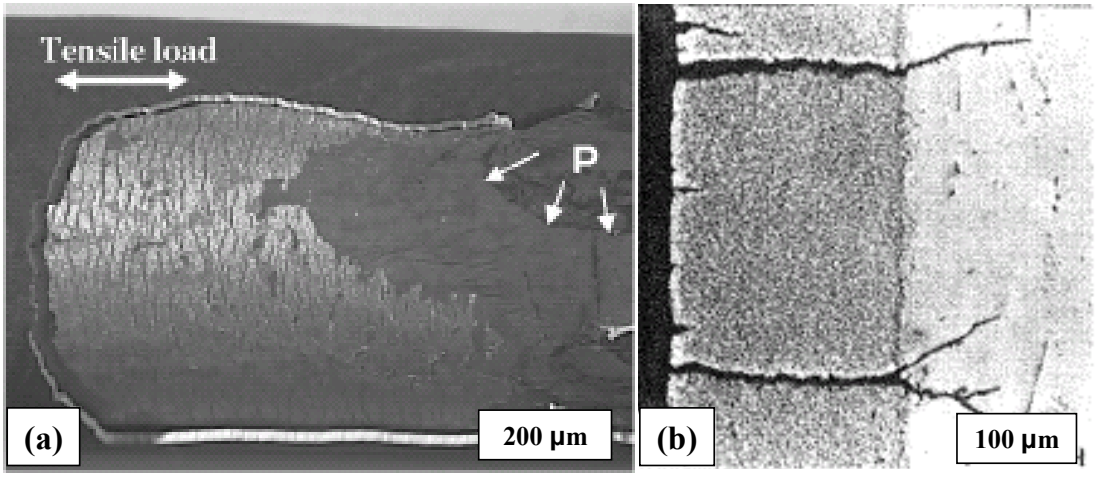

Figure 2-11: Coated Ni-base superalloys with fatigue damage from (a) coating spallation with crack fronts marked with white arrows and (b) crack propagation in the near-surface region of a longitudinal section [33, 37].

Bartsch et al. [33, 38] characterized the thermomechanical fatigue behavior of coated, directionally-solidified IN 100 DS tubular specimens subjected to a controlled thermal gradient through the wall thickness. Failure of the TBC system resulted from delamination of the ceramic top coat. This spallation, and the consequent exposure of the metallic bond coat, induced fatigue cracks in this layer which propagated parallel to the surface (normal to the primary loading axis). Although there was no observed cracking in the underlying IN 100 DS substrate, the accumulation of inelastic strain due to creep-fatigue damage imposed additional tensile loads on the coating and contributed to further crack growth.

Kowaleski et al. [37] investigated the effect of applied coatings to the fatigue life of PCA-1 (NiCrAlY) composite-coated CM247LC DS. The PCA-1 is a diffusion coating which often serves as the bond coat for TBC. Isothermal LCF and out-of-phase TMF tests were performed on both coated and uncoated cylindrical fatigue specimens. Results demonstrated that under both conditions, fatigue behavior of the coating/substrate alloy was governed by that of the coating. A minimum fatigue lifetime was observed at about 600°C, or near the ductile-to-brittle transition temperature of the PCA-1 coating material. This further demonstrated the reliance of composite on the fatigue properties of the coating material. In general, cracks which initiated in the coating easily traversed to the substrate material. Overall, the fatigue life of the coated alloy was shown to be less than that of the uncoated material for the same temperature history, as shown in Figure 2-12.

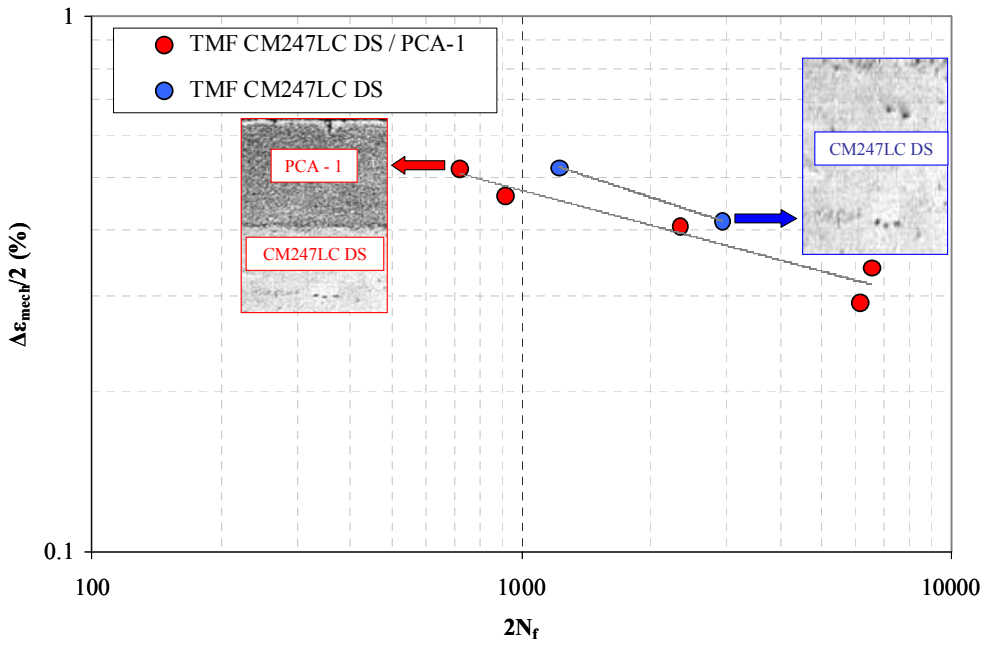

Figure 2-12: TMF life comparison of virgin CM247LC DS and coated with oxidation-resistant PCA-1. In all cases, T_{min} = 400°C, T_{max} = 1000°C, R = -1, and $\dot{\varepsilon} = 3.17\times10^{-3}\cdot 1/s$ [37].

2.4 Thermomechanical fatigue of notched specimens

Thermomechanical fatigue tests were performed by Mazza and Columbo et al. [15, 39] on circumferentially notched round bar specimens. Using a service-like TMF cycle with temperature ranging from 300°C to 565°C, experiments were run using both diametric and axial displacement control with electric potential drop as the crack detection method. Several TMF tests were conducted on unnotched uniaxial specimens, and several of these contained a one *hr* dwell at peak temperature to simulate baseload operation. Both TMF waveforms used are shown in Figure 2-13. Control profiles were selected so as to reproduce at the notch root turbine component conditions experienced during service. This was done by using finite element situations to define expected strain ranges in the notch. A constitutive model determined previously by Columbo [40] and

outlined in the literature included both time-independent and time-dependent plasticity as well as temperature-dependent material parameters determined through monotonic isothermal tests. Life results were compared to isothermal notched and unnotched LCF tests (some containing the 1 *hr* dwell at ε_{max}) conducted at 565°C.

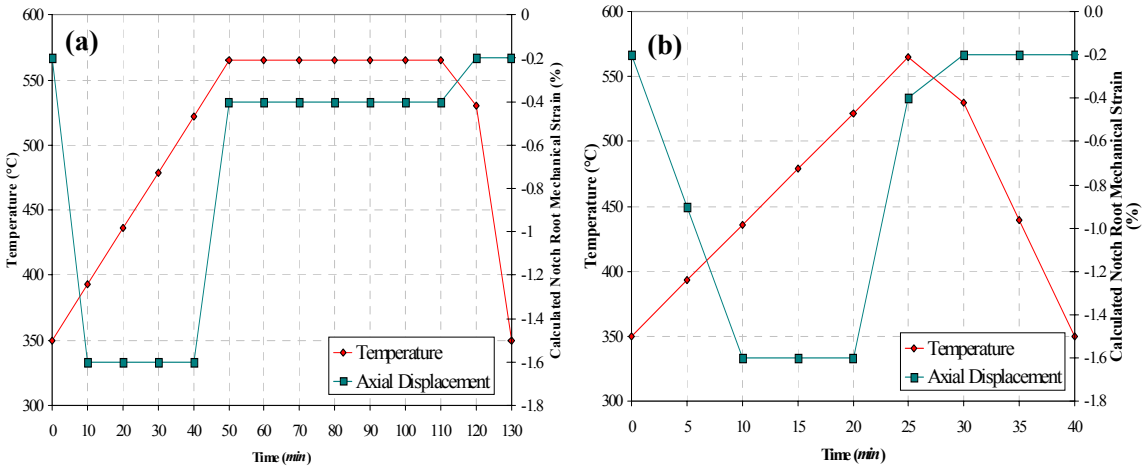

Figure 2-13: Service like TMF cycles (a) with 1 *hr* hold time and (b) as a continuous cycle [39].

Cycles to crack initiation for a crack size of 0.1 *mm* are plotted in Figure 2-14. Continuously-cycled notched TMF results correlated well with both uniaxial TMF and LCF tests with the 1 *hr* dwell period. The notched LCF test more closely matched the LCF and TMF tests with no dwells. Post test metallographic inspection revealed that cracks in notched specimens, in contrast with their smooth counterparts, were fully circumferential by the time they had penetrated to a depth of 0.7 *mm* [39]. Crack growth in notched specimens, however, was found to be much slower than that in uniaxial smooth samples for the same nominal TMF cycle. This was due to a decrease in the reference stress in the net section of the notched specimens, which was significantly

lower than that of uniaxial samples. The driving force for crack growth and creep damage development was thus substantially lower outside of the near field influence of the notch. Therefore, for identical crack initiation criteria, an increase in endurance could potentially be observed for notched tests in which the slow rate of crack growth would influence detection.

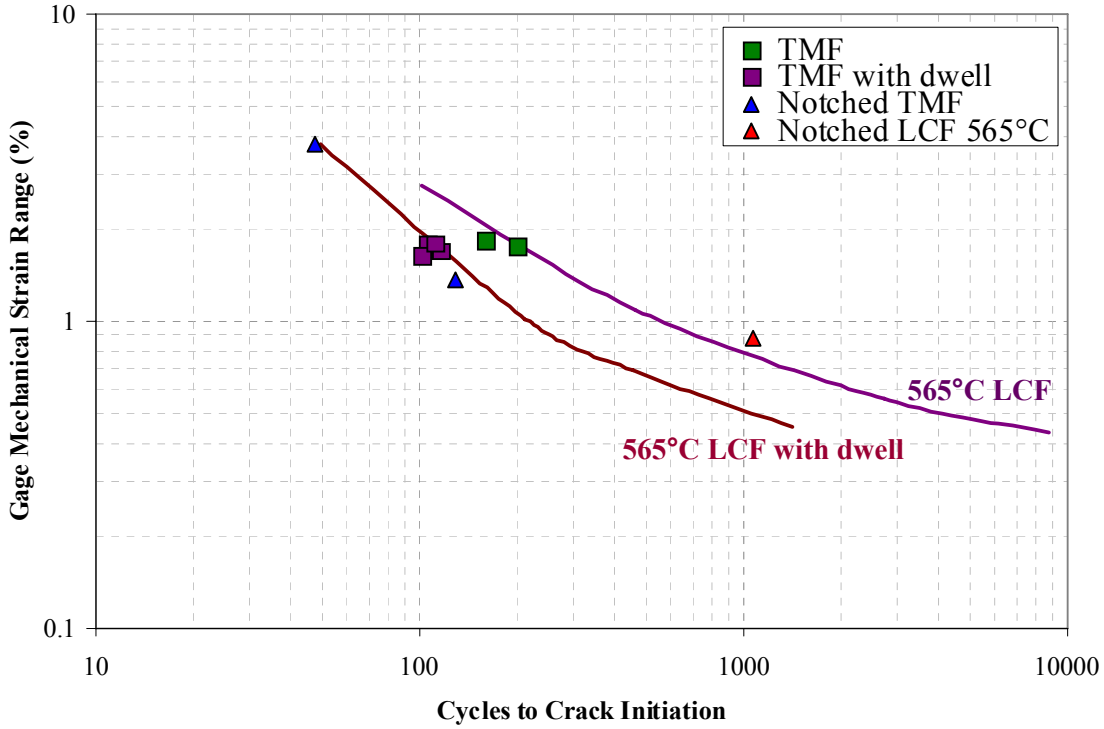

Figure 2-14: Cycles to crack initation for notched and unnotched 1CrMoV rotol steel subjected to several isothermal and TMF cycles [39].

The measured crack growth in notched TMF tests was shown to be greater than that of a comparable notched isothermal LCF test [15]. This was due to a greater strain range present at the crack tip under TMF conditions, as demonstrated by finite element analysis. Crack development in notched TMF specimens contained evidence of creep damage, unlike those under isothermal notched conditions.

These studies concluded that, assuming a crack of minimum initial size, it was possible to use uniaxial (unnotched) TMF fatigue data with appropriate dwell times and the same T_{max} to predict with reasonable accuracy the expected crack initiation lives of notched specimens [39]. Analysis showed that simple isothermal LCF data with holds could not be used for the same purpose in circumstances where stress relaxation at high temperature would be constrained by high triaxiality. Such cases would need to more comprehensively account for the interaction of creep and fatigue damage.

2.5 Microstructural Influences on Fatigue

As mentioned earlier, the distribution, density, and morphology of the γ' precipitate phase can substantially affect the deformation response and therefore the fatigue life of Ni-base superalloys. The role of these microstructural properties in fatigue at notch roots was investigated by Tjiptowidjojo et al. [41]. A cyclic visco-plasticity model was developed which contained explicit dependence on the underlying microstructure through the variation of grain size distribution and primary, secondary, and tertiary γ' volume fractions and size distributions. To populate the model, cyclic simulations were performed. The basis of the model comprised several parts; a.) a continuum-based crystal plasticity model at the grain scale which contained the kinematic formulations for lattice deformation, b.) a macroscopic creep-plasticity model which included both rate-dependent and independent deformation processes for differing loading conditions, and c.) a collective of representative γ-γ' microstructures exhibiting different characteristics to observe the effect of microstructure properties on the stress-strain response. Simulations indicated that a finer grain size or an increase in the quantity

of density of small secondary γ' precipitates yielded a greater resistance to primary creep deformation and the associated high temperature stress relaxation. The sensitivity of fatigue at the notch root to the microstructure indicated that crystal visco-plastic calculations can be applied to macroscopic constitutive relations and used for localized notch analysis. Because the model can target specific volume fractions and precipitate sizes, it can potentially be used to model the effects of γ' precipitate rafting in Ni-base superalloys.

This approach was expanded by Shenoy et al. [42] to create a microstructure-sensitive model for polycrystalline Ni-base superalloy IN 100 at 650°C. The rate-dependent crystal plasticity formulation correlated the mechanical behavior of the alloy to capture the effects of grain size, γ' precipitate size distribution, and γ' precipitate volume fraction. The contribution to the constitutive response of declining γ (increasing γ'), for example, could be incorporated into the macroscopic crystal plasticity formulation. This relational framework is shown in Figure 2-15. The work of Reppich [43] and Heilmaier [44] was used to determine the increase in the critical resolved shear stress (CRSS) based on precipitate size for a fixed volume fraction of precipitates in IN 100. Although the model is limited to uniaxial loading at 650°C, the framework is laid out to link microstructural variations to the macroscopic stress-strain response.

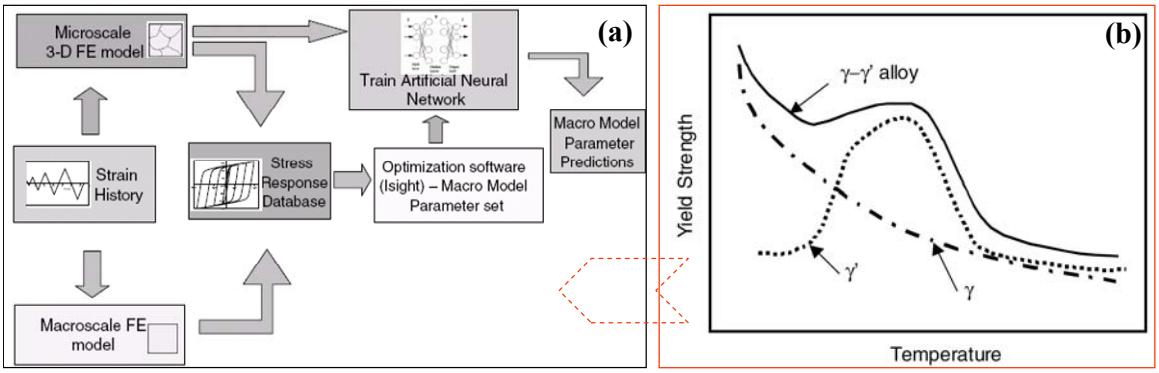

Figure 2-15: (a) Framework for linking the 'macro' model to the microstructural dependencies of the 'micro' model, such as (b) the combined effects of the γ and γ' phases on yield strength as a function of temperature in Shenoy's model for IN 100 [42].

A similar model was expanded by Shenoy [45] to account for non-metallic inclusions in Ni-base superalloys. The relatively random distribution and orientation of carbide inclusions within the alloy matrix results in a high probability there will be a critical location vulnerable to fatigue crack initiation. Relevant microstructure parameters, such as elastic properties and geometric attributes of the inclusion, as well as the crystallographic orientation of the surrounding grain, are incorporated into the crystal plasticity framework already discussed. FE models were developed containing inclusions modeled as partially de-bonded from the surrounding matrix, creating a stress concentration. The effects of inclusion spacing, orientation, and aspect ratio are included to model microcrack growth with LEFM approaches. The resulting plastic strains were computed, and the framework estimated fatigue crack initiation as a combination of formation and small crack propagation.

McDowell [46] suggested placing an emphasis on computational micromechanics to evaluate the cyclic plasticity which drives crack initiation at microstructural scales. As current correlations and predictive methods are suggestions in supporting fatigue resistant-designs, sorting the specific behaviors and trends derived from micro

structurally small crack initiation and growth is of primary importance. As the crack tip displacement range, ΔCTD, can be taken to be the driving force for small crack growth, a propagation such as

$$\left(\frac{da}{dN}\right)_{MS/PS} = G(\Delta CTD - \Delta CTD_{th}) \tag{2.4}$$

where da/dN is the microstructurally-small and physically-small crack propagation rate, and G is a constant which accounts for interactions with a given microstructure. As the crack propagates further, traditional da/dN versus ΔK_{eff} relations can be used. Such methods are capable of extending the current estimation of fatigue life at notches to stress concentrations on a microstructural scale.

CHAPTER 3. METALLURGY AND MECHANICAL BEHAVIOR OF CM247LC DS

This section introduces the microstructure, composition, properties, and manufacturing of CM247LC DS. First, the metallography procedure and virgin material structure are examined. Subsequently, previous studies regarding fatigue of the material and the associated impact on this work are addressed. Combined with an understanding of the metallurgy, this allows an overall characterization of the anticipated material behavior.

3.1 Metallography of Test Material

The material as received was in the form of three directionally-solidified casting slabs of nominal dimensions 106.7 *mm* x 26.7 *mm* x 215.9 *mm* (4.20" x 1.05" x 8.50") with the longitudinal orientation in each case being along the long axis of the slab. The slabs were heat treated to the specifications used for in-service CM247LC DS blade material to obtain an accurate representative microstructure. This is the closest representation which can be obtained short of removing material from a casting of the actual blade geometry.

Metallalography work was needed to prepare tested and un-tested specimens for microscopy and/or fractography. Both a light optical microscope (LOM) and scanning electron microscope (SEM) are used to observe the microstructure of the material. The

basic steps for preparing the specimens include sectioning, mounting, grinding, polishing, and etching.

Samples were first sectioned to reveal the desired viewing plane. After sectioning, all samples (except fracture surfaces) were cold-mounted in Struers® Epofix resin, HQ. The resin was solidified by adding the appropriate amount of Struers® Epofix hardener, HQ. The mount was allowed to cure for at least 12 *hrs* before being ground and polished via the procedure in Table 3-1. A Struers® RotoPol-15 polishing machine was used for all polishing steps, handling the applied force and spin speed. Between each step, specimens were rinsed gently in acetone and distilled water, then dried with compressed air.

Table 3-1: Grinding and polishing steps

Step	Procedure	Polishing Disk (Composition)	Applied Force (N)	Speed (RPM)	Suspension	Lubricant	Duration (min)
1	Coarse Grind	MD Piano (Resin bonded diamond disk)	30	150	None	Water	5
2	Fine Grind	MD Allegro (Composite disc)	25	150	DiaPro Allegro Largo	None	8
3	Coarse Polish	MD Mol (Woven wool)	20	150	DiaPro Mol	None	8
4	Fine Polish	MD Chem (Porous synthetic)	15	150	OP-S Suspension	None	2

A rainbow test was used to determine which etchant composition and exposure duration best defined the dendritic and grain boundary structures and which most distinctly brought out the γ-γ' microstructure. The best results for both structures was achieved with Kalling's 2, or Green contrast, which is listed as etchant #94 in ASTM standard E407-99. The etchant mix is listed in Table 3-2. Samples were submerged in the

etchant mixture for 45 *s* and immediately rinsed thoroughly in water. To ensure the etchant took effect, visibility of the dendritic structure was checked with an optical microscope. Grinding, polishing, and etching steps were repeated, if necessary, until satisfactory results were obtained.

Table 3-2: Etchant Mix

Cinstituent	Chemical Formula	Quantity
Ethanol	95% CH_3CH_2OH	80 *mL*
Copper Chloride	$CuCl_2$	2 *g*
Hydrochloric Acid	HCl	40 *mL*

3.2 Description and characteristics of CM247LC DS

Directionally solidified CM247LC DS evolved from a comprehensive study to improve the current Nickel-base superalloys in use by the industry. First developed by Cannon-Muskegon Corporation, it is currently used extensively in turbine blade and vane applications [47]. Both DS slab and bar product are provided and typically heat treated to the gas turbine designer's specification. An optimal solutioning procedure to obtain the ideal microstructure is determined by several factors, namely mechanical application, alloy stability, aging processes, and ease of DS castability.

Developed from the parent alloy Mar-M247, CM247LC DS resulted from an effort to enhance ductility during the casting process, the lack of which causes a wealth of grain boundary cracking during directional solidification. A study of the crack susceptibility during casting of CM247LC DS with respect to MAR-M247 detailed the microstructural composition changes in the refined alloy [48]. It showed that the reduction in C considerably improved DS grain boundary cracking when compared with

the parent alloy. This change was offset by tailoring the W and Mo content. This improved cracking resistance resulted from the additional reduction in composition of elements such as B, Si, and Zr, without compromising strength. The addition of Chromium (Cr) and Aluminum (Al) enhance corrosion resistance. In addition, the alloy has a relatively low Hf ingot content (1.4%), which allows for a very clean casting. This is in contrast to similar DS alloys with higher (>1.5%) Hf content which exhibit a greater number of inclusions due to high rates of reactivity with some ceramics used in the casting process [48]. The average composition of CM247LC DS and other similar Ni-base superalloys is shown in Table 3-3.

Table 3-3: Chemical composition of some advanced Ni-base casting alloys [17].

Selected Polycrystalline and Columnar DS Casting Alloys

Material	Composition by Weight Percent													
	Al	B	C	Cb	Co	Cr	Hf	Mo	Re	Ta	Ti	W	Zr	Ni
IN 738 LC	3.6	0.01	0.01	0.7	8.4	16	-	1.7	-	1.7	3.4	2.5	0.05	Bal.
IN 939	1.9	0.01	0.15	1	19	22.5	-	-	-	1.4	3.7	2	0.1	Bal.
IN 792	3.4	0.015	0.14	-	9	12.7	1	2	-	4.2	4.1	4.2	0.05	Bal.
Renè 80	3	0.015	0.17	-	9.5	14	-	4	-	-	5	4	0.03	Bal.
MM 002	5.5	0.015	0.15	-	10	9	1.5	-	-	2.5	1.5	10	0.05	Bal.
CM 247 LC	5.6	0.015	0.07	-	9.2	8.1	1.4	0.5	-	3.2	0.7	9.5	0.015	Bal.
CM 186 LC	5.7	0.015	0.07	-	9	6	1.4	0.5	3	3	0.7	8	0.005	Bal.
MAR M 247	5.5	0.015	0.15	-	10	8	1.5	0.6	-	3	1	10	0.03	Bal.
GTD 111	3	0.01	0.1	-	9.4	14	0.15	1.5	-	3	5	3.7	0.01	Bal.

Changes in composition of CM247LC DS resulted in a change in carbide morphology over similar DS alloys, which tests show results in improved fracture toughness through the inhibition of grain boundary sliding [5, 47].

Following solutioning at 1260°C, which provides an increased volume fraction of fine γ' particles and has the effect of homogenizing the as-cast structure, a two-step ageing process is usually applied. This involves the material being exposed to 1079°C and 871°C, respectively for four hours, with air cooling following each heating step [48].

Like most other Ni-base superalloys, CM247LC DS is a dual-phase intermetallic which consists primarily of a relatively soft austenitic FCC matrix (γ), into which is dispersed carbides, borides, and a hard FCC gamma prime (γ') precipitate throughout the matrix and collected along grain boundaries [5]. The primary component of the γ phase is Ni, yielding significant strength and corrosive resistance at high temperatures. The γ' precipitate phase consists of Ni_3Al and is generally spherical (first-generation superalloys) or cuboidal (second-generation) in shape. The cuboidal structure found in the CM247LC DS test material is depicted in Figure 3-1. These precipitates are the main strengthening mechanisms of the alloy. Measurements showed their average size was 0.5 μm square and their relative volume fraction within the microstructure was about 0.6. This is relatively standard among Ni-base superalloys. While a high volume fraction of γ' is desirable for high yield and tensile strengths at operating temperatures, the creep strength of pure γ' is poor. Additionally, with increasing volume fraction, finer γ' particles can also be found. These are not stable for long at high temperatures (982°C and above) and have a tendency to dissolve into the matrix at these temperatures [49].

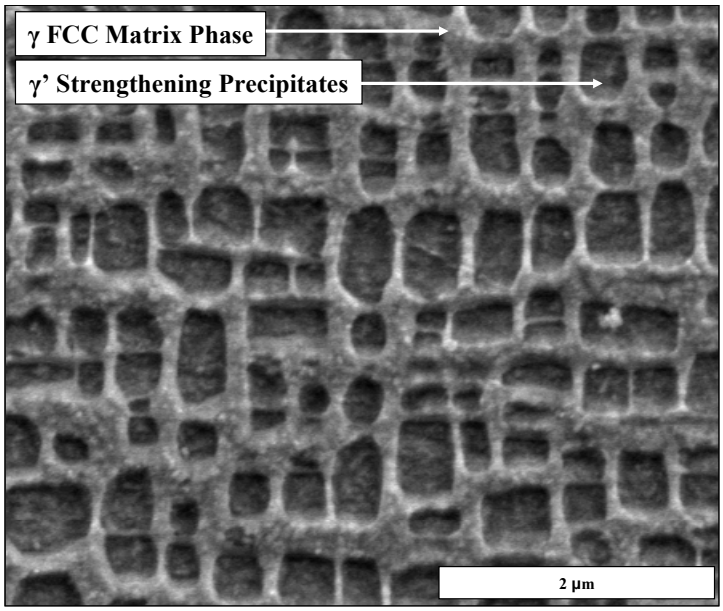

Figure 3-1: SEM image of the γ matrix and γ' precipitate phases in CM247LC DS.

The material contains large columnar grains as a result of the slow cooling process during solidification. Although their size can vary to a degree, they are typically on the order of 500 *μm* (0.5 *mm*) in diameter. The dendritic structure which forms within grains during solidification is illustrated in Figure 3-2. An optical microscope reveals the structure in the test material in Figure 3-3 and Figure 3-4. The primary dendrite stems are parallel to the solidification direction, with secondary branches in the c and [010] directions. The collective columnar structure of the primary dendrites serves as a fracture toughening mechanism, which temporarily arrests propagating cracks or prevent crack coalescence [50].

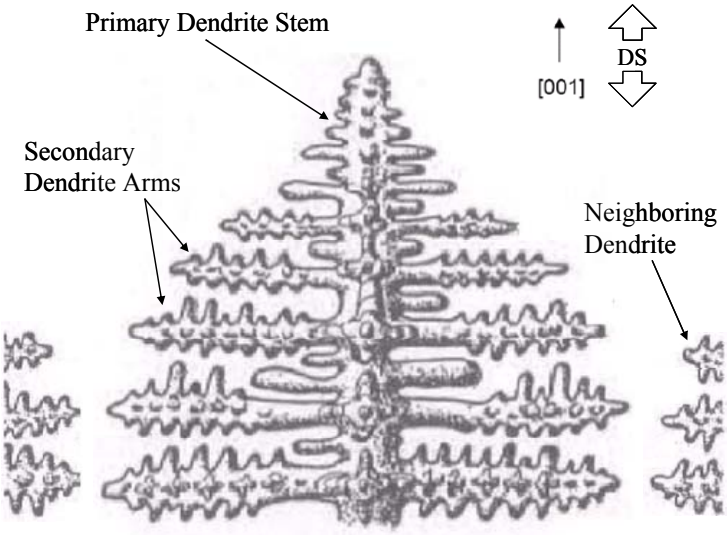

Figure 3-2: Depiction of typical dendritic structure within the grains of DS Ni-base superalloys [2, 51].

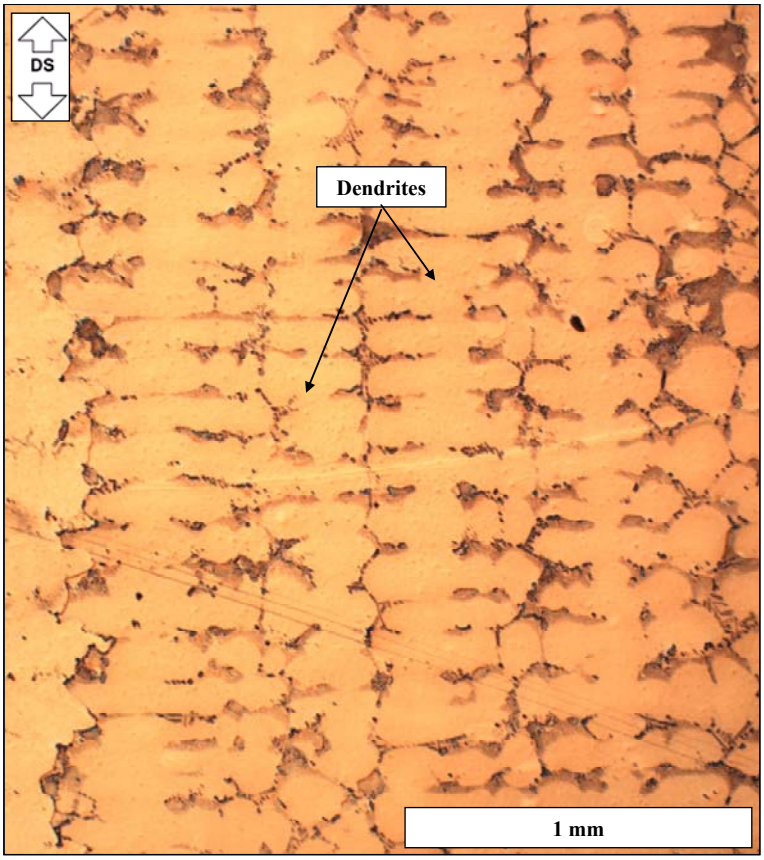

Figure 3-3: Optical microscope of a longitudinal section of L-oriented CM247LC DS showing the dendrite structure and interdendritic region in the test material.

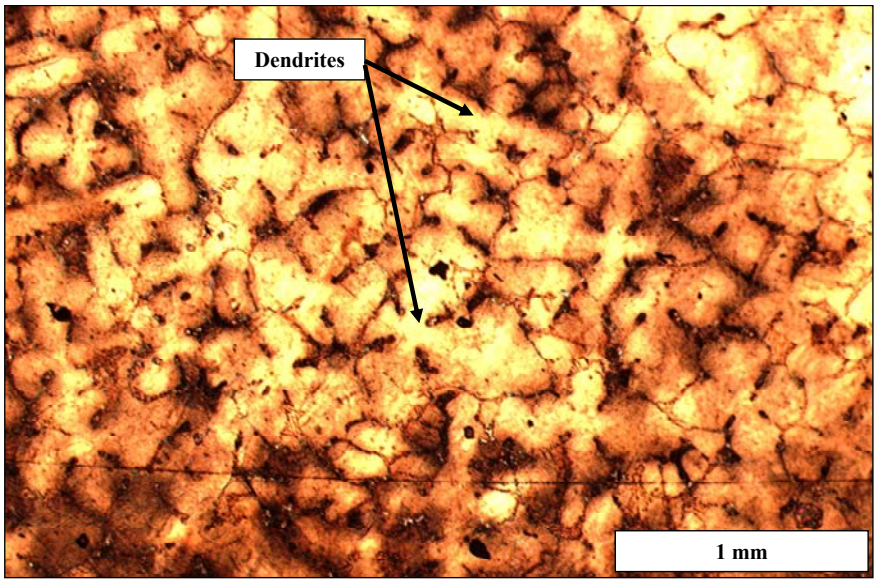

Figure 3-4: Optical microscope of a transverse section of L-oriented CM247LC DS showing the dendrite structure.

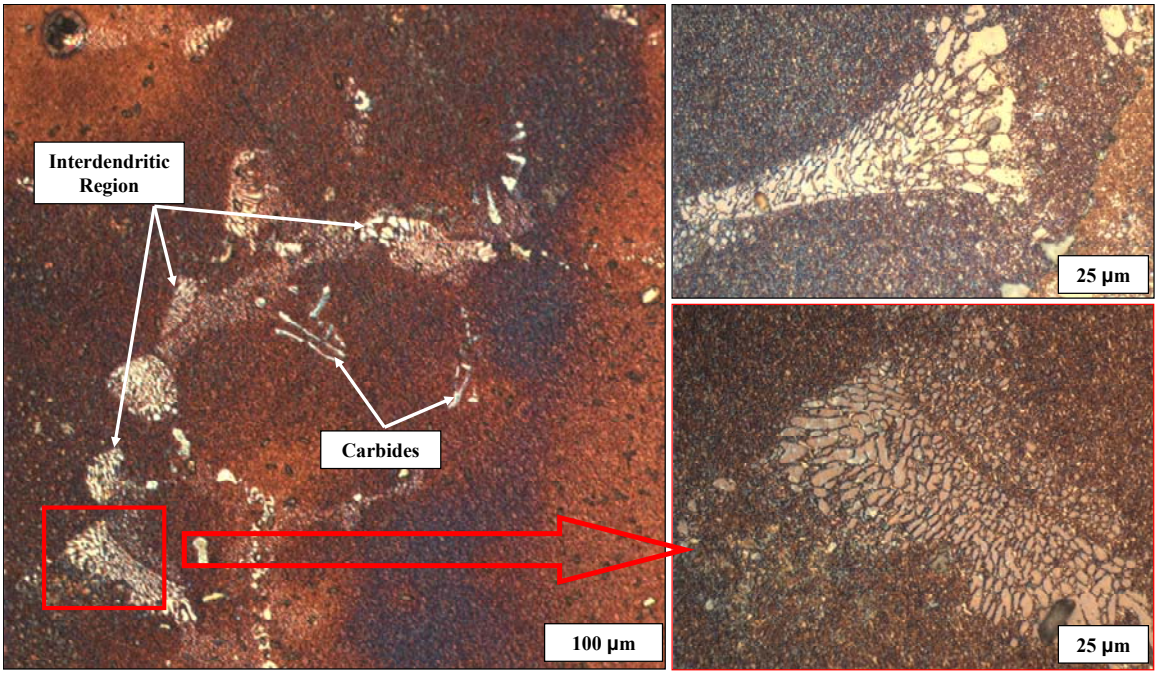

Figure 3-5: Optical microscope images of a longitudinal section of CM247LC DS showing the interdendritic region and carbides.

Carbides found throughout the microstructure also have a significant effect on the mechanical properties of Ni-base superalloys. The common types of these carbides are

MC, $M_{23}C_6$, and M_6C [49]. MC-type and have an irregular block-like or "script" morphology. The nominal shapes can be small cubes measuring a few microns up to elongated plates of over 100 μm. The solidification process results in $M_{23}C_6$ carbides collecting along grain boundaries, within a strip of γ matrix devoid of strengthening precipitates. This leaves the boundaries with the appearance of discontinuous blocky carbide particles, shown in the as-received material in Figure 3-6.

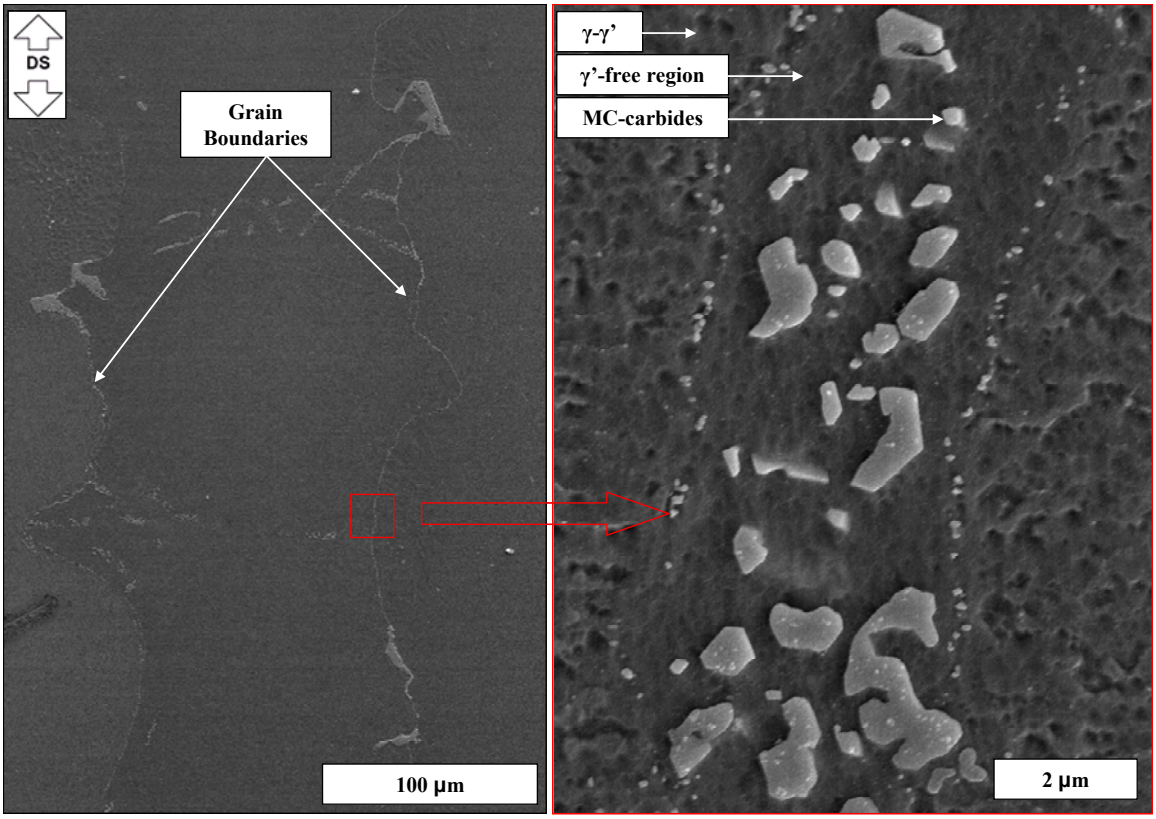

Figure 3-6: SEM images of grain boundaries in CM247LC DS showing the $M_{23}C_6$-type cabides and γ'-free zone.

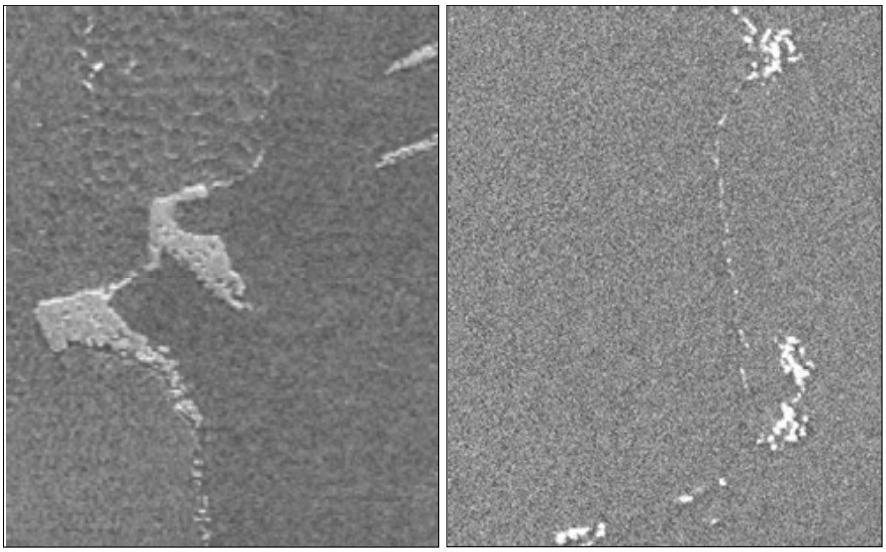

Figure 3-7: SEM image of script-like morphology of carbides in virgin CM247LC DS

M_6C carbides can also be found along grain boundaries, although they are more rare and generally avoided for best ductility and rupture life [49]. High temperature creep can result in the degradation of the carbide particles in CM247LC DS, as demonstrated by Komazaki et al. [52]. Energy dispersive X-ray (EDX) analysis showed that these particles were $(Ni, Cr, W)_{23}C_6$, and that the reaction at 900°C resulted in the formation of an Al-rich phase near grain boundaries which contained almost pure elemental aluminum. This reaction was of the form

$$M_{23}C_6 + \gamma' \rightarrow \gamma + \text{Al-rich phase}$$

and did not occur in un-stressed experiments at this temperature. Rupture failure could initiate due to fracture of these $M_{23}C_6$ carbides or de-cohesion of between them and the surrounding γ matrix.

Eutectic nodules of γ-γ' are also common at grain boundaries and in the interdendritic region (Figure 3-8 and Figure 3-9). These form as a result of the casting process and are the last constituents to solidify [53]. These can vary in size from about 20 up to 180 μm, and along with the carbides can act as local stress concentrations under remote loading [2]. The presence of the eutectic γ' in the heat treated structure indicates that it did not go fully into solution during the solution treatment.

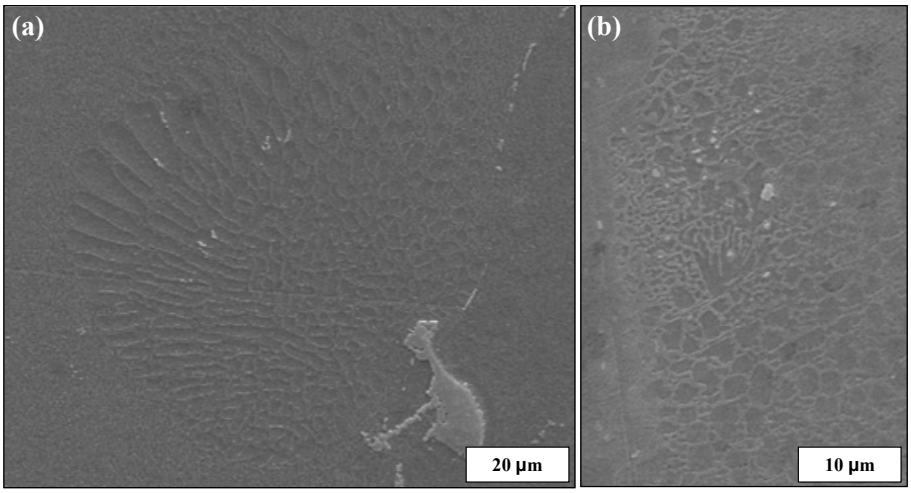

Figure 3-8: SEM images of γ' eutectic pools in CM247LC DS found (a) at a grain boundary and (b) in the interdendritic region.

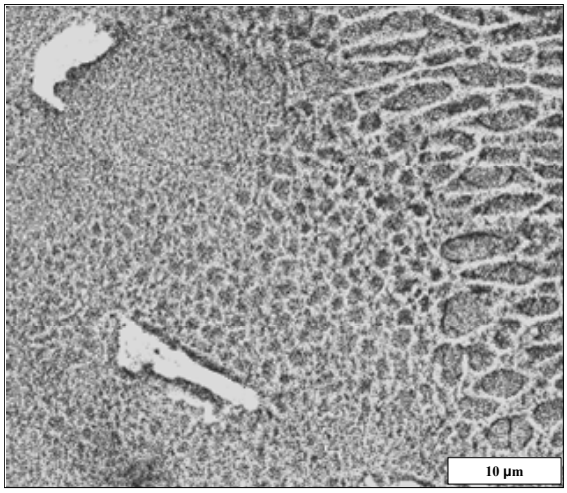

Figure 3-9: SEM image of eutectic γ-γ' and MC-type carbides

3.3 Deformation Response

The observed deformation response for CM247LC DS is similar to other Ni-base superalloys, which can be summarized as follows [54]:

- Slip is generally governed by the critical resolved shear stress (CRSS) acting along a favorably-oriented crystallographic plane. Actual slip is often influenced by the resolved stresses on other planes, as Ni-base superalloys do not obey Schmid's Law in all orientations.
- The elastic modulus of the DS material follows a parabolic curve, with the stiffest orientation being the off-axis 45° from the [001] longitudinal direction. Overall elastic stiffness modulus of CM247LC DS at 850°C as a function of orientation is shown in Figure 3-10.

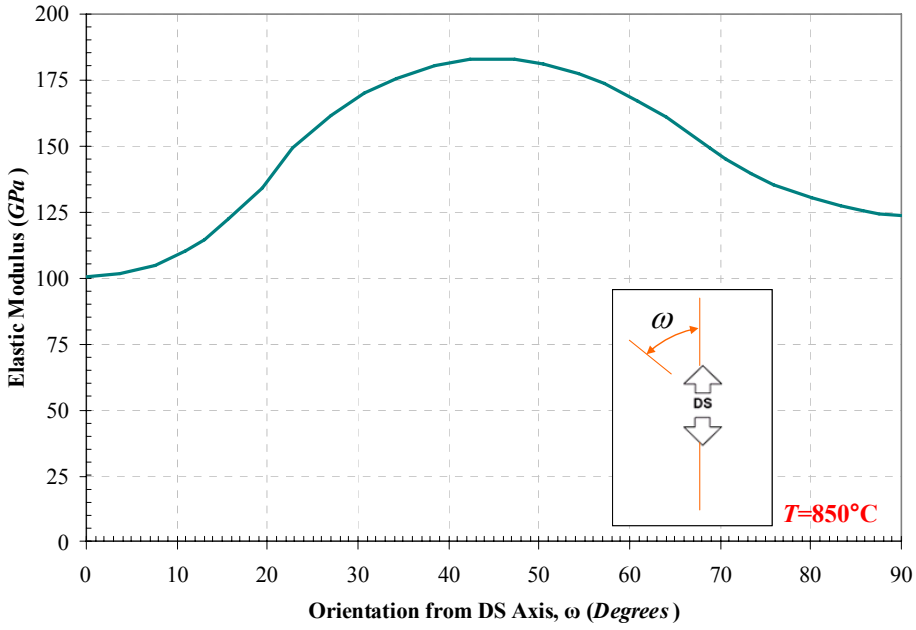

Figure 3-10: CM247LC DS Elastic modulus as a function of grain orientation [48].

- The yield strength for both the longitudinal and transverse orientations increases with increasing temperature, up to a peak between 750°C and 800°C, beyond which it drops off considerably, as shown in Figure 3-11.
- There is considerable tension-compression asymmetry of the flow stress for temperatures up to 750°C, which results from the properties of the γ' strengthening precipitates. As a result, the resolved shear stress for $[\bar{1}01]\{111\}$ slip and yield behavior are asymmetric in this temperature range, which violated Schmid's Law [55]. This behavior is shown in Figure 3-12.
- The initial yield behavior is temperature path history dependent, meaning the material will behave as virgin at a specific temperature regardless of prior deformation at low or high temperatures.

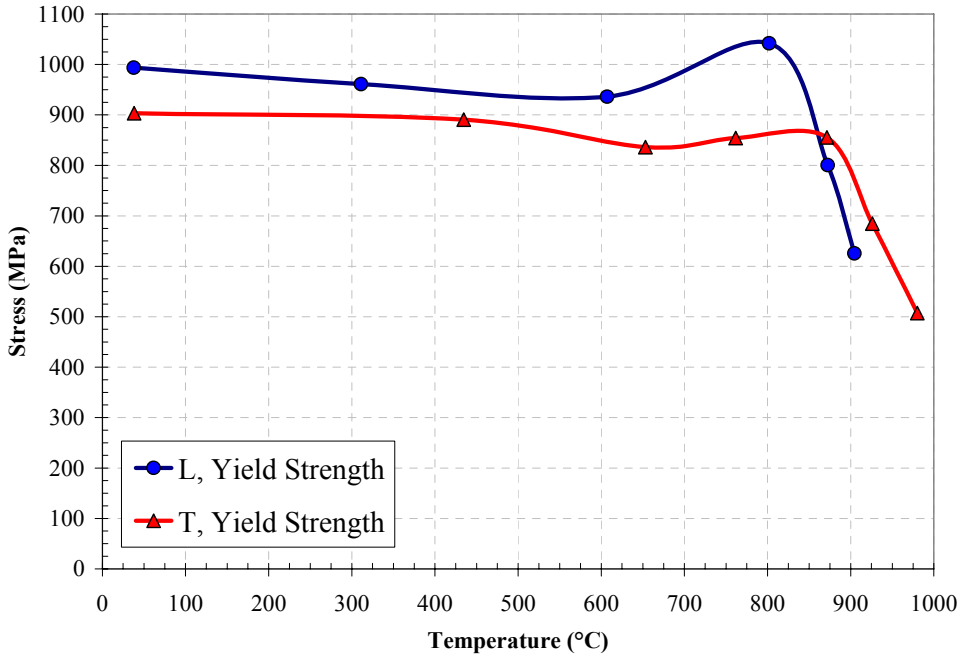

Figure 3-11: Variation in yield strength for L- and T-oriented CM247LC DS as a function of temperature [48].

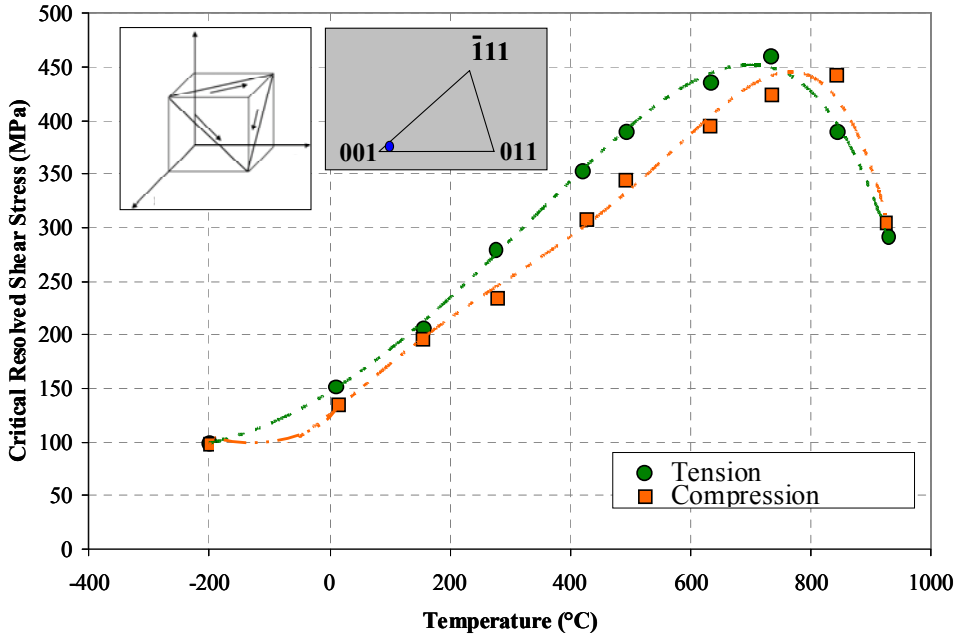

Figure 3-12: Variation in critical resolved shear stress for slip as a function of temperature for the γ' (Ni_3Al) single crystals in the [001] orientation measured in tension and compression [49].

3.4 Prior Research on the Fatigue Behavior of CM247LC DS

As the manufacturing and casting processes became much more refined, a considerable amount of research was devoted to developing behavior models and the intrinsic characteristics unique to DS Ni-base superalloys. Since its inception in 1984, CM247LC DS has attracted focus of a great deal of work, which has further driven the understanding of its complex nature and thereby improved the efficiency of the power generation process.

A study of DS and SC superalloys typically used for turbine blades was performed by Erickson and Harris (who is listed as the inventor on U.S. patent 4,461,659 for the CM247LC DS) of Cannon-Muskegon. This work evaluated the manufacturability of CM247LC DS in contrast with its parent alloy, Mar-M247. Additionally, the creep-

rupture capability at 982°C of longitudinal CM247LC DS was compared to equiaxed IN 738 LC and a single crystal alloy, CMSX-4, shown in Figure 3-13. S-N curves comparing CM247LC DS to a similar DS Ni-base turbine alloy is provided. These showed CM247LC DS had superior fatigue capabilities at a moderate temperature (T = 600°C) when compared with DS René 80H, as seen in Figure 3-14.

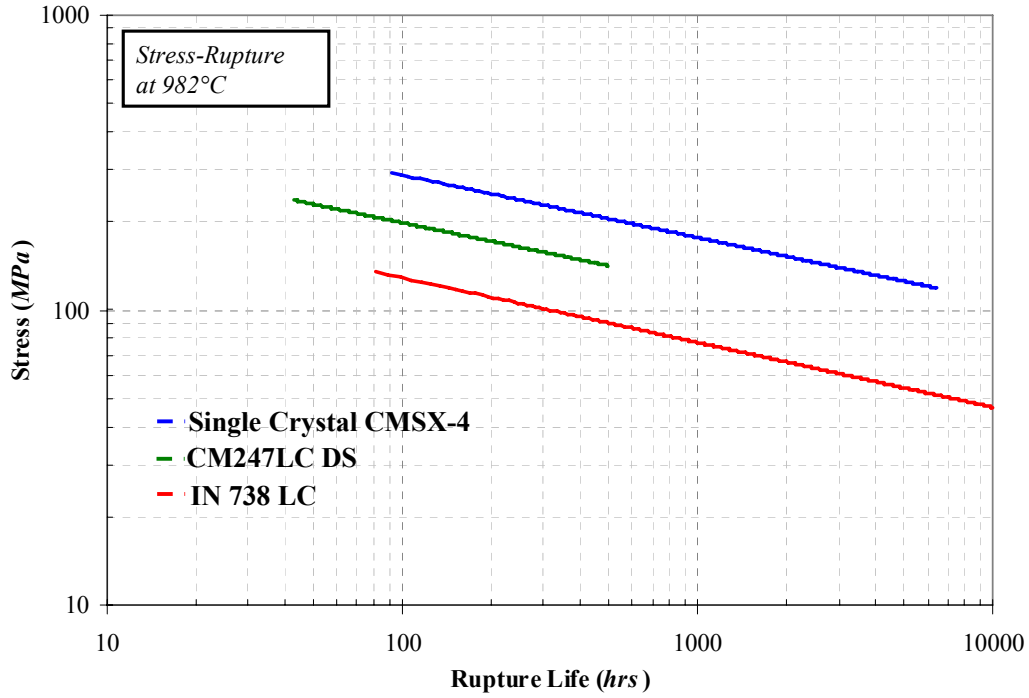

Figure 3-13: Stress-rupture strength of L-oriented CM247LC DS compared to CMSX-4 and IN 738 LC at 982°C [48].

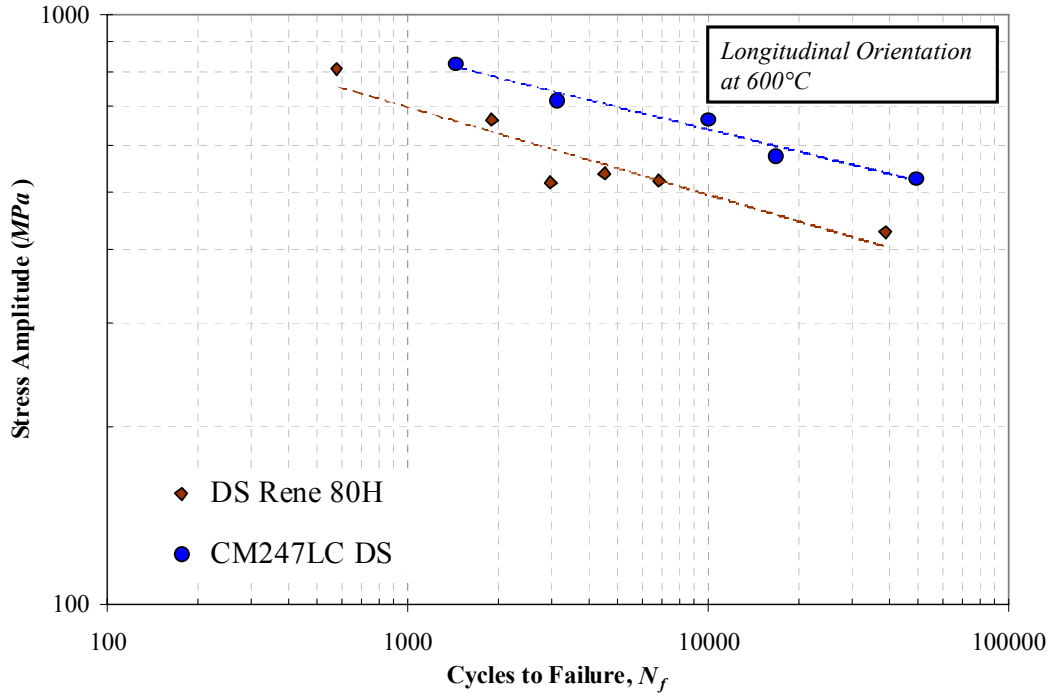

Figure 3-14: LCF of Longitudinal DS Rene 80H and CM247LC DS at 650°C [48].

The study is extended to include the effects of material orientation on strength and fatigue life. Isothermal LCF data gathered from strain-controlled experiments for several orientations was generated. Grain orientations with the greatest stiffness with respect to the loading direction would result in more extensive cyclic plasticity, and thus a greater amount of fatigue damage, for a given applied load. This was especially true at high plastic strain amplitudes where a significant fraction of the dislocation motion is irreversible [48].

Results showed that CM247LC DS had the shortest life span with columnar grains oriented 45° from the specimen axis normal, where the material has the greatest stiffness. Longitudinally orientation grains afforded the greatest fatigue resistance. LCF results for various orientations at the same temperature are shown in Figure 3-15.

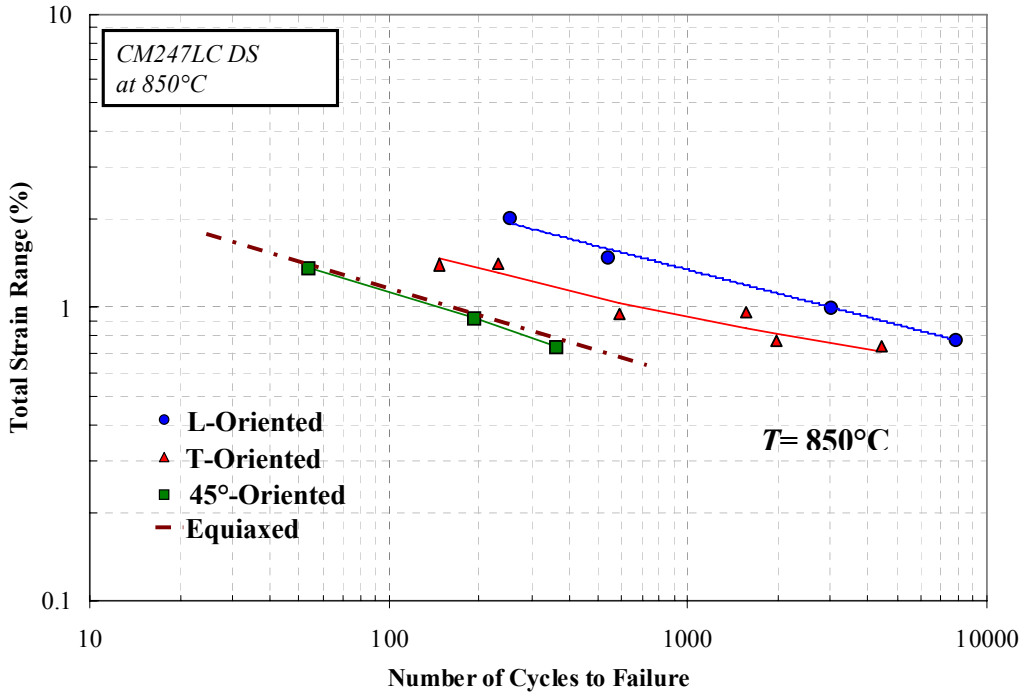

Figure 3-15: CM247LC DS LCF results for various orientations plotted against that of the equiaxed configuration [48].

Esser [7] conducted a similar study on a number of common DS blade alloys, including CM247LC DS, IN 792 DS, and IN 6203 DS. A wide variety of material properties were obtained through tensile testing and creep rupture testing. CM247LC DS outperformed the other alloys in all test cases, and the superior creep rupture properties and ductility in the L-orientation was demonstrated. The superior creep rupture capability of CM247LC DS is due to a reduced weight percentage content of Chromium, which results in the greatest abundance of γ' precipitate [7]. Full-scale castability studies were conducted, allowing the author to observe implicit grain geometry and surface characteristics consonant with differing regions of the blade.

The cyclic deformation response of CM247LC DS was studied by Marchioni et al. [56]. Low cycle fatigue tests were performed at 850°C and 950°C and the deformation

mechanisms and fatigue fracture processes were observed. The cyclic response of the material was found to be very stable, with only slight softening observed. The LCF tests did not show significant coarsening of the γ' precipitates, which could indicate that the stable cyclic response is due to dislocation motion through the matrix being impeded by the dislocation network at the γ-γ' interface. The initial fatigue cracks were shown to emanate from material flaws at or just below the surface of the test specimens. The compiled testing data was fit well by both the Basquin and Coffin-Manson relationships. Life data for the CM247LC DS was then compared favorably with several oxide-dispersion strengthened (ODS) superalloys, likely due to its higher ductility.

The effect of grain size and orientation on thermomechanical fatigue behavior of CM247LC DS was studied by Blümm et al [57]. Wedge shaped specimens were tested in both L and T material orientations with narrow and coarse grain structures (mean columnar grain diameters of 0.96 *mm* and 1.55 *mm*, respectively). Crack initiation lives plotted as a function of maximum temperature and strain range are shown in Figure 3-16. It was shown that while cracks initiated much more readily at higher T_{max} and strain range values, grain size had no observable effect. There was significant oxidizing of the grain boundaries in both orientations at higher T_{max} (>1000°C), but in general grains perpendicular to the loading axis (i.e. transverse) exhibited more cracks and shorter lives due to grain boundaries at the surface favorably oriented for slip. The increased number of grain boundaries in the narrow grain structure specimens retarded crack growth only slightly. Transgranular cracking observed in longitudinal specimens showed increased resistance to propagation compared with the intergranular cracking in those having transversely-oriented grains [57]. Both types of cracks are shown in Figure 3-17.

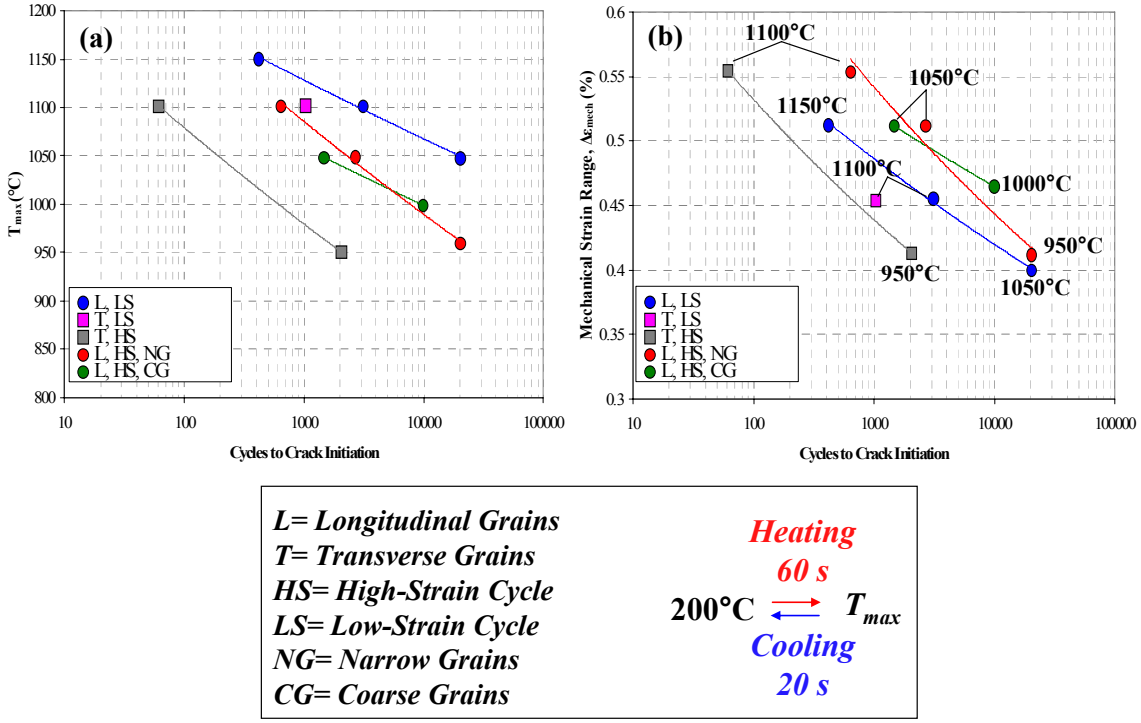

Figure 3-16: Effect of (a) T_{max} and (b) the mechanical strain range on the cycles to crack initiation of both L- and T-oriented CM247LC DS under various cycle types and with several grain sizes [57].

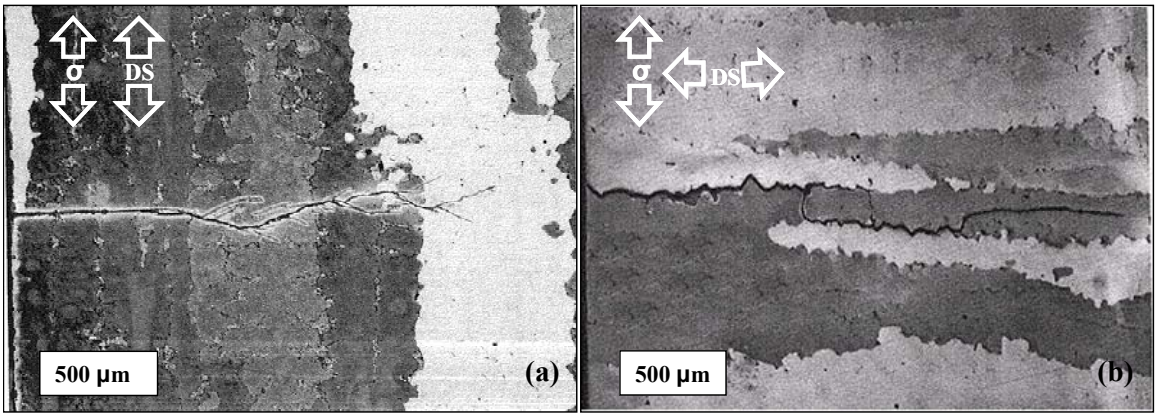

Figure 3-17: TMF fatigue cracks in CM247LC DS in the (a) longitudinal grain structure and (b) transverse grain structure [57].

Vasseur and Rèmy [58] investigated the high temperature LCF and TMF of the oxide-dispersion strengthened (ODS) Ni-base superalloy MA 760 and compared the

results to CM247LC DS. ODS alloys use powder metallurgical processing to disperse reactive metal oxides into the material substrate, enhancing high-temperature strength and oxidation resistance. For this study, all tests were performed using hollow, cylindrical specimens in the longitudinal orientation. The results demonstrated the effects of strain rate, temperature, and shape of the TMF cycle on cyclic stress-strain behavior, fatigue life, and microstructure stability. Two variations of diamond type TMF cycles were used, corresponding to the transient operations of an industrial and aeronautical gas turbine. LCF results were compared to TMF results for the aeronautical cycle as shown in Figure 3-18.

Drawing from strain-life data, TMF results were shown to be more detrimental than LCF at an intermediate temperature regardless of the strain rate. Both alloys were considerably less oxidation resistant in TMF than high temperature LCF. Cracks in TMF initiated from fatigue-oxidation interaction and spurred delamination along longitudinal grain boundaries. Observations of the microstructure showed a reduction in size of the γ' precipitates which was strongly dependent on the duration and minimum and maximum temperatures of the TMF cycle. Such a process, to which every cycle likely contributes, changes the deformation mode depending on the load level. Finally, CM247LC DS exhibited a greater high temperature fatigue life than MA 760 irrespective of the conditions, which runs contrary to previously suggested superiority of dispersion-strengthened alloys in fatigue [59].

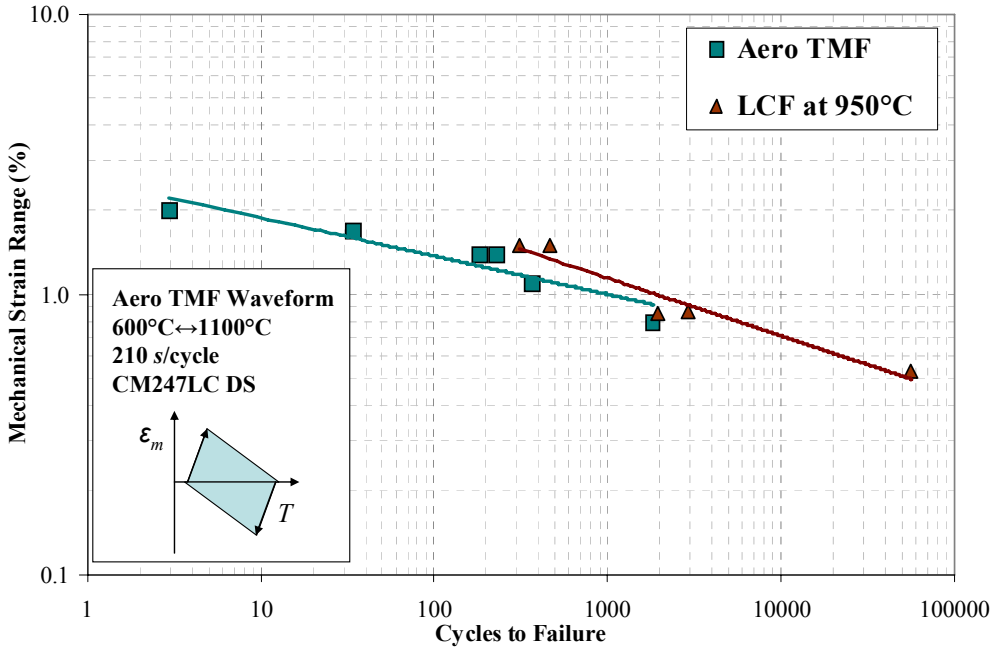

Figure 3-18: Fatigue life of longitudinal CM247LC DS subjected to aeronautical TMF and isothermal LCF at 950°C as a function of mechanical strain range [58].

Enlger-Pinto [12] and others studied the interaction between creep and thermomechanical fatigue of CM247LC DS. Both out-of-phase TMF tests and creep-rupture tests were performed; first independently, and then sequentially TMF-creep and creep-TMF to characterize the relationship. The OP TMF tests were continuously cycled between 600°C and 900°C.

Creep testing revealed that CM247LC DS follows the same three-stage creep curve similar to other Ni-base superalloys. A representative creep deformation curve at 900°C and 280 *MPa* is shown in Figure 3-19. Subsequent SEM observations revealed that both the surface and bulk were damaged. Subsurface cracks initiated from cavities forming at the interface with carbides or residual eutectics. Surface cracks resulted from the creep-oxidation interaction at grain boundaries.

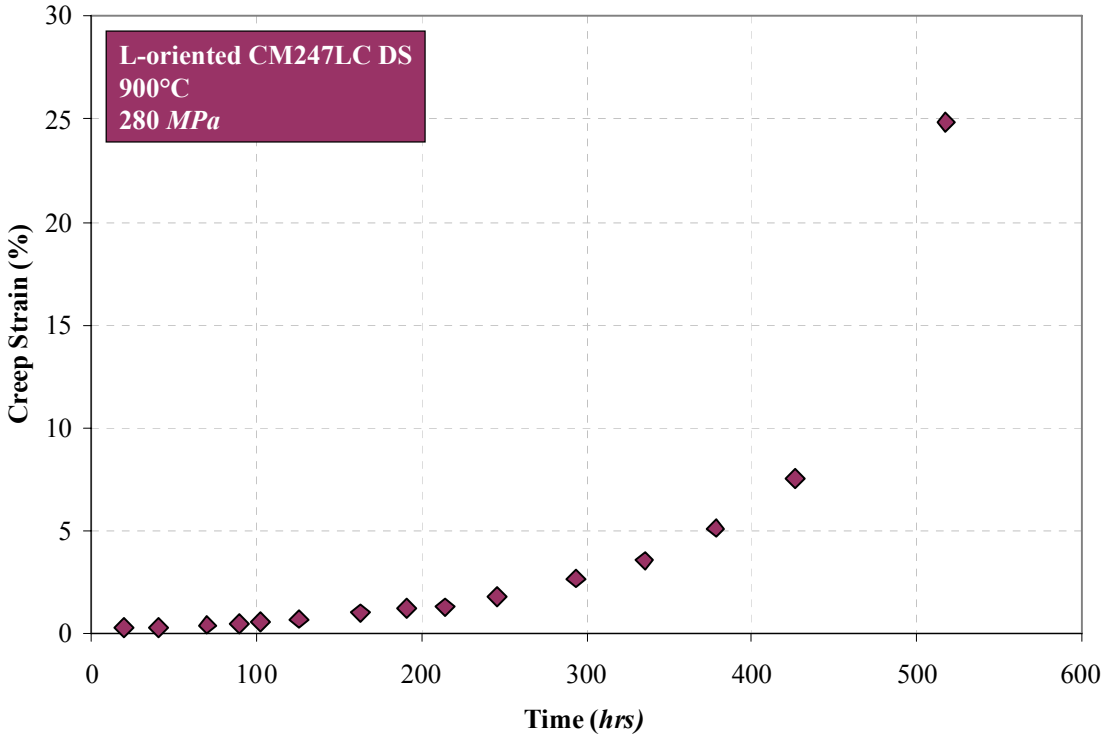

Figure 3-19: Creep deformation curve for a longitudinal CM247LC DS round bar specimen with diameter of 11 *mm* subjected to 280 *MPa* at 900°C [12].

It was found that heavy oxidation stimulated the formation of cracks during TMF and creep-TMF testing. Experiments showed an alteration of the γ- γ' structure with T_{max}= 900°C had a detrimental effect on creep rupture lifetime. TMF cycling prior to creep testing, however, did not affect the γ- γ' phases and therefore did not bring about the change in life. Therefore, although TMF cycling prior to creep tests did induce cracks into the load-bearing section, it did not affect creep-rupture lives. Conversely, under pre-crept conditions, the γ' precipitate structure is coarsened and rearranged directionally within the matrix, which results in a rafted γ- γ' microstructure [60]. Consequently, there was an increase in inelastic strain and a corresponding drop in crack initiation periods during subsequent high temperature TMF cycling. This sequence is illustrated in Figure 3-20. This differs from several other authors, who note that a reduction in the cyclic T_{min}

was needed to observe an increase in plastic strain [61, 62]. This may have been due to the fact that although the oxide layer was polished off after creep testing and prior to TMF cycling, the full depth of surface cracks and the γ' depleted zone were not removed. This residual damage served to reduce the crack initiation period of the alloy under subsequent fatigue testing. It was further shown that the creep-TMF interaction can be described in terms of a linear damage summation when pre-creeping precedes TMF cycling, but not for the reverse case [12].

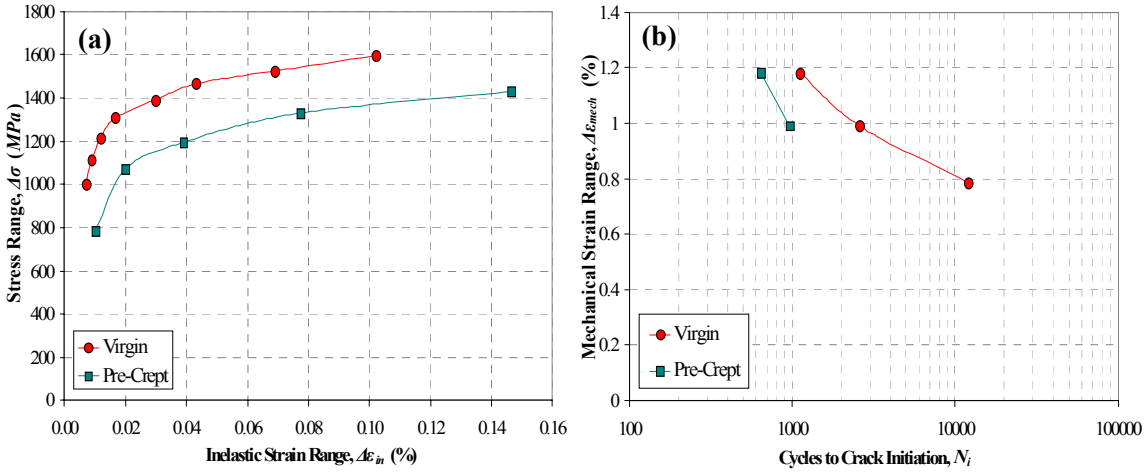

Figure 3-20: (a) Increase in inelastic strain range and (b) the corresponding drop in cycles to crack initation for longitudinal CM247LC DS pre-crept in tension at 900°C and 280 *MPa* for 241 *hrs*. Initation was defined by a 5% drop in the maximum tensile load [12].

Moore [17] developed an analytical fatigue life-prediction model for notched CM247LC DS under isothermal LCF conditions. Experiments conducted at 750°C and 950°C in the L and T orientations were used to describe the effects of orientation, rate, dwells (holds), and temperature. The response of smooth specimens were compared to those with elastic stress concentration factors of k_t=2 and k_t=3 to evaluate the severity of the stress concentration on LCF life compared to the aforementioned factors.

Computational simulations were used to determine the anisotropic material response at the notch and calibrate the inputs used in the analytical model.

Results from both the continuously cycled and time-dependent tests conducted in this study are shown in Figure 3-21. Key findings of these comprehensive studies included the reduced effect of any stress concentration at successively higher numbers of cycles. This demonstrated the for lower load levels, propagating cracks quickly outgrew the magnification of stress at the notch and grew at greatly reduced rates in areas of lower stress. This was especially true in the transverse orientation, which showed little sensitivity to notches and an enhanced susceptibility to crack initiation and propagation at favorably oriented grain boundaries. This overriding weakness was also demonstrated in the fact that dwells had a greater influence on fatigue life in the longitudinal orientation and a more muted effect in the transverse.

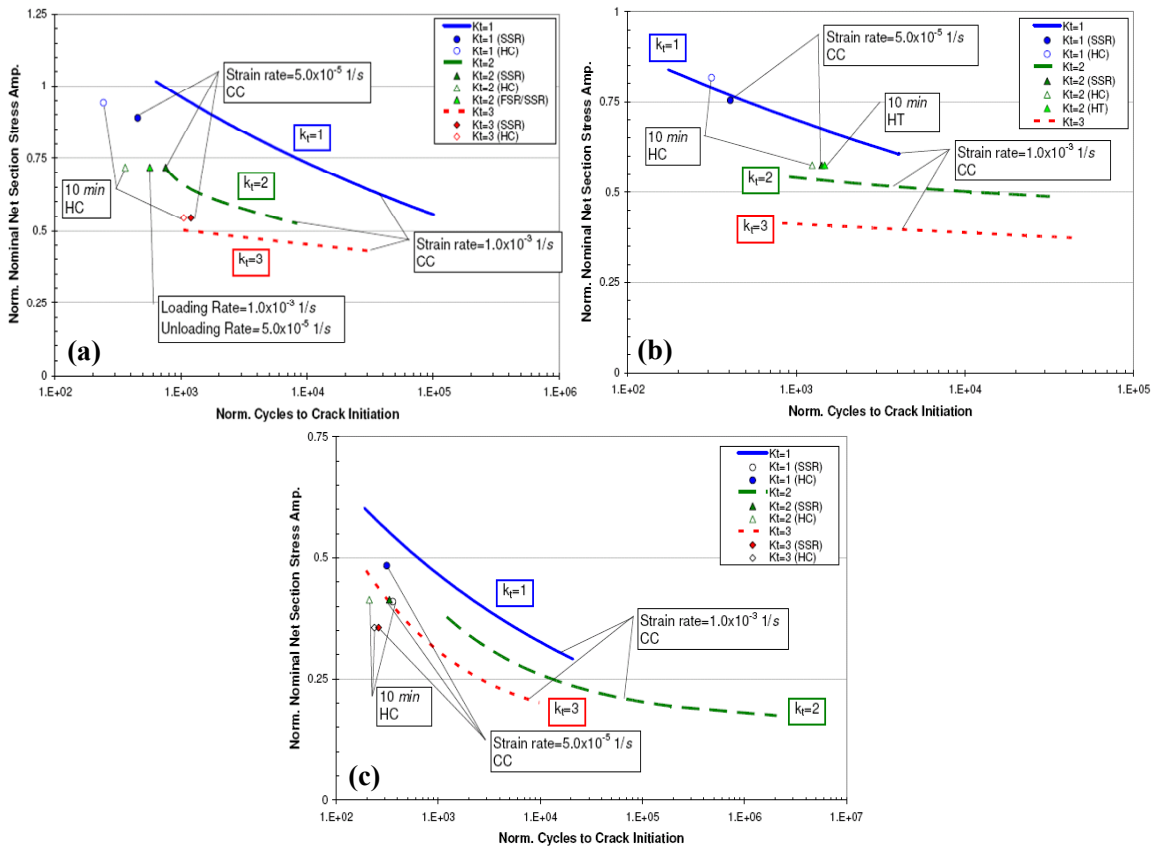

Figure 3-21: Normalized CM247LC DS smooth and notched specimen LCF results for (a) L-oriented and (b) T-oriented at 750°C, and (c) L-oriented at 950°C. For these tests, SSR= slow strain rate, FSR= fast strain rate, and HC= hold compression [17].

Additionally, the effect of holds at peak loads differed greatly between the two temperatures. At the lower temperature of 750°C, the dwell manifested itself in the development of a mean stress (compressive for tensile holds and tensile for compressive holds). This mean stress was the decisive element leading to the reduction in fatigue life. At 950°C, however, considerable relaxation of the mean stress results in a more dominant creep-fatigue mechanism.

CHAPTER 4. THERMOMECHANICAL FATIGUE-EXPERIMENTAL PROCEDURES

4.1 Specimen Preparation

To maintain as much harmony as possible with previous isothermal LCF testing done with CM247LC DS at Georgia Tech, specimen preparation was performed by the same vendor. This ensured there was as little variability as possible with respect to the production process. Individual specimens were cut from the three slabs of material delivered such that the desired grain orientation was obtained from the direction of solidification, as shown in Figure 4-1.

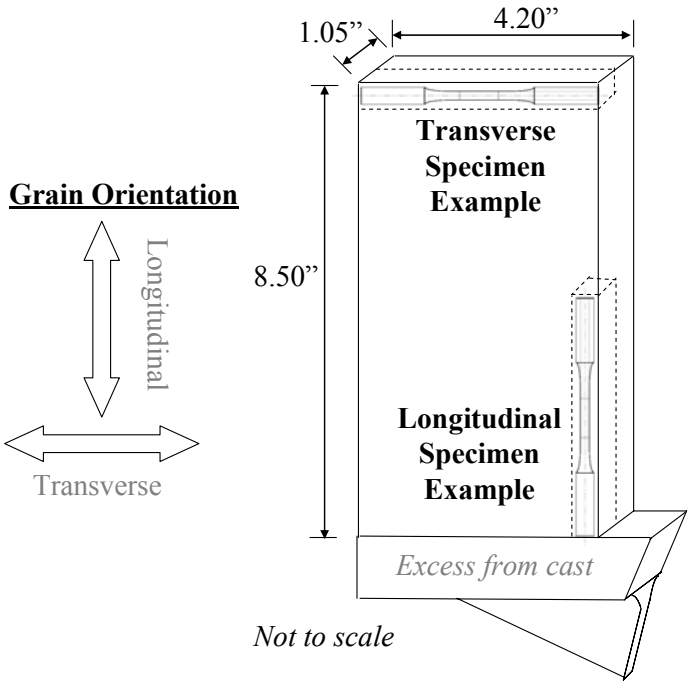

Figure 4-1: Orientation of longitudinal and transverse specimens within a cast slab

After a sponsor-directed heat treatment, machining was carried out by the manufacturing division of MAR TEST, Inc. (Cincinnati, Ohio). A total of 53 specimens (38 longitudinal and 15 transverse) were prepared to meet the requirements of the test matrix. Low-stress grinding was used for all machining steps to limit residual stresses from manufacturing. Machining parameters such as grinding wheel size and speed (7.5" DIA. A-120-S5-BA2 and 1260 RPM, respectively) were provided to the vendor along with required surface finish (P600-P1000 Circumferential). This was also done to maintain uniformity with the previous tests.

As there may be an extremely small variability in microstructure between slabs, each received a unique designation prior to cut-up. For tracking purposes, this designation was subsequently passed on as part of the individual specimen identifier. For example, the first longitudinal specimen cut from slab #037 was named **S**lab**037-L**ongitudinal**1** (S037-L1). Subsequently, the remaining fifteen L specimens cut from the same slab were given the unique identifiers S037-L2 - S037-L16, respectively. Solid specimens were designed such that they conformed to the ASTM standard requirements and the capabilities of the testing facilities and equipment.

To ensure failure occurs within the gage section, it is crucial to maintain the accuracy of the quality-critical dimensions of the specimens. As the comparability of tests is of particular importance, a surface tolerance of 0.001 *in* was required within the gage section length. In addition, since solid specimens have no wall thickness, it was necessary to keep the fatigued volume thin enough to avoid any radial temperature gradients which arise during thermal cycling.

One smooth and two notched specimen geometries are used in testing. The smooth specimen, shown in Figure 4-2, was designed to meet recommended dimensions of both ASTM Standard Practice for Strain-Controlled Fatigue Testing (ASTM E606-04) and ASTM Standard Practice for Strain-Controlled Thermomechanical Fatigue Testing (ASTM E2368-04). It will hereafter be referred to as k_t=1 or smooth specimen. The gage section has a diameter of 6.35 *mm* (0.25 *in*) and has a length of 12.7 *mm* (0.5 *in*), which ensures there is a reasonable continuum volume for testing. This aspect ratio satisfies the ASTM recommendations for LCF testing.

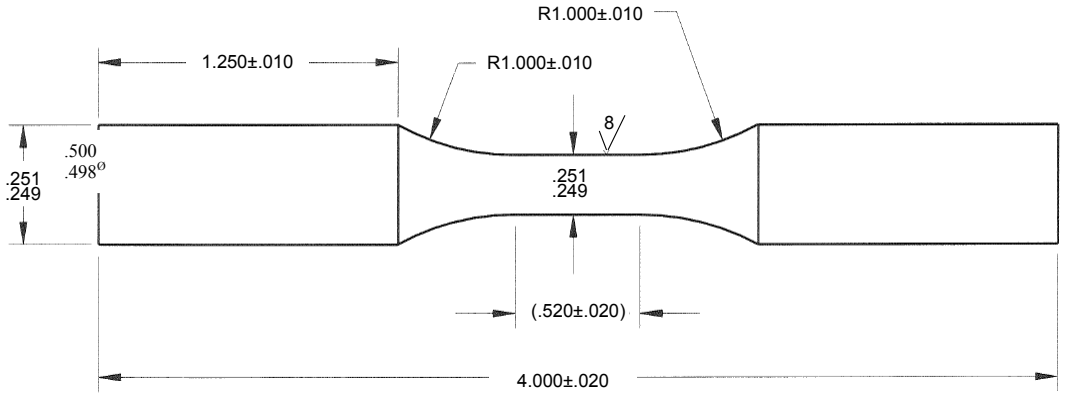

Figure 4-2: Smooth Specimen Geometry. Dimensions are in inches (not to scale).

Both notch geometries adhere to the ASTM Standard Test Method for Sharp-Notch Tension Testing with Cylindrical Specimens (ASTM E602-03). These notches are identical to those used in the earlier isothermal testing of CM247LC DS at Georgia Tech as part of this research. The geometry for each notch was characterized in FEA to obtain the desired elastic stress concentration value. This was done by starting with a 60° v-notch and then adjusting the notch root radii. A k_t of 2 was obtained with a notch radius of 0.9271 *mm* (0.036 *in*), while a result of k_t=*3* yielded a radius of 0.3175 *mm* (0.012 *in*).

Both notched specimens used the same 6.35 *mm* reduced net section diameter as the smooth specimens. The resultant geometries are shown in Figure 4-3.

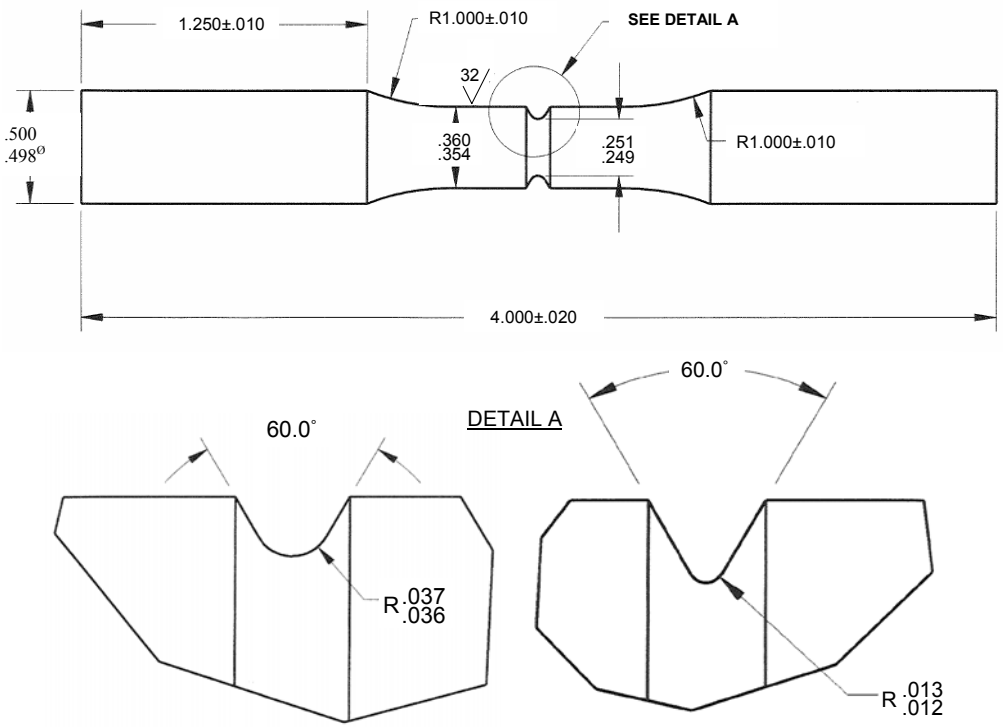

Figure 4-3: Notched Specimens Geometry. Dimensions are in inches (not to scale).

A summary of the specimen inventory including orientation and notch type are shown in Table 4-1. The 53 specimens manufactured covered the planned spectrum of tests which would fully characterize the behavior of the material and the notch sensitivity to various thermomechanical load conditions.

Table 4-1: Fatigue Specimen Count

Specimen Type	*No. of Longitudinal*	*No. of Transverse*
Smooth ($k_t = 1$)	14	5
Notched ($k_t = 2$)	18	6
Notched ($k_t = 3$)	6	4
Total	38	15

Upon receipt of all specimens a visual inspection was performed to ensure that any residual and polishing marks were along the stress axis, following ASTM Standard E606-04. Prior to conducting each test, specimens were cleaned and degreased in acetone and rinsed with ethanol. As acetone often leaves a residual film on the surface, the ethanol was used for the final stage of the cleaning procedure.

4.2 Thermomechanical Fatigue Experimental Setup

All thermomechanical fatigue tests of CM247LC DS were performed to characterize the anisotropic material response effectively enough to model. To better capture the effects of orientation, temperature, rate, and phasing, several different test cycles were designed beyond the baseline. All tests were fully reversed (R = -1) with T_{min}=500°C. Both L and T grain orientations and a T_{max} of 950°C were used for the baseline tests. Several tests were also conduced with a T_{max} of 750°C and T_{min}=100°C to compare the effect of the maximum and minimum temperatures on the active damage mechanisms. Smooth specimen experiments were conducted under mechanical strain control, while notched specimen tests were conducted in uniaxial load control. All tests used laboratory air and environmental conditions. A 44.5 *kN* (10 *kip*) axial servo-hydraulic MTS® testing machine with water cooled collet grips (MTS® model 646) and a dual-channel controller with TestStar software (Testware SX® 4.0D) was used. This machine had a load cell resolution of ±0.22 *kN*. Nominal hydraulic pressure applied to grip the specimens was 29 *MPa* (4200 *psi*).

Temperature feedback was provided by K-type (Omega® model GG-K-26_SLE) thermocouples (TC's) having 0.404 *mm* (0.159 *in*) diameter leads (26 gage). For each

test, two TC's were spot welded on either side of the gage section to monitor axial temperature fidelity. Placement of the TC's differed between smooth and notched specimens, as shown in Figure 4-4. These distinct configurations necessitated the application of slightly different (but previously validated) temperature set points to maintain uniformity of the temperature profile in the gage section. To ensure the gage section of all smooth specimens was clear of defects, the spot welds were positioned outboard of the extensometer rods.

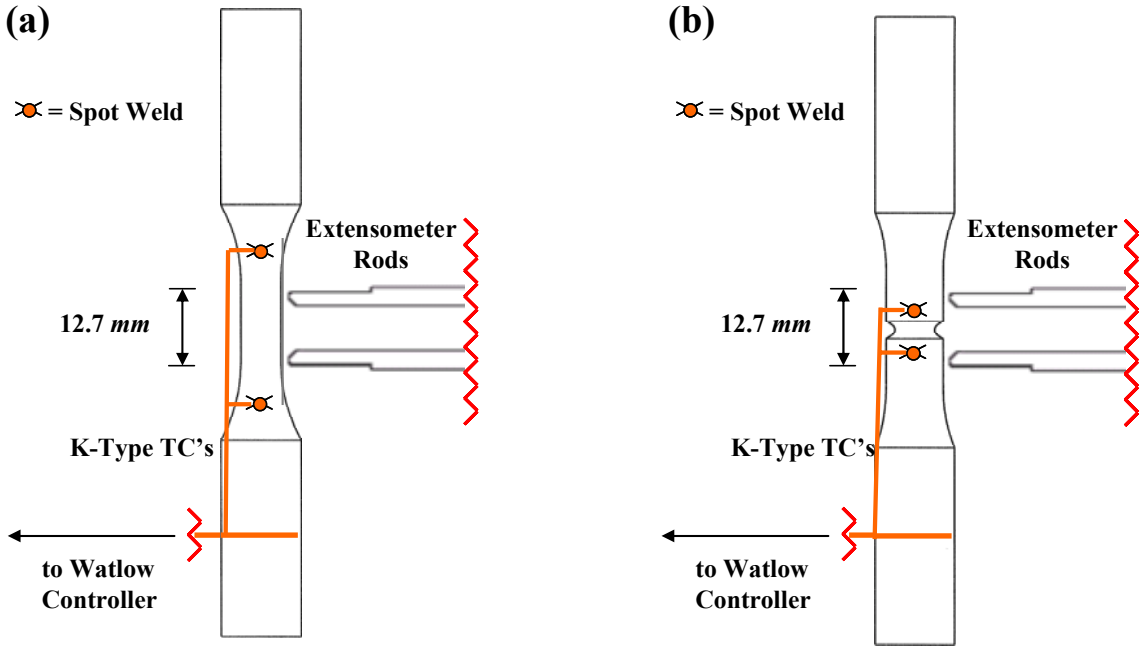

Figure 4-4: Reference TC placement for (a) a smooth specimen and (b) a notched specimen. The induction coil used for heating is not shown.

Heat was supplied using an Ameritherm® single phase 2 *kW* radio frequency (RF) induction heater with a control resolution of ±1°C. A PID controller (Watlow® model 945A-2FK5-A000) was used to maintain continuous closed-loop feedback control of temperature inputs and applied thermal increments during TMF cycling. Induction

heating provides the advantage of relatively rapid heat application, making it ideal for TMF tests where a reasonable cycle period is highly desirable. Water-cooled grips served the twofold purpose of avoiding overheating of the collets and providing prompt conduction cooling to the specimens. This cooling allows solid specimens to be used in place of thin-walled tubular specimens, which typically require some form of forced cooling.

The induction coil used for all testing was made from copper tubing having 4.7 *mm* (0.188 *in*) outer diameter. As more coil turns allow for more rapid heat transmission, the test setup utilized six turns covering almost the entire exposed axial length of the specimen between grips. Each turn had an inner diameter of least 23 *mm* (0.9 *in*). Brass Swagelok® fittings connected the coil to the supply device. Comprehensive visual inspection was conducted prior to each test to ensure the coil was properly centered on the gage section.

Axial displacements within the gauge section were measured using a high temperature extensometer (MTS® model 632.52E-14), with ceramic rods positioned between induction coils such that no interference would occur during testing. The 5.0 *mm* diameter rods had conical ends which were seated in dimples created on the specimen surface using a machined indenter jig with gentle taps from a hammer. The nominal gauge length for both smooth and notched specimens (position of zero travel) positioned between extensometer tips was 12.7 *mm* (0.5 *in*). The complete test setup is shown in Figure 4-5.

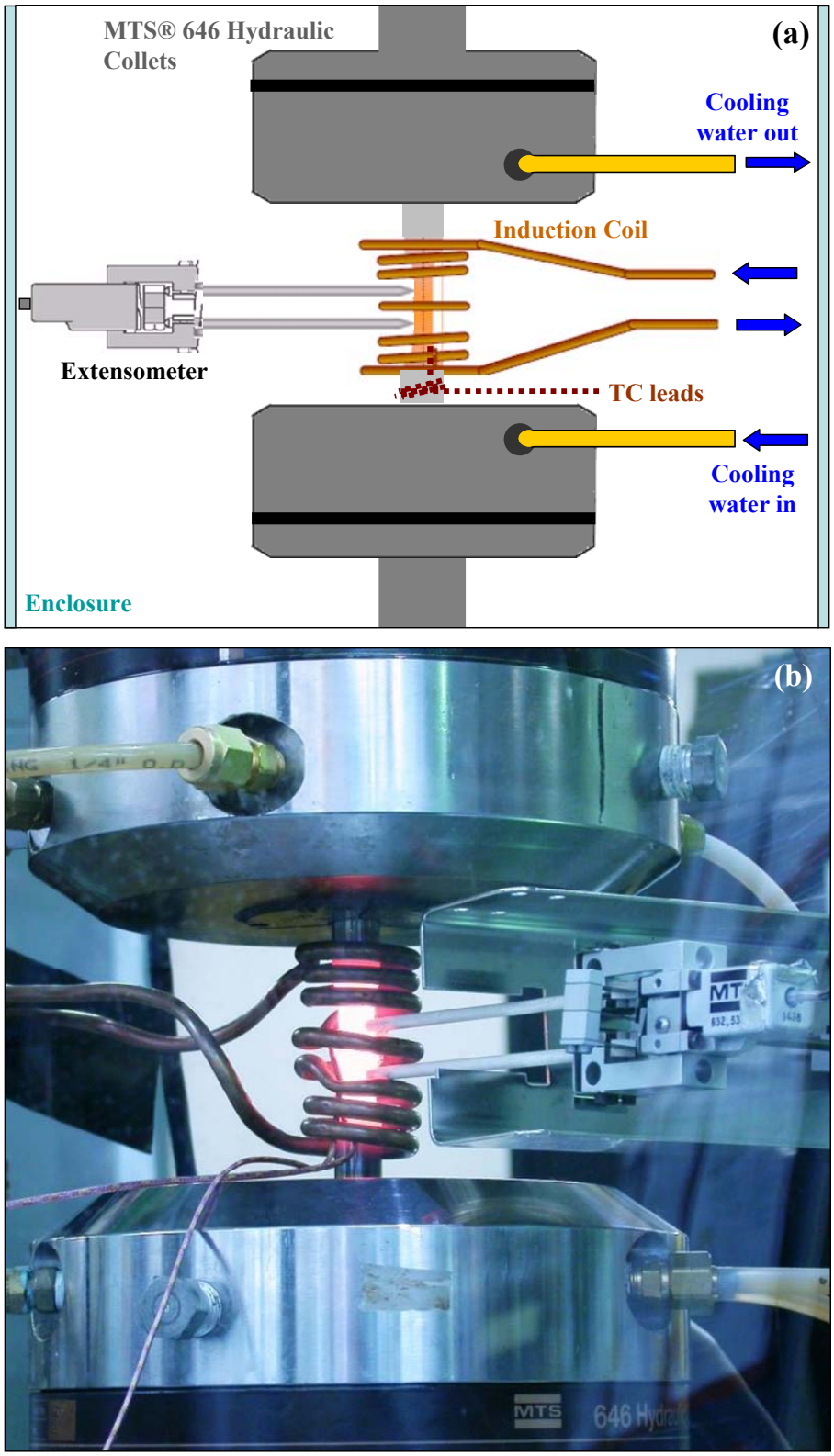

Figure 4-5: (a) Schematic and (b) photograph of experimental setup.

Visual verification prior to testing ensured the turns of the induction coil were centered on the specimen and would not disrupt the travel of the extensometer rods during cyclic thermal expansion and contraction. The extensometer response reading was verified during pre-cycling to ensure the tips were properly seated within the dimples.

A flow chart illustrating the equipment and transmitted signals involved in the TMF testing system can be seen in Figure 4-6. As TMF is a complex test technique, the setup demonstrated is by no means the only method of conducting experiments, but that which used available hardware and produced reliable TMF material property data using reproducible testing conditions. Other TMF testing methodologies and data interpretation, in addition to multiple other current testing applications, can be found in the literature.

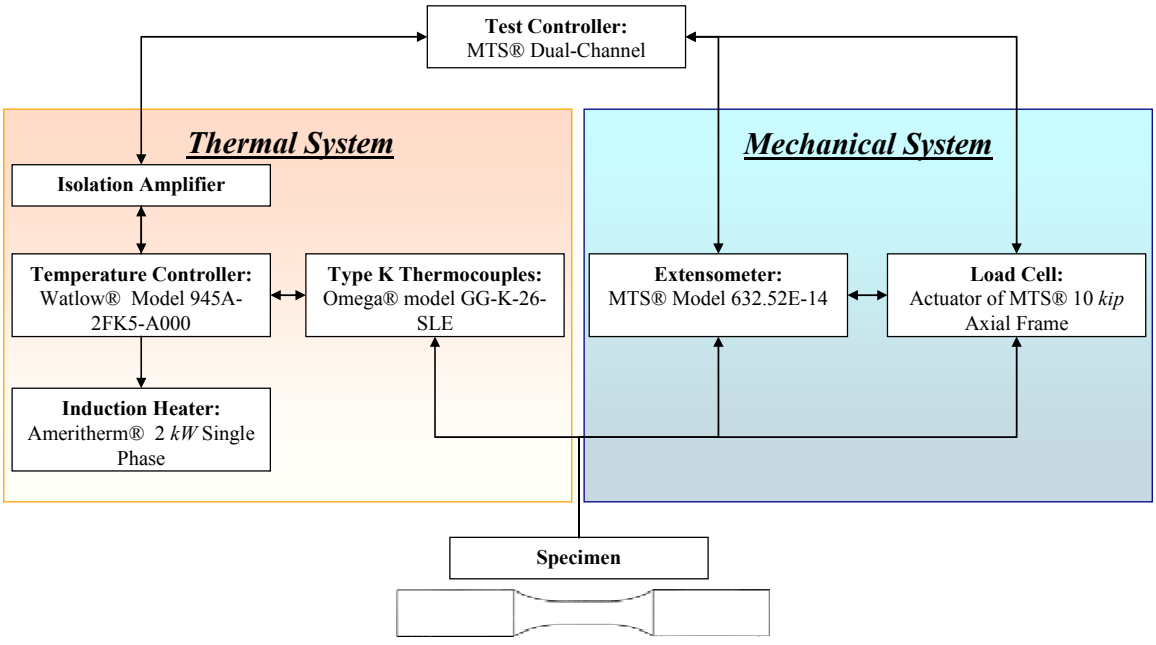

Figure 4-6: Components and signal flow in the dual closed-loop feedback control thermomechanical fatigue testing system.

4.3 Test Control and Thermal Strain Compensation

For both displacement and load control thermomechanical fatigue tests, the mechanical strain component can be expressed as the total measured strain response less the thermal strain component, i.e.

$$\varepsilon_{mech} = \varepsilon_t - \varepsilon_{th} \tag{4.1}$$

where ε_t is determined from the extensometer measurement and ε_{th} is some function of temperature. Errors in thermal strain calculations can manifest in several ways; disparities in axial and radial temperature gradients, small fluctuations in thermocouple readings due to weld quality, or small variations in induction coil placement between tests. In smooth specimen tests under mechanical strain control, an error in thermal strain is embodied in an over-under estimation of the corresponding mechanical strain. This results in additional axial forces in the TMF cycle, which are compressive during heating and tensile during cooling. As such, an error in the thermal strain calculation, or uncertainty in the total strain measurement, propagates directly to ε_{mech}. These errors are not nascent, therefore, as the control can directly impact deformation and life estimates. The variables of the test cycle must thus be controlled and tuned to mitigate the influence of any errors inherent in the thermal strain compensation method. The methods used comply with ASTM E2368-04 and are further explained later in this section.

The Testware SX software allows two different methods for controlling the thermal strain in TMF tests:

1. *File playback*: uses an ASCII file that defines a series of monotonic commands. The free response of the thermal strain is recorded as a function of cycle (time).

2. *Calculated variable control*: allows the user to specify the thermal strain as a function of another test variable, in this case temperature.

Although file playback allows for a composite approximation of the thermal strain curve (existing hysteresis), it does not allow for explicit control of thermal strain (control channels must be dedicated to temperature and total strain). Additionally, total Strain data requires post-processing in order to decompose into thermal and mechanical strain. By contrast, calculated variable control can be implemented rapidly, only requiring curve-fitting of the thermal strain with the control variable. Although the rapid and continuous calculation does adversely affect controller speed, the coupled variables are readily available and can be written to the output data file during testing. For these reasons, this compensation method was chosen for testing.

To calculate the thermal strain component, a linear relationship is often used, where

$$\varepsilon_{th} = \alpha(T - T_0) \tag{4.2}$$

where α is the coefficient of thermal expansion and T_0 is some reference temperature. While often quite sufficient for modest temperature ranges, the thermal strain in dual-

phase Ni-base superalloys often does not follow this linear relationship for high temperature ranges [2]. Thus, an interpolative measure based on experimental free expansion (thermal cycling with zero mechanical strain) data must be used. As per the ASTM E2368-04, the explicit temperature-based compensation of thermal strains can be given by a polynomial, i.e.

$$\varepsilon_{th} = \sum_{i=1}^{n} a_i (T)^i \tag{4.3}$$

where T is the actual feedback value measured by a thermocouple in the gauge section. Here, the quantity of digits included in the embedded polynomial becomes extremely important to the accuracy of the curve. A typical response is shown in Figure 4-7 for the baseline temperature cycle (500°C ↔ 950°C) and a cycle time of 180 *s*. The non-linearity is clearly distinguishable and the ε_{th} response distinct and asymmetric near the maximum and minimum temperatures. This discrepancy is due to axial and radial temperature gradients.

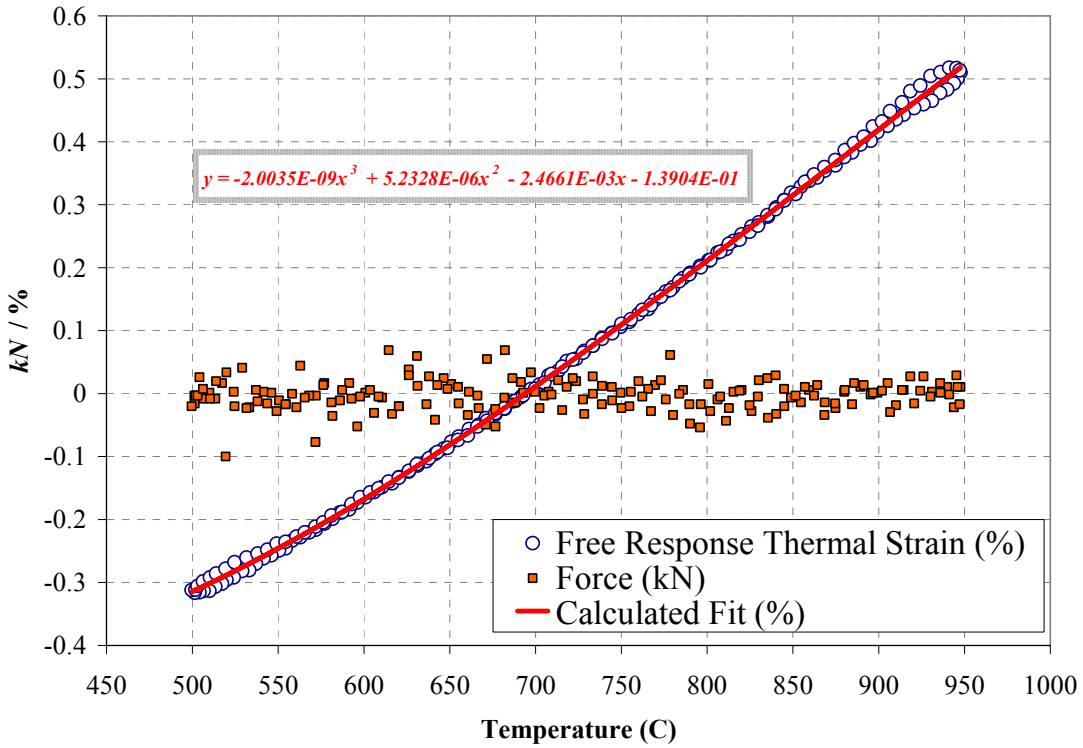

Figure 4-7: Thermal strain generated during free expansion under temperature cycling at zero load.

A consistent method was used to determine this stabilized response prior to each test, both to minimize error and inhibit slovenly calculations from substantially affecting the results of mechanical strain controlled tests. In all cases, the specimen temperature reading from the thermocouple was retransmitted to the TestStar controller and used to calculate the components of thermal and mechanical strain via Equation (4.3). During this exercise, it was later verified that the thermal strain hysteresis during the zero-load cycling was less than 5% of $\Delta\varepsilon_{th}$.

Comparing the magnitude and severity of cyclic fatigue-dependent and temperature-dependent damage mechanisms requires a consistent process relating the simultaneously varying thermal and mechanical forces (mechanical strain in the case of smooth specimens and applied stress in the case of notched tests) acting on the specimen.

This relation is defined as the waveform shift, or phase shift (the angle ϕ, expressed in degrees). This angle represents the shift between the maximum temperature response measured on the specimen and the maximum mechanical load response. In all cases, if the maximum thermal response leads the maximum mechanical load by 180° or less, the sign of ϕ is taken to be positive. As mentioned, linear in-phase and out-of-phase tests have repeatedly proven the most damaging and are therefore typically used in laboratory tests. The importance of studying both cycles is illustrated by the fact measurements have shown these conditions existing at different locations of an in-service turbine blade, as shown in Figure 4-8.

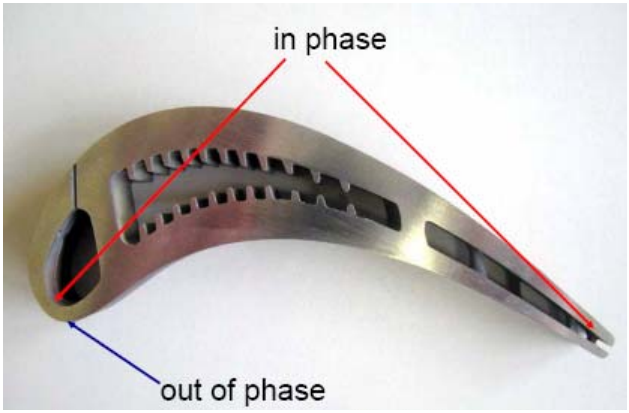

Figure 4-8: Cross section showing locations corresponding to linear in-phase and out-of-phase TMF cycling on an air-cooled turbine blade [63].

The strain vs. time waveforms for mechanical strain-controlled thermomechanical fatigue tests are shown in Figure 4-9.

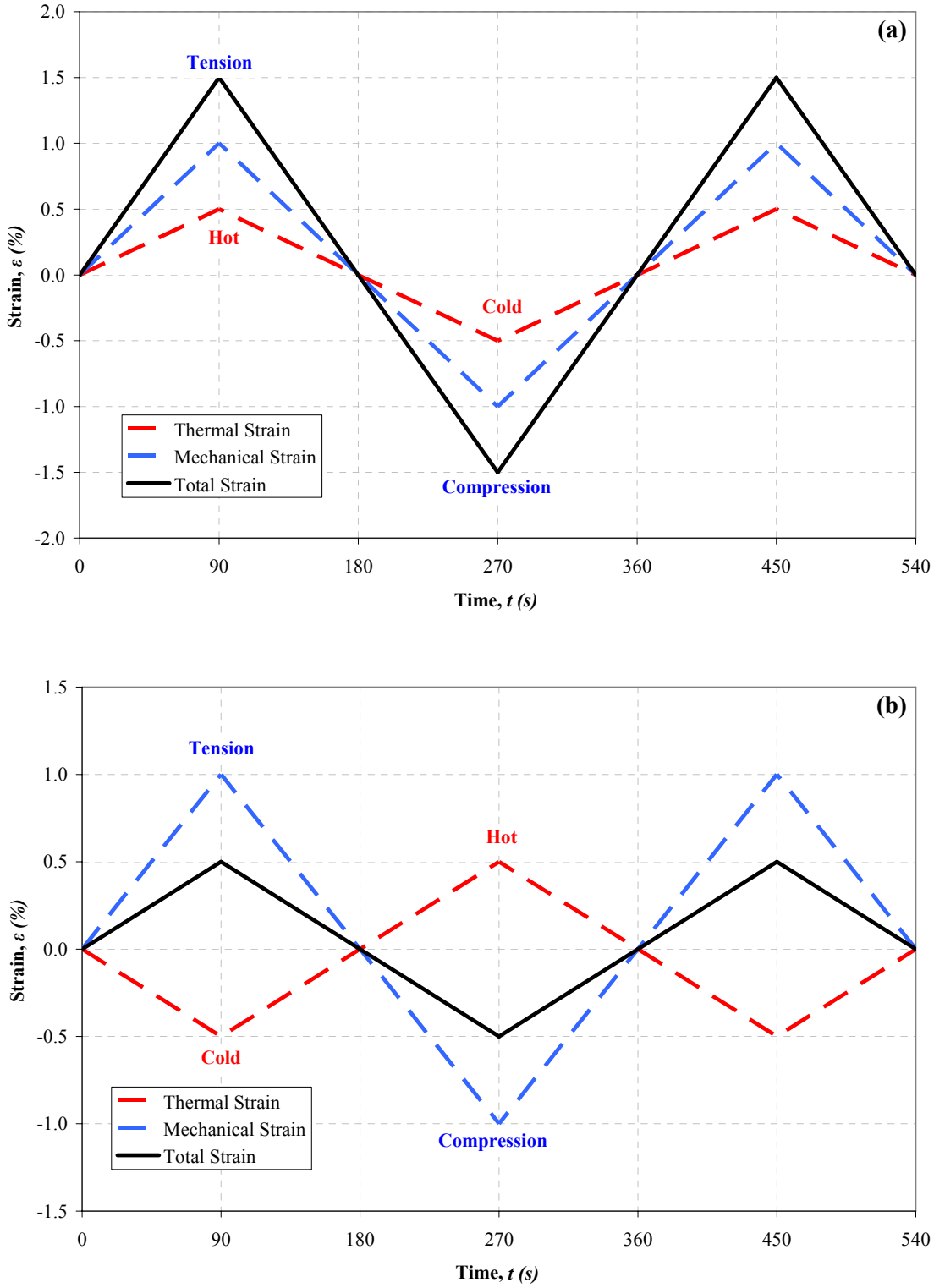

Figure 4-9: Example waveforms showing the strain history for both linear (a) in-phase and (b) out-of-phase thermomechanical fatigue cycling.

IP tests (ϕ = 0°) have maximum temperature corresponding to the maximum applied tensile mechanical strain, while OP tests (ϕ = 180°) have the same temperature congruous with the maximum compressive mechanical strain. The majority of tests in this study were linearly out-of-phase, as this has proven the most damage-inducing configuration for reasonable application strain ranges and thus the most conservative for life predictions.

The thermal strain range is dependent upon the minimum and maximum temperatures (T_{min} and T_{max}, respectively) used for a given continuously-cycled test. For example, the baseline TMF tests continuously cycled from 500°C to 950°C, this corresponded to a thermal strain range, $\Delta\varepsilon_{th}$, of approximately 0.83%. Thus, with the fixed 180 *s* cycle time, this range corresponds to a heating/cooling rate of 5°C/*s*. The temperature range of 500°C to 750°C resulted in a thermal strain range of approximately 0.49% with a cooling rate of 2.8°C/*s*. Reducing T_{min} for the 100°C to 950°C range necessitated 1700 *s* cycle time for a rate of 1.0°C/*s*. Forced cooling methods were not used for any experiments due to the radial thermal gradients induced. These gradients can influence deformation behavior and result in flawed tests.

4.4 Standards for Testing

All TMF testing was conducted according to ASTM E2368-04 for thermomechanical fatigue testing. For notched tests under force control, ASTM E466-02 was adhered to. In addition to maintaining constant load and temperature waveforms, these standards cite several criteria for test validity:

Criterion #1: The maximum allowable axial temperature gradient over the gage section at any given instant in time within the cycle shall be the greater of

$$\pm 1\% \text{ x } T_{max}, \text{ °K}$$

or

$$\pm 3\text{°K}$$

where T_{max} is the maximum cyclic temperature in °K under dynamic conditions (ASTM E2368-04)..

Criterion #2: During temperature cycling under zero force conditions, the ε_{th} hysteresis shall be no greater than 5% of the total induced thermal strain range (ASTM E2368-04).

Criterion #3: Under mechanical strain control, the mechanical strain range shall not deviate from the desired value by more than 2% of $\Delta\varepsilon_{mech}$ at any given instant throughout the duration of the test (ASTM E2368-04). Under force control, the imposed stress range should be maintained at all times within 2% of the desired test value (ASTM E466-02).

Criterion #4: Throughout the duration of the test, the error between the temperature and applied load phasing shall not exceed the bounds

$$\Phi \pm 5\%$$

where Φ is the desired phase shift for the test (ASTM E2368-04).

Static isothermal tests at various temperatures were used to optimize the shape of the induction coil to satisfy Criteria #1. This was done by attaching six Type K thermocouples to the gage section and recording the axial temperature gradient resulting from successively higher temperatures. Although no established standard exists to determine the dynamic temperature distribution, systematic readings from all thermocouples were used to analyze the dispersion within the gage section at various intervals while subject to thermal cycling under no load. The thermal cycle used for this examination and refinement was identical to that used for the thermomechanical fatigue cycle. The corresponding comparison of thermocouple responses ensured consistency and the satisfaction of Criteria #1.

In practice, large temperature ranges or short cycle periods can lead to large axial temperature gradients. In addition, in the absence of forced cooling, static convection and conduction from the water-cooled collets were the only methods used to cool the specimen. These limitations meant that the heating rate had to be adjusted to match the achievable cooling rate for a given combination of cycle period (t_c) and temperature range (ΔT). The accuracy can be measured by the amount of hysteresis which exists in the thermal strain response, ε_{th}, during cycling at zero force. Ideally, no hysteresis would exist, but limitations in equipment tuning capabilities typically results in a small amount near the cycle peaks. To limit this, t_c and ΔT were iterated until Criteria #2 was satisfied. The accuracy of (4.3) was measured by the amount of force generated on the specimen when thermally cycling while maintaining a control of zero mechanical strain.

In order to determine the evolution of the material's thermal expansion, a specific test was suspended after the specimen had been subjected a sufficient amount of real

TMF cycles (greater than the half life but before crack initiation was determined). Successive thermal cycling demonstrated that changes in the thermal response of the material were insignificant over the course of the test. As such, Equation (4.3), and the resulting mechanical strain calculation, was sufficiently accurate to cover the entire test duration. For notched tests conducted in force control, accurate tuning of the test frame insured the applied stress complied with the requirements of Criteria #3.

Phase compensation between command channels is built-in to the TestStar control software. Prior to initiating TMF cycling, the lag between the temperature set point command and thermal strain response was assessed to determine the correct value for the user-defined phase lag compensation. Once defined, this value would be sufficient to satisfy Criteria #4 for all tests with the same cycle period and temperature range. In addition, it would ensure that the mechanical loading remained synchronized with the thermal cycle for the entire duration of the test. It was found that an applied phase lag, Φ_{lag}, of -20° for a 180 second cycle with temperature range 500°C ↔ 950°C satisfied the requirements in ASTM E2368-04. Similarly, phase lags of -24° and -4° were applied to the 500°C ↔ 750°C and 100°C ↔ 950°C ranges, respectively..

4.5 Crack Initiation Criteria

A suitable crack initiation criteria is needed to isolate crack initiation. A crack depth of 0.5 - 1 *mm*. is commonly used for Ni-base superalloys. As the control method was not uniform for all tests, a unique criteria was established for both mechanical strain-controlled and force-controlled experiments.

4.5.1 Mechanical Strain-Controlled Experiments

For smooth (mechanical strain-controlled) specimens, the common force drop method was used. For this investigation it involved identifying the cycle at which the maximum tensile force (when the crack is open) has dropped 5% from the cyclically stable peak. When this decrease occurs, a crack of sufficient size has initiated. This cycle is calculated as the cycle of crack initiation (N_i) by

$$0.95 = \frac{P_i(N_i)}{P_0} \tag{4.4}$$

where P_0 is the stabilized maximum cyclic force and P_i is the maximum force for the cycle in which the crack is said to have initiated.

4.5.2 Force-controlled Experiments

For force-controlled experiments, a stiffness drop method was developed which utilizes the tension-compression asymmetry in the force-displacement response prevalent after crack formation. This method uses the loss of tensile stiffness which results from crack opening in the TMF half-cycle. A stiffness ratio at selected cycles can be calculated as the ratio (R_E) between tensile stiffness (E_T) and compressive stiffness (E_C), or

$$R_E = \frac{E_T}{E_c} \tag{4.5}$$

As propagation progresses, this stiffness continues to drop until failure. A measure of this reduction can therefore be correlated with crack size. Plotting R_E vs. cycles (N) allows for the identification of specific cycles which correlate to a discrete crack depth. This behavior is demonstrated in Figure 4-10.

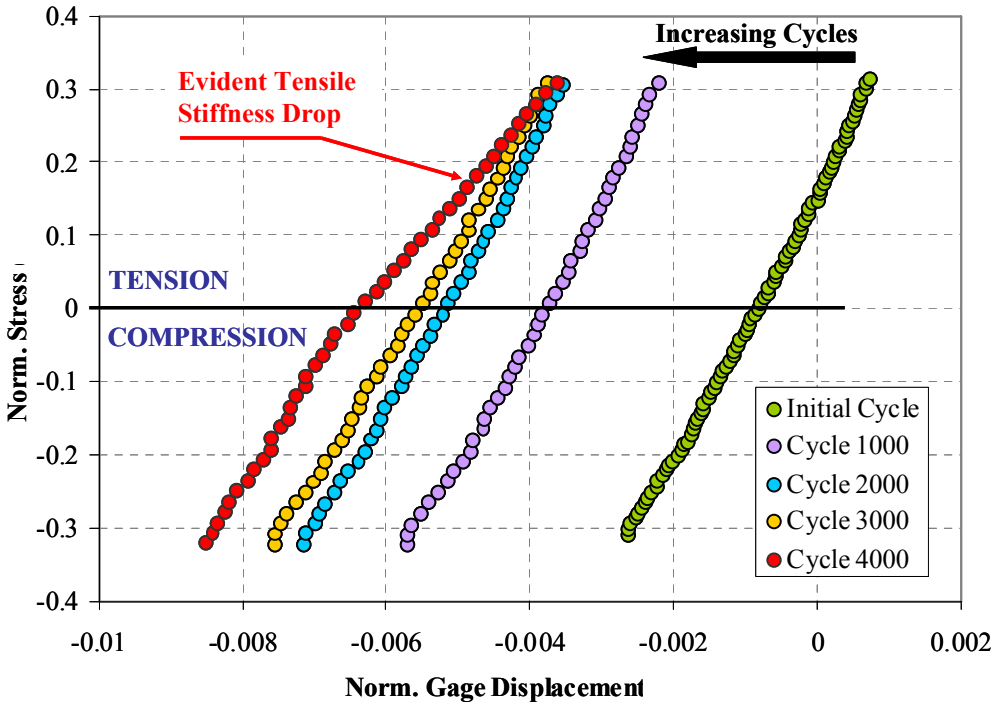

Figure 4-10: Example of the effect of a crack on the stress-displacement response used to determine crack initiation in notched specimen tests. The compressive shift in the curves was a result of creep ratcheting in the gage section during the high temperature half-cycle.

The stiffness ratio of the 10th TMF cycle was used as the stabilized reference. In order to select the R_E which corresponded to the desired crack size, select tests were interrupted prior to final fracture and the specimen broken under tensile load at room temperature.

For a crack size of 0.5 - 1 *mm*, it was found that the stiffness had consistently dropped 10% (i.e. R_E=90%).

A potential drop is another commonly used method for determining crack initiation. If a continuous AC or DC current is applied to a specimen, cracks growing through the cross section will result in a drop in the measured voltage. This method offers the advantage of more precise resolution, but could not be used in this study as the induction heating could manipulate the required voltage reading.

CHAPTER 5. COMPUTATIONAL MODELLING PRELIMINARIES

Directly obtaining the localized deformation and stress-strain information from the notch would require complex laboratory instrumentation. As this is impractical, various numerical simulations are employed to predict material behavior, which is helpful in interpreting the experimental results. These simulations also relate notched to unnotched specimens to evaluate the change in stress state on the deformation response and the impact of changes in the control method (force control vs. mechanical strain control). They also serve to outline the material behavior characteristics which are associated and may be unique to Ni-base superalloys or anisotropic DS alloys. To meet these objectives, non-linear finite element calculations have been performed using the ABAQUS v6.7 [64] software platform.

At the notch root, the stress state is multiaxial and the plastic zone constrained by the bulk elastic regions. This leads to considerable strain gradients, which compound the already complex anisotropic material behavior history within the notch. In addition, the most highly stressed regions may lie offset from the notch root, adjusting the likely location for crack initiation. As such, a series of simulations will focus on geometrical influences of the stress concentration as they relate to probable initiation sites.

This chapter describes the geometric models for smooth and notched specimens, and a description of two material models: a simpler elastic anisotropic model, and a physically-realistic, though considerably more computationally-expensive, crystal visco-plasticity model.

5.1 FE Models

5.1.1 Smooth Specimens

For smooth specimens containing no significant flaws or stress concentrations, a single element model containing the appropriate FCC slip systems contained in the crystal plasticity formulation is sufficient to model the anisotropic response. The simulations are performed in displacement control which effectively simulates uniaxial mechanical strain-controlled experiments. The simplified boundary conditions, as shown in Figure 5-1, reflect this. One face (four nodes) of the unit cube element had displacement and rotation constrained for the loading direction. The opposite face (four nodes) was applied an appropriate uniform displacement in the loading direction.

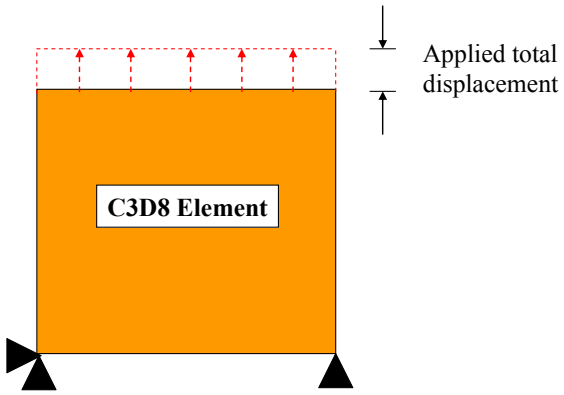

Figure 5-1: Boundary conditions for smooth specimen uniaxial simulations in displacement control.

The stress-strain response in the longitudinal orientation was for one grain with loading in the [001] direction. The response of a directionally-solidified material loaded in the transverse direction (normal to the axis of solidification), however, is an average comprising several grains. Modeling the transverse orientation utilized the same model, but with a different formulation to arrive at the response. This approach utilized the

average of 30 different grain orientations, all of which were subjected to the same deformation gradient. This method is demonstrated graphically in Figure 5-2. Orientation of the grains relative to the stress axis was described using the Euler angles (ϕ, θ, and ψ). For the longitudinal case, (ϕ, θ, ψ) = (0, 0, 0), as all grains are grown along the loading direction. For T-oriented simulations, all grains are aligned normal to the loading axis. In this case, (ϕ, θ, ψ) = (ϕ, 0, 0), where ϕ was randomly generated for each grain within the range (0, 2π).

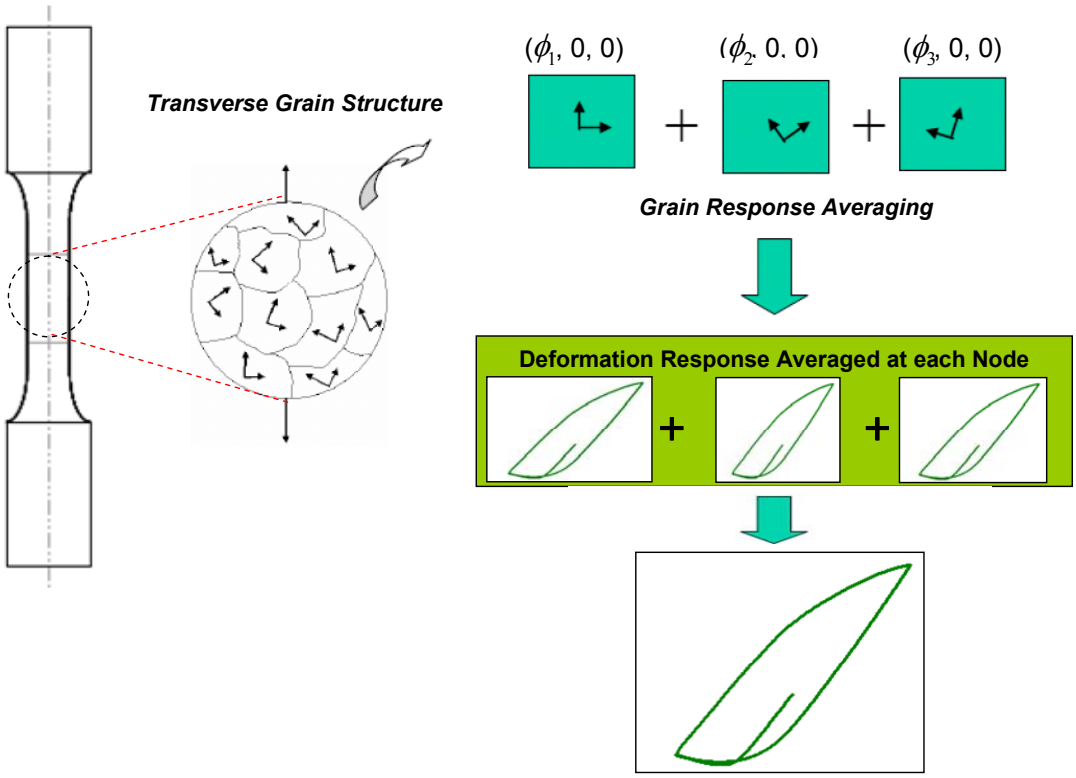

Figure 5-2: Method used to model the approximate response of a DS material loaded in the transverse orientation.

5.1.2 Notched Specimens

To model stress concentrations contained within the blade geometry, notched simulations were performed using the fatigue specimen geometry. Symmetry allowed for simplification to an eighth of the gage section, as shown in Figure 5-3. Both types of specimens were simulated using three-dimensional, linear, solid eight-node brick elements (ABAQUS designation C3D8).

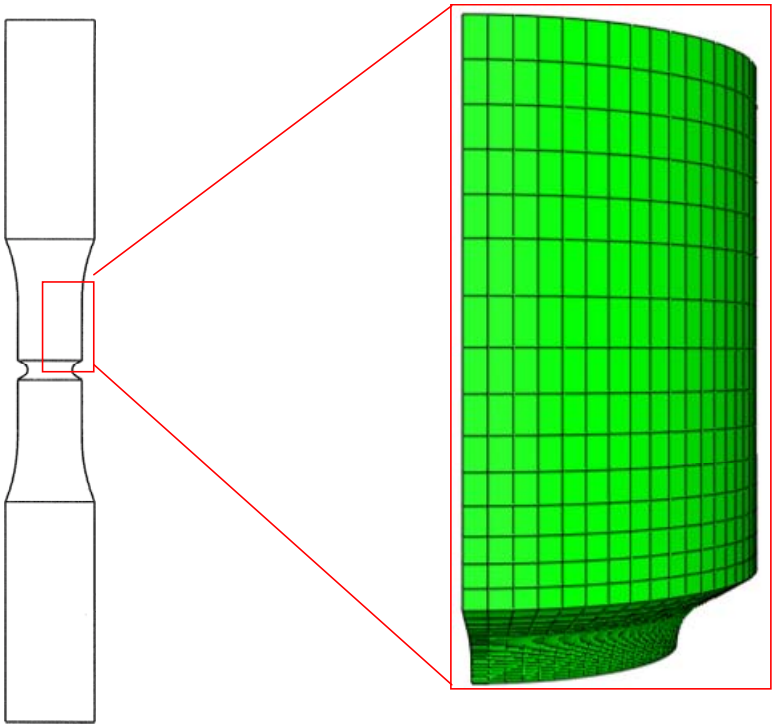

Figure 5-3: Finite element mesh used for notched simulations

Symmetry boundary conditions are applied to several faces of the model as shown in Figure 4-2.

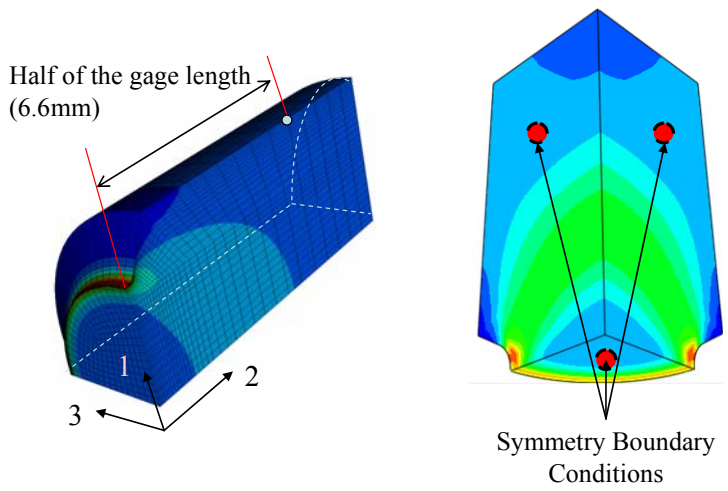

Figure 5-4: Boundary conditions and orientation definition for notched FE model

5.2 Transversely-Isotropic Elastic Modeling

To accurately describe the pseudo-elastic stress state and geometric effect of the notch, a fully elastic model was employed. Performing an elastic analysis decouples the more material-dependent behavior from the geometric effect of the notch. An anisothermal, transversely-isotropic elastic analysis of the notched specimen was performed to characterize this effect. The standard algorithms within ABAQUS for orientation and temperature-dependent properties were utilized.

5.2.1 Material Parameters

As the geometry is rotationally symmetric about a unique axis, the transversely anisotropic model had five independent elastic constants necessary to define the entire compliance matrix for a given material orientation. These are the Young's moduli E_1 and E_3, the Poisson's ratios v_1 and v_3, and the shear modulus G_{31}. This is due to orthotropic symmetry, where

$$\frac{-\nu_{12}}{E_1} = \frac{-\nu_{21}}{E_2} \text{ and } \frac{-\nu_{13}}{E_1} = \frac{-\nu_{32}}{E_3}$$

The majority of these constants were previously determined from experimental data collected by Moore [17]. Those which were not were taken from the closely related parent material, MarM247 DS, given in the literature by Mücke and Bernhardi and others [65, 66]. Orientation-dependent elastic parameters assigned to the elements are shown in Table 5-1 for the baseline temperature range.

Table 5-1: Elastic parameters used in analysis.

Property	**500°C**	**750°C**	**850°C**	**950°C**
E_1 (Mpa)	152550	134523	132200	119517
E_2 (Mpa)	152550	134523	132200	119517
E_3 (Mpa)	111280	102203	92520	85819
ν_{12}	0.175	0.175	0.175	0.175
ν_{13}	0.561	0.585	0.594	0.601
ν_{21}	0.175	0.175	0.175	0.175
ν_{23}	0.561	0.585	0.591	0.601
ν_{31}	0.409	0.445	0.416	0.431
ν_{32}	0.409	0.445	0.416	0.431
G_{12} (Mpa)	64915	57244	56255	50858
G_{23} (Mpa)	110600	99700	94300	87500
G_{31} (Mpa)	110600	99700	94300	87500

The proof of orthotropic symmetry can be found analytically by assuming each columnar grain has the elastic anisotropy of a cubic crystal. The material coordinate axis can then be aligned with the crystal axis of [100], [010], and [001]. The deviation of the direction of solidification with respect to the [001] axis can then be described with the eularian angle θ. The corresponding rotation around this axis is given by ϕ. These angles

serve to relate the material coordinate system with spatial coordinate system for any applied rotation, as shown in Figure 5-5.

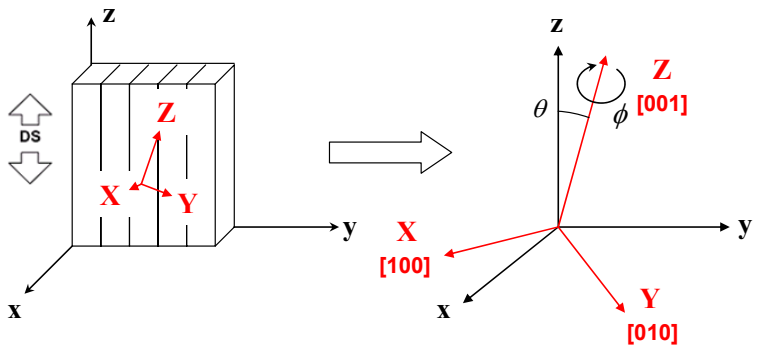

Figure 5-5: Eularian angles θ and ϕ which relate the material coordinates (X,Y,Z) to the special coordinates (x,y,z).

The complete formulation of the compliance matrix with respect to DS orientation and its incorporation into FE models is detailed in Hasebe et al. [67].

5.3 Continuum Crystal Visco-plasticity Modeling

Other elastic-plastic FEM codes do not account for the complex cyclic and temperature-dependent behavior of Ni-base superalloys. As a result, the continuum crystal plasticity model developed by Shenoy [68] has been used to simulate the cyclic material response under different loading conditions and better illustrate the complex and distinct deformation at the notch. The model was originally developed and calibrated for a similar directionally-solidified Ni-base blade superalloy, DS GTD-111, utilizing experimental data. Created to model slip activities in SC superalloys, the crystal plasticity formulation has the ability to account for grain orientation, microstructure, and creep in the material deformation response. Anisotropy is automatically accounted for through the

discrete definition of the crystallographic slip systems which govern deformation. The model is implemented as a User-Defined Material Subroutine (UMAT) in the ABAQUS FE software. At each time increment of a given step, the UMAT updates stresses, accumulated inelastic strain, internal state variables, the deformation gradient, and the Jacobean matrix to reflect the current state of the material.

A series of simulations served to approximate the phenomenon occurring at the stress concentration during high temperature TMF cycling. The deformation response and time-dependent behavior aided in interpreting experimental results.

5.3.1 Model Framework

The constitutive model can account for the effects of microstructure, including slip activity controlled by crystallographic orientation. As a basis, this method utilizes the deformation gradient, **F**, given as

$$\mathbf{F} = \mathbf{F}^{e} \cdot \mathbf{F}^{p} \tag{5.1}$$

where $\mathbf{F}^{e}$ describes the recoverable elastic stretch and rigid body rotation of the lattice structure and $\mathbf{F}^{p}$ models the irreversible dislocation motion corresponding to a permanent change in grain shape but not its overall crystal lattice. This decomposition is shown in Figure 5-6. It should be noted that although the model describes the behavior of dual-phase DS GTD-111 through the crystallographic orientation of the slip systems, it does not explicitly delineate between the distinct matrix and precipitate phases.

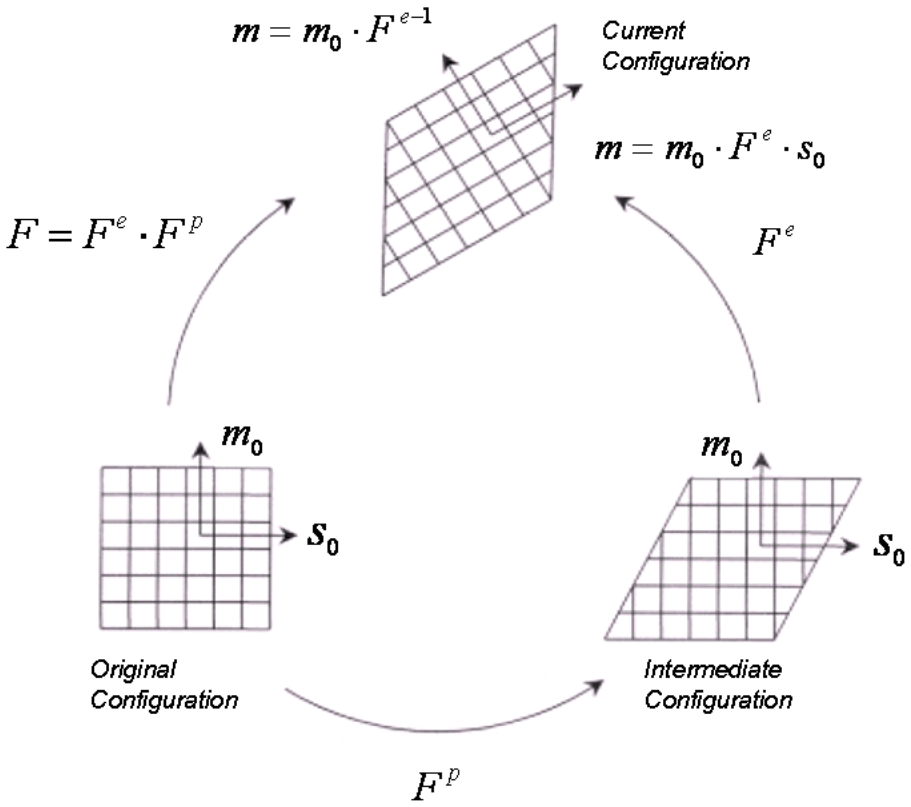

Figure 5-6: Decomposition of the deformation gradient [2]

For non-isothermal events, the thermal configuration needs to be incorporated into the deformation gradient. The kinematic relationship given in (5.1) is further modified with respect to a reference temperature configuration and can be described as

$$\mathbf{F} = \mathbf{F}^e \cdot \mathbf{F}^p \cdot \mathbf{F}^\theta \tag{5.2}$$

and the current material configuration updated to include the thermal deformation component. This further expansion of the deformation gradient with respect to the reference configuration is shown in Figure 5-7.

.

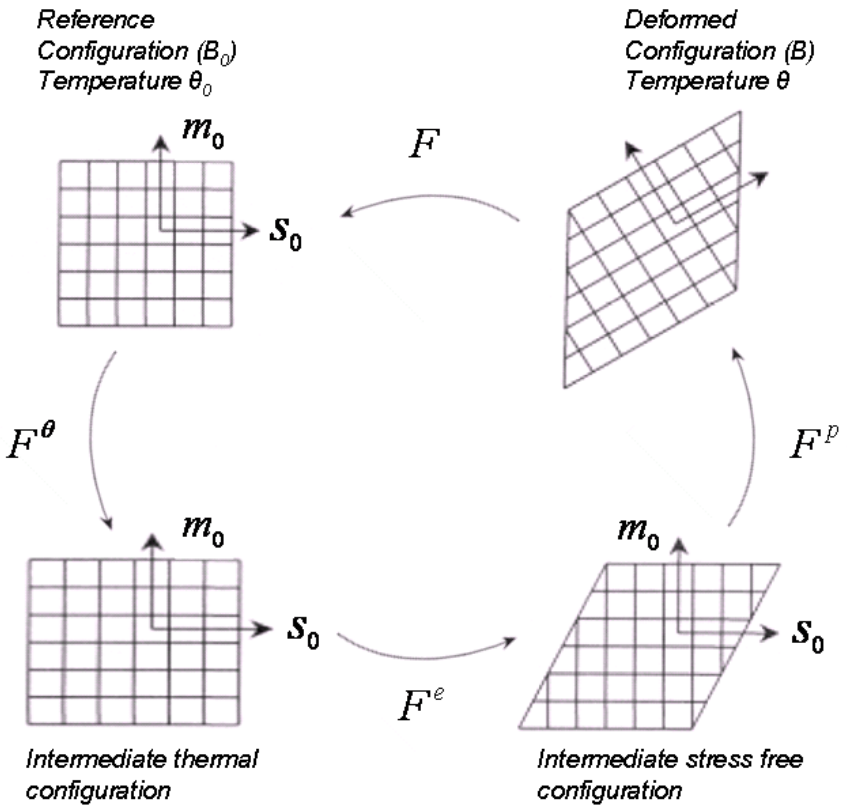

Figure 5-7: Deformation gradient with temperature dependence [2]

Eighteen slip systems are used for an FCC single crystal to describe the underlying temperature and strain rate dependent dislocation behavior, of which twelve are octahedral <110> systems active for the entire range of temperatures, and six macroscopic cubic systems of the {100}<110> type are present at high temperatures for which octahedral slip occurs in matrix channels [68]. As a rule, all systems are assumed active above the threshold stress.

To capture the temperature, stress, and strain dependence of the deformation on each slip system, the flow rule is used, for which the shearing rate on the α^{th} system is given as

$$\dot{\gamma}^{\alpha} = \dot{\gamma}_0 \Theta(T) \left\langle \frac{\tau_v^{\alpha}}{D^{\alpha}} \right\rangle^{n} \exp\left\{ B_0 \left\langle \frac{\tau_v^{\alpha}}{D^{\alpha}} \right\rangle^{n+1} \right\} \mathrm{sgn}(\tau^{\alpha} - \chi^{\alpha}) \tag{5.3}$$

where the viscous overstress for each slip system, τ_v^{α}, is given in terms of the resolved shear stress, τ^{α}, by

$$\tau_v^{\alpha} = \left| \tau^{\alpha} - \chi^{\alpha} \right| - \kappa^{\alpha} \frac{\mu}{\mu_0} \tag{5.4}$$

where κ^{α} and χ^{α} are internal state variables (ISV's) describing the hardening of each system, μ is the bulk modulus, and μ_0 is the bulk modulus at absolute zero. The coefficient B_0 and the power law exponent n are constants. The drag stress, D^{α}, is dependent on the temperature and visco-plastic deformation history. This assumes that though the dissipative nature of plasticity destroys the unique relationship between stress and plastic strain, the stress can be uniquely determined from a proper set of internal state variables [69].

The diffusivity parameter, $\Theta(T)$, is a temperature-dependent term given by

$$\begin{aligned} \Theta(T) &= \exp\left(\frac{-Q_0}{RT} \right) && \textit{for} \quad T \geq \frac{T_m}{2} \\ \Theta(T) &= \exp\left(\frac{-2Q_0}{RT_m} \left[\ln\left(\frac{T_m}{2T} \right) + 1 \right] \right) && \textit{for} \quad T < \frac{T_m}{2} \end{aligned} \tag{5.5}$$

where Q_0 is the activation energy for thermally-activated dislocation bypass of obstacles, R is the universal gas constant, and T_m is the absolute melting point temperature in Kelvin.

As the current yield surface is deformation history-dependent, the back stress increment for slip system α, $\dot{\chi}^{\alpha}$, must be able to account for shifts in the visco-plastic flow potential of that slip system. This is done through the internal state variables. The backstress evolution is then given as

$$\dot{\chi}^{\alpha} = h_x \left|\dot{\gamma}^{\alpha}\right| \mathrm{sgn}(\tau^{\alpha} - \chi^{\alpha}) - h_{\chi d}\chi^{\alpha}\left|\dot{\gamma}^{\alpha}\right| + \left(\frac{1}{R_{\chi}}\frac{\partial R_{\chi}}{\partial T} + \frac{1}{h_{\chi d}}\frac{\partial h_{\chi d}}{\partial T}\right)\chi^{\alpha}\dot{T} - \Omega_{\chi}^{\alpha} \qquad (5.6)$$

where

$$\Omega_{\chi}^{\alpha} = h_{\chi s}(T)\left|\chi^{\alpha}\right|^{r_{\chi s}} \qquad (5.7)$$

is the static thermal recovery term, needed to properly model hysteresis under TMF conditions [2]. This term captures the temperature rate dependence of the material under non-isothermal conditions. For these relations, the terms h_x, $h_{\chi d}$, $h_{\chi s}$, $r_{\chi s}$, and $R_{\chi} = h_x / h_{\chi d}$ are material constants.

As deformation will result in material hardening, the increase in dislocation density and other micromechanics factors will result in a change in the overall visco-plastic flow potential. This is especially true in the incipient stages of TMF cycling in Ni-

base superalloys, where high-stress deformation and copious dislocation motion have a significant effect on the current flow stress [70]. The resistance to this flow is manifested in the threshold stress, which can be written as

$$\kappa^{\alpha} = \kappa_c^{\alpha} + \kappa_e^{\alpha} \tag{5.8}$$

where

$$\kappa_c^{\alpha} = \kappa_0^{\alpha}(T) + h_{pe\tau}\tau_{pe}^{\alpha} + h_{se}\tau_{se}^{\alpha} + h_{cb}\left|\tau_{cb}^{\alpha}\right|$$

and

$$\dot{\kappa}_e^{\alpha} = h_0 \sum_{\beta=1}^{N_{slip}} q^{\alpha\beta}\left|\dot{\gamma}^{\beta}\right| - h_{\kappa s}\kappa^{\alpha}\sum_{\beta=1}^{N_{slip}}\left|\dot{\gamma}^{\beta}\right| - h_s\Theta(T)\left\langle\kappa^{\alpha} - \kappa_{th}\right\rangle^{r_s}$$

τ_{pe}^{α}, τ_{se}^{α}, and τ_{cb}^{α} are the temperature-dependent resolved shear stresses corresponding to the primary, secondary, and cubic slip systems, respectively. This is a good representation of the resistance to dislocation motion along a slip plane seen in real materials. Under cyclic loading, this resistance is manifest by motion of a certain similar distance along a slip plane upon load reversal.

Initially, there is no deformation, elastic or otherwise, and thus both the threshold stress and back stress are zero (i.e. $\chi^{\alpha}(0)=0$, $\kappa_e^{\alpha}(0)=0$). Due to the work of Shenoy and Gordon, it is assumed that the flow rule given in Equation (5.3) is sufficient for modeling the γ-γ' phases. The constants for DS GTD-111 necessary to complete these relations

were optimized experimentally in the literature [68]. Optimization involved an iterative approach to fitting the material parameters with LCF test results.

5.3.2 Material Parameters

The crystal visco-plastic model utilizes and interpolation scheme to determine temperature-dependent material parameters at each incremental change in temperature. These DS GTD-111 material constants were derived from the cyclic material response obtained from isothermal data, and thus the initial loading phase is less accurately captured. The procedure used to expand them to accommodate temperature-dependence is described in detail by Shenoy [68]. To ensure convergence of the material response at differing temperatures, a time step subroutine was implemented with a linear search algorithm at each increment. In addition, for the temperature ranges under consideration, the precipitate phase structure (size, shape, morphology) is assumed to be stable so that further microstructural changes can be neglected within the crystal plasticity framework. This is an important limitation when considering the effect of long term creep/TMF cycling on the material microstructure. The DS GTD-111 temperature-dependent material parameters used are presented in Table 5-2. Dashes indicate parameters which are either zero or could not be fitted using experimental data.

Table 5-2: Octahedral and cubic slip system constants for DS GTD-111

Octahedral Slip System

Temperature (°C)	h_χ (MPa)	R_χ (MPa)	$h_{\chi s}$	$r_{\chi s}$	κ_0^α (MPa)	h_0 (MPa)	$h_{\kappa s}$	h_s	r_s	$q^{\alpha\beta}$
427.0	55160	110.0	-	-	93.0	6895	135	-	-	1
760.0	186165	148.0	2.37E-07	1	148.0	0	0	-	-	-
871.1	137900	92.0	7.77E-08	1	70.0	0	0	-	-	-
982.2	41370	69.0	-	-	14.0	0	0	-	-	-
1037.8	17238	64.3	-	-	14.0	0	0	-	-	-

Cubic Slip System

Temperature (°C)	h_χ (MPa)	R_χ (MPa)	$h_{\chi s}$	$r_{\chi s}$	κ_0^α (MPa)	h_0 (MPa)	$h_{\kappa s}$	h_s	r_s	$q^{\alpha\beta}$
427.0	-	-	-	-	-	-	-	-	-	-
760.0	-	-	-	-	-	-	-	-	-	-
871.1	172400	81.2	-	1	64.2	0	0	-	-	-
982.2	55160	54.5	-	-	11.0	0	0	-	-	-
1037.8	17238	44.8	-	-	11.0	0	0	-	-	-

For both slip systems, the initial values are $\chi^\alpha(0) = 0$ and $\kappa_0^\alpha(0) = 0$. The most sensitive material parameters presented here are $h_{\chi d}$ and $h_{\chi s}$, which control the backstress evolution. Experiments have shown the backstress is extremely important to the behavior of Ni-base superalloys, often reaching magnitudes up to 50%-60% of the flow stress [71]. As it is temperature-rate dependent, and incorporates thermal recovery elements, this backstress term (which itself is a function of temperature- dependent parameters) is extremely important in modeling stress-strain hysteresis under conditions of TMF cycling.

Table 5-3: Common Constants for DS GTD-111

Common Constants

Temperature (°C)	C_{11} (MPa)	C_{12} (MPa)	C_{44} (MPa)	n	B_0	μ (MPa)	h_{pe}	h_{cb}	h_{se}
427.0	169617	70675	132000	5	0.05	132000	0.15	0.1	-0.03
760.0	151690	70329	125750	5	0.05	125750	0.15	0.1	-0.03
871.1	138830	69980	120360	4	0.05	120360	0.0	0.0	0.0
982.2	134450	69980	113880	4	0.05	113880	0.0	0.0	0.0
1037.8	131000	69980	108180	4	0.05	108180	0.0	0.0	0.0

Q_0 (KJ/mol)	R (J/mol*K)	μ_0 (MPa)	$\dot{\gamma}_0$ (s^{-1})	κ_{th} (MPa)	D_0 (MPa)
309	8.314	166000	1.15×10^9	0.0	102.0

The common constants contained in Table 5-3 consist of physical elastic parameters and activation energy constants for thermally-activated diffusion processes obtained from the literature [6]. The calibration range for the temperature-dependent variables within the model is stated as room temperature up to a maximum of 1038°C.

5.3.3 Response Validation-Isothermal

The ability of the crystal plasticity code to accurately capture the material response at various temperatures was assessed by simulating various different isothermal and thermomechanical cycles. These were compared with experimental LCF data collected at those temperatures and under the same load and strain rate. These examples verify the accuracy of the temperature-dependent deformation response predicted by the crystal plasticity formulation in the UMAT. In each case, these plots were generated for the first cycle from the same representative element. Simulations were conducted in displacement control with a triangular waveform for the mechanical strain and temperature inputs. The actual experimental results for DS GTD-111 obtained by Gordon

are superimposed [2] in Figure 5-8. As the material was shown to be nearly cyclically stable after a single cycle, only the first is shown for simplicity.

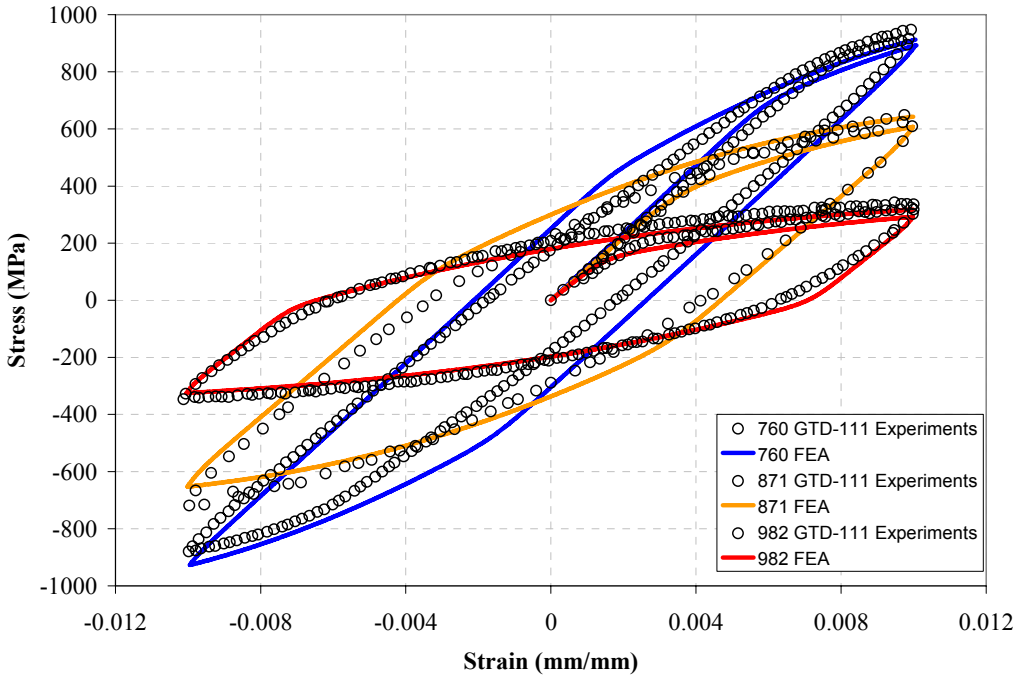

Figure 5-8: Isothermal response of temperature-dependent crystal plasticity formulation for DS GTD-111 in the longitudinal orientation with $\Delta\varepsilon_{mech}$=1.0% at 760°C, 871°C, 982°C with that of experimental results. In each case, R=-1 and $\dot{\varepsilon}$=0.5 %/s.

5.3.4 Response Validation- TMF

Accounting for the thermal component of total strain in anisothermal simulations required a "pre-cycling" exercise similar to that used in laboratory experiments. The temperature boundary conditions are prescribed and the model was thermally cycled under no load. The free response was extracted and the appropriate displacement bounds set to yield the desired amount of mechanical strain. It should be noted that the same third-order polynomial approximation for the coefficient of thermal expansion was used

for all orientations. This assumption was supported by experiments, which indicated a negligible change in thermal strain response between L- and T-oriented samples.

With the model calibrated to isothermal test data, IP and OP TMF responses are adequately predicted, thereby validating the model for uniaxial fatigue loading. Figure 5-9 shows the simulated stress-strain behavior under uniaxial TMF conditions as compared with experimental results for DS GTD-111 obtained Gordon.

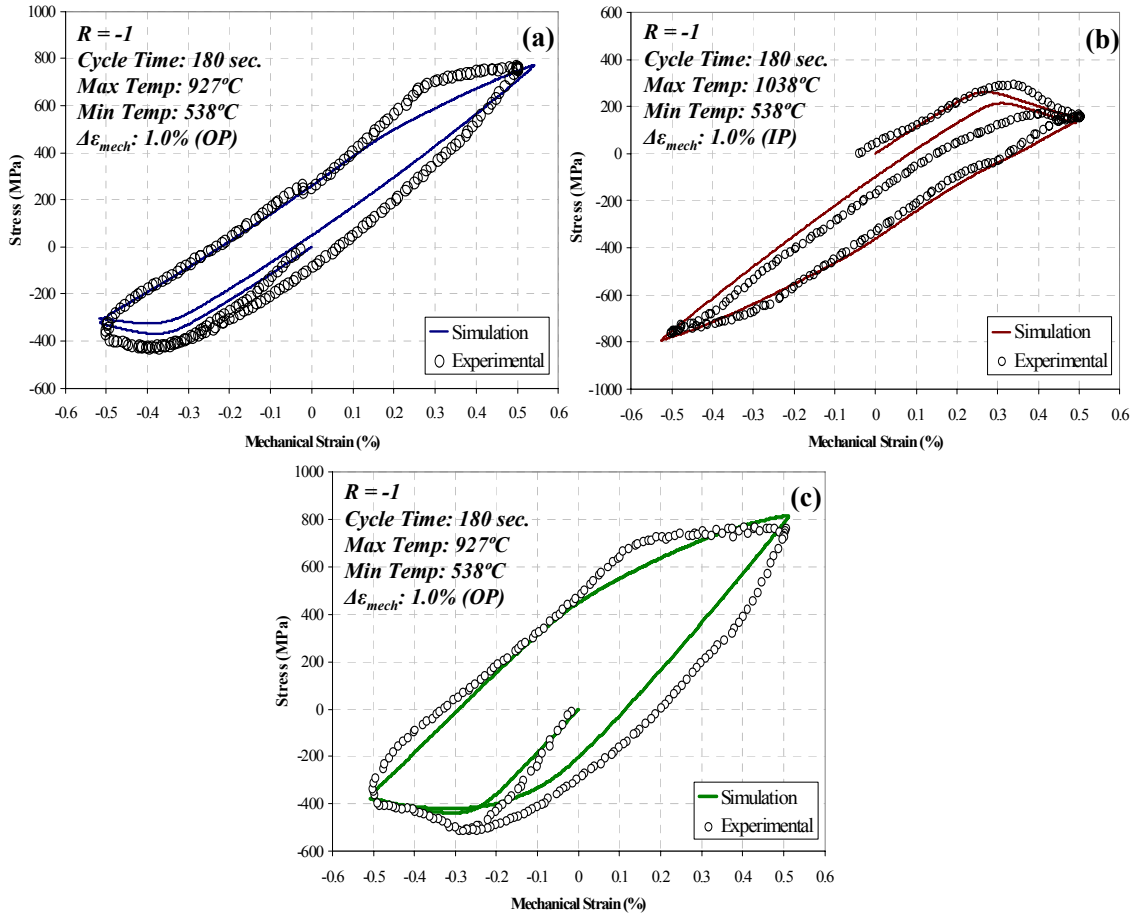

Figure 5-9: TMF response of temperature-dependent crystal plasticity formulation for DS GTD-111 in (a,b) the longitudinal orientation and (c) the transverse orientation with that of experimental results.

5.3.5 TMF Simulations

To evaluate the deformation response of experiments compared to elastic visco-plastic FE predictions, various TMF simulations were performed for both smooth and notched specimens in mechanical strain-control and force-control. Simulations modeled both cycles (0° IP and 180° OP), temperature ranges (500°C↔950°C baseline and 500°C↔750°C) with a total cycle time, t_{tc}, equal to 3 *min*. As stress and strain response values reflect GTD-111 material properties, these simulations could not actually predict the actual response at the notch root for CM247LC DS. However, as it is capable of simulating time-dependent deformation such as the effects of strain rate and tertiary creep, the stabilized response of the DS material can be predicted for a wide range of conditions.

CHAPTER 6. THERMOMECHANICAL FATIGUE-EXPERIMENTAL RESULTS

A wide variety of experiments were performed on CM247LC DS to evaluate its response to mechanical, thermal, and environmental factors. Associated microscopy and fractography were necessary to identify not only the active damage mechanisms, but the extent of their synergistic contributions throughout the life of a tested sample. Detailed results and trends in both the TMF deformation response and cycles to crack initiation are discussed. Also included is a description of microstructural observations and evolution as a result of high temperature cycling.

The majority of experiments were continuously cycled between 500°C and 950°C. This range is of particular importance because it straddles regions where the yield strength peaks and oxidation behavior becomes increasingly important. For this reason, the set of experiments conducted using this temperature range will be considered the "baseline". These constitute a benchmark from which to compare and analyze all other conditions. Additionally, most experiments utilized L-oriented specimens, as this is the primary orientation of actual service components.

To protect proprietary information, much of the data presented is normalized by reference values. The same factors of stress, strain, and life are used throughout, preserving the experimental trends and visual progressions from test results.

6.1 Baseline Smooth Specimen Results

6.1.1 Life and Deformation Response

Since all stresses, strains, and temperatures are uniform within the gage section, smooth specimen results comprise a metric from which to compare variations in TMF conditions. Crack initiation in each case was determined using the load drop method described in Chapter 4. In the vase majority of cases, fracture was not sudden, indicating that load was shed while the dominant crack(s) propagated through the gage section.

The strain-life and stress-life plots of smooth k_t=1 tests are plotted as a function of cycles to crack initiation in Figure 6-1. For comparison, the life curves for continuously-cycled isothermal tests conducted at 950°C in a previous study are shown. IP cycling resulted in lower stress amplitudes than OP TMF for the same mechanical strain amplitudes. Unlike the stress amplitude, the mechanical strain amplitude collapses both the OP and IP data at a normalized value of 0.525%, indicating that fatigue is the dominant mechanism. Both cycle types proved more damaging than a corresponding isothermal LCF test conducted at 950°C with the same mechanical strain range [17]. Cycles to crack initiation for both TMF tests were approximately a factor of three shorter than this test. This is due primarily to the additional damage mechanisms activated in non-isothermal cycling.

Figure 6-1(a) demonstrates the material-dependent crossover in IP and OP fatigue lives for the longitudinal orientation. It should be noted this crossover occurs at a greater mechanical strain amplitude than that shown for the Ni-base superalloys alloys IN-718, Mar-M247, DS GTD-111, M963 [2, 4, 13, 72]. This is testament to the impressive fatigue resistance of L-oriented CM247LC DS.

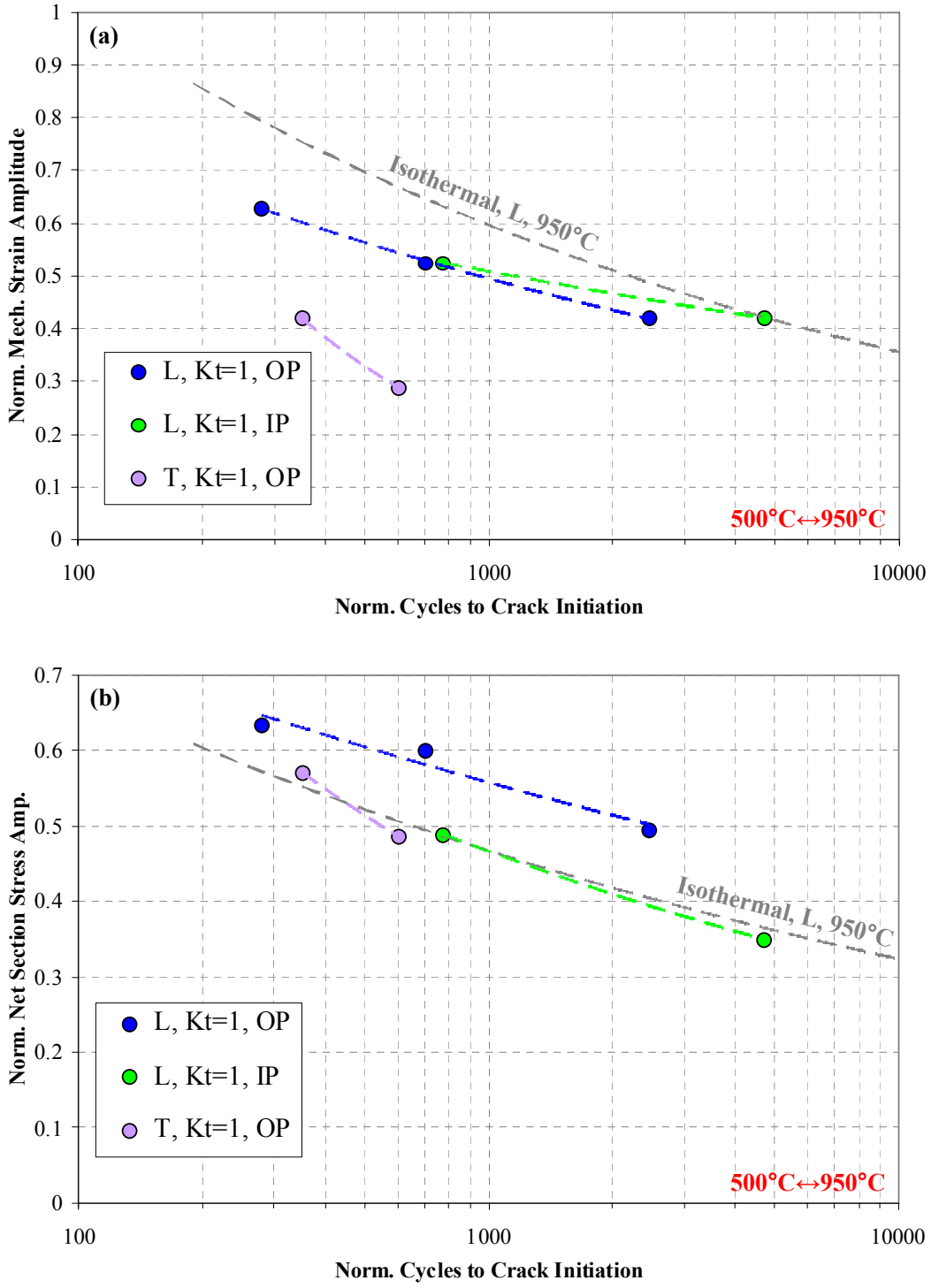

Figure 6-1: Baseline longitudinal smooth specimen results plotted as a function of (a) mechanical strain amplitude and (b) net section stress amplitude.

As the mechanical strain amplitude was reduced, a greater disparity developed between the lives of IP and OP tests. Below the intermediate strain crossover point, the IP test resulted in a test duration more than 1.9 times that of an OP test with the same applied amplitude. The relatively flat slope of the IP curve indicates this cycle phasing is extremely sensitive to the applied load.

Figure 6-2 shows the typical stress-mechanical strain hysteresis loops for the first and half-cycle of OP and IP tests of equal applied strain amplitudes. Typical of the high-strength, limited-ductility of CM247LC DS, the generated hysteresis curves showed very limited cyclic plasticity. The plastic strain ranges are very small when compared to the mechanical strain range (the ratio is never more than 1/10 in longitudinal tests) even for relatively high applied loads. The stress-strain response was shown to stabilize after only a few cycles during which limited cyclic softening occurs at T_{max}. Note that for both OP and IP tests, the maximum tensile strain does not correspond to the maximum tensile stress, which indicates that creep and stress relaxation take place during the high temperature half-cycles.

The stabilized tensile mean stress developed in the OP test was approximately 1.2 times the magnitude of the compressive mean stress of the IP, which was proportional to the ratio of their stress ranges. In addition, a shift in the hysteresis loop for both TMF cycles is evidenced by comparing the half-life plots (Cycle $N/2$) in Figure 6-2 to those of the first cycle. This shift is in the tensile direction for OP TMF and compressive for IP cycling. It results from continual stress relaxation during the high temperature half cycle, which increases the corresponding stress reached at T_{min}. This shift in the mean stress typically stabilized after approximately 100 cycles.

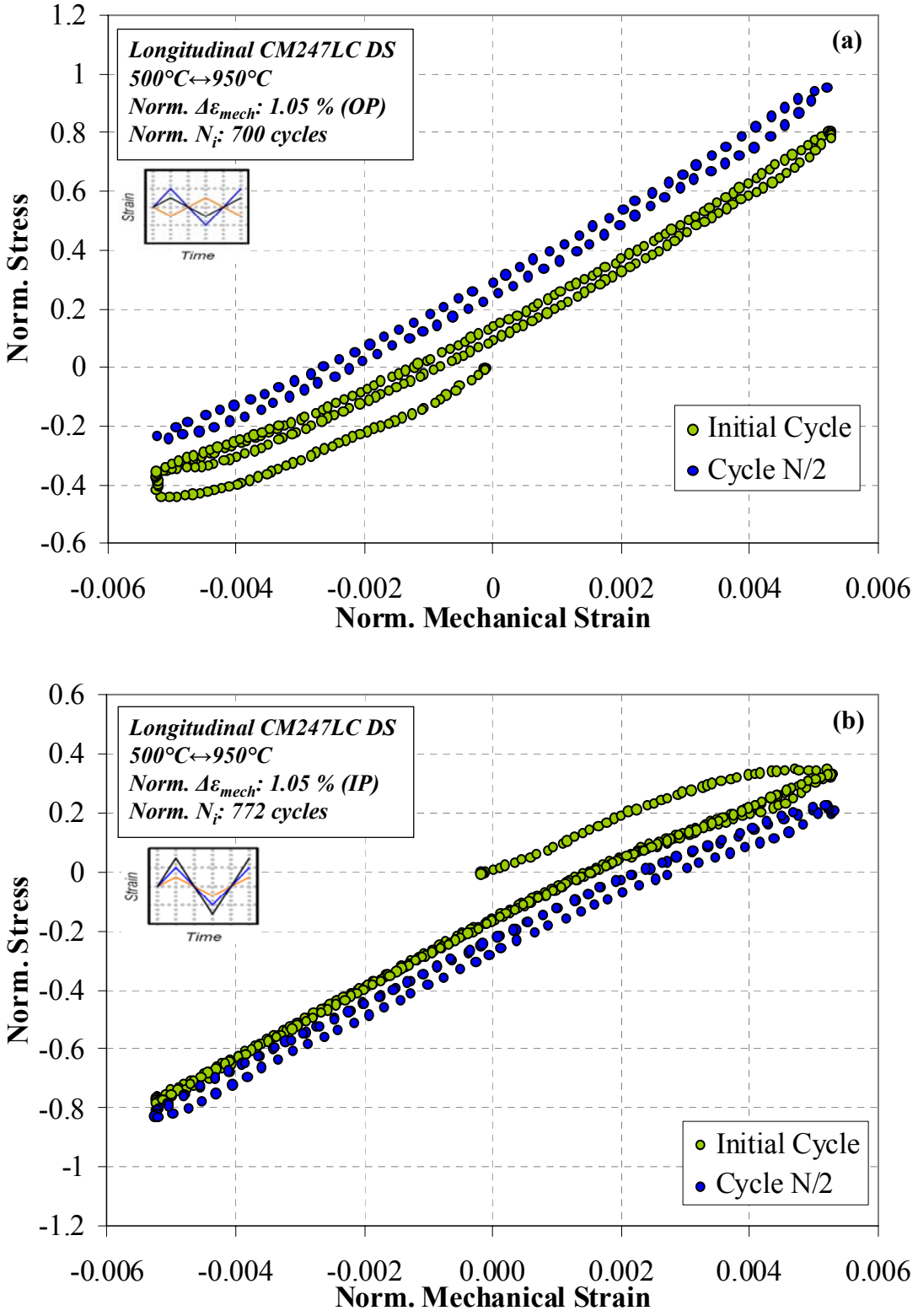

Figure 6-2: Stress-mechanical strain hysteresis response of CM247LC DS subjected to (a) out-of-phase and (b) in-phase TMF.

The cyclic behavior of the alloy was very stable. When defined in terms of the change in cyclic stress amplitude, most hardening or softening occurs in the first few cycles. The stress range then stabilizes within the first five to ten cycles. This stress-history evolution is supported using finite element analysis, as shown in Figure 6-3. The simulations showed for both OP and IP cycling, the maximum and minimum stresses are 95% cyclically stable after five complete cycles.

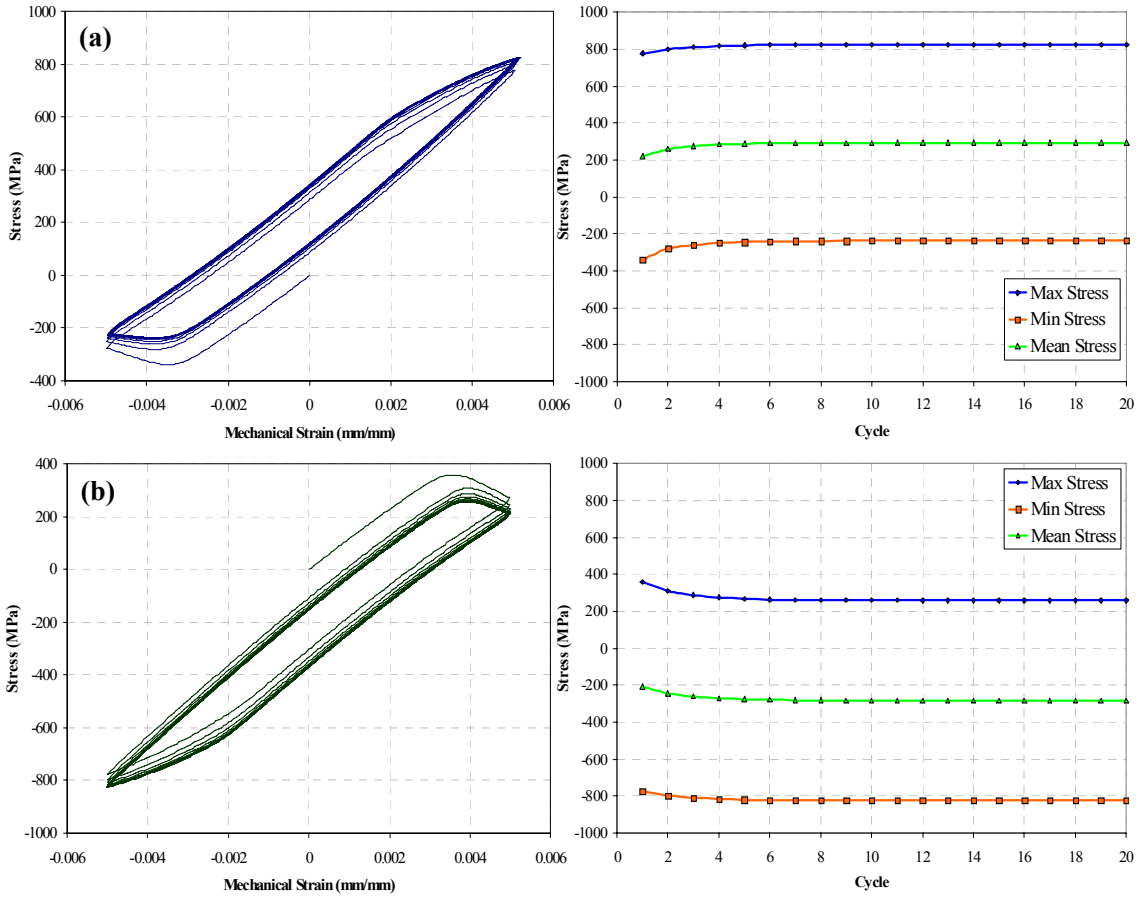

Figure 6-3: Simulated response and stress evolution for the first 20 cycles of longitudinal (a) out-of-phase and (b) in-phase TMF using the crystal visco-plasticiy model.. For both, $\Delta\varepsilon_{mech}/2$=0.5% with T_{min}=500°C and T_{max}=950°C.

The stress ranges developed during the OP tests tended to be 12-18% greater than those of their comparable isothermal counterparts at 950°C, though their mechanical strain ranges were actually lower. This is a result of the high tensile stresses achieved during the cool half-cycle of the TMF cycle, where an increasing elastic modulus accelerates the stress resulting from the same strain increment. In contrast, IP TMF followed nearly the same stress-life curve as isothermal tests for the range of life considered.

6.1.2 Phasing Dependence

Both IP and OP smooth specimens showed a propensity for thumbnail cracks growing nearly perpendicular to the loading axis, like that in Figure 6-4. IP tests usually exhibited fewer and smaller cracks on the fracture surface, but also internal creep damage and voids formed in the interdendritic regions. In both types of cycles, oxidation results in the diffusion of Al and Cr away from exposed surfaces (including those of the crack) [29]. These elements are the primary constituents of the γ' strengthening phase. The weakened γ' depleted zone in the substrate near the surface is then more susceptible to crack initiation and subsequent accelerated crack growth.

Typical OP and IP fracture surfaces are shown in Figure 6-5. Under high magnification, no fatigue striations were observed for smooth specimens subjected to either cycle type. For both cycles, cracks tended to nucleate at the surface, often in the interdendritic region or at carbide inclusions, and coalesce into a dominant thumbnail crack. More numerous crack initiation sites were observed in OP samples, evidence of

increased environmentally-assisted damage. Although in some IP cases observed cracks nucleated in the interior of the material, the majority began at or nearby the surface.

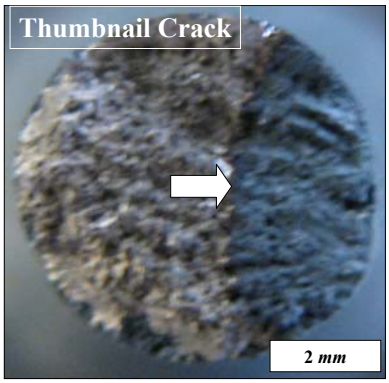

Figure 6-4: Thumbnail crack in a smooth specimen subjected to OP TMF with $\Delta\varepsilon_{mech}$=1.26% and T=500°C↔950°C.

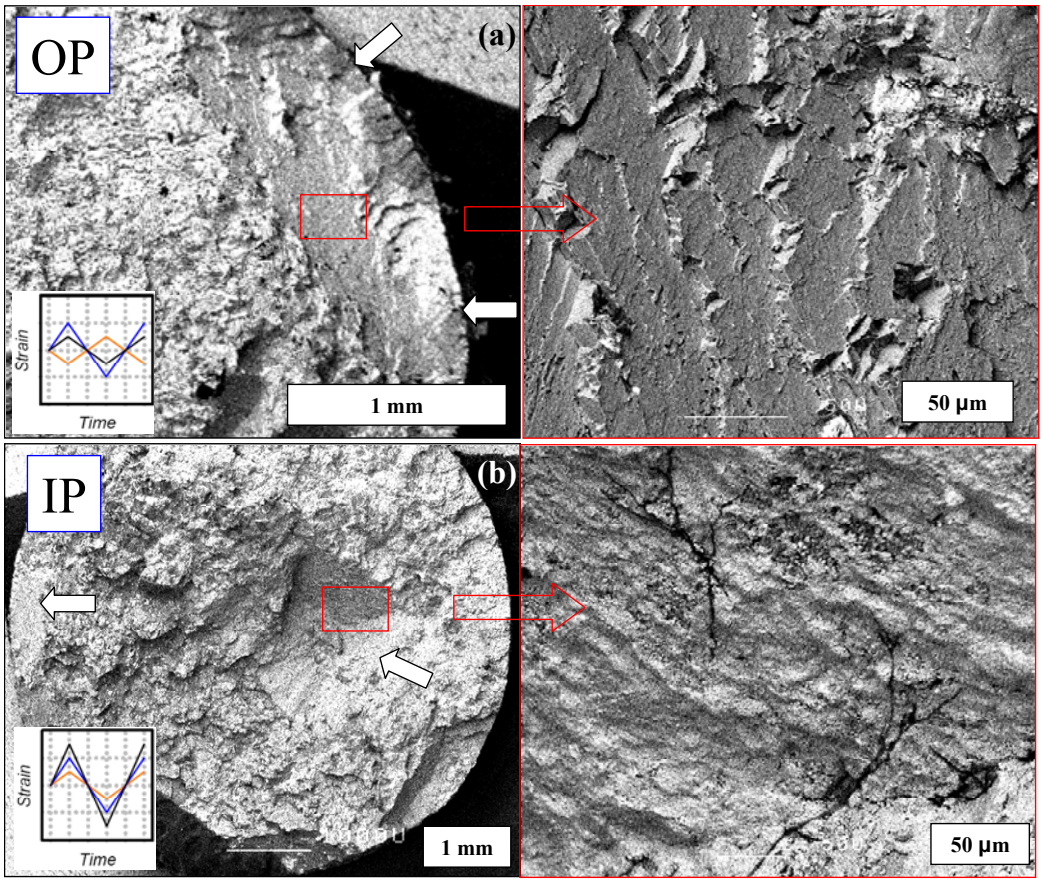

Figure 6-5: Smooth specimen fracture surface examination of L-oriented CM247LC DS showing crack initiation in (a) OP and (b) IP TMF with normalized $\Delta\varepsilon_{mech}$=1.05% and T=500°C↔950°C. Crack initiation sites are indicated with white arrows.

Thermal mismatch between the accrued oxide layer and the underlying base metal results in distinct surface behavior in IP (where oxides are in compression at T_{min}) and OP (tension at T_{min}) tests. The cumulative effect of oxidation-assisted surface cracking in tension creates oxide spikes as shown in Figure 6-6.

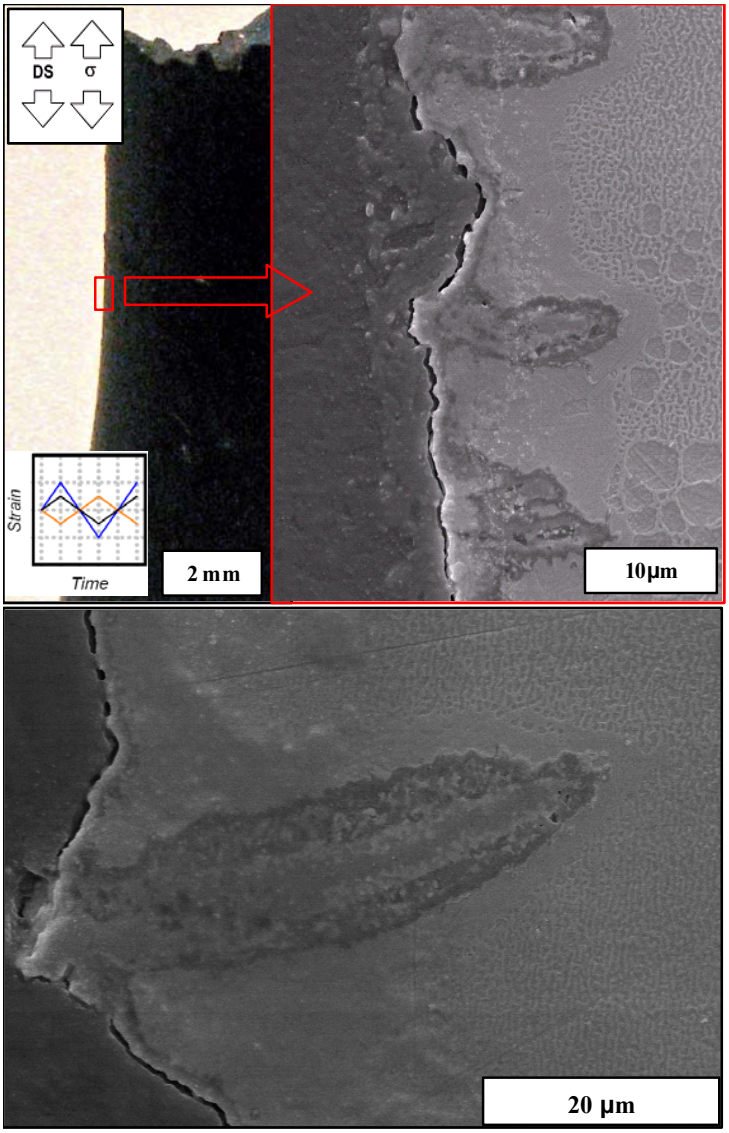

Figure 6-6: Smooth specimen crack initation at oxide spikes resulting from continuous out-of-phase TMF cycling, Test conditions: normalized $\Delta\varepsilon_{mech}$=1.05 %, and T=500°C↔950°C.

Of the specimens tested, those with the lowest applied loads increased N_i, and thus the time spent at maximum temperature. In these cases, more extensive cracking of the oxide spikes occurred. Many of these cracks protrude into the alloy substrate within dendrite channels.

In-phase tests had different damage mechanisms contributing to the crack initiation process, as shown in Figure 6-7.

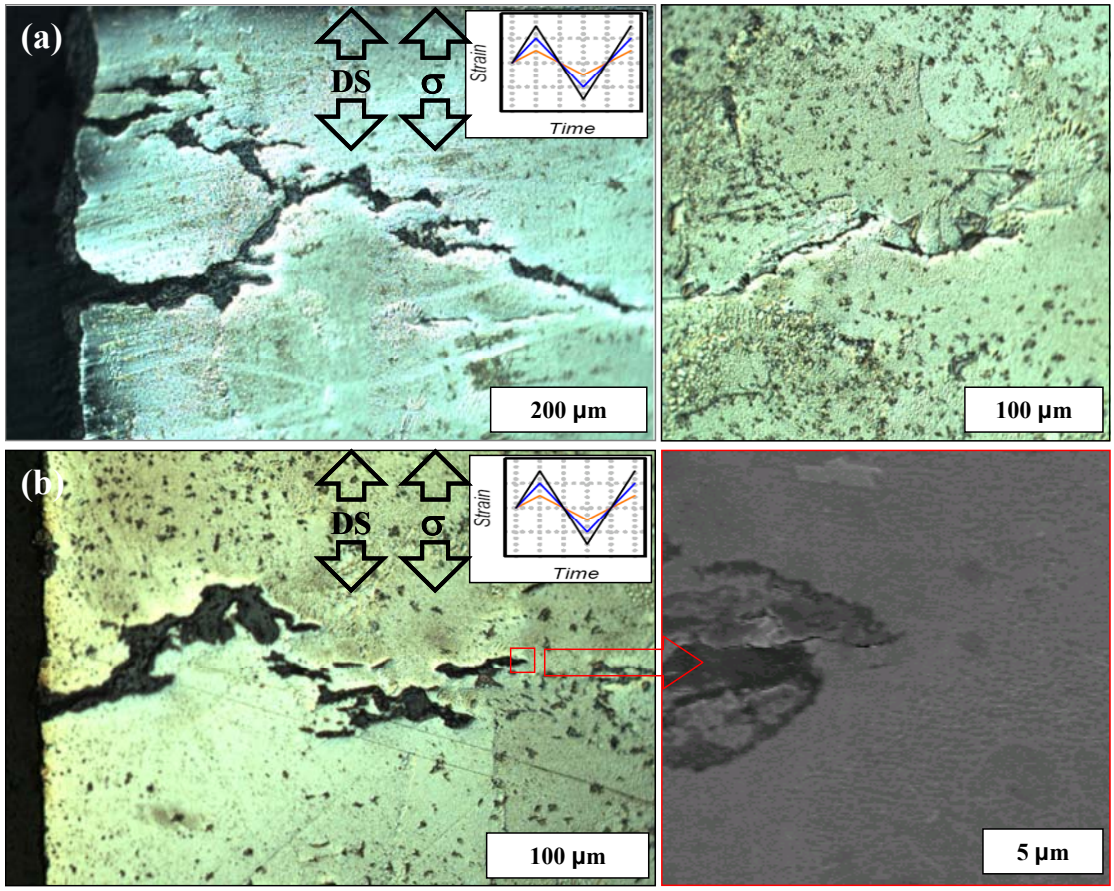

Figure 6-7: Smooth specimen crack initation in longitudinal CM247LC DS resulting from continuous in-phase TMF cycling wth normalized mechanical strain ranges of (a) 1.05% and (b) 0.84%. In both cases, T=500°C↔950°C.

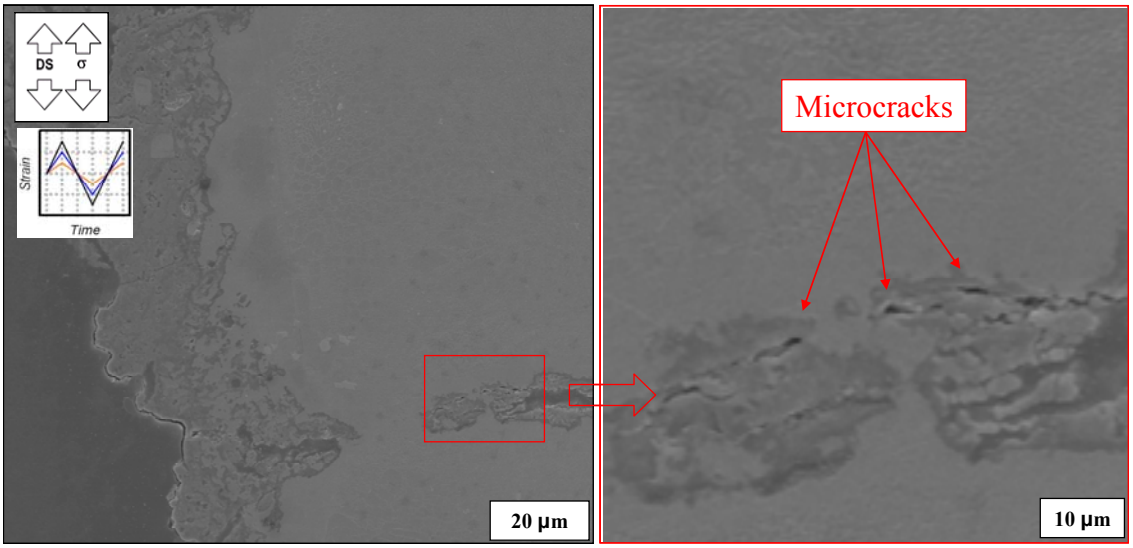

Figure 6-8: SEM image showing crack initation at subsurface voids in longitudinal CM247LC DS resulting from IP TMF cycling wth normalized $\Delta\varepsilon_{mech}$=1.05% and T=500°C↔950°C.

Subsurface damage, consisting primarily of microcracks forming and coalescing at microstructure in-homogeneities like grain boundaries, carbides, and eutectic γ' comprises a significant portion of damage under these conditions. Due to the distribution of these features and their non-homogeneity with the surrounding γ-γ' matrix, their cracking behavior is not uniform.

Whereas OP TMF produced surface cracking and oxide spikes (Figure 6-9(a)) in tension, compressive loads at T_{min} occur during IP testing. With time, the continuous mismatch in CTE between the oxide layers and the bulk substrate can cause wedged oxides to detach or spall from the surface, revealing subjacent virgin metal. Post-test inspection of the surface revealed spallation of oxide scales, as shown in Figure 6-9(b).

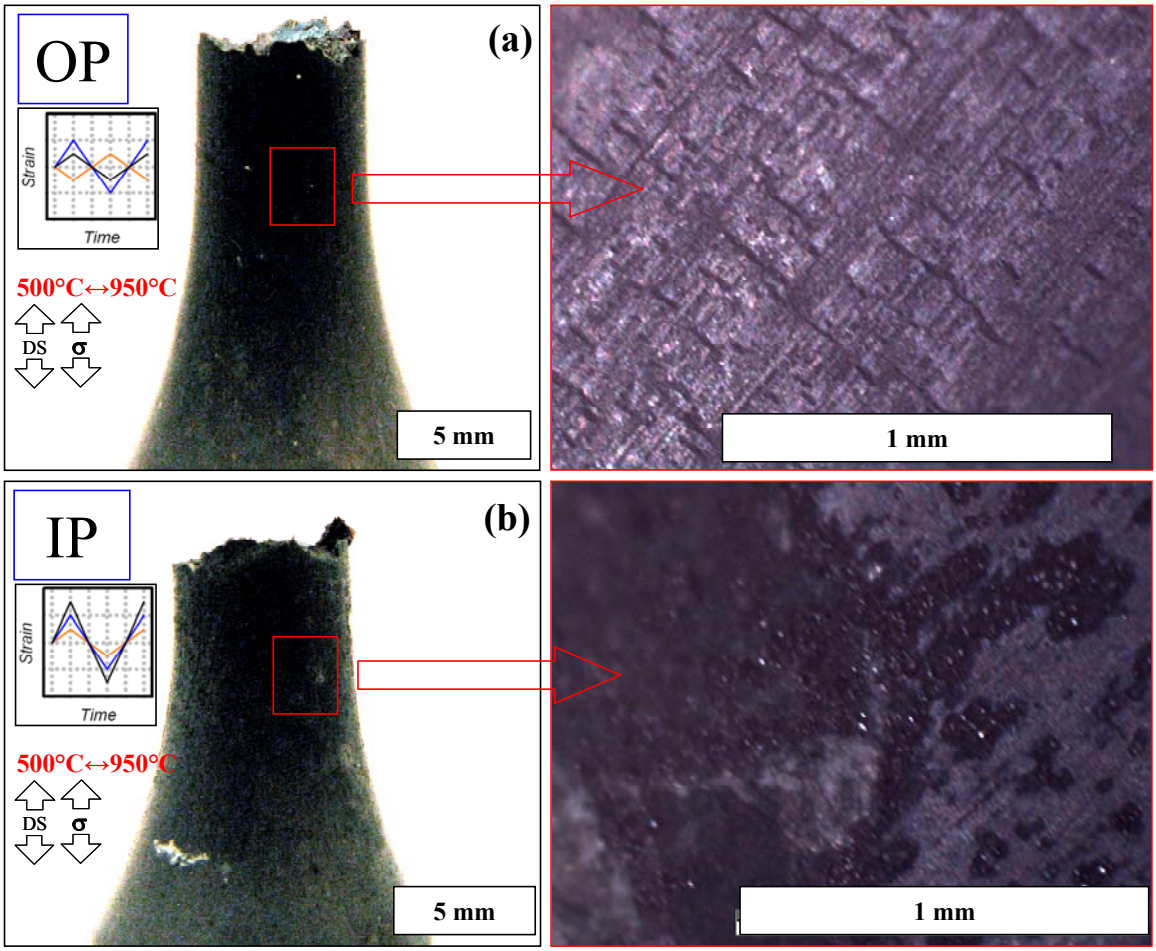

Figure 6-9: Tensile and compressive stresses during the cool TMF half cycle results in a.) surface cracking and oxide spikes in OP cycling and b.) oxide spallation during IP cycling. For both tests, norm. $\Delta\varepsilon_{mech}$=1.05%.

This spalling behavior influences oxidation kinetics but did not induce cracking in any of the samples examined. As a result, cycles to crack initiation in IP TMF is little affected by the surface oxide layer.

6.1.3 Orientation Effects

Whether based on $\Delta\varepsilon_{mech}$ or $\Delta\sigma$, orientation demonstrated a strong influence on crack initiation lives. Crack initiation in smooth specimens occurs at intervals along the gage section, as shown in Figure 6-10. The spacing of cracks can typically be associated

with weak points in the material, such as grain boundaries for the transverse orientation or the interdendritic region for longitudinal.

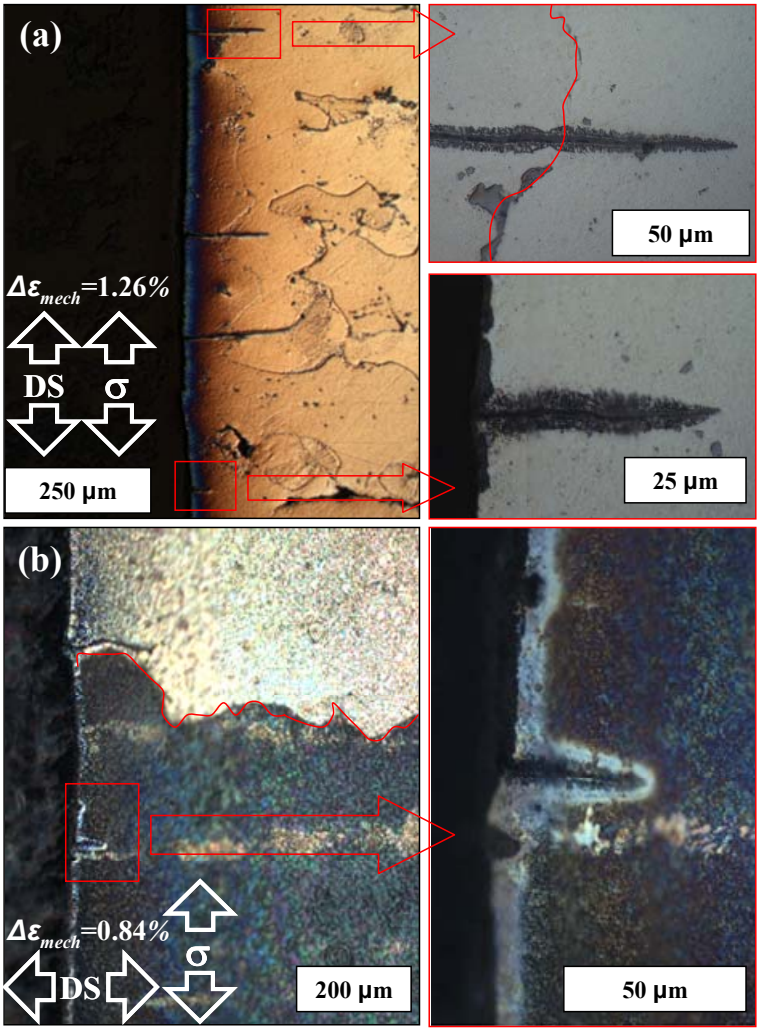

Figure 6-10: Smooth specimen crack initation resulting from OP TMF of (a) longitudinal and (b) transverse CM247LC DS. In both cases, T=500°↔950°C. The irregular red lines denote grain boundaries.

L-oriented samples always outlasted their transverse counterparts. In all cases, the T-orientation resulted in greater stress amplitudes for the same applied mechanical strain amplitude than the L-oriented samples. These loads result in extensive grain boundary cracking along the length of the gage section, as well as through weaker interdendritic

channels on the specimen surface. For the same applied mechanical strain amplitude in OP TMF, the longitudinal orientation provided a crack initiation life more than seven times as long as the transverse case. The lower T-orientation yield strength, coupled with the lower elastic modulus in the L direction, resulted in a reduction of the induced inelastic strain range by a factor of nearly three. Increasing the mechanical strain range in both L and T tests resulted in an increase in the fraction of plastic to total strain. FEA simulations predicted this disparity to increase for the baseline temperature range as the mechanical strain range increased, as shown in Figure 6-11. Due to tension-compression asymmetry of the yield stress, the resulting plastic strain was predicted to be slightly larger for out-of-phase cycling for the same mechanical strain range.

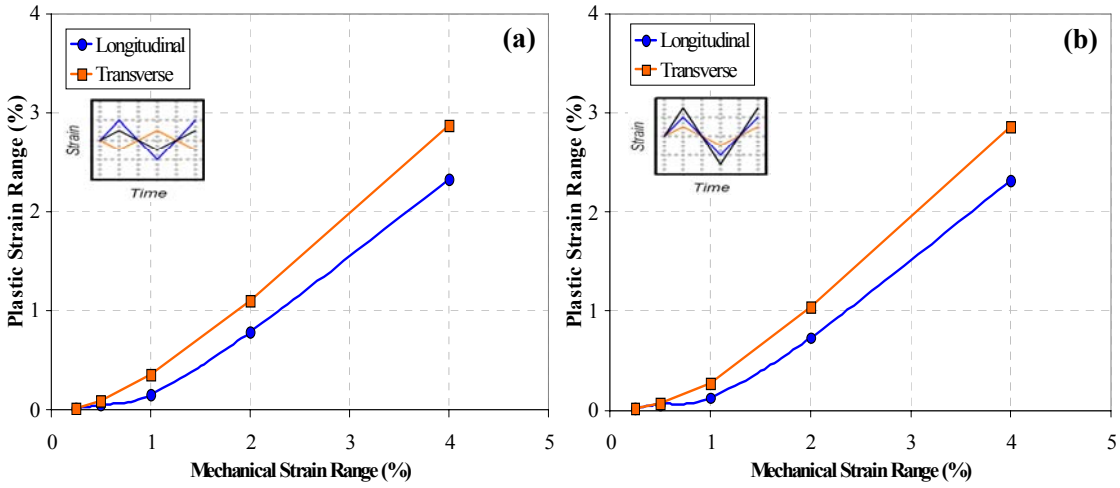

Figure 6-11: FEA simulations of L- and T-oriented plastic strain ranges with DS GTD-111 material constants resulting from (a) OP and (b) IP TMF. Both cases are for a 180 *s* cycle time and *T*=500°C↔950°C.

Surface cracking around the circumference of TMF-tested specimens also demonstrated a strong dependence on grain orientation. These were in the interdendritic region for L-oriented samples, where multiple cracks curved to mirror the outline of

dendritic arms at the specimen surface as shown in Figure 6-12(a). Spacing was largely determined by the number of dendrites at the surface and their depth of plane. Large cracks trace the outline of grain boundaries at the surface of transverse specimens, as in Figure 6-12(b). In both of these cases, the majority of cracks were constrained to the surface periphery and rarely penetrated far into the material.

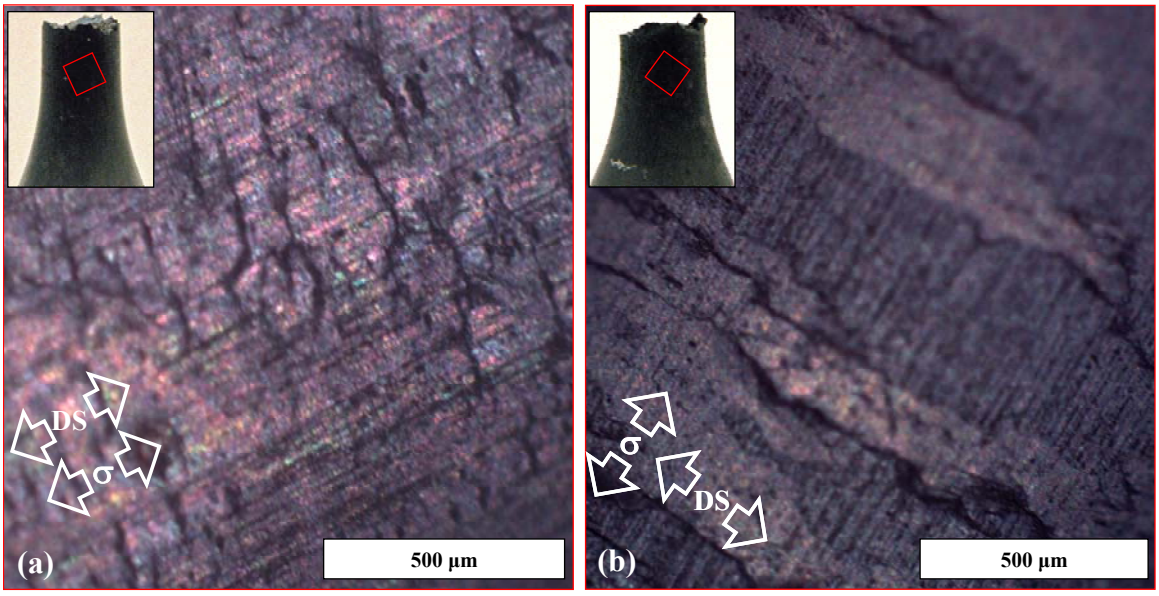

Figure 6-12: Surface cracking of TMF-tested smooth specimens (a) in the interdendritic region for the longitudinal orientation and (b) along grain boundaries in transverse.

Fractography revealed that final fracture of transverse specimens also occurred along weaker interdendritic paths.

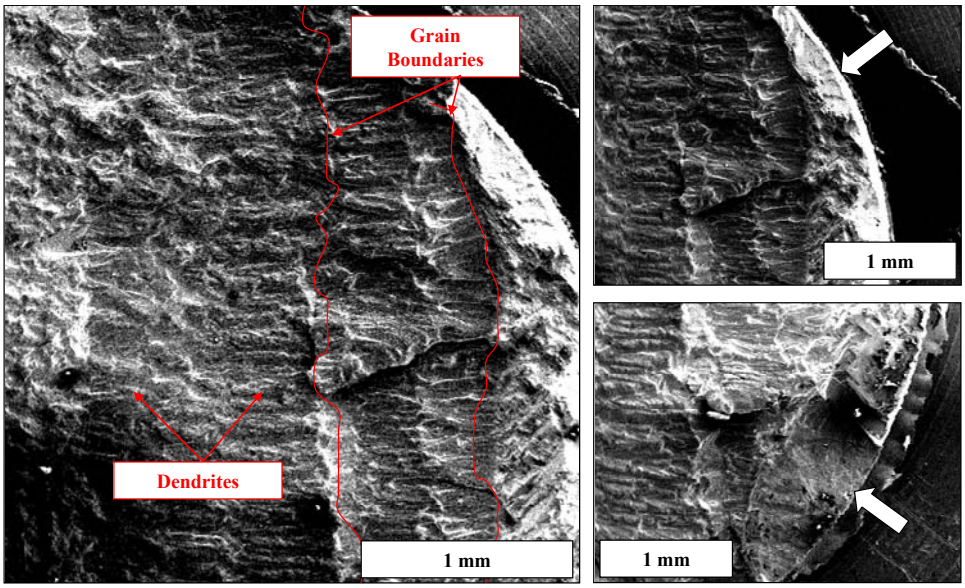

Figure 6-13: Fracture surface of a transverse smooth specimen subjected to OP TMF. Crack initation sites are indicated with white arrows. For this test, normalized $\Delta\varepsilon_{mech}$=0.84% and T=500°C↔950°C.

Longitudinal sectioning revealed the effect of orientation on crack behavior as shown in Figure 6-14. The fracture surfaces and crack planes of both orientations revealed a great many surface and subsurface carbides along the crack path. Most L-oriented samples exhibited transgranular cracking through adjacent grains. The transverse orientation showed a slightly more torturous fracture surface, evidence of the intergranular cracking typical of this case. Though multiple cracks formed, eventually a dominant crack shielded and inhibited the growth of those neighboring it. For almost all smooth specimen tests, a single dominant crack was responsible for final failure of the sample.

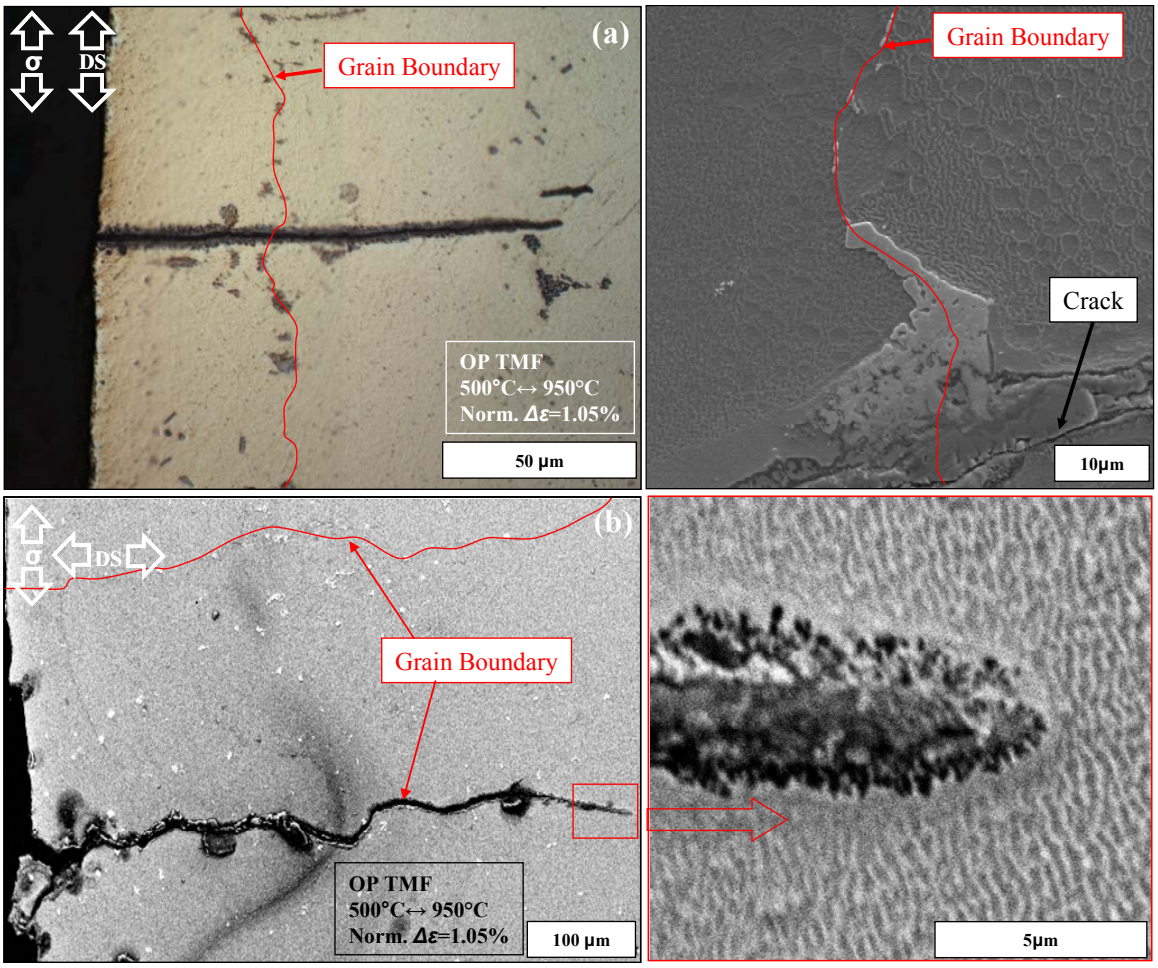

Figure 6-14: Smooth specimen longitudinal sections from OP TMF of CM247LC DS showing (a) transgranular cracking in a longitudinal specimen and (b) intergranular cracking along grain boundaries in a transverse sample subjected to OP TMF.

Both orientations showed acute sensitivity to microstructure. Microstructural inhomogeneities near the surface (e.g. grain boundaries, carbides, and eutectic γ' in the interdendritic region) were prime locations for crack initiation, as shown in Figure 6-15. The early phases of this process are often oxide-assisted, where the growth of microcracks is spurred by environmentally-weakened material.

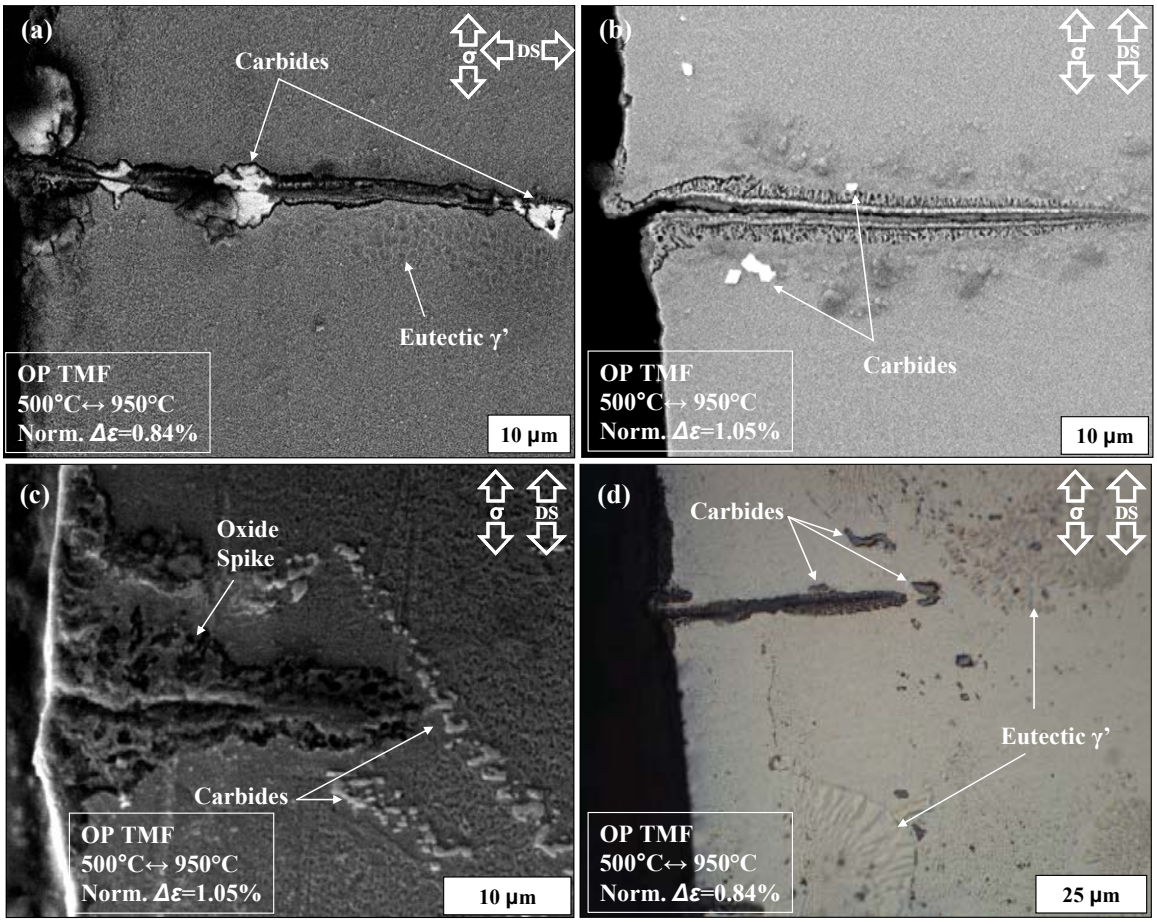

Figure 6-15: SEM and optical micrographs showing crack initiation at microstructural inhomogeneities in (a) a T-oriented sample and (b,c,d) various L-oriented specimens under various conditions.

The load histories for baseline OP L- and T-oriented CM247LC DS are shown in Figure 6-16. The force-cycle behavior varies significantly with a change in orientation. While the longitudinal tests usually fractured abruptly, the transverse suffered a more gradual decline in load. This is because the T-oriented specimens contain numerous weak points normal to the stress axis (i.e. grain boundaries and interdendritic channels) at which multiple cracks initiate. Thus, the load-carrying capability is lost piecemeal until final fracture due to a dominant crack. The lack of similar weak points in L-oriented

samples indicates that a dominant crack quickly to shield others, and controls the cross section's capability to bear load until final fracture.

In all OP tests, the tensile mean stress increased rapidly in the first few cycles and reached a stabilized value at the midlife cycle. While most tests exhibited this evolution in the tensile direction, those with the most significant plastic strain ranges of greater than 0.05% (longitudinal with normalized $\Delta\varepsilon_{mech}$=1.26% and transverse with normalized $\Delta\varepsilon_{mech}$=0.84%) deviated from this behavior. This was consistent with the observations on the Ni-base superalloy IN 738LC [73].

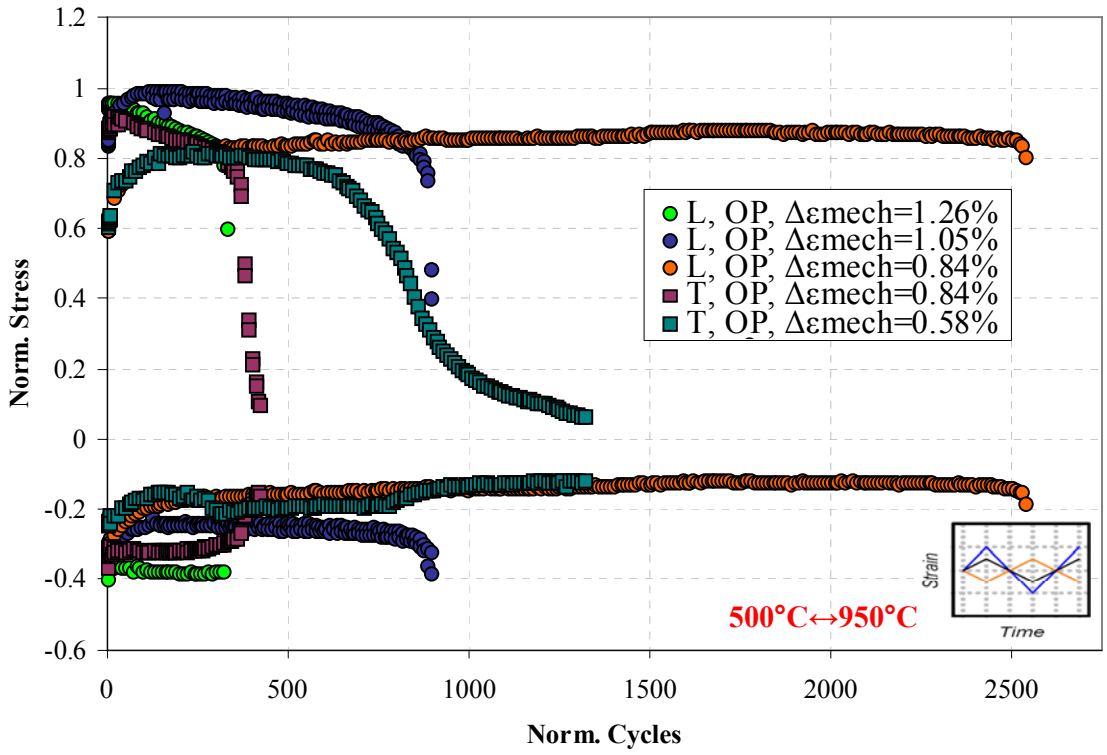

Figure 6-16: Load histories for smooth OP L- and T-oriented CM247LC DS with normalized. In all cases, R= -1.

For tests with high mechanical (and thus inelastic) strain ranges, the stress state is on the yield surface during both the high and low temperature half-cycles. In this case,

the material reaches a stabilized state after only a few cycles. At low mechanical strain ranges a considerably larger tensile shift in the hysteresis loop was required to reach the yield surface at low temperature. Often several hundred cycles were required for the stress response to stabilize under these conditions.

6.1.4 Mean Stress Effects

As compared to completely reversed, continuously-cycled isothermal tests, all TMF tests resulted in a mean stress (Figure 6-2), which has traditionally had a significant effect on the fatigue life of Ni-base superalloys. An in-phase test behaves similarly to a high temperature isothermal LCF test with a hold in tension (HT). In a similar fashion, an OP test resembles a hold in compression (HC). Similar to dwell periods, additionally visco-plastic deformation occurs at the peak of the high temperature half-cycle of a TMF test, and the applied stress is relaxed.

Previous isothermal testing of CM247LC DS with dwells showed that at 950°C, the effect of rate on deformation played a more significant role than the mean stress, which relaxed considerably. Figure 3-21(c) illustrated that for the same strain range and cycle period, a test with 10 *min* HC had nearly the same life as a continuously-cycled sample. Both had a similar number of cycles to crack initiation as a baseline OP TMF experiment with a similar applied strain range, as shown in Figure 6-17. This suggests similar active damage mechanisms. The stabilized mean stress for the OP TMF test was twice that of an isothermal 950°C test with a 10 *min* HC and nearly the same strain range. The stabilized (cycle N/2) hysteresis loops for these two tests are shown in Figure 6-18.

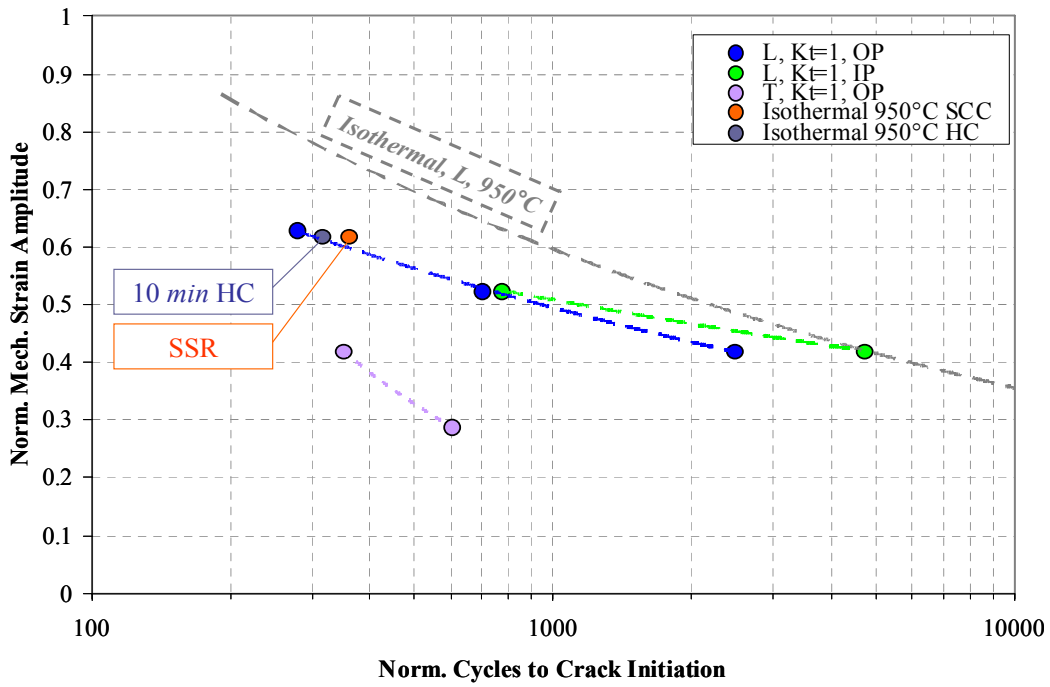

Figure 6-17: Longitudinal smooth specimen OP TMF results compared with isothermal creep-fatigue tests of CM247LC DS conducted at 950°C.

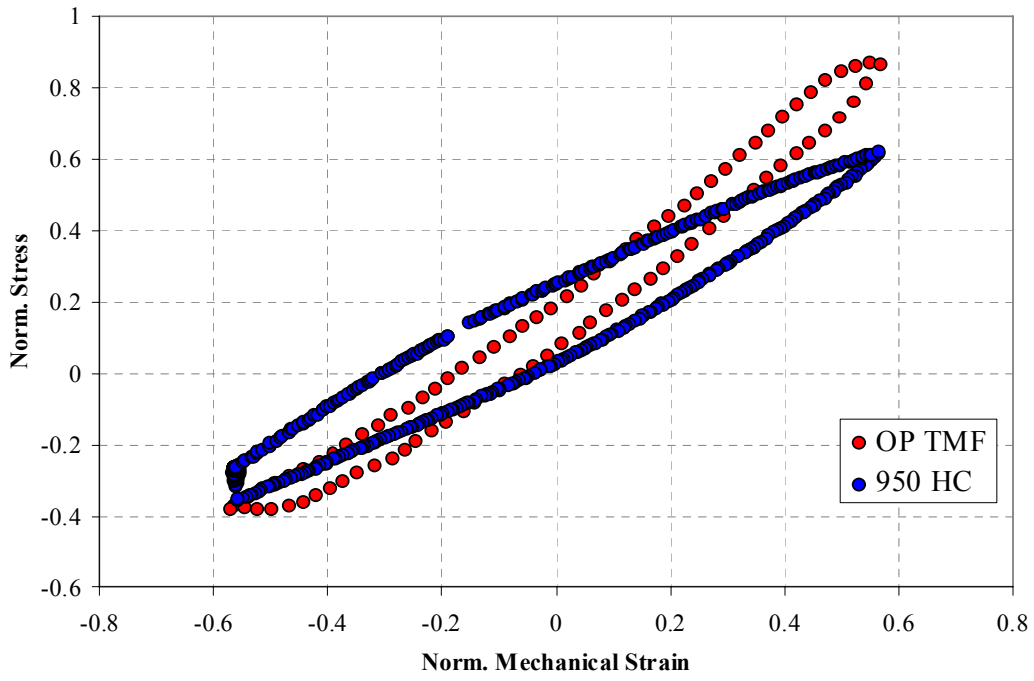

Figure 6-18: Half-life hysteresis loop comparison for longitudinal CM247LC DS cycled under baseline OP TMF and with a 10 *min* hold in compression. Both tests have nearly the same applied strain range.

The isothermal 950°C HC test stabilized with a greater inelastic strain range that the OP TMF test, but its developed mean stress was substantially smaller. These factors combine to give the HC test a slightly longer fatigue life, by a factor of 1.1.

Microscopy of HC samples revealed the same oxide spiking behavior seen in OP TMF, as shown in Figure 6-19. This indicates a similarity in the manifestation of environmental damage between the two, which is important in terms of life prediction modeling. Comparing several HC tests, an increase in temperature under the these conditions resulted in approximately the same number of surface cracks but a substantial increase in measured $\Delta\varepsilon_{pl}$ (a factor of 1.8) for the same strain range. The same increase in inelastic strain was true for an increase in $\Delta\varepsilon_{mech}$ of OP TMF tests. The oxide spiking mechanism is thus heavily dependent on temperature and the plastic strain range.

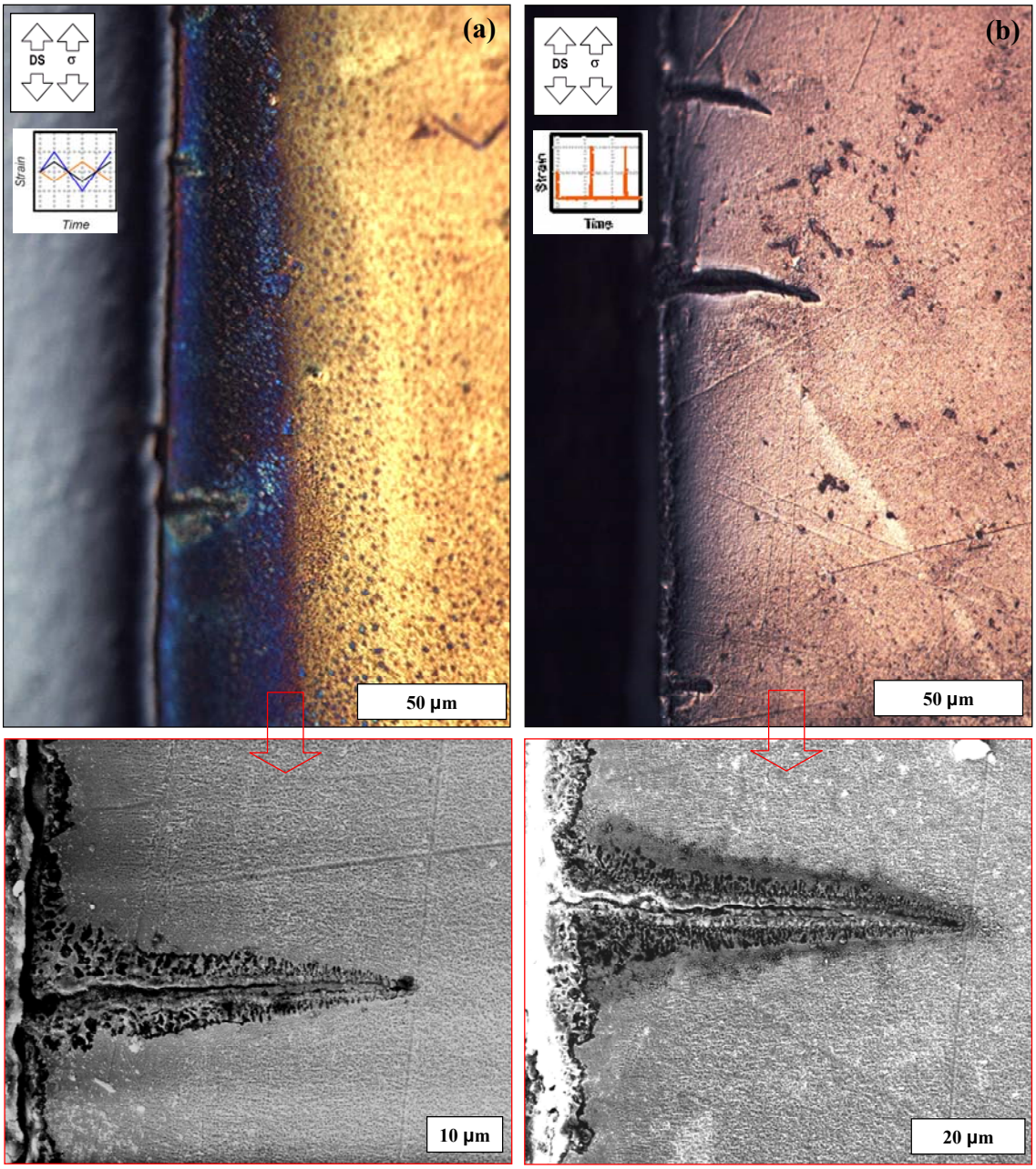

Figure 6-19: Surface cracking of oxide spikes in L-oriented CM247LC DS under (a) OP TMF cycling from 500°C↔950°C with normalized $\Delta\varepsilon_{mech}$=1.26% and (b) isothermal 950°C cycling with 10 *min* HC.

6.1.5 Effects of reduced T_{min}

To determine the influence of the minimum temperature of the OP TMF cycle on the resulting damage mechanisms, a smooth specimen test was conducted in mechanical

strain control with T_{min}=100°C. This allows a better recreation of turbine startup and shutdown sequences, where component often reach and experience loads near ambient temperature.

The effect of reducing T_{min} is shown in Figure 6-20. For the same mechanical strain amplitude, fatigue life was reduced by a factor of 3.4 when compared with the baseline temperature range. This was a result of the considerably greater stresses reached resulting from the increase in elastic modulus at temperatures lower than the baseline minimum of 500°C. The onset of yielding thus occurred earlier (though at nearly the same stress) in the low temperature half cycle, and a corresponding increase in inelastic strain of nearly three times that of the baseline cycle. The resulting substantial increase in the width of the hysteresis loop is shown in Figure 6-21. This width continued to increase over the duration of the test, as demonstrated by the half-life loop. Also evident is the significant cyclic softening, which resulted in a 14% reduction in peak tensile stress between the first cycle and stabilized half-life, as shown in Figure 6-22(b). There is not a notable change in the high temperature response. As a result, the stabilized tensile mean stress was 1.4 times lower than the comparable baseline test (14% of the total stress amplitude, as compared with 20.3%).

Initial yielding occurred at nearly the same stress level as with the baseline test (Figure 6-22(a)), indicating not only that strength was similar at the two minimum temperatures, but also that rate effects did not contribute notably to the deformation response. This lends validity to the life comparison between the two tests, as the strain rate with T_{min} was 9.4 times slower than that with T_{min}=500°C. This, coupled with the similar stresses reached at peak compressive strain, indicated that the reduction in the

minimum temperature of the TMF cycle was primarily responsible for the reduction in fatigue life.

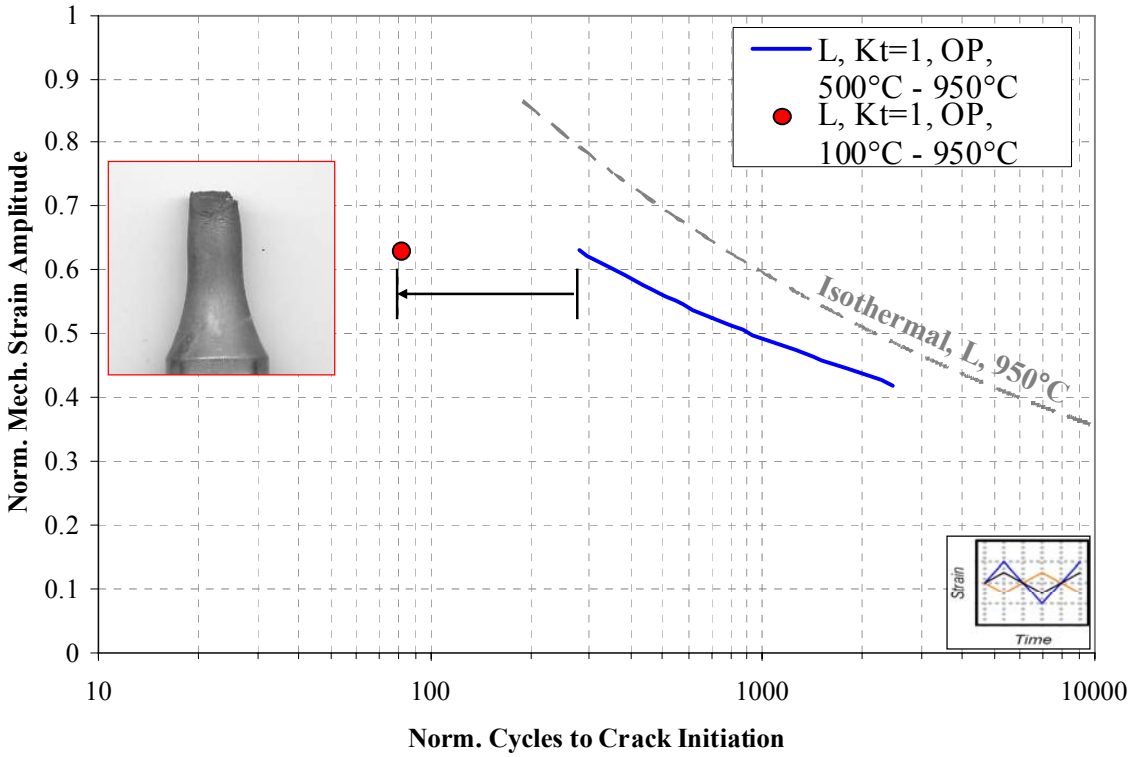

Figure 6-20: Effect of reducing T_{min} to 100°C on the life of a smooth specimen subjected to OP TMF with norm. $\Delta\varepsilon_{mech}$=1.26%.

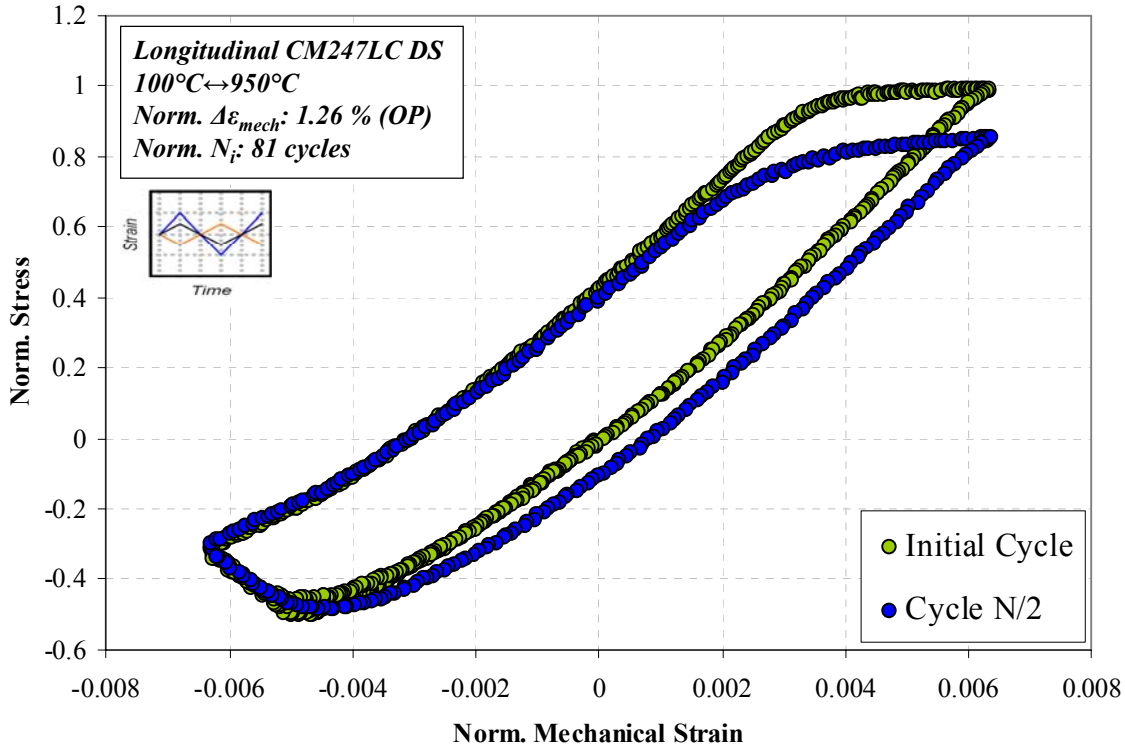

Figure 6-21: Stress-mechanical strain hysteresis of longitudinal CM247LC DS subjected to OP TMF with $\Delta\varepsilon_{mech}$=1.26% and T=100°C↔950°C.

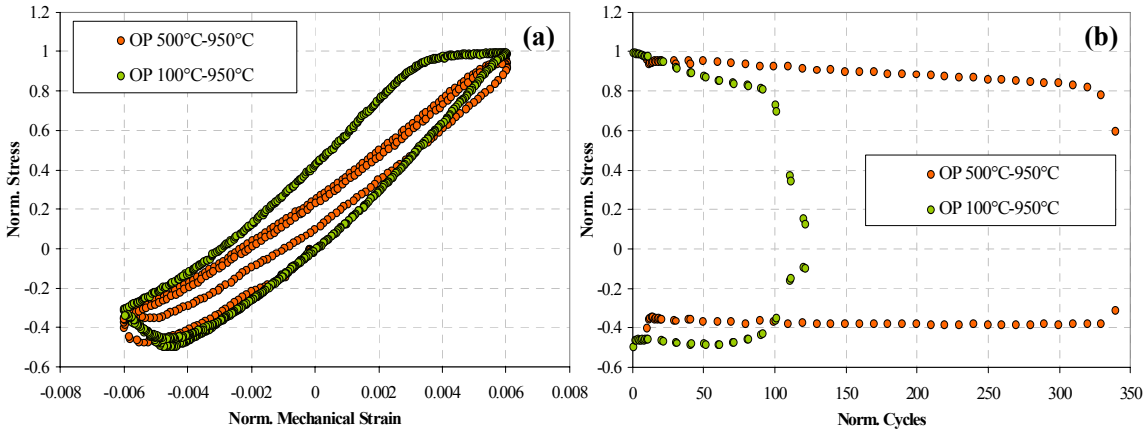

Figure 6-22: (a) First cycle hysteresis and (b) stress histories for longitudinal CM247LC DS subjected to OP TMF with norm. $\Delta\varepsilon_{mech}$=1.26% and T=500°C↔950°C.

6.1.6 Smooth Specimen Summary

Microscopically-observed crack initiation is used to identify the damage mechanisms acting for a given set of thermomechanical fatigue conditions. Dominant

damage mechanisms were identified primarily through extensive metallographic analysis of tested specimens. Select longitudinal tests are included in the damage mechanism map shown in Figure 6-23. The boundaries of test conditions which lead to dominant damage can thus be roughly determined. Fatigue is prevalent for the higher strain ranges. Under these conditions, oxide layer accrual is minimal due to the shorter experiment duration. Oxide spiking is only a factor for normalized mechanical strain amplitudes below 0.6. Creep damage resulting in crack initiation was observed for all baseline IP tests, indicating this mechanism is active for at least the range tested.

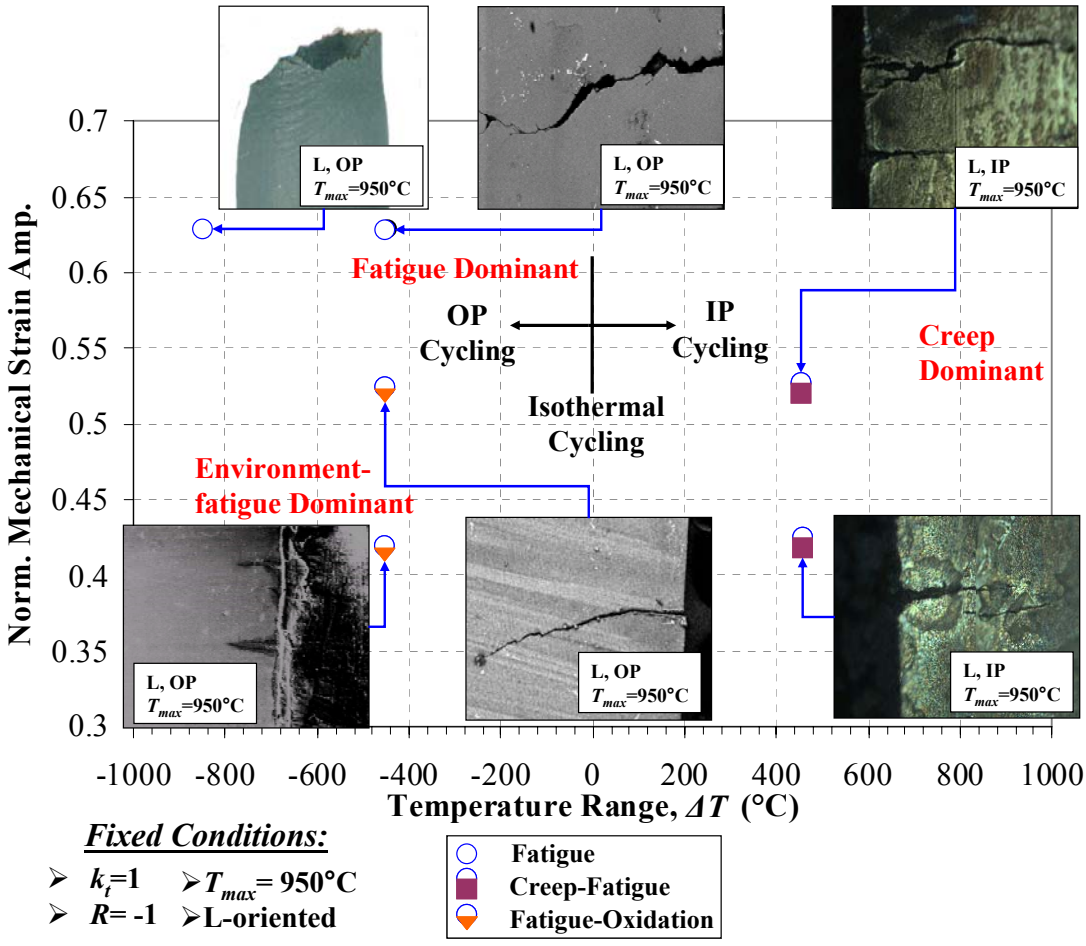

Figure 6-23: Smooth specimen damage mechanism map of crack initation in longitudinal CM247LC DS subjected to OP and IP TMF.

6.2 Baseline Notched Specimen Results

6.2.1 Life Results

As anticipated, the stress concentration resulted in a life reduction when compared to smooth specimen tests. Figure 6-24 shows the longitudinal OP life plots (as a function of the nominal stress amplitude based on the notch root net section, $\Delta\sigma_N/2$) for both k_t=2 and k_t=3 notches compared with smooth specimen results. Interestingly, the fatigue life trend for both notches follows the same curve, indicating that the severity of the stress concentration had a negligible effect on crack initiation. Consequently, under TMF a sharper notch is no more severe in terms of total fatigue damage for an identical loading history. For the same net section stress over the range studied, the difference in life between smooth and notched tests was at least a factor of 1.5. The similar slope observed between smooth and notched life curves again indicates the same dominant active damage mode, and that the tensile mean stress in all OP tests produced a similar effect on overall life.

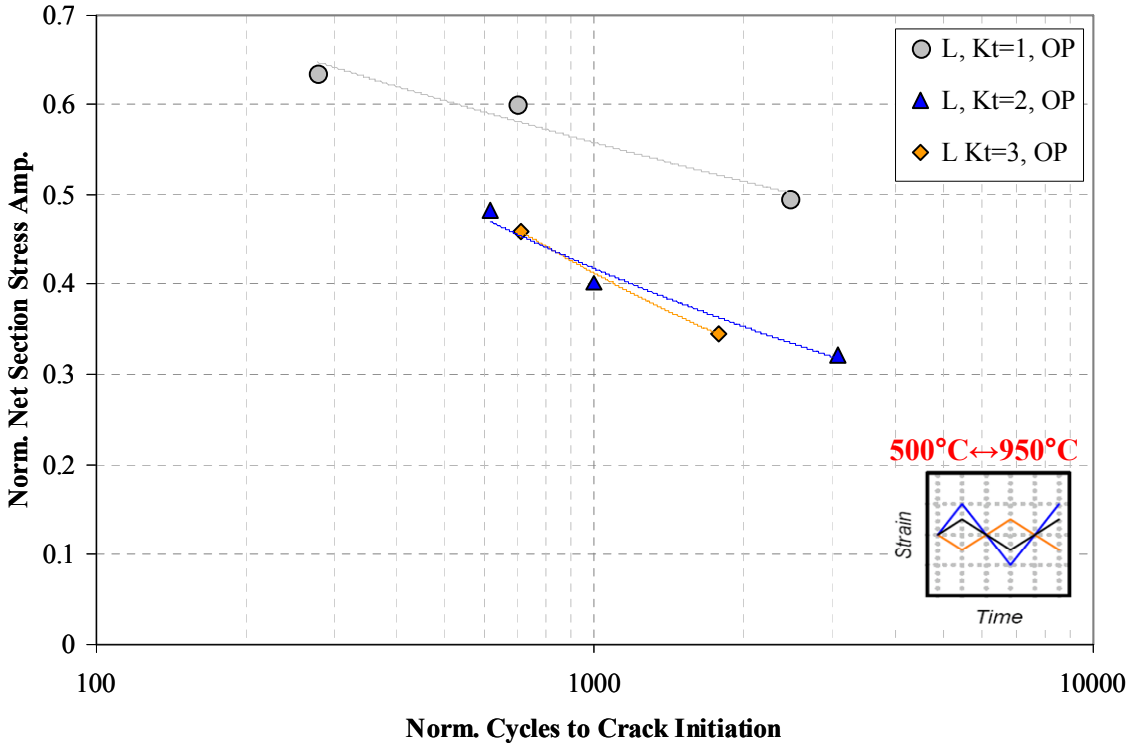

Figure 6-24: Baseline notched results for longitudinal OP TMF conducted in force control. Cycles to crack initation is plotted as a function of the applied net section stress amplitude at the notch root. Smooth specimen results are shown for comparison.

When compared to the longitudinal data, the transverse orientation had the effect of significantly collapsing the life curves for all specimen types, as demonstrated in Figure 6-25. Regardless of stress concentration severity, cracks initiated rapidly at grain boundaries along the surface. Beyond this point, the majority of life was spent in crack propagation along grain boundaries and interdendritic channels. In all notched cases, crack initiation lives were only slightly shorter (by a factor of approximately 1.1 - 1.2) than the longitudinal cases with the same net section stress amplitude. The single transverse k_t=2 IP test resulted in nearly the same TMF life as that subjected to OP cycling, indicating that a normalized stress amplitude of 0.4 is the likely crossover point for the two cycles in this orientation. This is important, because although cracks initiate

quickly at weak microstructural features in all transverse tests (Figure 6-14 and Figure 6-15), life is still influenced by the phasing of the TMF cycle.

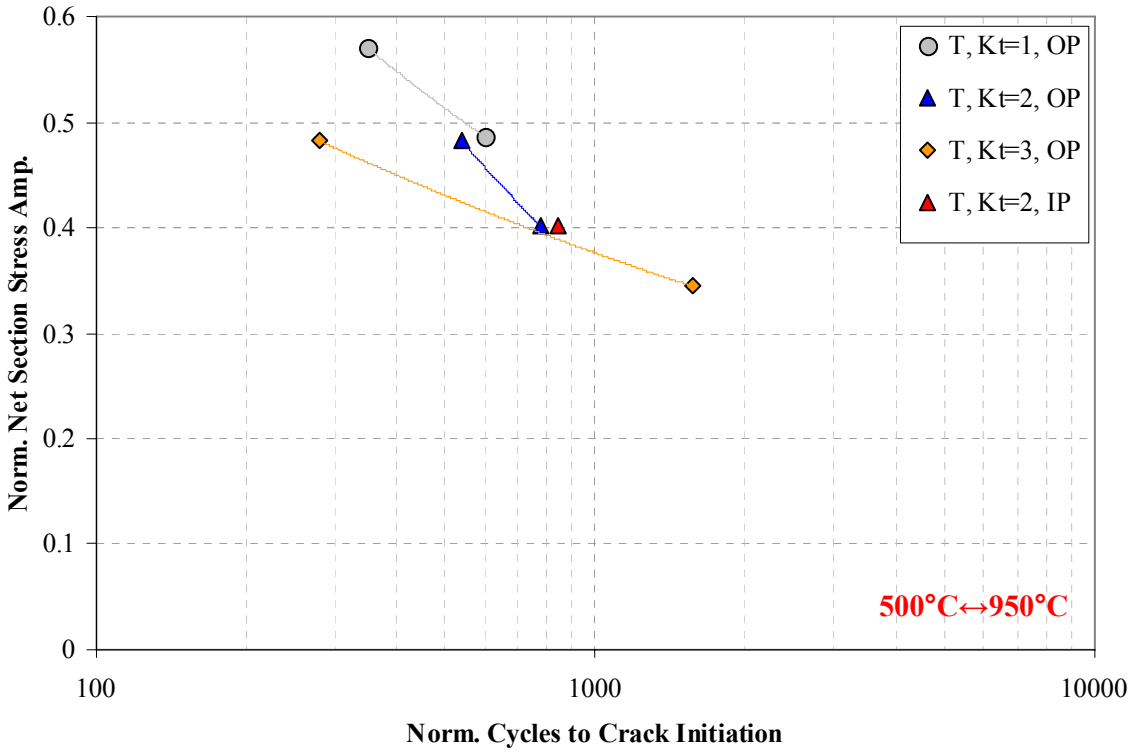

Figure 6-25: Baseline notched results for transverse OP TMF conducted in force control. Cycles to crack initation is plotted as a function of the applied net section stress at the notch root. Smooth specimen results are shown for comparison.

The comparison of longitudinal OP and IP notched tests in force control are shown in Figure 6-26. The acute sensitivity of IP tests to the applied stress level is clearly visible, where a 15% reduction in applied load resulted in a life more than 43 times as long. The IP test with the normalized net section stress amplitude of 0.4 failed via creep rupture; for clarity, the point is included as the point of crack initiation.

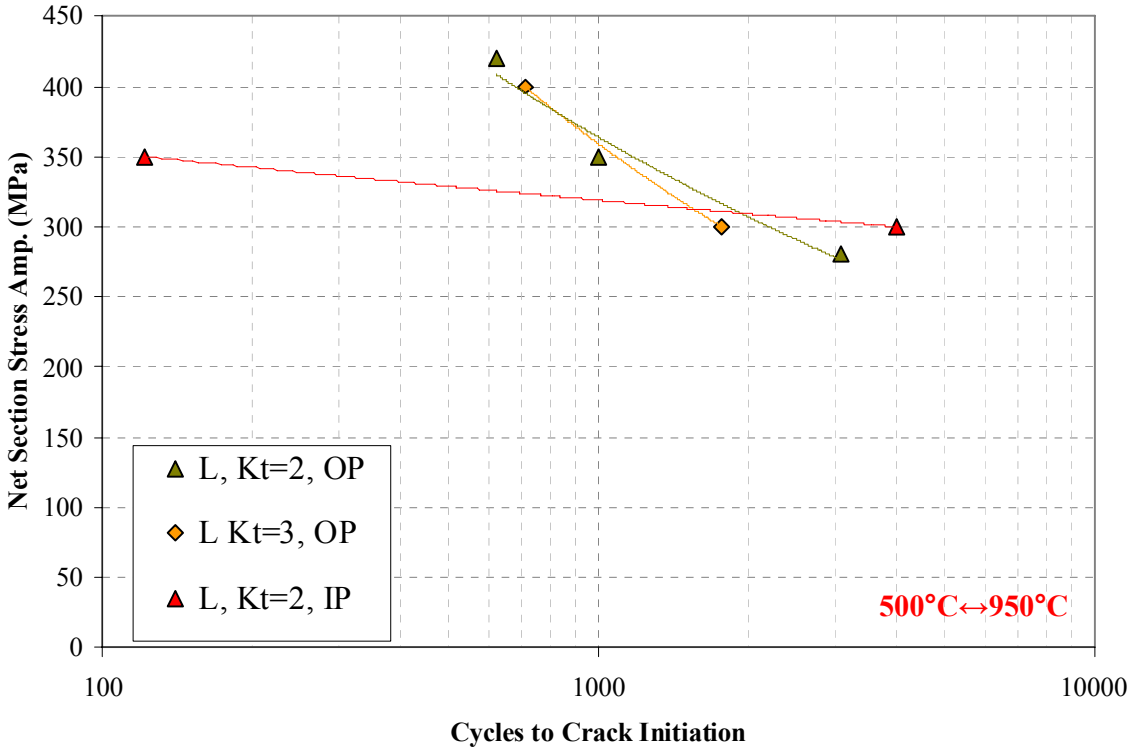

Figure 6-26: Longitudinal OP and IP notched specimen results conducted in force control

The characteristic crossover in IP and OP TMF lives can be seen at a normalized stress amplitude of approximately 0.35.

6.2.2 Effects of reduced T_{max}

Force-controlled OP testing with T_{max} reduced to 750°C was conducted to determine the effect of the maximum temperature on TMF damage mechanisms in notched specimens. Specifically, fatigue damage should be isolated from significant oxidation or creep. The resulting low temperature OP (OPL) life curves are plotted against the baseline (T_{max} =950°C) notched and smooth specimen data in Figure 6-27. A significant increase in life was observed over the baseline results. For tests with nearly the same lifespan, the net section stress amplitude for the OPL tests was nearly 1.5 times

that of the baseline tests. This was due to the fact that the longitudinal 0.2% yield strength of CM247LC DS at 750°C (966 *MPa*) is 1.9 times that at 950°C (510 *MPa*).

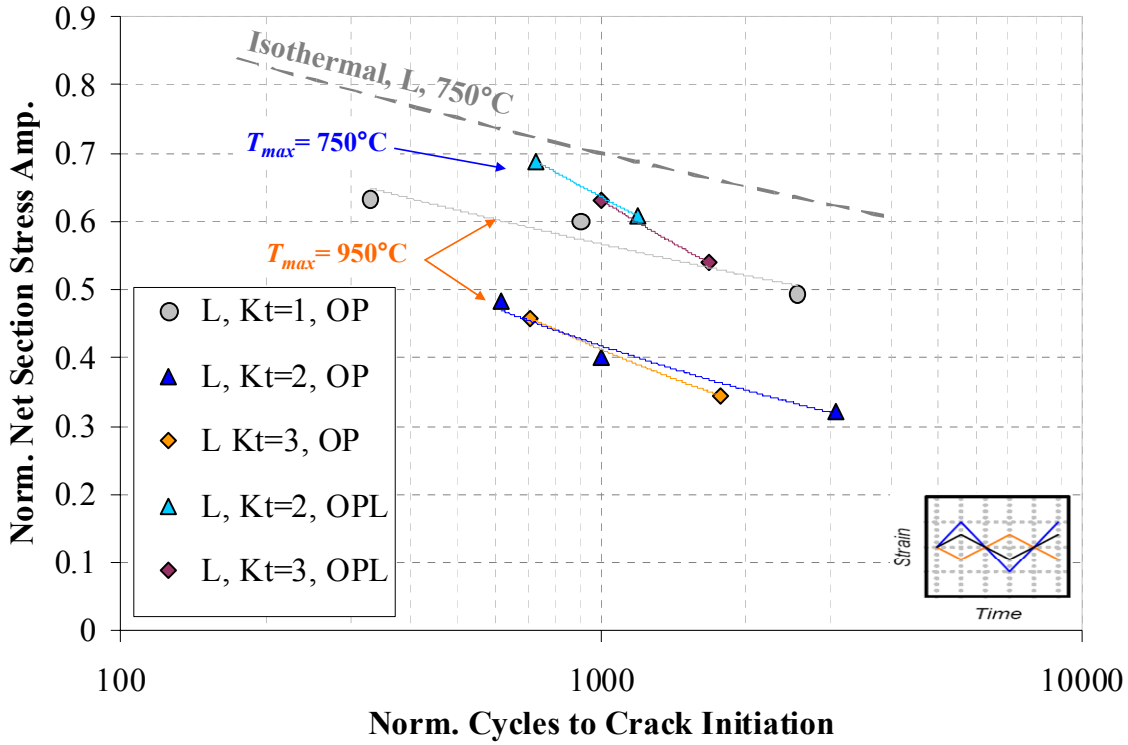

Figure 6-27: Comparison of longitudinal OP and OPL notched specimen results conducted in force control.

As seen with the baseline results, the sharpness of the notch has no appreciable effect on cycles to crack initiation. There is, however, a marked increase in fatigue resistance for both notches in the OPL case compared to baseline k_t=1 tests above a normalized stress amplitude of 0.55. This indicates that the damage mechanisms active at the higher temperature have a more substantial influence on crack initiation than the stress concentrations.

Similar life results were seen when comparing data from isothermal notched creep-fatigue tests conducted by Moore et al. [74]. When T_{max} was increased from 750°C

to 950°C, the stress concentration had a reduced impact on life due to stress relaxation and redistribution within the notch.

6.2.3 Crack Initiation and Notch Effects

The mechanisms driving crack initiation between smooth and notched tests were similar. Crack initiation in several k_t=2 samples is shown in Figure 6-28. OP testing resulted in oxide spiking and a large number of cracks around the highly stressed areas at the notch surface. Many of those found had propagated well over 1 *mm* from the notch surface. All OP notched tests resulted in considerable oxidizing of the crack flanks and ahead of the tip. IP tests resulted in far fewer cracks in and around the notch root, but exhibited an abundant number of voids, especially in the interdendritic regions, due to creep damage.

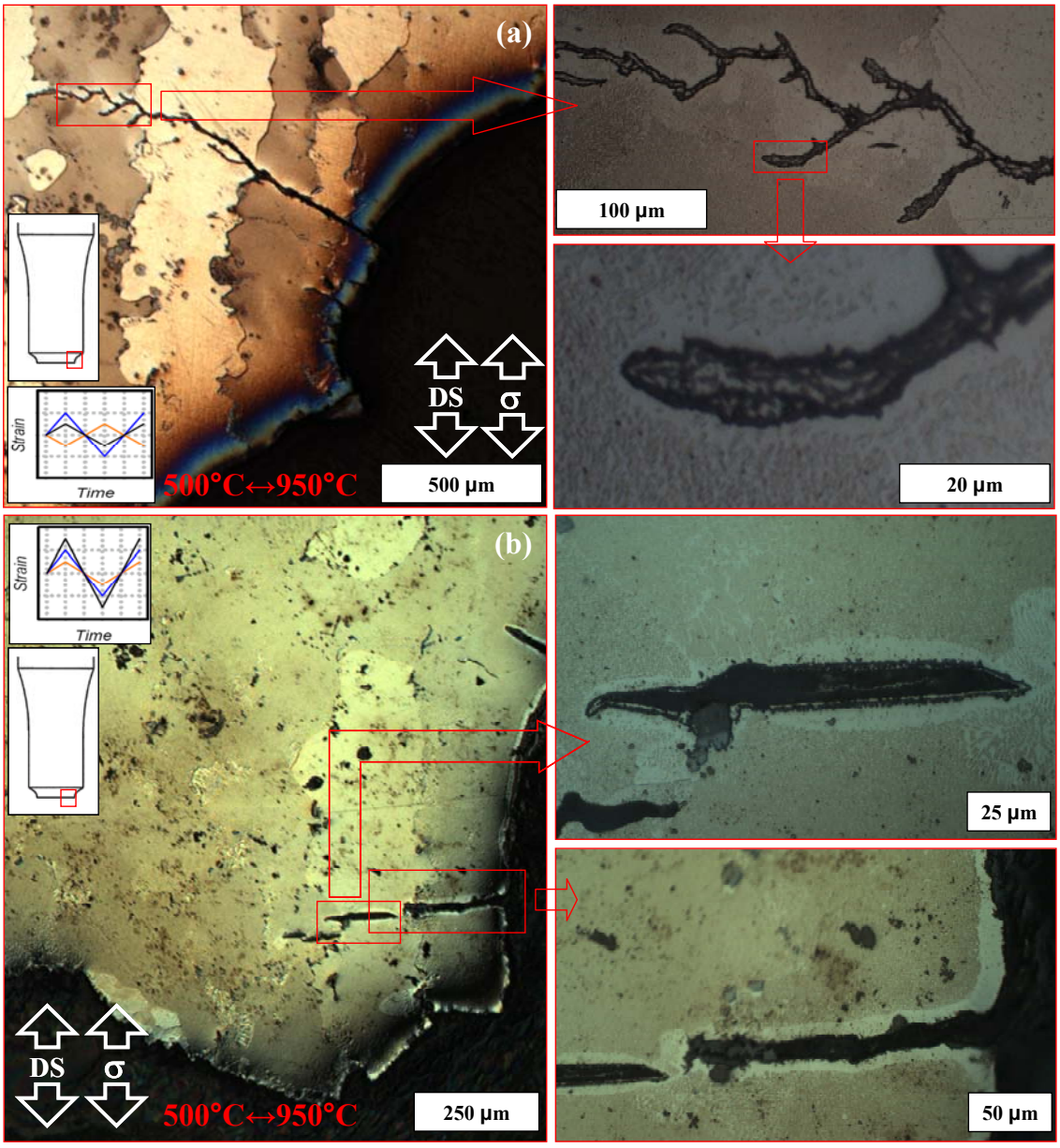

Figure 6-28: Crack initiation in L-oriented k_t=2 specimens subjected to (a) OP TMF with norm. $\Delta\sigma$=0.48 and (b) IP TMF with norm. $\Delta\sigma$=0.34.

Similarly, the k_t=3 specimens which experienced OP TMF demonstrated the same initiation behavior, as seen in Figure 6-29. This supports the life results for both orientations, which showed no significant dependence on notch geometry.

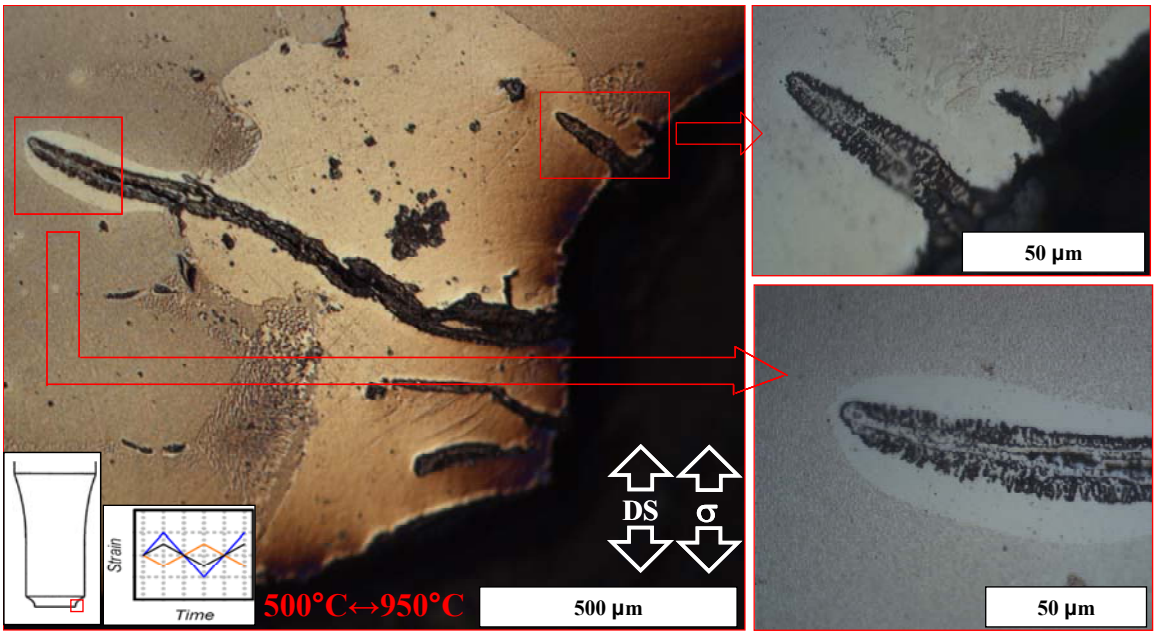

Figure 6-29: Crack initiation in a L-oriented k_t=3 specimen subjected to OP TMF with $\Delta\sigma$=0.34.

For T_{max}=750°C, the absence of oxide spikes and a γ'-depleted layer removes a primary source of crack initiation in OP cycling, as shown in Figure 6-30. Although multiple fatigue cracks form in the highly stressed region of the notch, crack surfaces are free of oxidation and there was no precipitate depleted zone ahead of the crack tips. This temperature is also insufficient to develop significant creep damage or induce thermodynamic microstructural changes. The magnitude of the developed tensile mean stress within the notch would be greater than that of the baseline tests, as there would be substantially less stress relaxation during the high temperature half-cycle. Although cracking is still circumferential, in most cases a dominant crack develops and grows until failure.

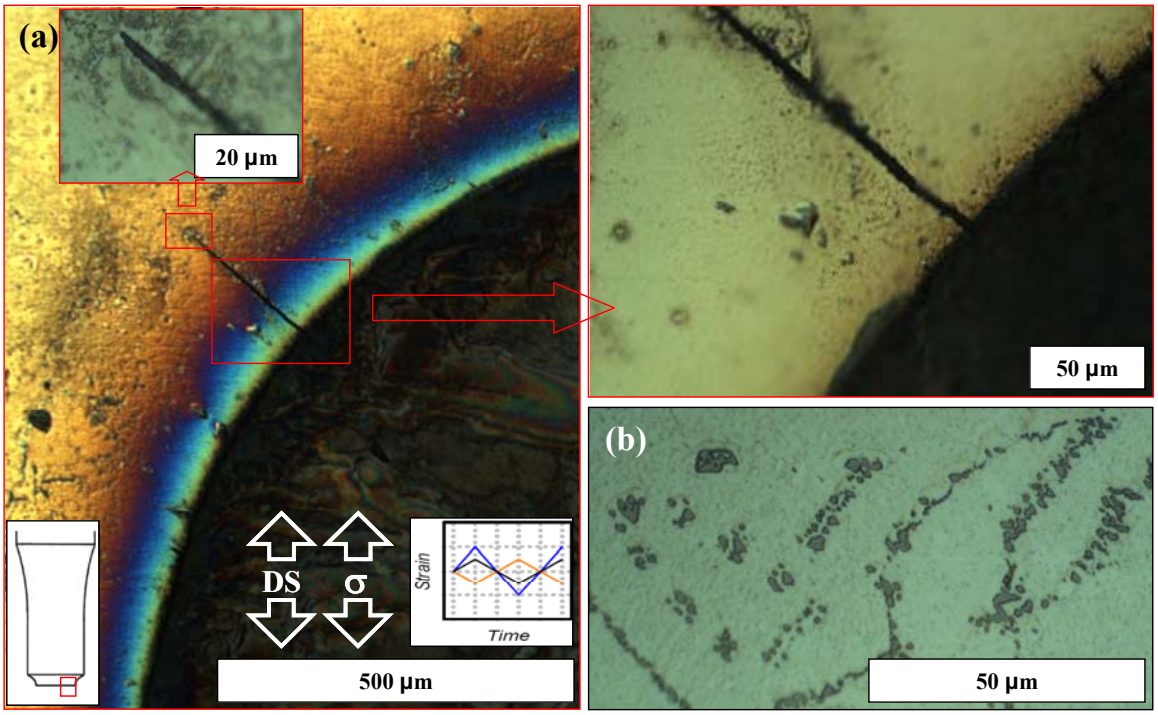

Figure 6-30: (a) Crack initation and (b) the post-test microstructure in a longitudinal CM247LC DS k_t=2 specimen subjected to OPL TMF from 500°C↔750°C and norm. $\Delta\sigma$= 0.61.

The multiaxial state of stress outside the notch root resulted in multiple crack initiation sites on alternate sides of the notch for both k_t=2 and k_t=3 notch geometries. Images of these locations and corresponding measurements are shown in Figure 6-31. Typically there were multiple initiation sites, all near the same axial distance offset from the notch root. This distance was between 300-450 μm for k_t=2 and 100-200 μm for k_t=3. These ranges indicate that cracks form at multiple weak points within the highly stressed zone, namely the interdendritic region for L-oriented samples and grain boundaries for transverse.

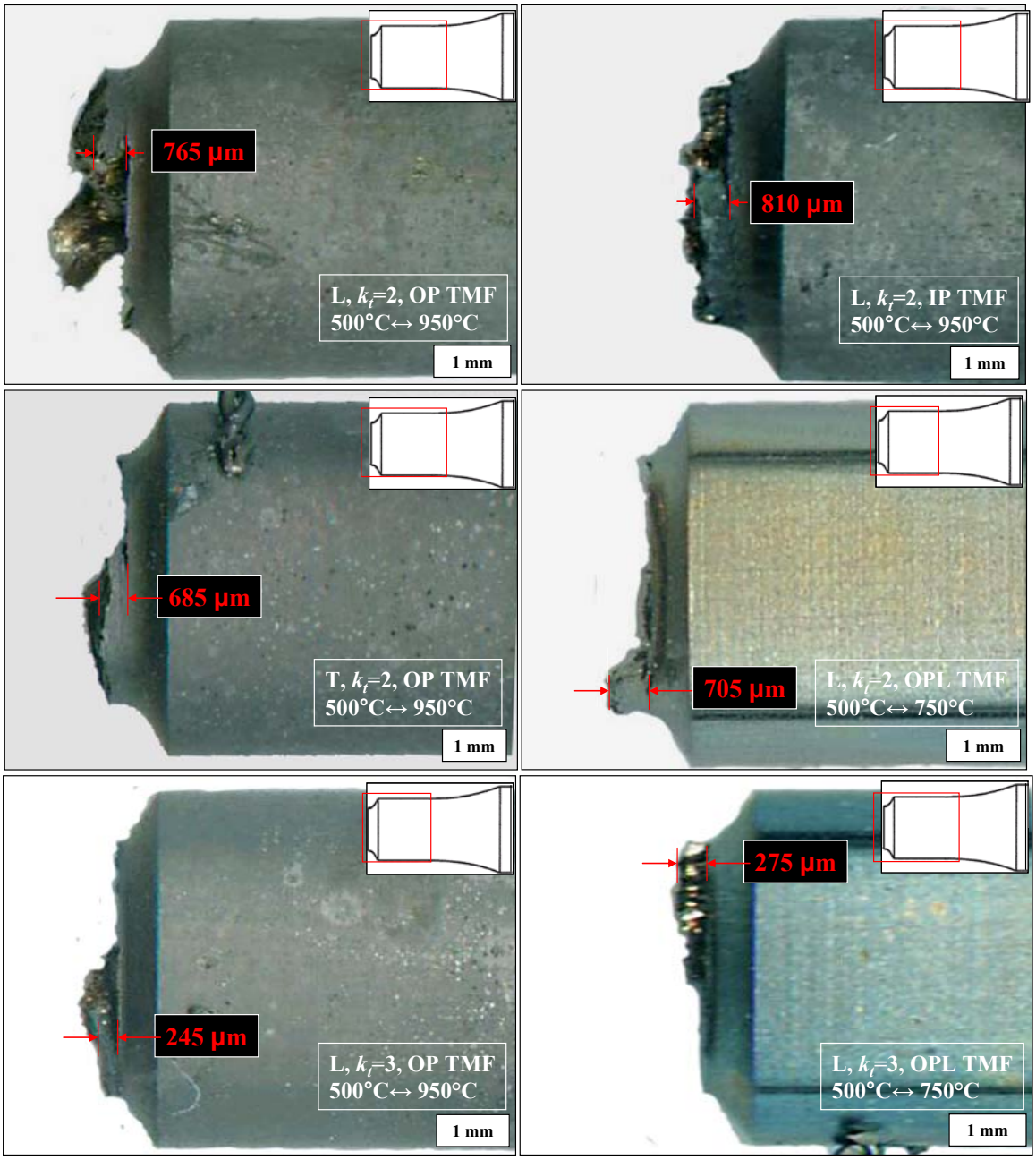

Figure 6-31: Notch crack initiation sites in CM247LC DS subjected to various TMF tests.

These locations were very consistent across different cycles, orientations, and temperature ranges, indicating that initiation sites are more a function of notch geometry than an inherent aspect of testing. Additionally, measurements taken were quite similar to those from isothermal LCF tests on CM247LC DS specimens with identical dimensions

[17]. Locations of offset bands of the greatest equivalent stress (as opposed to normal stress) within the notch are responsible for this phenomenon. This behavior is supported finite element simulations, as shown in Figure 6-32. The location is the same regardless of orientation or which TMF half-cycle peak is used.

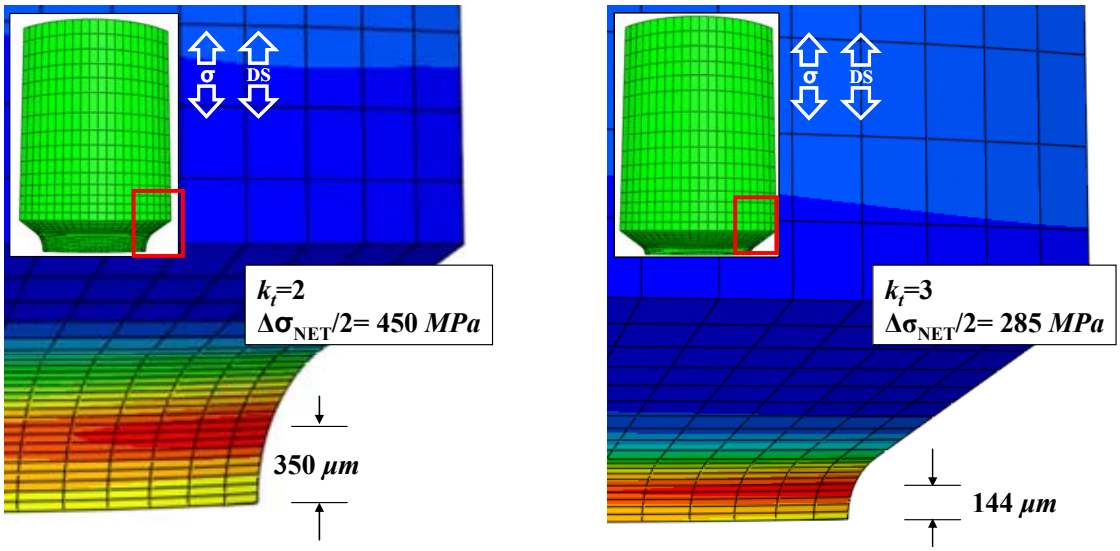

Figure 6-32: Elastic visco-plastic finite element analysis showing the location of maximum Hill's equivalent stress.

Almost all notched IP and OP tests resulted in extensive circumferential cracking, and in most cases, it was nearly impossible to distinguish specific radial initiation sites based on visual observation. In the vast majority of cases, crack initiation was detected only after several of the cracks had linked circumferentially. The axial position of crack initiation was very consistent in all notched tests. At higher load levels, angled cracks grow rather than purely radial ones. FEA demonstrated that the effective multiaxial stress was at a maximum normal to the crack plane. This has the considerable effect of creating a "dome" shaped fracture surface (Figure 6-33). This angle was consistently around 25° off the loading plane (i.e. 65° from the [001] direction) for k_t=2 and approximately 20°

for k_t=3 notches. The fracture surfaces from notched isothermal LCF tests conducted at 950°C by Moore [17] showed very similar behavior. When T_{max} of the TMF test was reduced to 750°C, the angular crack growth was considerably muted. This also held true for isothermal tests at the same temperature.

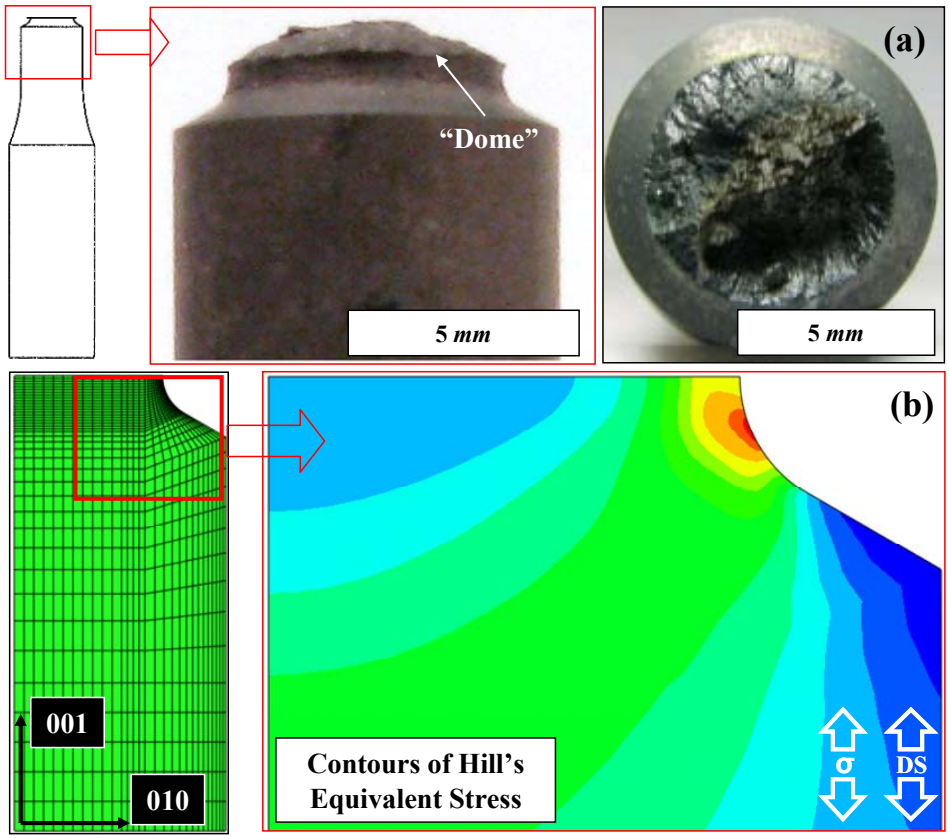

Figure 6-33: (a) Fracture profile and surface of a longitudinal k_t=2 sample after OP cycling and (b) finite element simulations showing contours of equivalent stress angling away from the notch root resulting in the "dome" shape.

Longitudinal sectioning supported the "dome" observation by frequently revealing additional cracks at the notch root propagating in this non-planar fashion. In all cases, cracks which propagated beyond approximately 1 *mm* reverted to growth perpendicular to the loading axis, where the crack was no longer influenced by the notch.

Similar to smooth specimen tests, when T_{max}=950°C the crack fracture surfaces of these angled cracks oxidize and there is continuous oxide rupture at the crack tip (Figure 6-34). This effect was seen for both k_t=2 and k_t=3 notches.

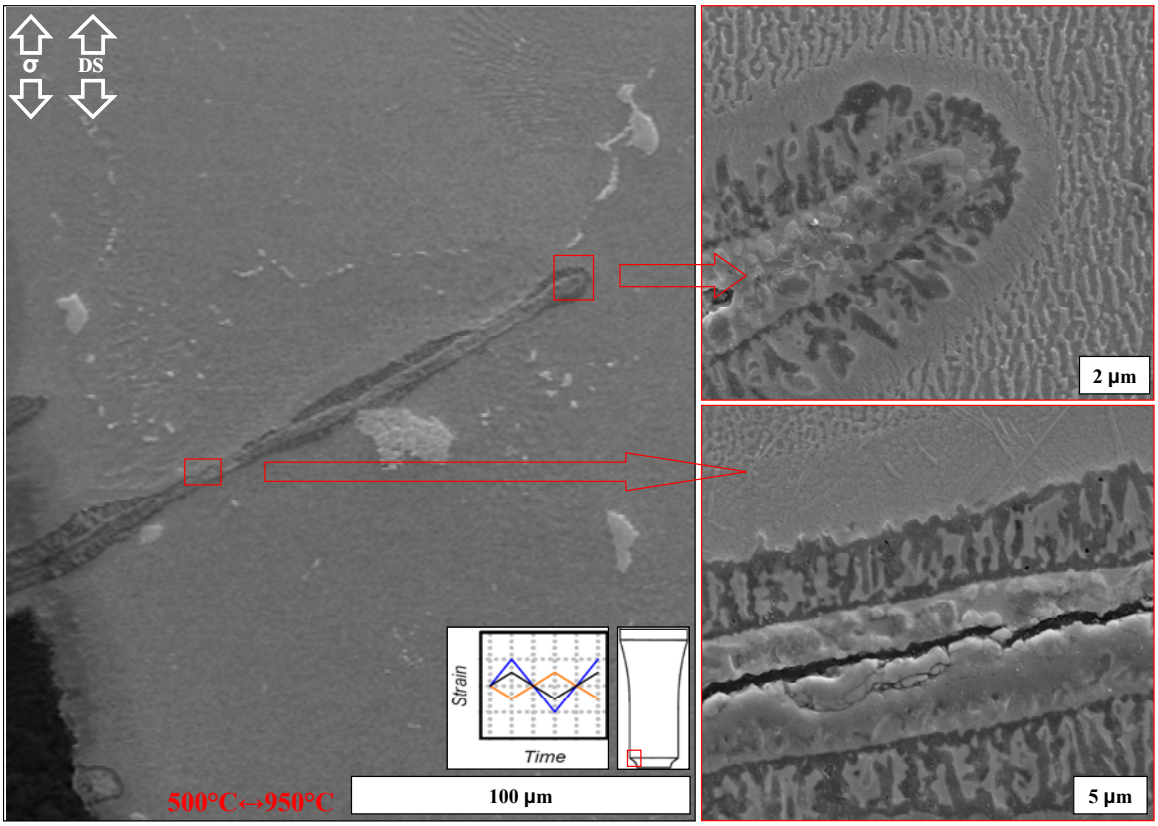

Figure 6-34: Angular crack growth away from the primary fracture surface in an OP, notched k_t=2 sample. Test conditions: norm. $\Delta\sigma$=0.64 and T=500°C↔950°C.

Fractography of notched samples typically revealed many smaller circumferential cracks which had linked around the majority of, or the entire, circumference. A typical k_t=2 OP fracture surface demonstrates the different planes of crack initiation, seen in Figure 6-35. Cracks initiate from oxide spikes in the interdendritic region and grow radially inward until they extend out of the highly stressed region of the notch.

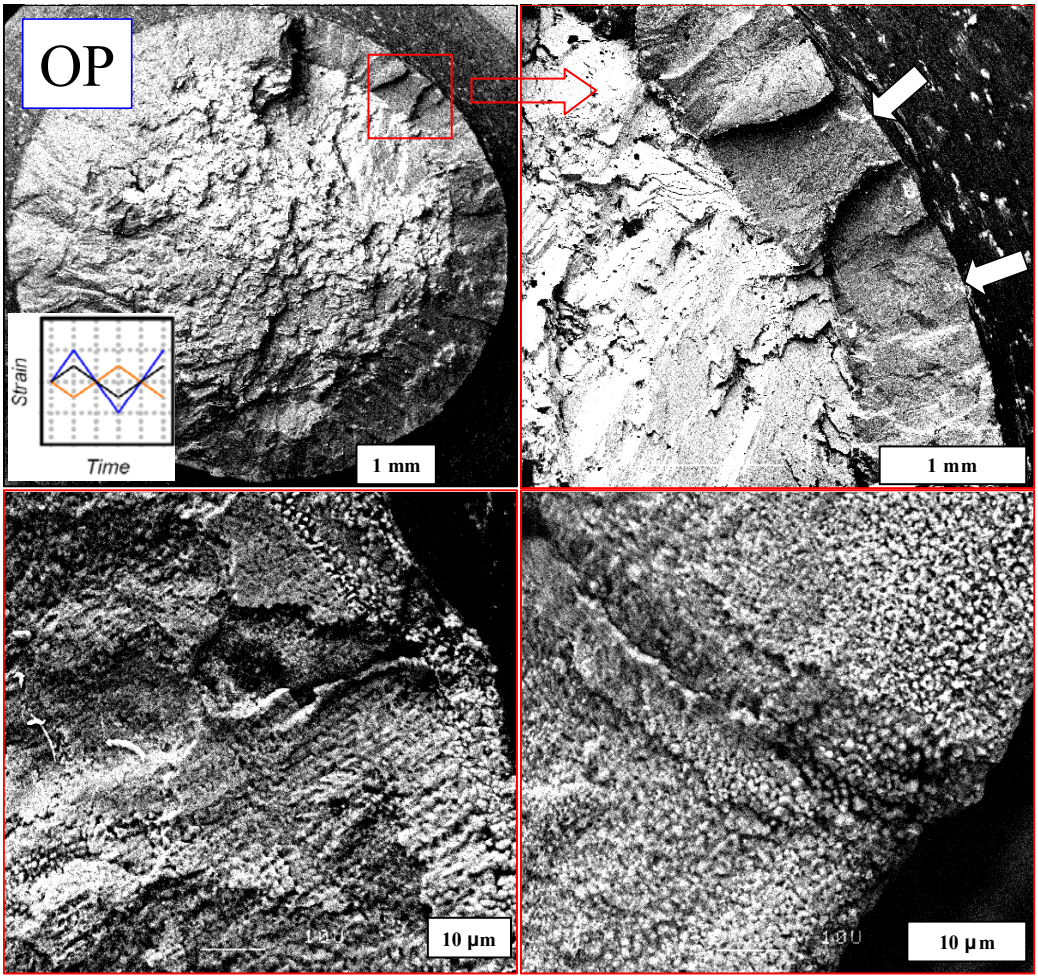

Figure 6-35: OP Notched specimen fracture surface examination of L-oriented CM247LC DS showing continous circumferential cracking. Crack initiation sites are indicated with white arrows. Test conditions: norm. $\Delta\sigma$=0.80 and T=500°C↔950°C.

A summary of the fracture behavior of notched tests under various conditions can be seen in Figure 6-36. Included in this list for comparison are isothermal tests from a previous study. Notched TMF tests with T_{max}=750°C on CM247LC DS are also characterized by circumferential cracking, as seen in notched isothermal LCF at 750°C. At this temperature, cracks initiate and propagate through fatigue (Figure 6-30) rather than an environmentally-assisted mechanism. This indicates the notch stress concentration is responsible for the circumferential crack formation trends.

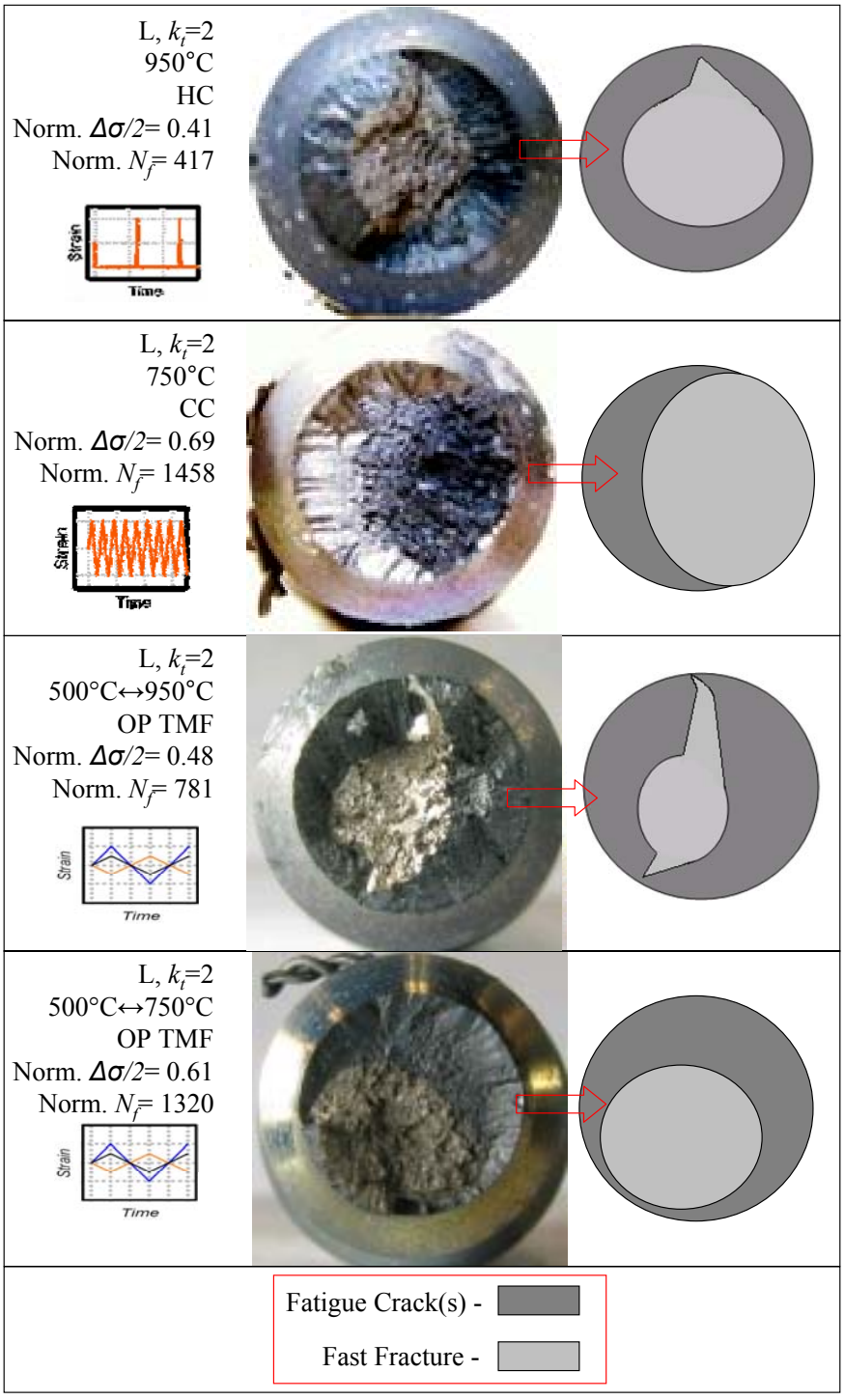

Figure 6-36: Fracture characteristics and circumferential cracking of k_t=2 samples subjected to a variety of conditions.

Individual initiation sites are often difficult to distinguish due to heavy oxidation of the crack surfaces. Often, cracks coalesce after initiation on different planes transverse to the

loading axis, supporting the multitude of initiation sites seen on visual inspection of the notch surface.

6.2.4 Creep Ratcheting

Evidence of creep was found in the interior of many IP notched specimens, resulting in the formation of voids and the nucleation of cracks at grain boundaries and in the interdendritic region (Figure 6-38 and Figure 6-38). This indicates that even the comparably low net section stresses across the notch root are sufficient to accumulate inelastic creep strain.

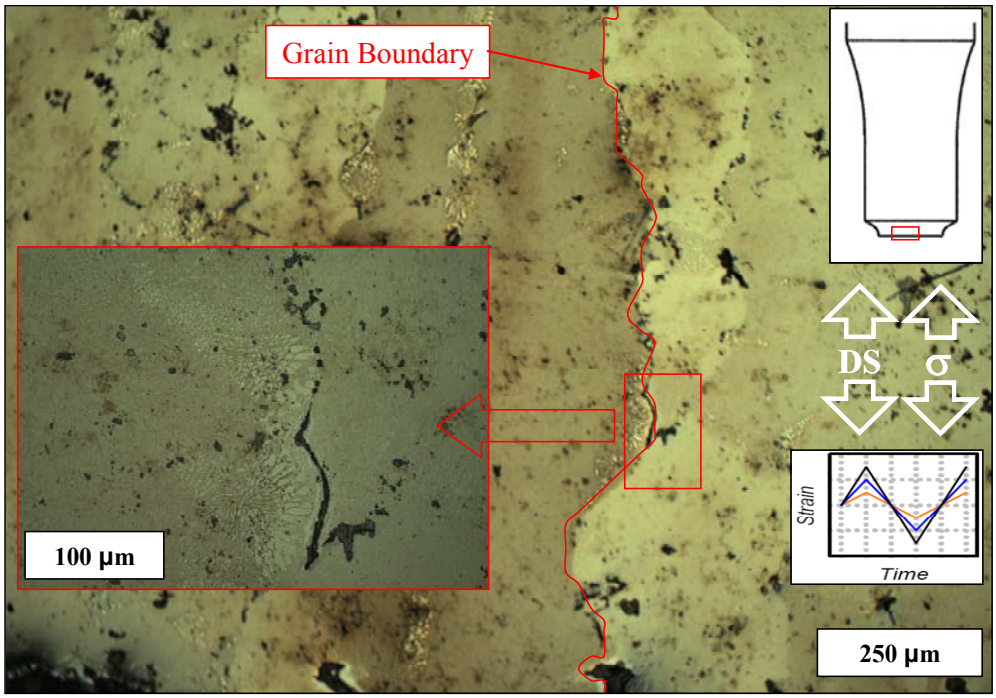

Figure 6-37: Optical microscope images of the interior of a longitudinal k_t=2 specimen near a grain boundary subjected to IP TMF. Test conditions: Normalized $\Delta\sigma$=0.34, T=500°C↔950°C.

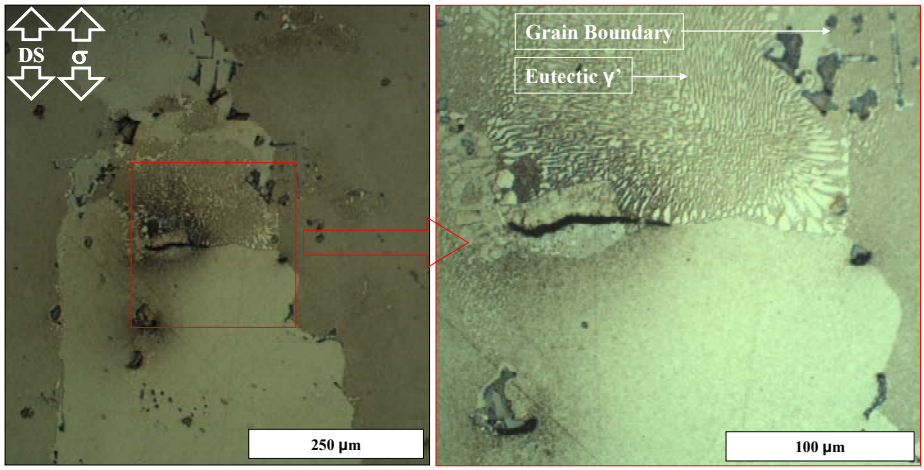

Figure 6-38: Optical microscope images of the interior of a longitudinal k_t=2 specimen subjected to IP TMF near the interdendritic region. TMF conditions: Normalized $\Delta\sigma$=0.34, T=500°C↔950°C.

As a result of these net section stresses, all notched, force-controlled tests with a T_{max} of 950°C resulted in creep ratcheting in either the compressive (if OP) or tensile (if IP) direction. As a result, the stress-gage displacement response shifts over the course of the test, as demonstrated in Figure 6-39. Similar behavior occurred for notched, isothermal creep-fatigue tests with dwells conducted at 950°C, but was absent from those tests which were continuously-cycled or whose temperature was 750°C.

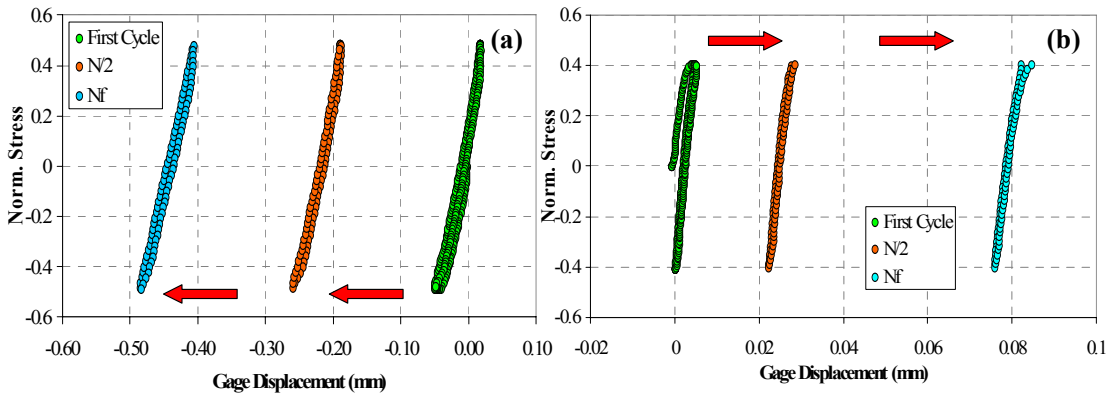

Figure 6-39: Global creep ratcheting of force controlled, L-oriented k_t=2 specimens in response to TMF cycling (a) out-of-phase with normalized $\Delta\sigma$=0.96 and (b) in-phase with $\Delta\sigma$=0.80. In both cases, T= 500°C↔950°C.

The severity of the ratcheting was very sensitive to the magnitude of applied net section stress amplitude. The ratcheting was significantly more severe in the IP (tensile) cases, where there was nearly a three-fold increase in accumulated ratcheting displacement for tests at the same applied loading (nearly 1.02 *mm* IP as compared to only 0.381 *mm* OP). A plot of accumulated ratcheting (creep) displacement as a function of cycles (time) is shown for all baseline longitudinal and transverse notched tests in Figure 6-40. In general, longitudinal specimens exhibited significantly more ratcheting than T-oriented samples; for the same net section stress amplitude, the net ratcheting displacements were greater by a factor of four and seven for longitudinal OP and IP TMF, respectively. The severity of tensile creep ratcheting (IP) as compared to compressive (OP) can also be seen, as the accumulated inelastic displacement accelerates near the end of the test. The trends of this behavior follow the creep curve for CM247LC DS, as shown in Figure 3-19. The three distinct phases (primary, steady-state, and tertiary) of creep deformation can be seen.

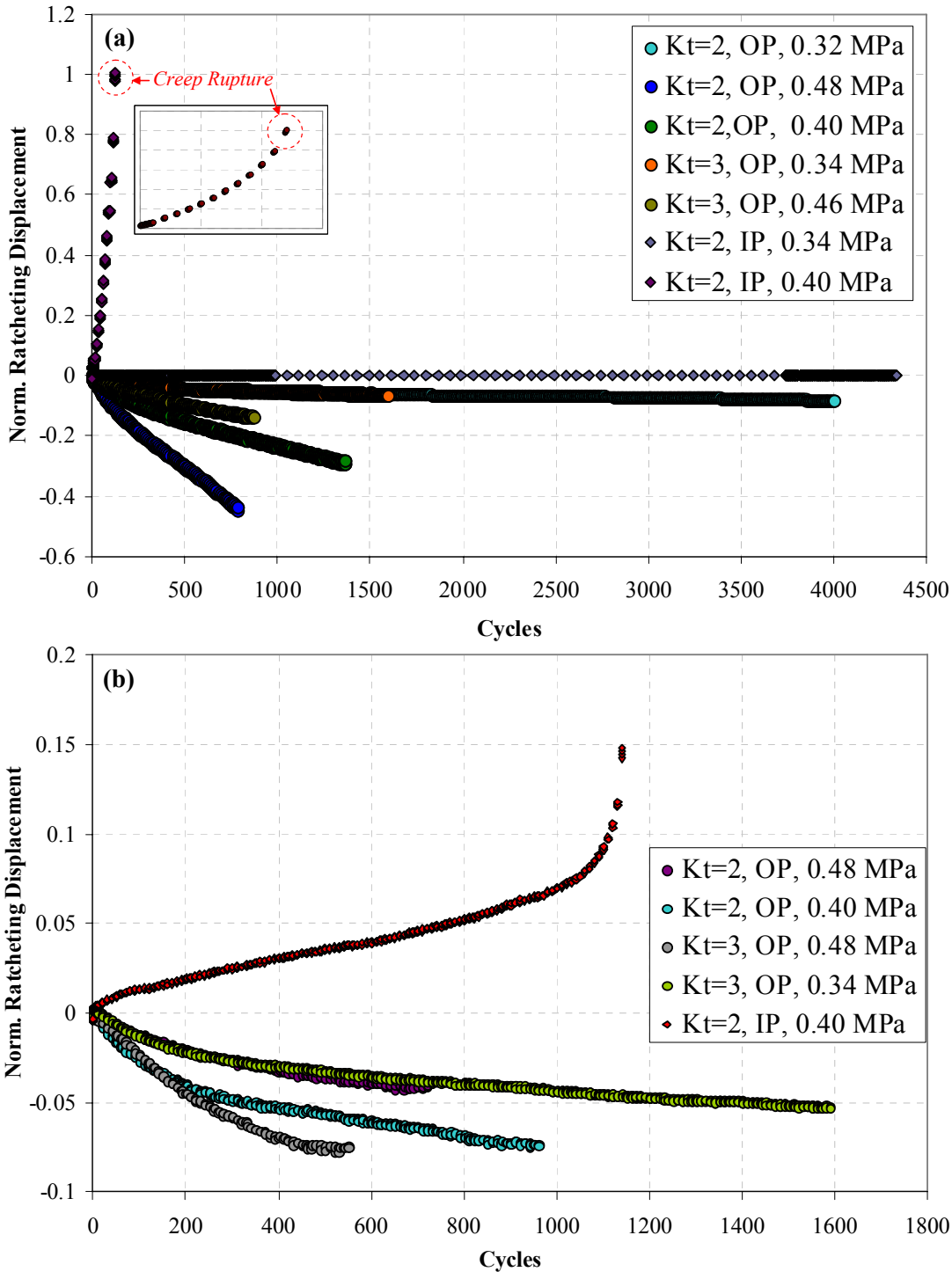

Figure 6-40: Accumulated plastic ratcheting strain up to N_f for notched (a) longitudinal and (b) transverse tests with T_{max}=950°C. Reference measurement was the point of zero stress for each cycle.

For the longitudinal specimen with net section stress amplitude of 0.40, this resulted in direct failure due to creep rupture rather than a cyclic fatigue mechanism. The number of cycles to failure for this test was more than 11 times less than that of its out-of-phase counterpart with the same applied stress range. Observation of the fracture surface revealed the absence of what otherwise would have been fatigue crack(s), and looked similar to the rupture of a creep-fatigue experiment conducted by Gordon on DS GTD-111 [2]. This comparison is shown in Figure 6-41. The fact that a similar failure was not seen in notched creep-fatigue experiments conducted by Moore on CM247LC DS indicates that the extensive ratcheting directly contributes to failure through creep rupture.

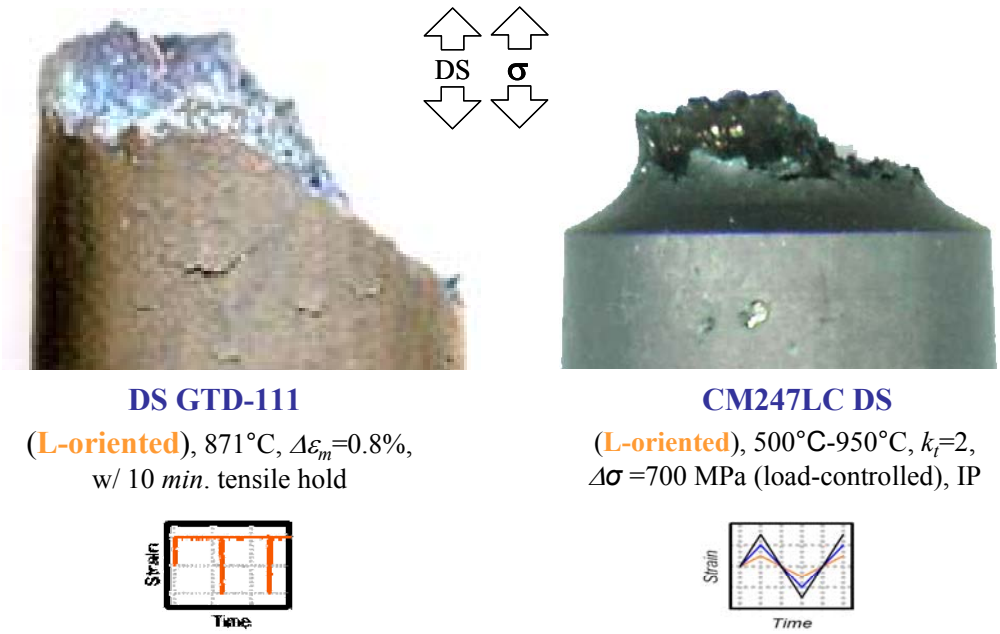

Figure 6-41: Comparison of fracture profile between an isothermal creep fatigue test and notched IP TMF test after creep-rupture failure.

Though a creep-rupture failure does not contribute a crack initiation point, it does lend insight into the cyclic creep-fatigue interaction occurring during TMF cycling. During the high temperature half-cycle, creep relaxes and redistributes the stresses in the localized plastic zone at the notch. Upon repeated cycling, these stresses can result in the further accumulation of creep damage. This may help explain the extreme effect seen in the IP notched test which failed through creep rupture. Fatigue cracks were evident in the IP test subjected to a lower load (Figure 6-42). Due to the duration of this test, oxidation and a γ' depleted zone extended a considerable length (~6 μm) ahead of the crack tip.

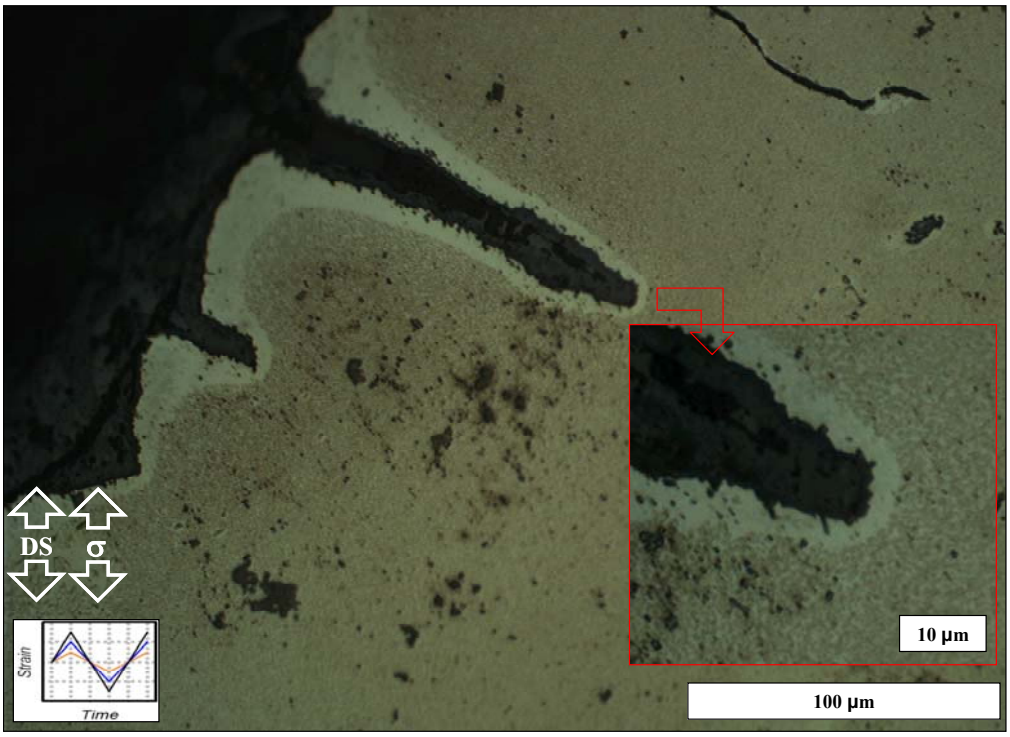

Figure 6-42: Crack initation of longitudinal k_t=2 CM247LC DS under IP TMF conditions with normalized $\Delta\sigma$=0.34 and T=500°C↔950°C.

The severity of creep ratcheting in notched specimens also depends on factors other than the applied load. Since global ratcheting within the gage section relies on the

magnitude of the net section stress, the corresponding difference in stress profiles at the root of k_t=2 and k_t=3 notches will influence this behavior. Figure 6-40 shows that for the same applied net section stress, k_t=2 notches result in a greater magnitude of accumulated ratcheting strain. Profiles from elastic visco-plastic finite element simulations, shown in Figure 6-43, demonstrate the difference in net section stresses for k_t=2 and k_t=3 notches after a complete IP TMF cycle. Although the sharper k_t=3 results in higher stresses near the surface, k_t=2 has a greater effective stress (shown to be of critical importance in Figure 6-32) from a point 190 μm and deeper into the notch. Higher interior stresses in the net section would promote more substantial ratcheting in k_t=2 as compared to k_t=3. Note also that stress redistribution during the cycle results in a loss of hydrostatic stress at the notch surface, shifting the component stress peaks radially away from the root near the end of the cycle.

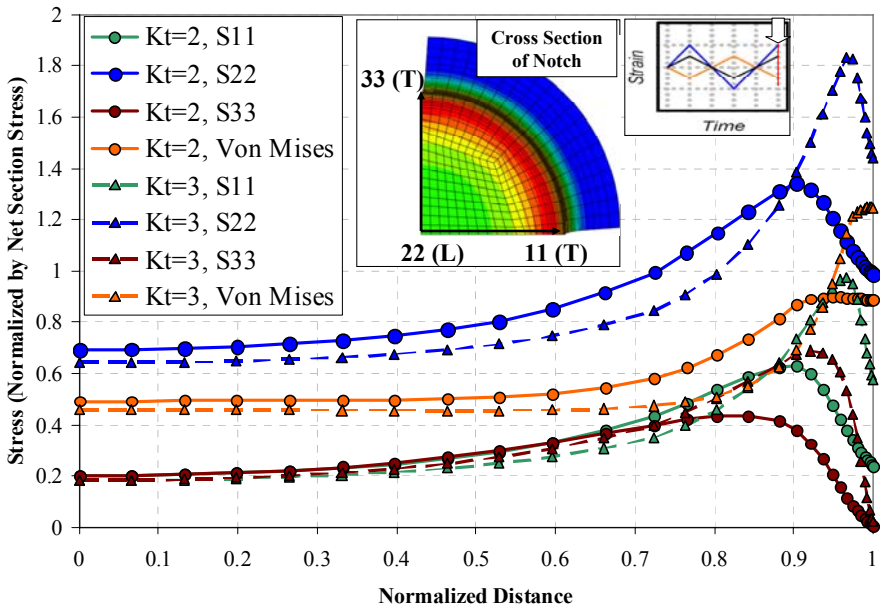

Figure 6-43: Stress component profiles for longitudinal k_t=2 and k_t=3 notches across the net section at the completion of one complete OP TMF cycle with T=500°C↔950°C.

Microstructural changes and grain orientation will also play a role, as the overall creep resistance of the alloy is orientation-dependant. The influence of various factors on the global creep ratcheting of several tests is summarized in Table 6-1. Using a longitudinal k_t=2 notch as a baseline, decreases in the net change in ratcheting displacement resulting from a sharper notch, decrease in net section stress, and the transverse orientation are shown.

Table 6-1: Influence of various factors on accumulated creep ratcheting displacement up to N_f as compared a typical L-oriented, k_t=2 sample with other test parameters held constant. Measurement reference was the point of zero stress. All comparisons are between other baseline tests with T=500°C↔950°C.

	Resulting % Change in Ratcheting Displacement vs. L, k_t=2 Notch	
	OP	IP
k_t=3 notch	-69.6%	-
50 MPa decrease in net section stress	-76.6%	-89.5%
T-orientation	-23.0%	-84.5%

The global creep ratcheting is a mechanism resulting both from tests being conducted in force control and the natural thermal asymmetry of a TMF cycle. Although this behavior is not shared between notched and smooth specimens, Figure 6-7 and Figure 6-38 reveal that the resulting creep damage in both cases manifests in the same way. Although the accumulation of microstructural creep damage in tension differs from that in compression, such damage was only clearly evident in IP tests.

The elastic-plastic FEA analysis was used to determine the local stress strain deformation response at the root of the notch. Simulations for the first cycle of both in-phase and out-of-phase force-control TMF using DS GTD-111 material constants

indicate the onset of ratcheting after saturation of the stress state during the high temperature half cycle of the notch root hysteresis, as shown in Figure 6-44. Extending the OP simulation to three cycles demonstrates the simultaneous mean stress and plastic ratcheting evolution.

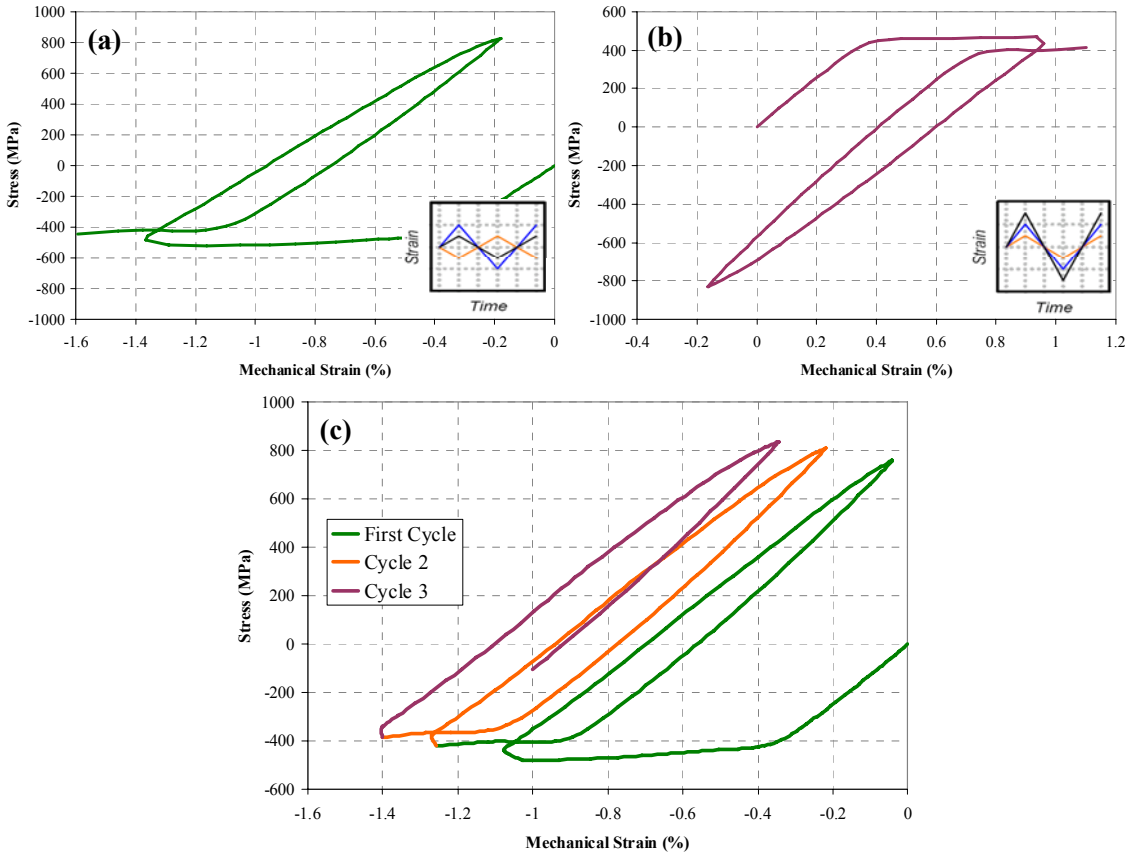

Figure 6-44: FEA hysteresis response with DS GTD-111 material constants for (a) OP, (b) IP, and (c) the first three cycles of OP TMF taken from an element at the notch root.

6.2.5 Notched Specimen Summary

Damage mechanisms for notched tests were analogous to those observed in smooth specimens for similar conditions (i.e. phasing, T_{max}, test duration). Oxidation of crack surfaces occurred in all tests with T_{max} =950°C. Oxide penetration and γ' depletion

ahead of the crack tip gave a relative measure of the extent of environmental damage. OP tests with T_{max} =750°C showed only fatigue damage, but demonstrated the same initial angular crack growth common of baseline notched fracture surfaces. Unlike that of smooth specimen tests, the comparatively slow growth of cracks outside the near-field stress concentration allowed a more synergistic combination of all three damage mechanisms for the IP test of significant duration subjected to the baseline temperature range. No difference in active mechanisms was observed between k_t=2 and k_t=3 notches. A representative damage mechanism map shown in Figure 6-45 for select longitudinal notched k_t=2 tests summarizes these findings.

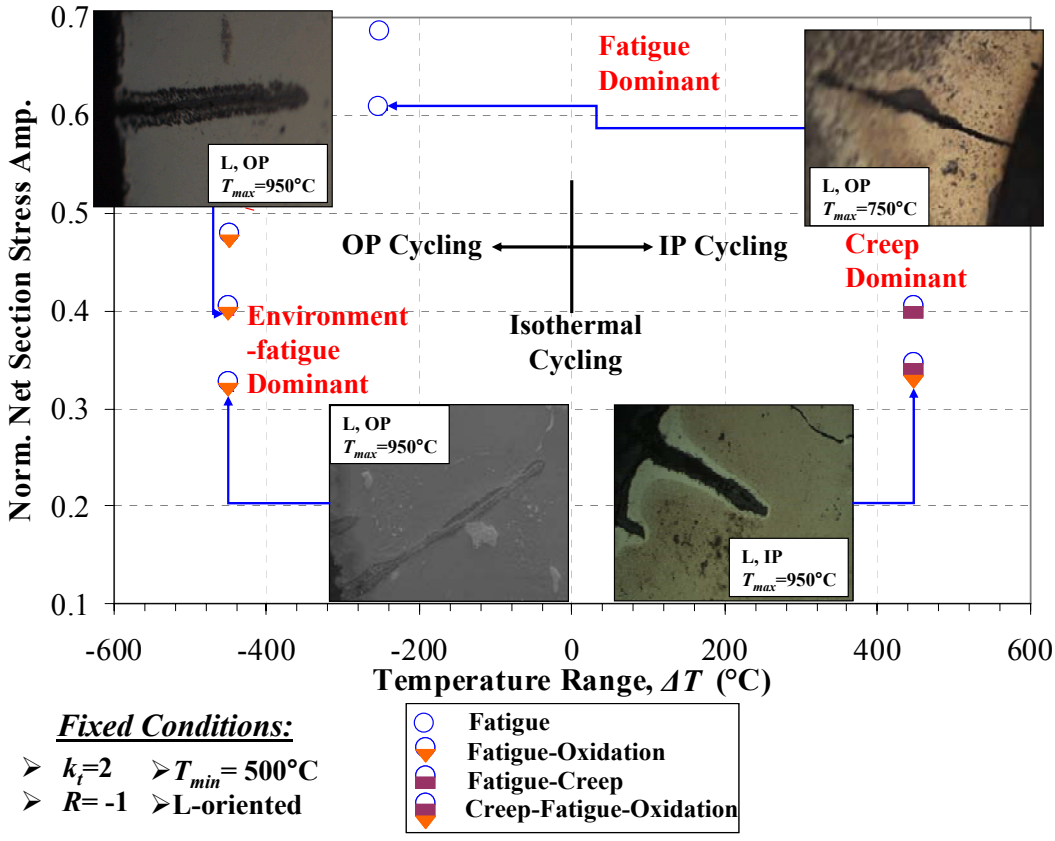

Figure 6-45: Notched k_t=2 specimen damage mechanism map for crack initation in CM247LC DS subjected to OP and IP TMF.

CHAPTER 7. EFFECT OF γ' MORPHOLOGY ON MECHANICAL PROPERTIES

7.1 Background

Because of the high degree of constituent optimization to achieve high temperature strength, the microstructure of Ni-base superalloys is inherently unstable and prone to morph as a result of thermodynamic processes. Due to centrifugal force at peak operating temperatures, blades in service can experience a severe directional coarsening, often called rafting, of the γ' precipitate phase [75-78]. The γ-γ' microstructure of Ni-base superalloys is thermodynamically unstable above a threshold temperature, where directional coarsening and rafting of the precipitates can become important. Rafting results from a thermally-activated diffusion mechanism which seeks to reduce energy and relax the coherency stresses between the phases. This behavior can affect the low temperature strength, as the optimized γ' size and volume fraction is the main strengthening mechanism of the alloy.

Considerable effort has been devoted to understanding microstructure response to thermodynamic processes during TMF. This process follows well-established kinetics and typically results in the precipitates taking the form of platelets on planes normal or perpendicular to the applied stress. Directionality depends on whether the stress is tensile or compressive. Tensile stresses causes rafting perpendicular to the stress axis, while compressive rafting is parallel to the same axis. This is shown for the single crystal alloy CMSX-4 in Figure 7-1.

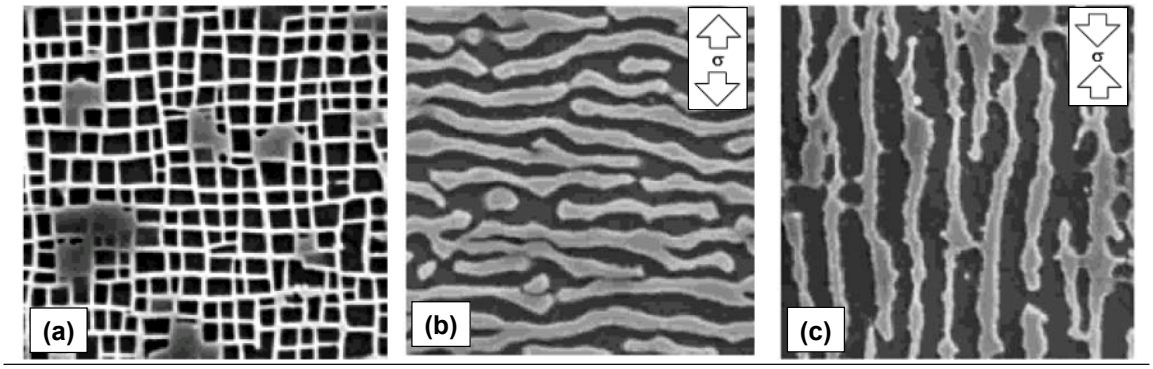

CMSX-4: As Aged *(virgin microstructure)*

CMSX-4: Pre-Rafted in Tension *(T= 1100°C, σ= 115 MPa)*

CMSX-4: Pre-Rafted in Compression *(T= 1100°C, σ= -115 MPa)*

Figure 7-1: Effect of pre-rafting on the microstructure of a single crystal Ni-base superalloy (CMSX-4) showing (a) the as aged microstructure, (b) pre-rafted in tension, and (c) pre-rafted in compression. Pre-deformation was conducted in a vacuum [79].

The rafting is governed not only by the external applied stress, but also the build up of internal plastic strain. This occurs only when the alloy has a negative relative lattice mismatch, δ, where [80]

$$\delta = \frac{2(a_{\gamma'} - a_{\gamma})}{(a_{\gamma'} + a_{\gamma})} \tag{7.1}$$

where a_{γ} and $a_{\gamma'}$ are the lattice parameters of the γ and γ' phases, respectively. Under these conditions, internal back stresses develop in the γ phase when under load at high temperatures, which can influence material strength.

In the laboratory, rafting has also been observed during thermomechanical fatigue tests [58, 81]. Work has been done to determine if γ-γ' rafting is damaging or advantageous, and also to see if this behavior can be avoided through further optimization of the initial microstructure constituents. While most of these attempts have been

unsuccessful, it is now commonly understood that rafting can lead to creep acceleration and a reduction in creep strength, although these are not mutually exclusive [80]. However, testing these effects on the properties of Ni-base superalloys in the laboratory involves two-phase tests, which are both time intensive and expensive.

Ott and Mughrabi [79] conducted high temperature isothermal tests on several single crystal Ni-base superalloys to compare the fatigue lives of microstructures with cuboidal γ' as aged, rafted parallel to the stress axis (compression), and rafted perpendicular to the stress axis (tension). Fatigue cracks usually followed along the γ channels or along the γ -γ' interface and avoided cutting through the γ' phase. This was beneficial to both fatigue and creep resistance in cases where pre-rafting occurred in compression, and detrimental to those rafted in tension, as shown in Figure 7-2. Fatigue life of the as-aged specimens fell in between these two cases. TMF testing conducted by Neuner et al. [82] on single crystal SRR 99 confirmed these results.

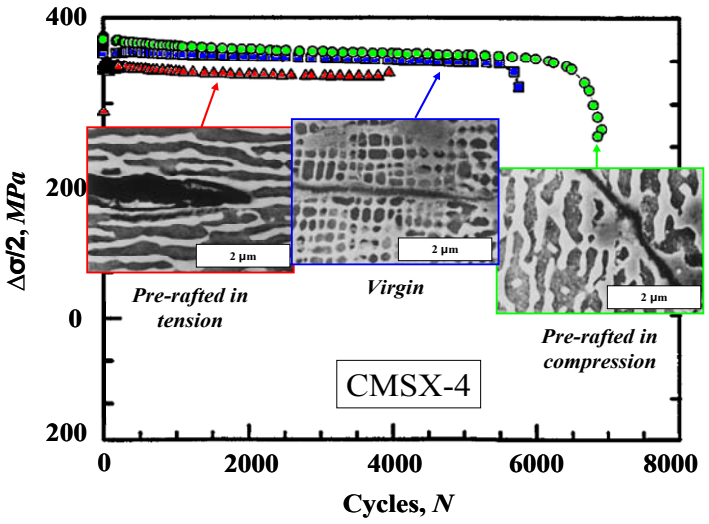

Figure 7-2: Cyclic deformation curves and crack tips for SC CMSX-4 specimens with the three variations in microstructure. In all cases, T= 950°C, $\Delta\varepsilon_t$= 0.9%. Crack tips are in (100)-sections parallel to the [001] stress axis. [79, 80].

Further work by Mughrabi concluded that it was not possible to optimize the γ -γ' lattice through ageing without simultaneously inducing coarsening of the γ' precipitates, which results in a loss of creep strength [80].

Typical temperature ranges for TMF testing are usually chosen with T_{min} near 400°C - 500°C. This is done to shorten cycle times on the assumption that LCF and tensile properties are relatively uniform from room temperature through T_{min}. Coarsening and rafting of the γ -γ' structure had little effect on the yield and tensile strengths of Ni-base superalloys at typical test temperatures above 400°C, where the yield strength is high regardless of microstructure characteristics. The changes to the structure at high temperatures can have an effect on low-temperature strength, however, which is more sensitive to particle morphology [61]. To test this effect, Hasselqvist and Moverare conducted OP TMF tests on IN 738LC with temperature cycling between 100°C - 950°C [61]. Baseline tests contained a five minute hold time in compression, while others included intermediate ageing for 4000 *hrs* at peak temperature after the initial 25 cycles. This was done to obtain a coarsened microstructure where secondary strengthening particles had largely dissolved within the matrix, with the objective being that midlife cycles should experience a similar level of degradation when compared to service components. Results showed that when compared to the baseline stress-strain response, yielding occurred at much lower stress values for the same temperature upon resumption of TMF cycling after intermediate ageing. As a result, the stabilized inelastic strain range was consistently higher in tests with intermediate ageing. Consequently, fatigue life was substantially reduced. Arrell et al. [62] demonstrated that this reduction in low temperature strength could be captured in a constitutive life prediction model through the

increase in plastic strain which accompanied a rafted microstructure. This behavior is depicted in Figure 7-3.

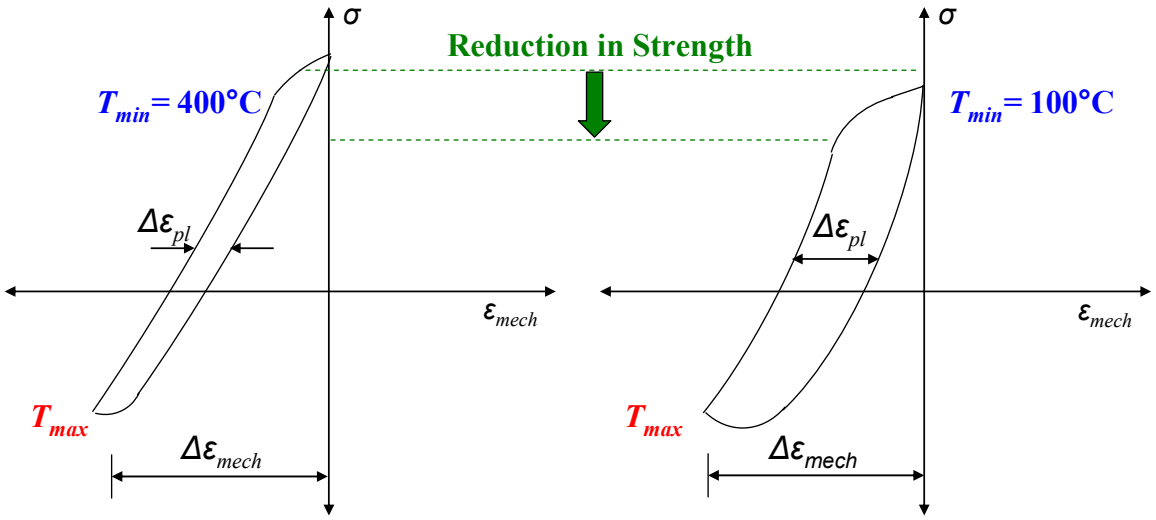

Figure 7-3: The predicted effect of the minimum cyclic temperature on the stabilized OP TMF hysteresis loop if the material had a rafted microstructure [62].

7.2 Microstructure Morphology

Resulting from TMF Experiments

Figure 7-4 shows rafting which was observed during post-test microscopy of TMF-tested samples. Only tests with a T_{max} of 950°C were shown to result in this behavior, indicating that 750°C was below the threshold temperature and did not provide sufficient thermal energy to initiate the process. All TMF tests resulted in stresses greater than those needed to induce this change, and thus the occurrence of rafting was only a function of the length of the test. In the virgin microstructure, the cuboidal precipitates are arranged quite regularly in the solid-solution hardened γ matrix. After extensive TMF, the γ' platelets align parallel to the stress axis in OP cycling, where the specimen is in compression at T_{max}. In IP TMF, tensile loads during the high temperature half cycle

results in the γ' rafts orienting normal to the stress axis. For notched tests, although the stress state within the notch is highly multiaxial, the rafted structure still aligns relative to the axis of applied stress.

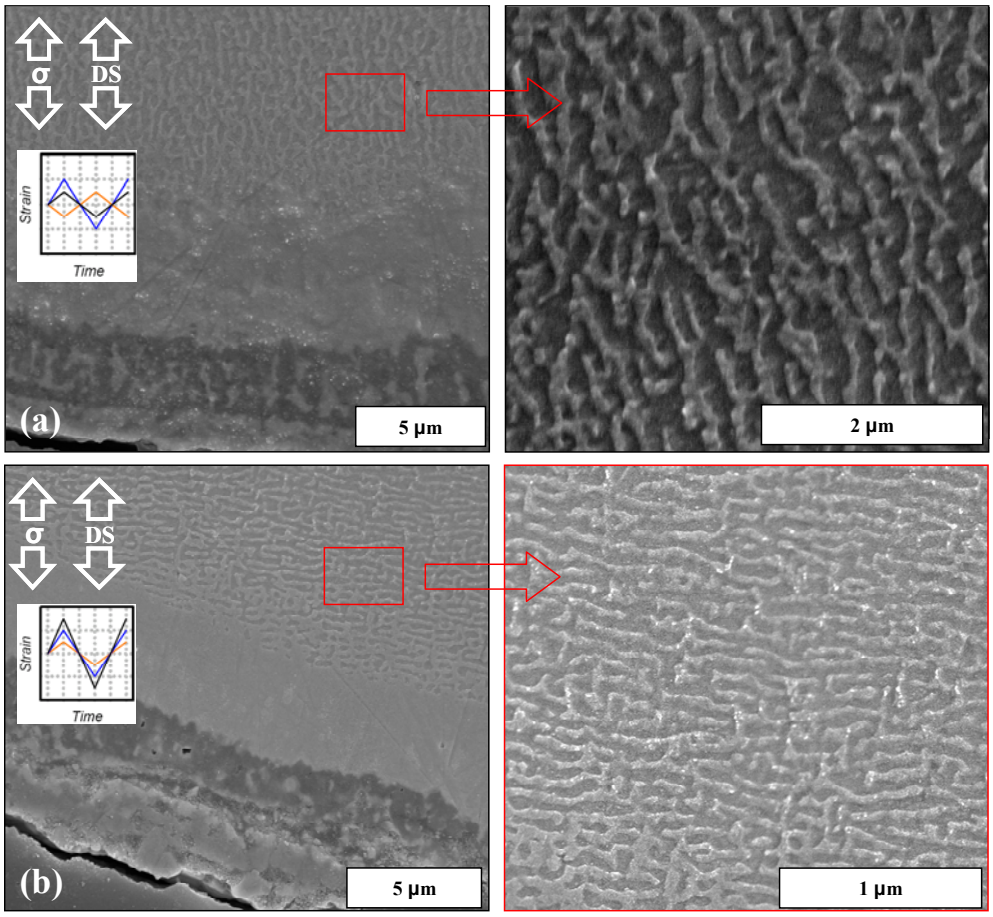

Figure 7-4: Rafting of the γ' precipitates (a) parallel in OP and (b) perpendicular in IP to the loading axis. For each, a k_t=2 sample was selected after TMF cycling between 500°C and 950°C.

For tests of shorter duration, the increased stress intensity around crack tips was often sufficient to promote localized rafting, while leaving the majority of the microstructure in a virgin or partially-rafted state. In several cases, such as those shown in Figure 7-5, elongated platelets formed in the vicinity of a crack although failure of the

specimen occurred prior to any significant morphology of the bulk microstructure. It can thus be surmised that the rafting process can be accelerated by significantly increasing the stress.

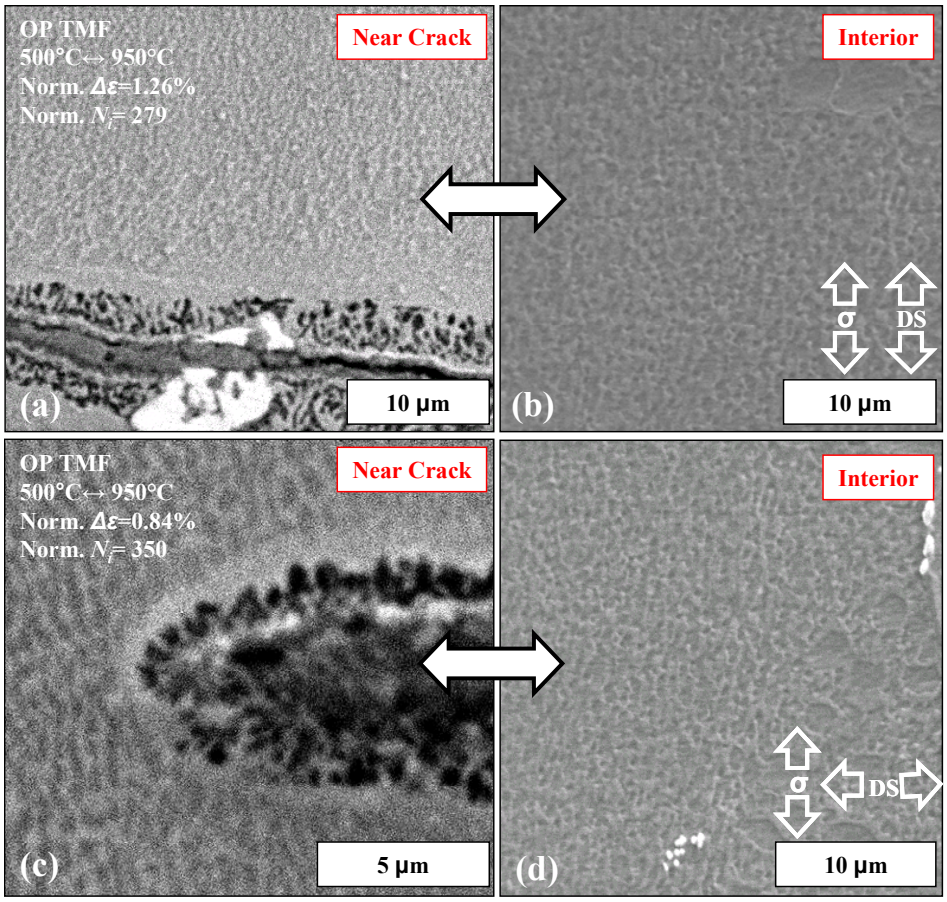

Figure 7-5: Microstructure of CM247LC DS following OP TMF tests with relatively short lives showing (a,c) rafting near a crack tip and (b,d) the bulk microstructure.

7.3 Creep Pre-deformation Experimental Setup

To determine the influence of microstructural changes on the mechanical properties and crack initiation lives of CM247LC DS, creep pre-exposure tests were conducted. These were designed to induce a rafted morphology of the microstructure while simultaneously limiting permanent creep deformation. Resulting factors, such a

reduction in fatigue strength, acceleration of creep, and/or influence on microcrack propagation can then be captured in through analytical modeling.

Although rafting had been observed in various OP and IP TMF experiments with a T_{max} of 950°C, indicating that this temperature was sufficient to induce the change, these tests did not provide the discrete load or duration requisite to catalyze the process. Therefore, prior to pre-rafting actual fatigue specimens, preliminary experiments utilized unused shank portions of those which had already been TMF-tested to determine these bounds. The diameters were turned down to the equivalent 0.25 *in*. of the specimen gage section. To facilitate loading of specimens of this geometry, a jig of MAR-M247 was used which would fit a creep test frame. Upon application of a tensile load, sample specimens positioned at the outer edges of the jig would be subjected to a compressive stress, as shown in Figure 7-6. Using the creep frame, the specimens were subjected to several static uniaxial stress levels (-80 *MPa*, -112.5 *MPa*, or -120 *MPa*) at 950°C for variable durations from 96 *hrs* (4 *days*) up through 336 *hrs* (2 *weeks*). Different stress levels were chosen so as to determine which load was required to fully raft the material. Upon completion of exposure, these preliminary specimens were removed, sectioned, and polished for examination. SEM examination revealed that specimens subjected to 112.5 *MPa* at 950°C for 144 *hrs* (6 *days*) was sufficient to fully raft the microstructure, as seen in Figure 7-7. These conditions limited inelastic creep strain deformation to 0.16% prevented the material from reaching the tertiary creep regime.

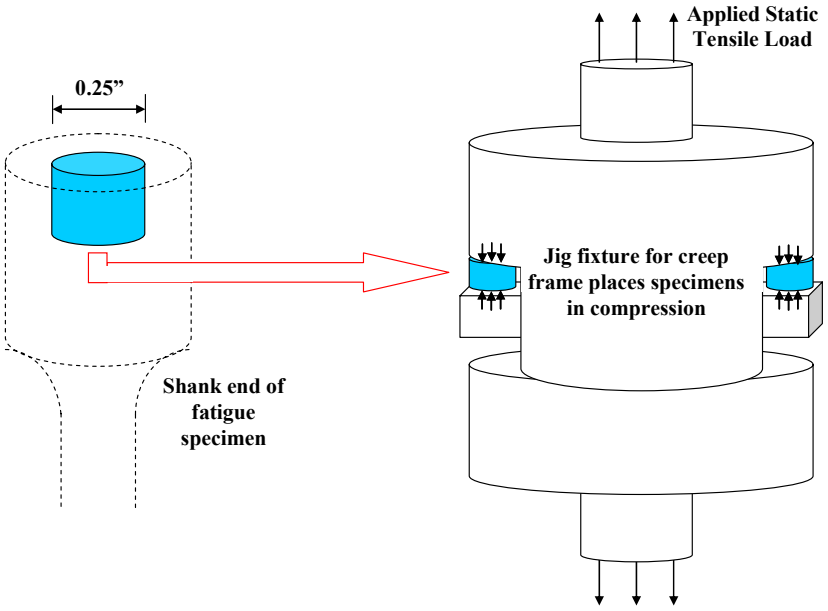

Figure 7-6: Sample cylindrical test specimens and jig fixture used to determine the stress and duration bounds within which rafting will occur.

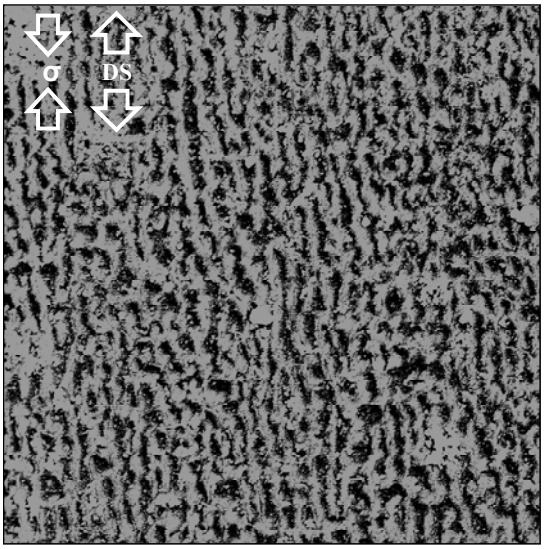

Figure 7-7: Rafted microstructure of longitudinal CM247LC DS after 144 *hrs* of pre-exposure at -125 *MPa* and 950°C.

7.3.1 Tensile Pre-raft

Once the required load and duration which would result in a fully-rafted microstructure were established, select specimens were pre-exposed to this procedure.

This required machining ½”-13 UNC threads 0.375” (9.525 *mm*) into the specimen shank ends to facilitate loading into the creep frame. This thread depth gave sufficient engagement to support the pre-raft load at 950°C without resulting in extensive creep of the threads. It also left a sizeable remainder of the shank to allow a proper grip area during subsequent use in the servo-hydraulic test frame. Pull rods of 0.75” (19.05 *mm*) diameter and specimen adaptors made of IN 713C were used to support the fixture under load. Temperature was monitored via TC’s welded to the specimen shoulders, as in TMF experiments. Images of the test setup are provided in Figure 7-8. Heat within the furnace was allowed to stabilize prior to the application of load. Creep deformation and temperature were monitored to ensure the consistency of results. Once the desired time had elapsed, specimens were removed and the gage section polished to remove the accumulated oxide scales and γ’ depleted zone.

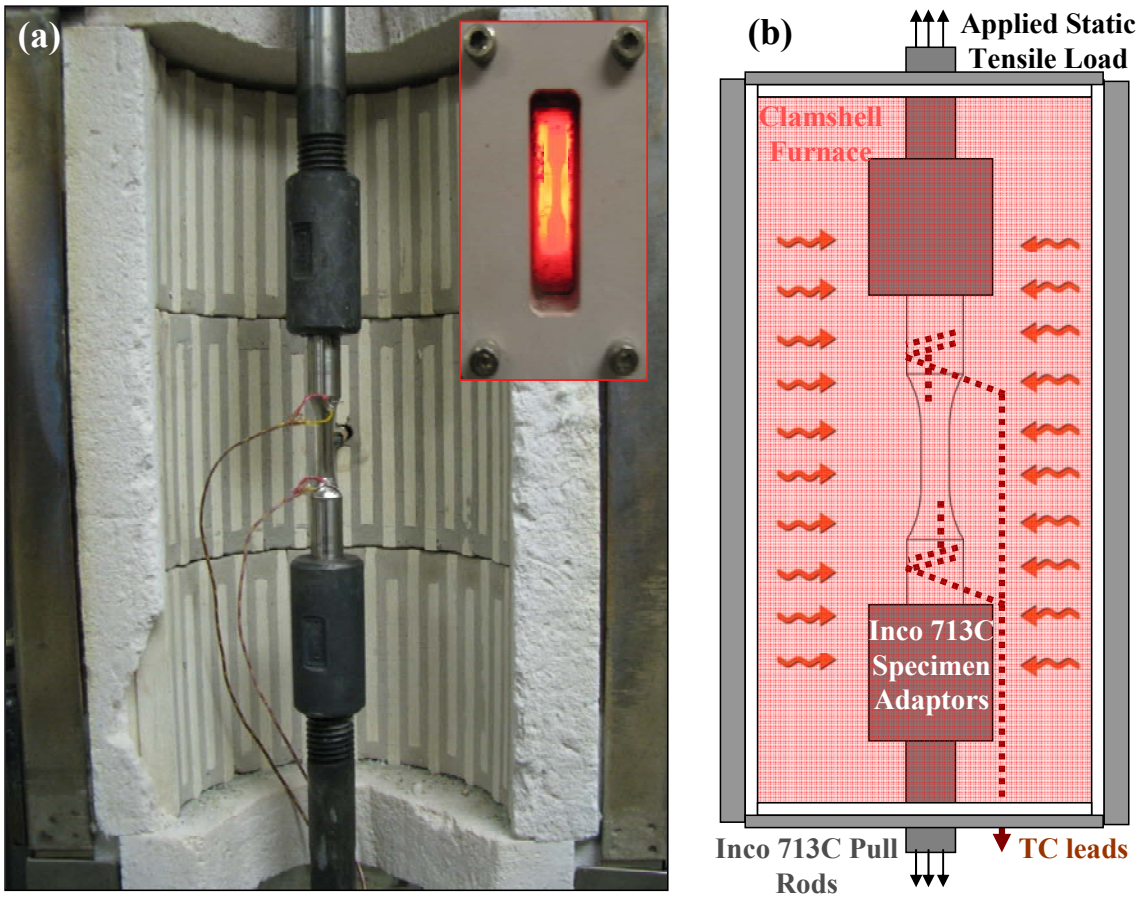

Figure 7-8: (a) photograph and (b) schematic of experimental setup.

7.3.2 Compressive Pre-raft

Due to the inability of uniaxial creep frames to subject specimens to compressive loads, this type of pre-raft needed to be performed in the servo-hydraulic test frame with the same induction heating used for TMF experiments. Unlike the tensile pre-raft, the compressive required cycling the applied load at 0.25 *Hz* over a small range (±7 *MPa*) to avoid fouling the hydraulic valve.

7.4 TMF Testing with Rafted Microstructure

Using the same setup and procedure outlined in Chapter 4, specimens with microstructures rafted in tension and compression were subjected to full thermomechanical fatigue cycling to determine the effect to which material degradation influences the crack initiation life of the alloy. At low temperatures, strength is drawn primarily from the interaction between the matrix and the precipitates, and is thus more sensitive to the microstructure morphology [61]. As both the γ matrix and γ' precipitates are relatively weak near room temperature, a minimum temperature of 100°C was used. Additionally, the full thickness of the oxide layers and γ' depleted zone were polished off and the specimen surface returned to the as-received condition prior to testing.

The mechanical strain-life results for specimens with the virgin (see also Figure 6-20 and Figure 6-21) and tensile-rafted microstructures are compared in Figure 7-9.

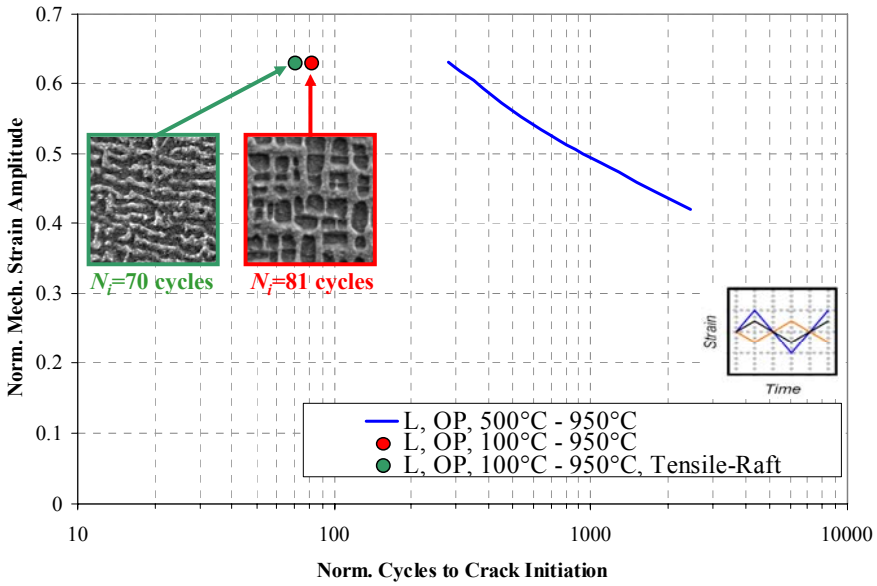

Figure 7-9: Fatigue life of longitudinal CM247LC DS subjected to OP TMF from 100°C↔950°C with virgin microstructure and γ' precipitates rafted in tension. these two tests, normalized $\Delta\varepsilon_{mech}$=1.26%.

A slight 13.6% reduction in life from virgin was observed for the specimen with the tensile-rafted microstructure. Platelets in this orientation can facilitate crack growth. Both rafted microstructures produced greater inelastic strain ranges, as seen in the initial hysteresis loops in Figure 7-10. The cyclic behavior of the tensile rafted microstructure was considerably more stable than that of the virgin, which softened significantly in tension over the first 40 cycles. By comparison, the tensile rafted sample showed limited softening over this period, as shown in Figure 7-11b. By comparison, the specimen with rafts parallel to the stress axis hardened considerably in the compressive high temperature half-cycle, but was significantly weaker in tension.

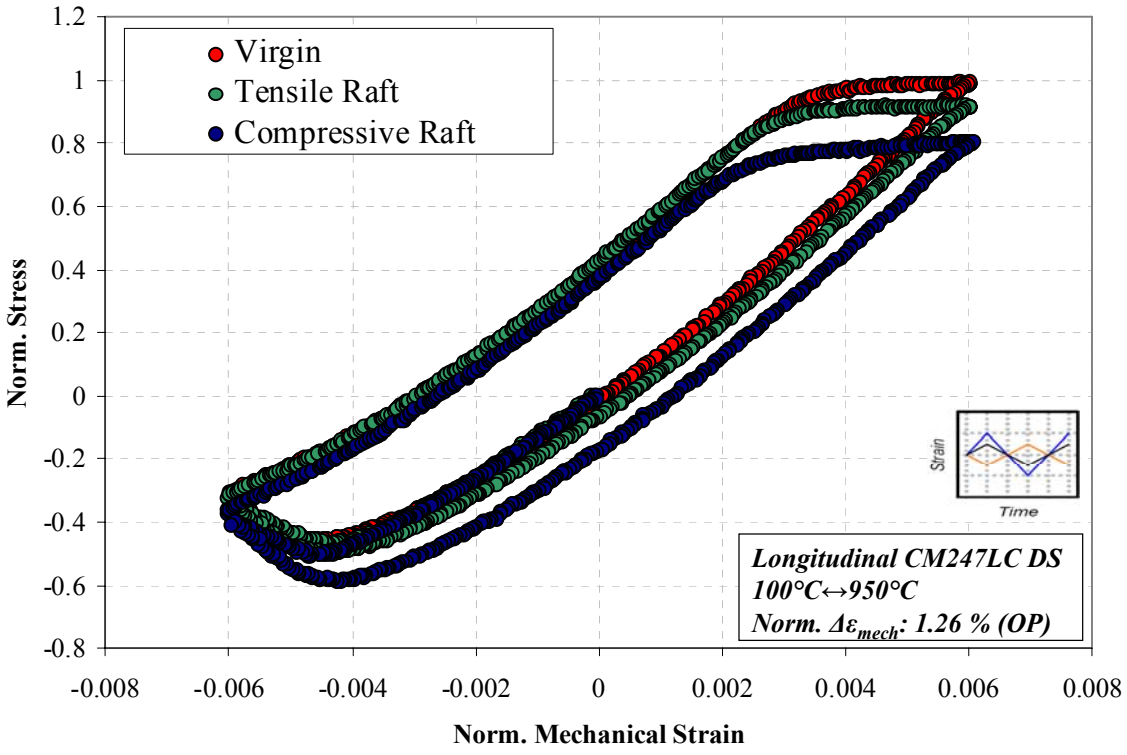

Figure 7-10: First cycle hysteresis loops for L-oriented CM247LC DS with virgin and rafted microstructures.

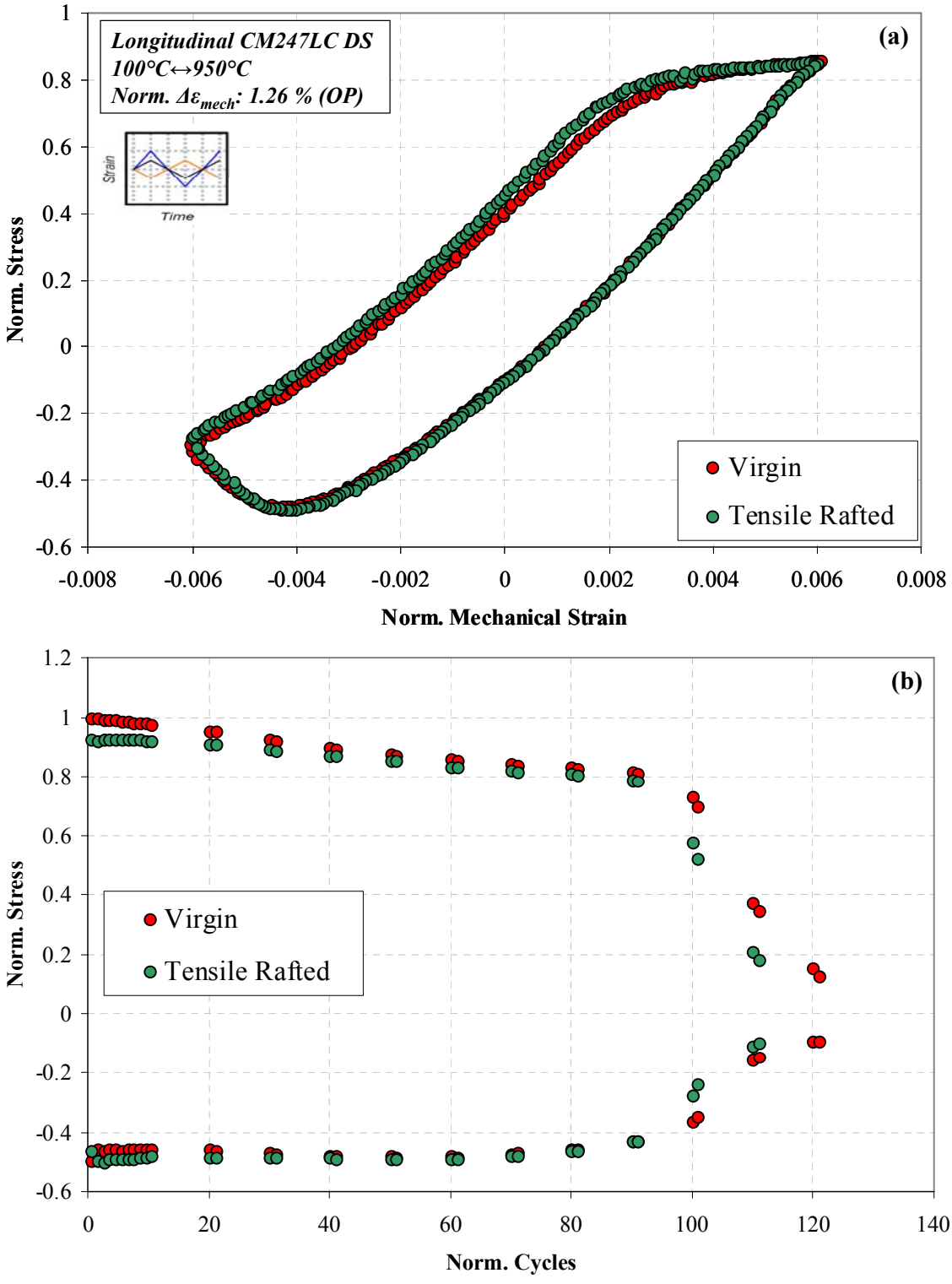

Figure 7-11: (a) Stabilized half-life hysteresis loops and (b) stress histories for L-oriented CM247LC DS with virgin and tensile-rafted microstructures.

Both rafted samples showed only a very slight tensile shift in the mean stress over the first ten cycles. Therefore, the pre-raft procedure likely acts as an ageing process for the alloy, which more quickly establishes the stabilized hysteresis loop. This stabilizing effect or pre-exposure was also seen in IN 738 by Hasselqvist et al. [61]. For the specimen subjected to prior tensile pre-exposure, the stabilized mean stress was comparable to that of the virgin cuboidal microstructure (Figure 7-11a).

7.5 Effect of Rafting on Yield Strength and Elastic Modulus

7.5.1 Procedure

In light of the need for temperature-dependent material properties in microstructurally-sensitive constitutive modeling, the yield strength and elastic modulus for the current batch of material needs to be determined. This will ensure the properties obtained will be for the same microstructure and heat treatment as the TMF tests. A procedure was developed to use a single smooth specimen in strain control for multiple data points. As with the TMF test, the oxides were removed and the specimen surface returned to the polished condition. Once completed, the specimen is cycled elastically to progressively higher strain amplitudes, using fully-reversed (R = -1) cycles at each strain level. This avoids large-scale yielding that would otherwise affect subsequent measurements. Near the onset of yielding, three cycles are used at each strain level, which allows the response to stabilize (cyclically harden or soften, depending on temperature). Once yielding occurs, the response is allowed to stabilize and the yield strength determined through a 0.02% offset formulation. The result of this procedure conducted on CM247LC DS at 450°C is shown in Figure 7-12.

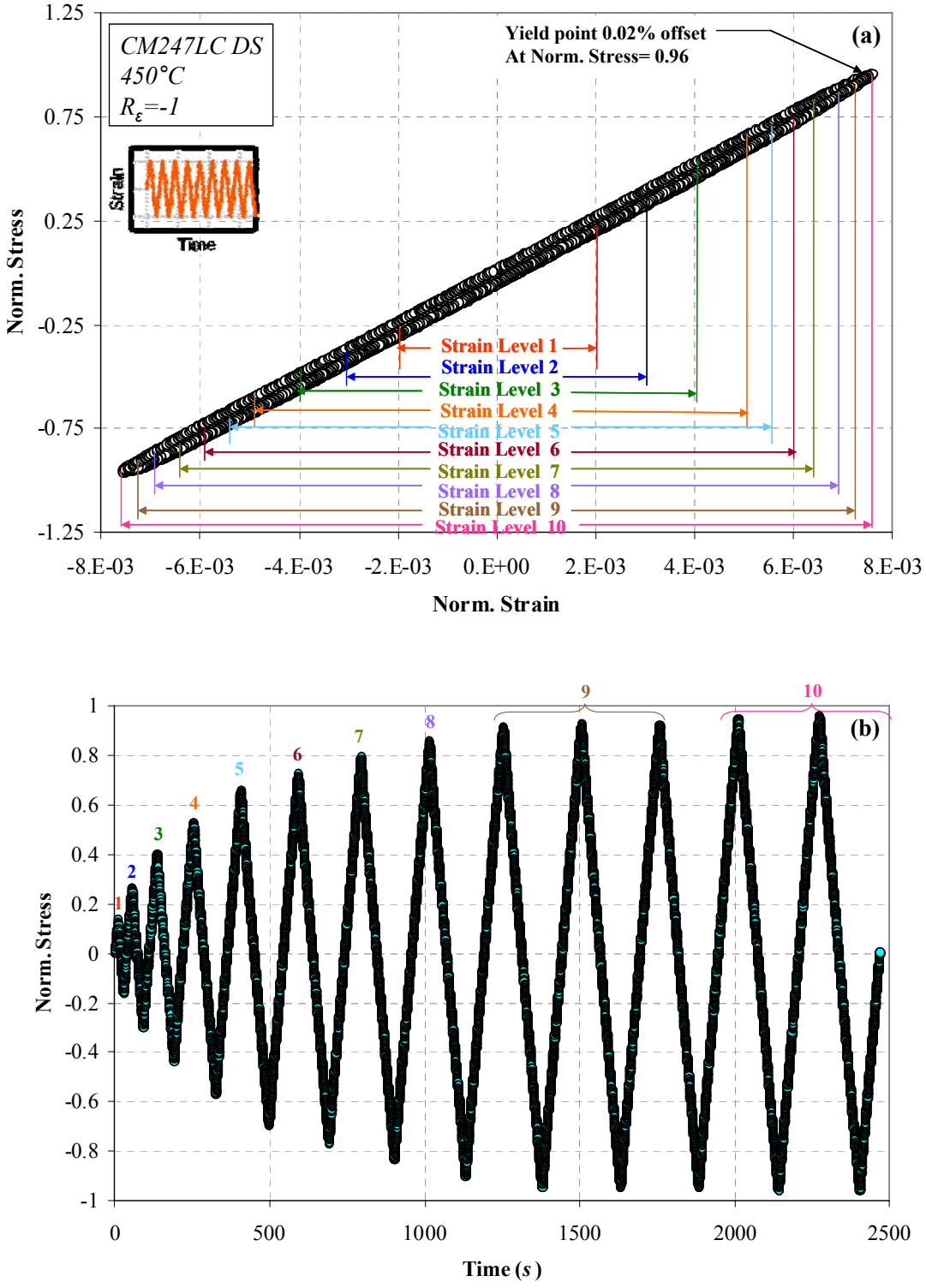

Figure 7-12: Results for the tensile test performed on CM247LC DS in the longitudinal orientation at 450°C showing (a) the stress-strain response and (b) the stress time history. Three fully-reversed cycles were performed at strain levels 9 and 10.

The 0.02% offset is used instead of the standard 0.2% offset because of the limited plasticity observed in typical tensile curve of Ni-base superalloys. Additionally, the use of a tighter offset further limits the extent of plastic deformation and its impact on the yield strength. This allows for the repeated use of a single specimen for multiple tests. This sequence is repeated at regular intervals from room temperature through 1050°C. This method allows the use of a single, uniform microstructure for all acquired data. This procedure is also used for the transverse orientation and determining a change in strength resulting from a pre-rafted γ -γ' microstructure. Other authors [61, 62] had reported that the rafted alloy has dissimilar mechanical properties between 100°C and 400°C. As the objective was to determine if this microstructure morphology had any influence on strength, various data points were obtained within this range to capture the extent to which the material's low temperature properties were affected.

7.5.2 Results

The trends in the virgin strength versus temperature plot were consistent, as seen in comparing Figure 7-13 and Figure 7-14 with Figure 3-11. Since the tighter offset of 0.02% and a strain rate of 0.0111%/s were used, the resulting virgin yield strengths were approximately 10% lower than those compiled from other sources [5, 17, 48]. In the absence of a reported value, the literature sources were assumed to have used the standard 0.2% offset. This indicates that changes and trends in the yield strengths determined within the scope of the current investigation will likely apply for small changes in microstructural composition and heat treatment cycles.

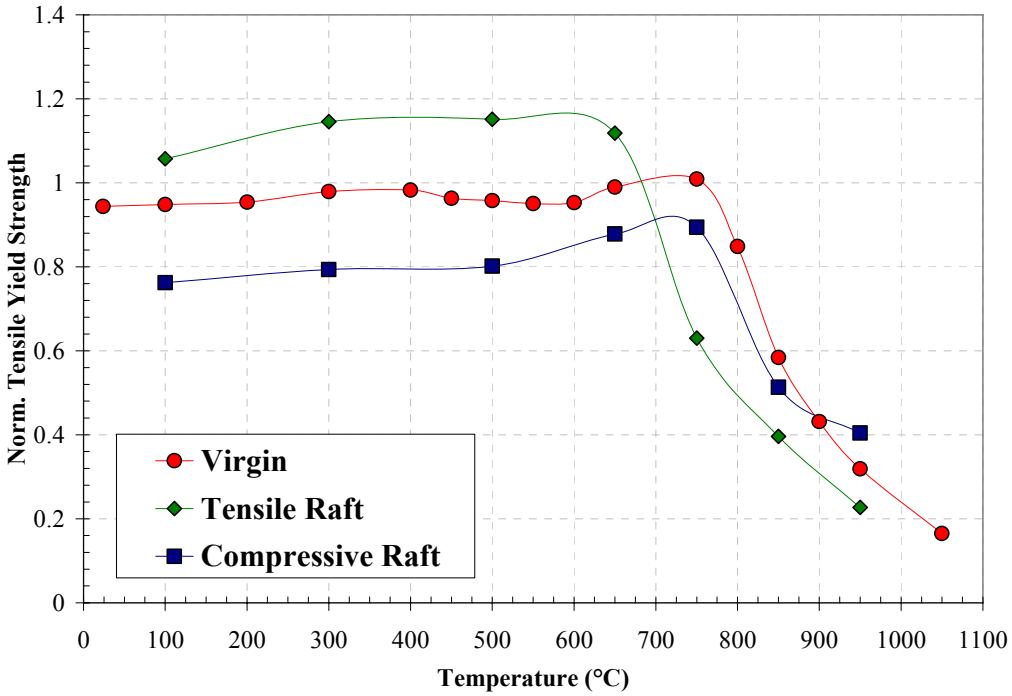

Figure 7-13: 0.02% yield strength of L-oriented CM247LC DS with the γ-γ' microstructure in the virgin, tensile-rafted, and compressive-rafted condition.

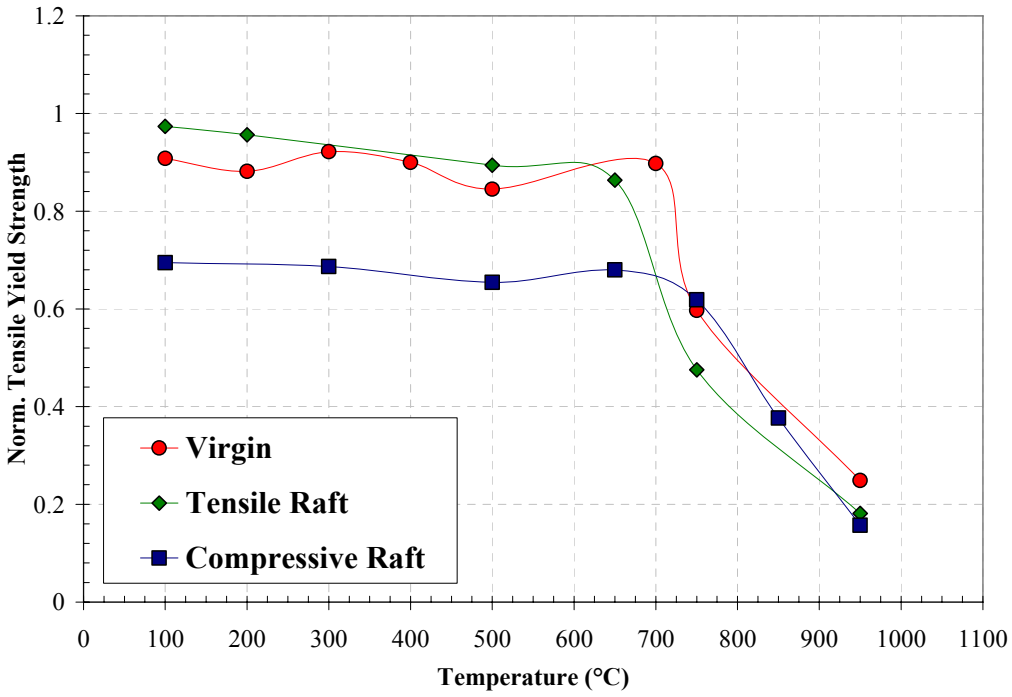

Figure 7-14: 0.02% yield strength of T-oriented CM247LC DS with the γ-γ' microstructure in the virgin, tensile-rafted, and compressive-rafted condition.

The sample with the tensile-rafted microstructure resulted in a strength increase at temperatures below 600°C and a decrease at high temperatures when compared to the virgin material for both orientations. Note this is different to the trends observed for the corresponding first-cycle hysteresis loops shown in Figure 7-10, where material yielded sooner in tension than with the virgin cuboidal structure. This may indicate that the γ-γ' rafted structure introduced by prior tensile pre-exposure becomes unstable during OP TMF testing, which would normally favor the formation of rafts lying parallel to the stress axis. Prior compressive pre-exposure resulted in the opposite behavior, where low temperature strength is substantially decreased, but becomes more comparable to that of the virgin sample at temperatures greater than 750°C. Both orientations demonstrated similar behavior trends, although the degree to which strength was affected was less in transverse. The extent of the strength increase (γ-γ' raft structure normal to the stress axis) or decrease (γ-γ' raft structure parallel to the stress axis) for the L-oriented samples was significant even at temperatures beyond 500°C, the minimum temperature of the baseline thermomechanical fatigue experiments.

For both rafted structures, the yield strength curve remains reasonably constant from room temperature up to approximately 650°C, as in the virgin material. This indicates strength is likely still affected by the precipitate-matrix interaction in CM247LC DS. These results are somewhat different with those from similar testing conducted on the single crystal Ni-base superalloy MC2 by Pessah-Simonetti et al. [83]. Tensile rafting in MC2 induced a decrease in 0.2% yield strength behavior more closely resembled that of pure Ni_3Al γ' (Figure 3-12). These differences may be due to the slightly more chaotic distribution of precipitates in the matrix of CM247LC DS as compared to single crystal

Ni-base superalloys [84]. As a result, there is less of a well-defined particle morphology to lose, and thus rafting might have different influences on CM247LC DS.

Rafting also had a small effect on the elastic modulus of the material over this temperature range, as shown in Figure 7-15. Both rafts parallel and perpendicular to the stress axis resulted in nearly the same modulus, which for the longitudinal orientation was slightly higher than that of the virgin material for temperatures below 800°C and slightly lower for higher temperatures. These observations are also accurately reflected in the hysteresis loops of Figure 7-10. In transverse, the elastic modulus was very similar to that of the virgin material over the entire temperature range.

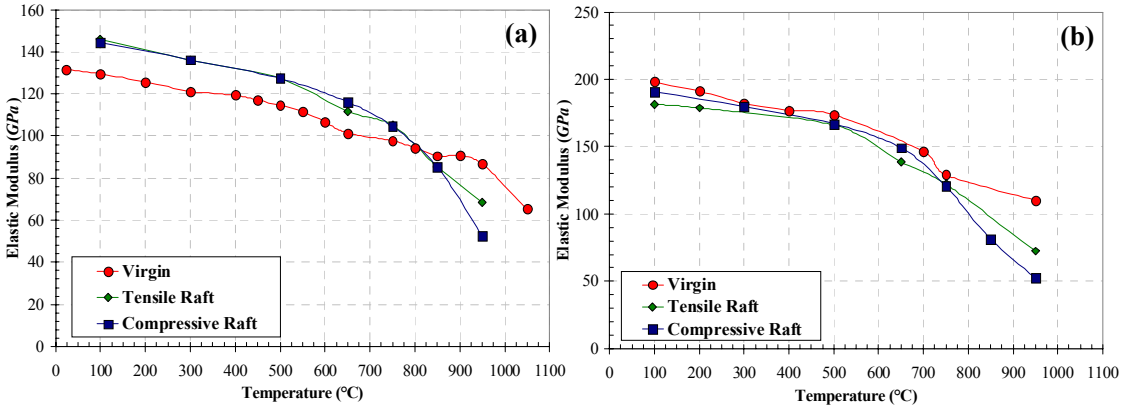

Figure 7-15: Elastic modulus of (a) L-oriented and (b) T-oriented CM247LC DS with microstructure in the virgin, tensile-rafted, and compressive-rafted condition.

7.6 Summary of γ' Morphology Effects

Table 7-1 presents a summary of pertinent experiments characterizing the effect of γ' precipitate phase morphology on the mechanical behavior of L- and T-oriented CM247LC DS as presented in the preceding sections. The alteration of material properties depends on the pre-exposure conditions. Beyond the hysteresis loops,

transmission electron microscopy (TEM) is needed to precisely determine the effect of rafting on the deformation behavior at a microstructural level, and is left for a future study.

Table 7-1: Experiments characterizing the effect of precipitate morphology on the fatigue and tensile properties of CM247LC DS

Pre-Exposure					*Fatigue and Tensile Testing*					
Orien.	**Temp. (°C)**	**Environ-ment**	**Load (*MPa*)**	**Duration (*hrs*)**	**T_{min} (°C)**	**T_{max} (°C)**	**Norm. Mech. Strain Range, $\Delta\varepsilon_{mech}$ (%)**	**Norm. Plastic Strain Range, $\Delta\varepsilon_{mech}$ (%)**	**Norm. Cycles to Crack Initiation, N_i**	**Figure**
L		*No Pre-Exposure*			500	950	1.26	0.131	279	6-22
L		*No Pre-Exposure*			100	950	1.26	0.385	81	6-21, 7-9, 7-10
L	950	Air	112.5	144	100	950	1.26	0.425	70	7-9, 7-10
L	950	Air	-112.5	144	100	950	1.26	*Elec. fault buckled specimen*		7-9
L		*No Pre-Exposure*					Tensile Test			7-12, 7-15
T		*No Pre-Exposure*					Tensile Test			7-13, 7-15
L	950	Air	112.5	144			Tensile Test			7-12, 7-15
T	950	Air	112.5	144			Tensile Test			7-13, 7-15
L	950	Air	-112.5	144			Tensile Test			7-12, 7-15
T	950	Air	-112.5	144			Tensile Test			7-13, 7-15

Regardless of rafting orientation, a larger plastic strain range demonstrated the reduced fatigue resistance of the L-oriented material to OP TMF when compared with the virgin cuboidal microstructure. The majority of the increase in inelastic strain over the baseline temperature range was due to the higher elastic modulus at temperatures below 500°C. Interestingly, tensile tests demonstrated that material with rafts lying parallel to the stress axis had a higher yield strength than the virgin at low temperatures for both orientations. The opposite effect was seen when the γ' platelets were oriented parallel to the stress axis. Overall, the elastic modulus was not significantly affected by the microstructure morphology.

CHAPTER 8. OXIDATION GROWTH AND ANALYSIS

8.1 Background

Investigating high temperature oxidation can reveal the nature and kinetics of the oxidation process. Mechanistic studies usually involve careful examination of the reaction products' composition as well as the alloy substrate. Alloy oxidation is complex, as various compositional metals have different affinities for oxygen. Similar to other metals, the initial oxide layers forming on the surface of Ni-base superalloys can be protective, slowing the successive penetration of oxygen into the material. As the process continues, the growth of accumulated oxides follows the parabolic law (without the presence of stress), and elemental diffusion of oxidizing species through the scales becomes the rate-governing process [36]. Successively, the depth of oxide scale layers, as well as the response of microstructural elements, is a good indication of how susceptible the current state of the material is to environmentally-assisted crack initiation.

The extent to which material and crack surfaces are oxidized can be correlated to stress-free oxidation experiments. They can also be used to determine the combined effects of pre-exposure on the microstructure and oxidation behavior of the alloy. Previous studies conducted by Antolovich et al. [14], Gordon [2], and Reuchet et al. [85] characterized the effects of pre-exposure on the Ni-base superalloys Rene 80, DS GTD-111, and Mar-M 509, respectively, through high temperature LCF tests. It was demonstrated that by machining off the full thickness of the oxide layers and γ'-depleted zone prior to commencing fatigue tests, no reduction in life would occur. Similarly, the

cycles to crack initiation of tests conducted in a vacuum were comparable to that of a polished sample.

8.2 Stress-free Oxidation Testing

To study the effects of thermal exposure on CM247LC DS and its properties, small disks were cut from the shank portions of used fatigue specimens. These sections remained in the water-cooled grips during TMF testing, and thus were not exposed to the high testing temperature. The disks measured 12.7 *mm* in diameter with a thickness of 2.5 *mm*. Prior to exposure, each was polished up to 1200 grit to provide a level surface from which to measure the thickness of accrued oxide layers. They were then cleaned in acetone and arranged on a float made from rigid insulating foam, as shown in Figure 8-1. Each was then exposed to laboratory air at several temperatures and lengths of exposure.

A 3-zone Lindberg 240 *V* Model 59744-A electric-resistance tube furnace was used to provide heat. Temperature was monitored with a thermocouple to ensure the furnace was set appropriately to yield the desired metal temperature. Specimens were exposed to 850°C, 950°C, and 1050°C for various durations ranging from 2 *hrs* to 300 *hrs* in static laboratory air. Experiments monitored using a thermocouple to ensure the furnace maintained constant temperature throughout the test period. Individual specimens were removed from the float when the appropriate time had elapsed; they were then sectioned, mounted, and prepared for microscopy.

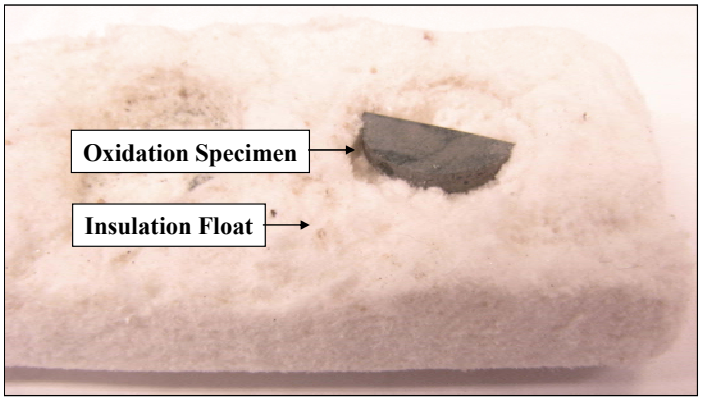

Figure 8-1: Oxidation specimen seated on insulation float.

8.3 Results

Three distinct layers could be observed in CM247LC DS which resulted from high temperature exposure. This is consistent with findings for other Ni-base superalloys [28, 86, 87]. The cross-sectional view of these layers is shown in Figure 8-2. The outer layer is a relatively uniform mixture of Ti- and Cr-rich scales, while the inner layer comprises significant Al and is a more heterogeneous with the base metal substrate [87]. These surface oxides are generally blocky and often non-uniform in thickness. Beneath these layers is the aforementioned γ'-depleted zone, devoid of strengthening precipitates which partitions the oxide layers from the substrate alloy. In Ni-base superalloys at room temperature, this zone was found to be more ductile and had a Vickers Hardness less than that of the base material [86].

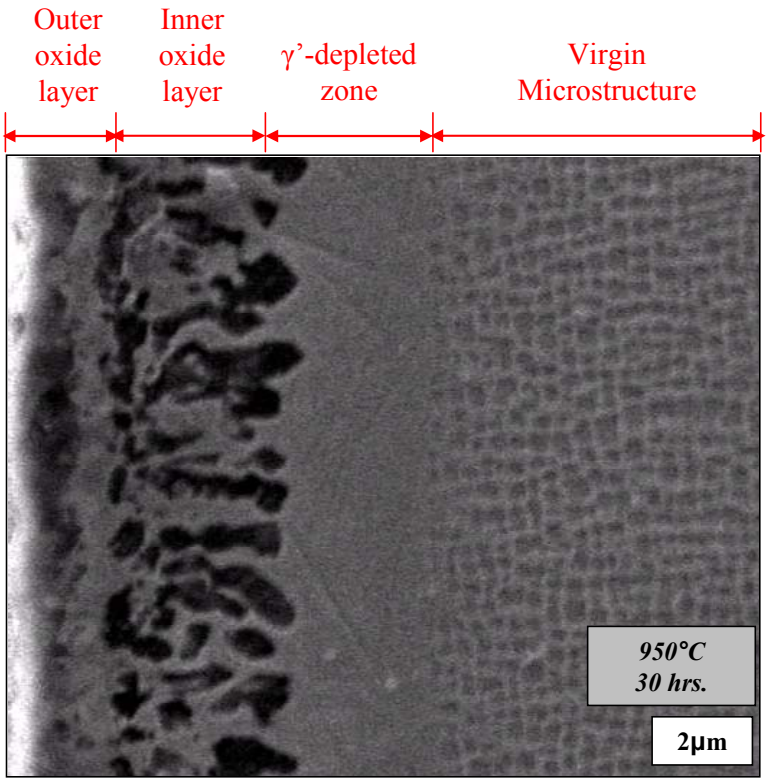

Figure 8-2: SEM image of surface oxidation in unstressed CM247LC DS as a result of exposure to 950°C for 30 *hrs*.

Previous work by Das et al. [87] on CM247LC DS showed that elemental oxygen penetrated as far as the γ' depleted layer but was not present in the base material. This source used X-ray diffraction to determine the composition of the various layers. The compositions reported in this work are summarized in Table 8-1, and were found to be comparable irrespective of the temperature or nature (cyclic or isothermal) of exposure. The outer layer was primarily composed of NiO and Spinel ($NiAl_2O_4$) and was shown to form first. The inner oxide layer consisted of a non-uniform layer of alumina oxide (Al_2O_3), which formed only after the diffusion processes provided a sufficient Al concentration. The structure of this layer gave the appearance of channel-like projections (dark in Figure 8-2) extending perpendicular away from the outer oxide layer interface

and into the surrounding γ matrix (light in Figure 8-2). These channels were usually no more than 1-2 *μm* in width and their length depended on the exposure duration.

Table 8-1: Composition of surface oxide layers in CM247LC DS exposed to laboratory air for 2-500 *hrs* for constant temperatures between 1000-1200°C [87].

PRIMARY COMPOSITION					
Virgin Material		Inner Oxide Layer		Outer Oxide Layer	
γ Matrix-	Al, B, C, Co, Cr, Hf, Mo, Ta, Ti, W, Zr, Ni	***Alumina-***	Al_2O_3	***Nickel Oxide-***	NiO
γ' precipitates-	Ni_3Al			***Spinel-***	$NiAl_2O_4$

An increase in temperature resulted in an increase in the relative rate of aluminum loss towards the outer oxide scales, increasing the thickness of the γ (γ'-free) layer. The same behavior also results from an increase in oxidation exposure [87].

Images of the oxidation behavior of CM247LC DS as a function of time spent at a constant temperature are shown in Figure 8-3 through Figure 8-5. After only 3 *hrs* of exposure, distinct layers of both the outer oxide and alumina have already formed. At 850°C, however, the development of the inner layer occurred at a significantly reduced rate. After 150 *hrs*, these layers have expanded and a sufficient amount of Al has diffused towards the surface to form an ample γ'-depleted zone. Subsequently, after 300 *hrs*, all the layers were expansive and the depleted zone had penetrated a further 63% of the total oxide thickness into the material.

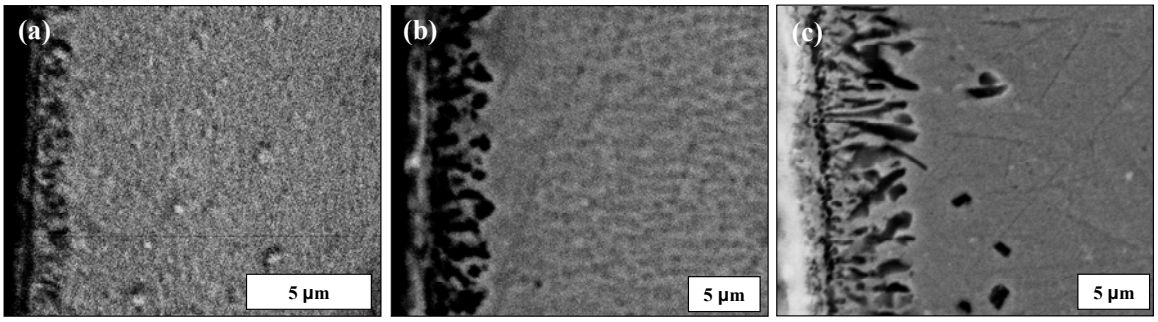

Figure 8-3: Stress-free oxidation of CM247LC DS exposed to 850°C and laboratory air for (a) 20 *hrs*, (b) 74 *hrs*, and (c) 210 *hrs*.

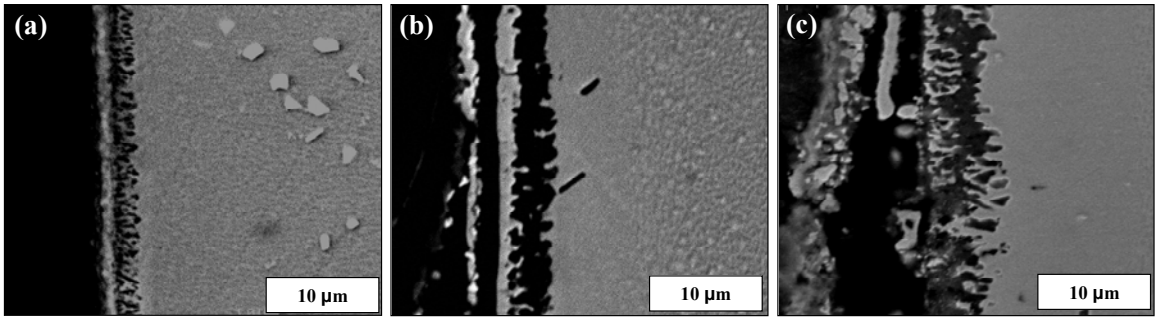

Figure 8-4: Stress-free oxidation of CM247LC DS exposed to 950°C and laboratory air for (a) 3 *hrs*, (b) 150 *hrs*, and (c) 300 *hrs*.

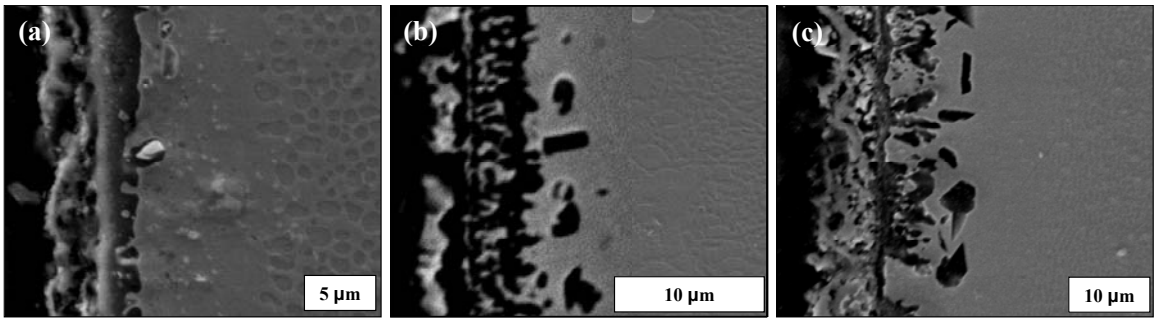

Figure 8-5: Stress-free oxidation of CM247LC DS exposed to 1050°C and laboratory air for (a) 3 *hrs*, (b) 200 *hrs*, and (c) 300 *hrs*.

Average depth measurements were recorded as measured from SEM micrographs. The values obtained from these experiments are listed in Table 8-2 and plotted in Figure 8-6. The depth of the γ'-depleted zone was defined as the total depth into the sample until the virgin microstructure was reached, including both oxide layers. As a result,

measurements for this layer always yield larger values than those for the cumulative oxide layers. Limited spallation of the outer oxide sometimes occurred for specimens at 1050°C upon cooling, indicating there were compressive residual stresses in the oxide layers. Therefore, depth measurements were made from locations where the sample retained its full-exposed thickness.

Table 8-2: Average oxidation and γ'-depletion measurements for CM247LC DS exposed to air

Temp. (°C)	Exposure Time, (*hrs*)	Cumulative Oxide Depth, (*μm*)	γ'-depleted Depth, (*μm*)
850	20	1.7	2
	74	4.95	5.875
	210	5.15	7.9
950	3	3.4	4.9
	30	5.5	7.9
	150	11.75	17
	300	17.6	28.75
1050	3	6.45	7.35
	30	9.1	13.5
	200	22	38
	300	30	41

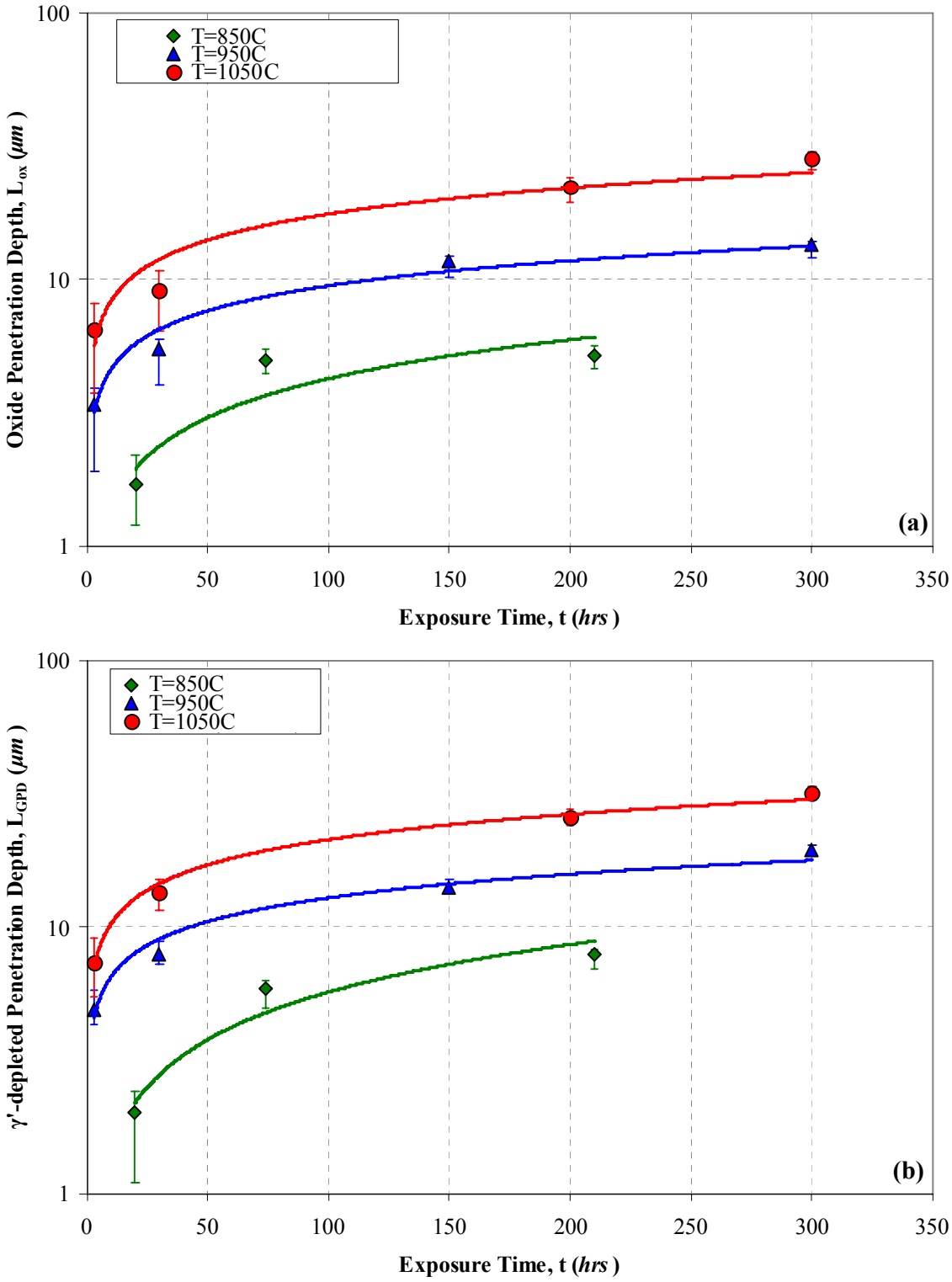

Figure 8-6: Depth of (a) cumulative oxide layers and (b) γ'-depletion in CM247LC DS.

8.4 Oxide Growth Kinetics

The thickness of the oxides and γ'-depleted zone as a function of exposure time and temperature yielded information such as the rate of formation and physical kinetics behind the thermodynamic process. This information can then be captured within an analytical model as a good approximation of surface layer depths developed by high temperature exposure of components.

As the oxidation accumulation follows a parabolic trend, it can be described as

$$h_{OX} = \alpha_{OX}\Theta_{OX}(T)t^{m_{OX}} \tag{8.1}$$

where the diffusivity, Θ_{OX}, is related to the activation energy of the oxidation process, Q_{OX}, and the temperature, *T*, by the Arrhenius form

$$\Theta_{OX} = D_{OX}\exp\left(\frac{-Q_{OX}}{RT}\right) \tag{8.2}$$

where D_{OX} is a material property, *R* is the universal gas constant (8.314 *J/mol-K*), and *T* is the material temperature in Kelvin.

The growth of the γ' depleted zone can be described similar to Equation (8.1) as

$$h_{\gamma'} = \alpha_{\gamma'}\Theta_{\gamma'}(T)t^{m_{\gamma'}} \tag{8.3}$$

and thus a similar expression follows for $\Theta_{\gamma'}$, i.e.

$$\Theta_{\gamma'} = D_{\gamma'} \exp\left(\frac{-Q_{\gamma'}}{RT}\right) \tag{8.4}$$

The activation energies Q_{OX} and $Q_{\gamma'}$ can be found by plotting the normalized rate term for accumulation of the oxide layer, $h_{OX}/t^{m_{OX}}$, and depleted zone, $h_{\gamma'} = t^{m_{\gamma'}}$, versus the inverse temperature. The exponents m_{ox} and $m_{\gamma'}$ were obtained through the best-fit two-parameter power laws using (8.1) and (8.3).

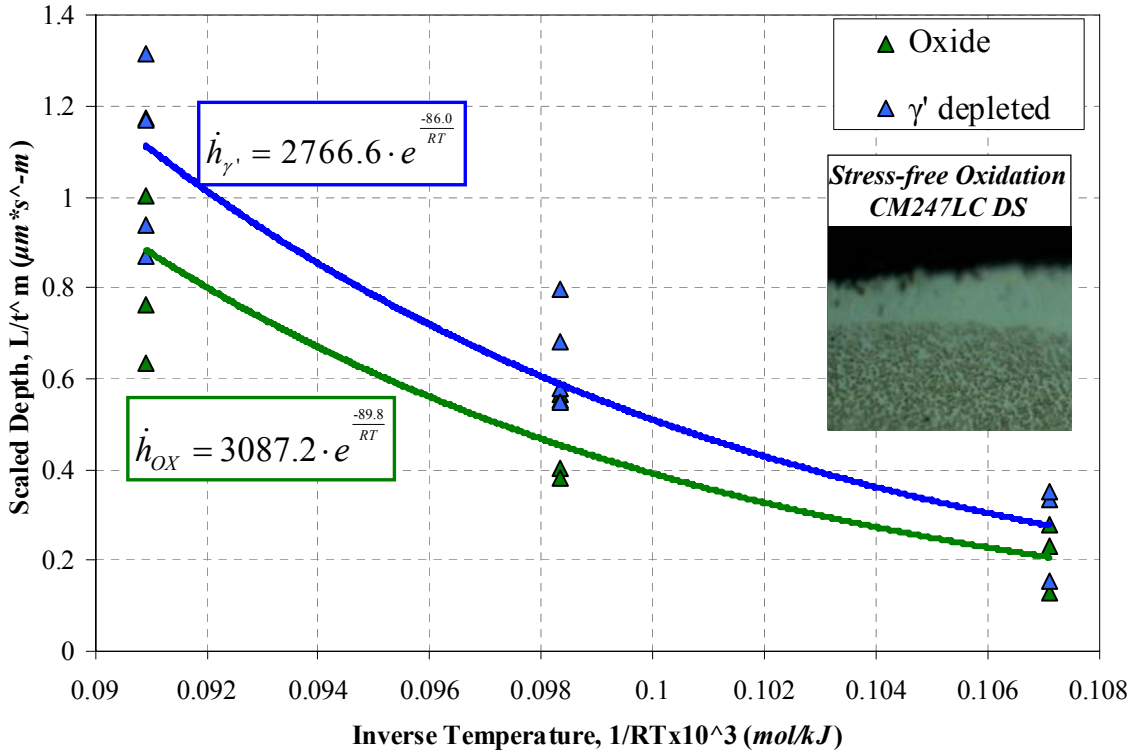

Figure 8-7: Regression of oxidation ingression and γ' depletion in CM247LC DS as a function of temperature for between 2 and 300 *hrs* at 850°C, 950°C, and 1050°C.

For the purpose of units, the constants α_{OX} and $\alpha_{\gamma'}$ were defined as 1 μm. Regression fits interpolated using (8.2) and (8.4) then allowed the appropriate constants to be determined, as shown in Figure 8-7. Studies on other Ni-base superalloys yielded similar activation energies and constants, as presented in Table 8-3.

Table 8-3: Oxidation constants obtained for CM247LC DS compared with MAR-M247 [9], DS GTD-111 [29], and Rene 80 [14].

Alloy	$\mathbf{Q_{OX}}$ ***(kJ/mol)***	$\mathbf{m_{OX}}$
CM247LC DS	89.8	0.23
MAR-M247	175.9	0.5
DS GTD-111	77.9	0.24
Rene 80	40.2	0.5

Correlations between model predictions and experimentally-measured depths are shown in Figure 8-8. All points lie within a factor of two of those predicted, indicating a strong association between the model physics and the kinetics of the oxidation process.

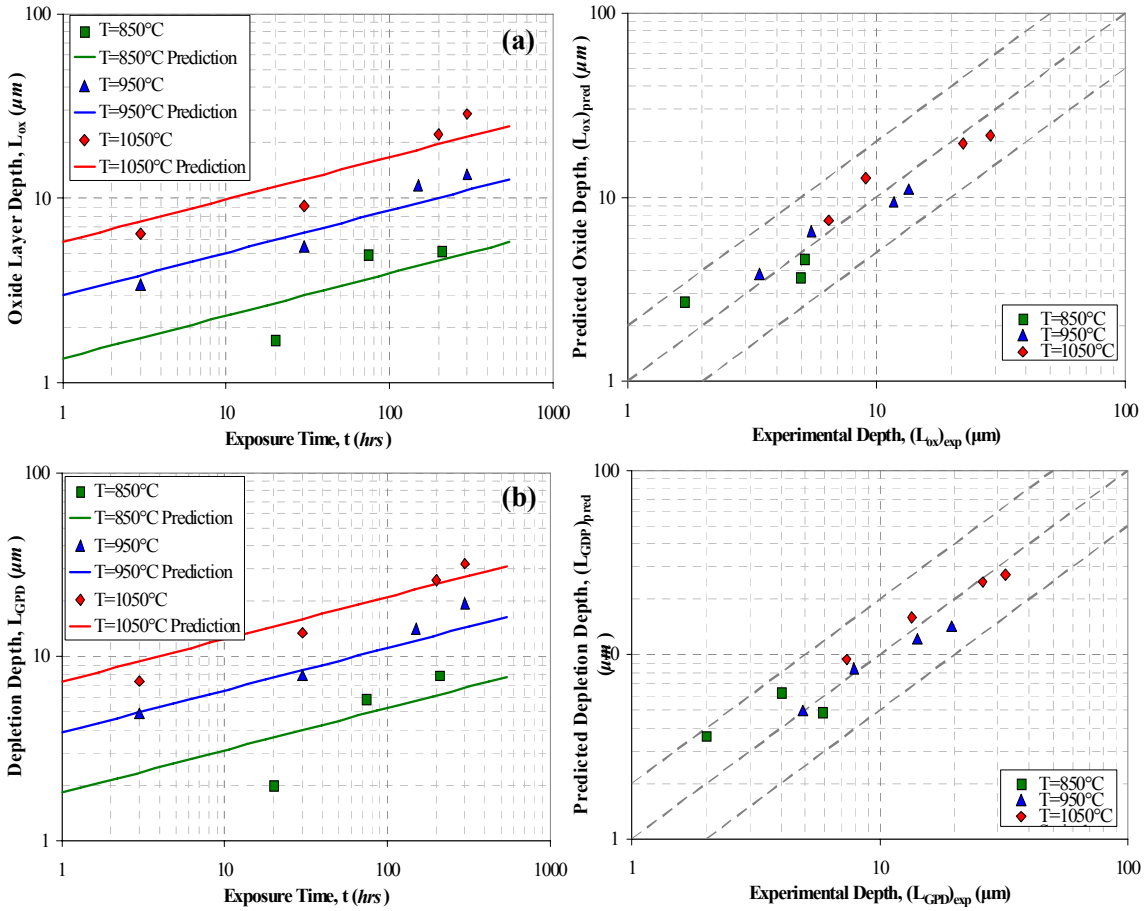

Figure 8-8: Correlations between model predictions and experimental measurements of (a) oxide layer and (b) depletion zone growth in CM247LC DS for durations between 3 and 300 *hrs* at 850°C, 950°C, and 1050°C.

8.5 Stress-Assisted Oxidation

As seen in the previous sections, oxidation ingression into advancing cracks also results in the degradation of those exposed surfaces. The comparatively slower strain rates of TMF experiments with 180 *s* cycle times result in prolonged exposure of virgin material behind the crack tip to the environment. Additionally, load variations between tests have the effect of increasing or decreasing the stress intensity at each crack tip, thereby altering the exposure time of susceptible surfaces.

The oxide layer at the crack tip was found to be considerably thicker for IP tests, as illustrated in Figure 8-9. This is because the layers crack more frequently in OP experiments. In addition, decreasing the applied mechanical strain or stress amplitude lengthens the test and the corresponding time of exposure, also leading to an increase in thickness. Similar observations were observed for tests involving isothermal fatigue, creep-fatigue, and TMF of DS GTD-111.

The cracks in notched tests (Figure 8-9(c) and Figure 8-9(d)) also seem to boost the level of accrued oxidation. This is likely due to the extremely slow propagation of cracks extending into the net section away from the notch stress concentration. This behavior is evidenced by the prevalence of completely circumferential cracking in notched specimens and measured crack growth at notches from other sources [15]. Although cracks form quickly in the region of the notch itself, the lower stress profile in the net section (Figure 6-43) reduces the stress intensity at the tip, and therefore, the rate of growth. This process results in an increase in cycles to failure and the corresponding degree of oxidation.

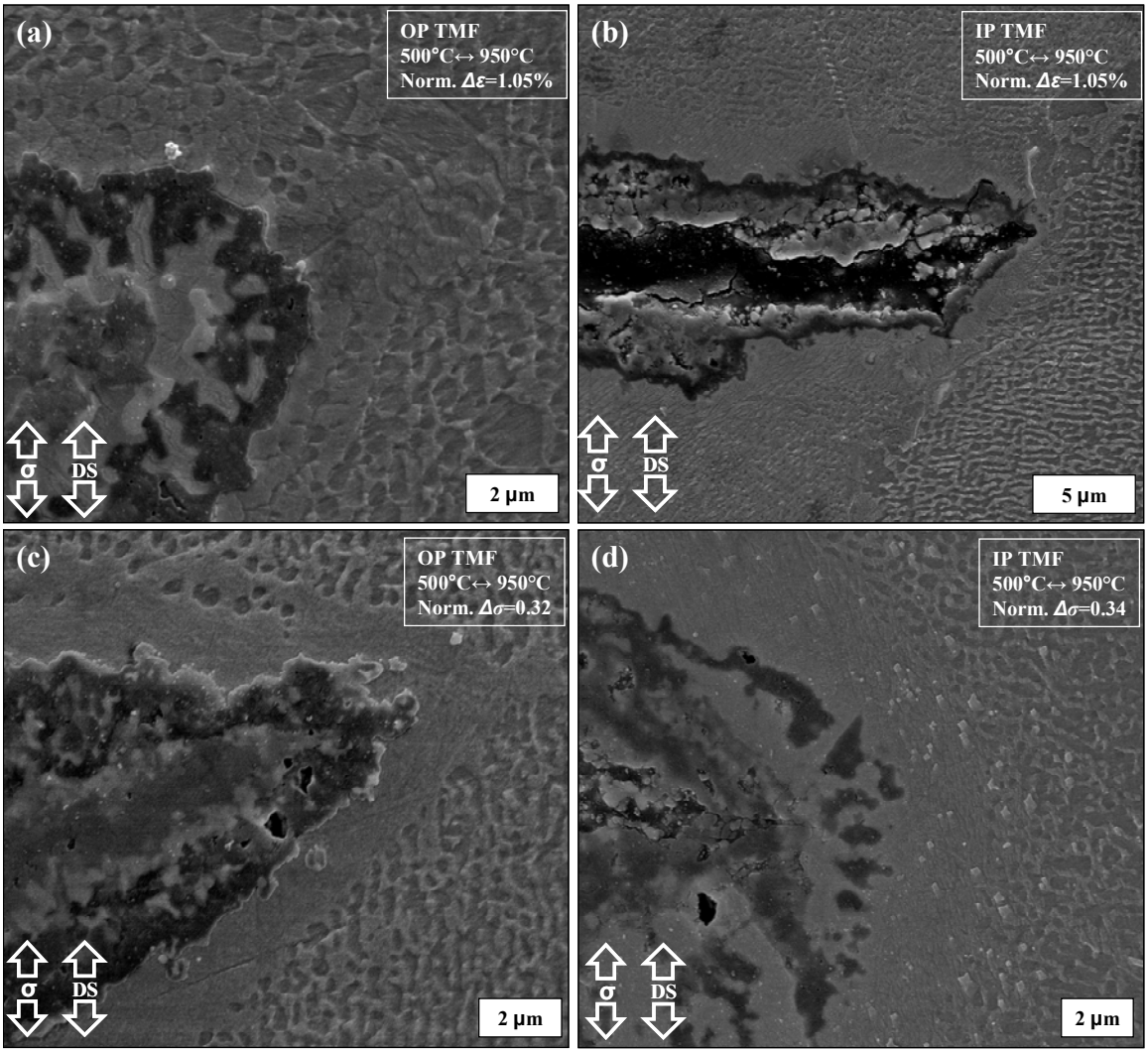

Figure 8-9: Crack tip oxidation for longitudinal (a) OP and (b) IP smooth specimens in mechanical strain control and (c) OP and (d) IP notched tests conducted in force control.

Some evidence of preferential oxidation of grain boundaries and the interdendritic region was observed due to the slow growth of cracks out of the highly stressed region in longitudinal notched tests. Several examples are shown in Figure 8-10. Transverse tests resulted in primarily intergranular cracking, and as a result this behavior was more difficult to distinguish. Clearly, only for cracks large enough to have traversed such features could exhibit any degree of preferential oxidation.

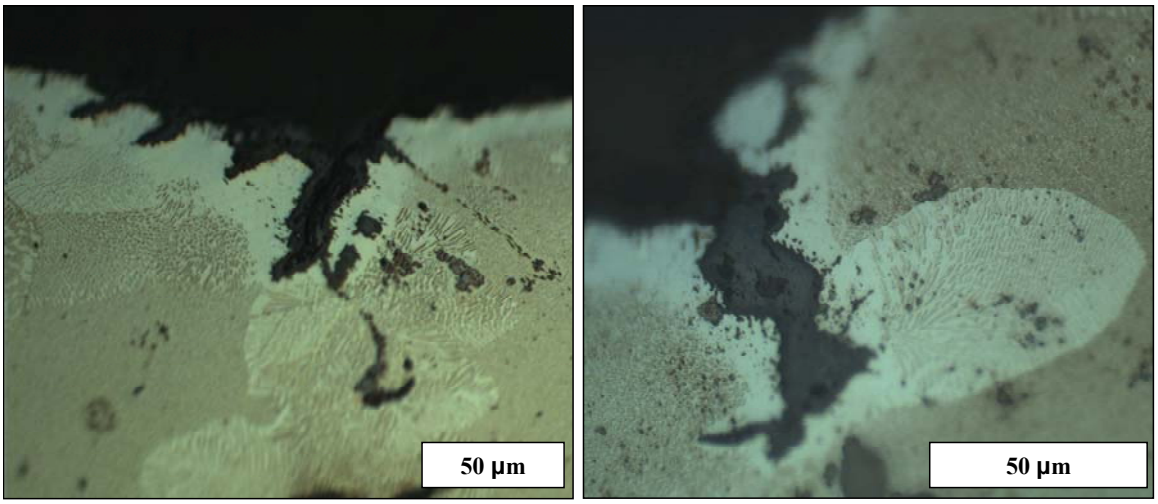

Figure 8-10: Examples of preferential oxidation of the interdendritic region in a longitudinal in-phase test. For this case, k_t=2, $\Delta\sigma$ =600 *MPa*, and T=500°C↔950°C.

CHAPTER 9. LIFE MODELING

Modeling efforts have focused on a variety of approaches to determine which best characterizes the multitude of conditions explored through experimentation. Although not the emphasis of this work, modeling helps to portray the sensitivity of CM247LC DS to various conditions which influence life. The ability of simple damage parameters and physics-based methods to capture a wide range of these conditions allows them to be used at various stages in the design process. Some observations, such as the effect of a rafted γ-γ' microstructure, were beyond the resources and scope of this research to fully account for explicitly in the modeling presented here.

Accurate life prediction needs to account for a multitude of interwoven mechanisms. The phasing of the thermal and mechanical loads must be reflected in modeling, as both in-phase and out-of phase tests have a significant impact on how life-limiting damage evolves. Characteristics such as the minimum and maximum temperatures and the evolution of a mean stress also play a significant role in which mechanisms are active and dominant for a set of conditions. Additionally, the consequences of microstructure characteristics and stress concentrations need to be taken into account. Capturing all these influences within the framework of a single model, however, is complex and often very computationally expensive. As a result, instead of focusing on a single model, this Chapter presents several methods which have traditionally been used to predict life. First, simple damage function correlations can aid in preliminary design work and require only a rough estimation of operating conditions.

Second, more physically-complex models can account for the individual contributions and severity of the fatigue, creep, and environmental damage mechanisms. Finally, predictive notch analysis tools which utilize finite element simulations are investigated.

9.1 Smooth Specimen Life Prediction

9.1.1 Background

General models for uniaxial, strain-controlled TMF life prediction are primarily based on the fundamental mechanisms of crack initiation and propagation. Although no generally-accepted TMF fatigue life prediction methodologies exist, the dominant damage mechanisms operating under this type of loading (fatigue, oxidation, and creep damage) have been generally recognized. A strong correlation with a few key design variables can provide critical insight into which factors govern life, and does not require exhaustive testing or coupling experiments with visco-plastic models. Under conditions where these correlations break down, more complex mechanistic models are often required. Several methods are explored to categorize their capabilities with respect to the range of conditions tested.

9.1.2 Damage Function Correlations

Most low cycle fatigue predictive techniques for high temperature applications have been derived from the well-known Coffin-Manson Equation [88]:

$$\Delta\varepsilon_p N_f^{\beta} = C \tag{9.1}$$

where $\Delta\varepsilon_p$ is the plastic strain range, N_f is the number of cycles to specimen failure, and β and C are material constants. This relation provides a good prediction for fatigue life on a wide range of metals, and requires only the plastic strain range to parameterize damage.

The Ostergren model [89] is based on energy during the TMF cycle and is given by

$$C = N_f^{\beta}\Delta\varepsilon_p\sigma_{\max} \tag{9.2}$$

where C and β are material constants, N_f is the number of cycles to failure, and $\Delta\varepsilon_p$ and $\sigma_{\max}$ are the plastic strain range and maximum stress in the half cycle, respectively. For Ni-base superalloys, where the plastic strain component is often negligible, the mechanical strain can also be used, yielding

$$C = N_f^{\beta}\Delta\varepsilon_{mech}\sigma_{\max} \tag{9.3}$$

The inclusion of $\sigma_{\max}$ allows the damage function to account for the effects of a mean stress important to the LCF behavior of cast Ni-base superalloys. It is also based on the assumption that low cycle fatigue is essentially a problem of crack propagation, and thus only the tensile deformation when the crack is open is damaging [89].

As an exercise, isothermal LCF data for CM247LC DS at the T_{max} of 950°C was used to predict TMF life using this empirical relationship. Due to the difference in driving force for crack initiation between longitudinal and transverse orientations, a separate fit was used for each. The Ostergren energy ($\Delta\varepsilon_p \sigma_{\max}$ or $\Delta\varepsilon_{mech} \sigma_{\max}$) is plotted as a function of cycles to crack initiation for the smooth specimen TMF results in Figure 9-1. For high Ostergren energy values correlated with isothermal data, OP TMF in both orientations is relatively well predicted. This included cases where T_{min}=100°C, in which significant plasticity occurred at both peaks of the cycle. Additionally, if the result of γ' precipitate rafting manifests primarily as an increase in inelastic strain range, the Ostergren parameter may be a useful tool in the early stages of design for giving a rough estimate of component degradation due to service.

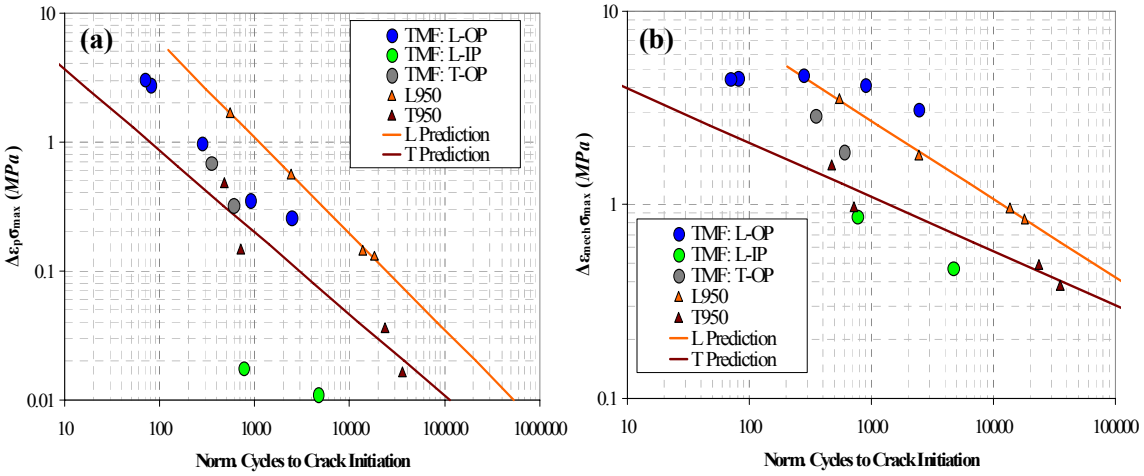

Figure 9-1: Relationship between life and the Ostergren parameter using (a) the plastic strain range and (b) the mechanical strain range for isothermal LCF and TMF of CM247LC DS.

IP TMF, however, is woefully over-predicted. Although the fatigue life results presented earlier in Figure 6-1 show a relatively small difference in life between IP and

OP TMF over the range tested, the Ostergren damage parameter does not effectively describe all the damage occurring in TMF experiments for this range. In particular, the measured plastic strain of IP tests was significantly smaller than that of OP for the same loading and temperature range.

The correlations of TMF life based on the isothermal calibration of the Ostergren parameter and the actual experimental life are shown in Figure 9-2. Although it captures the mean stress important to fatigue, the maximum stress used in the Ostergren model does not account for the phasing of the test. Therefore, for tests where fatigue is not the dominant mechanism, the Ostergren model is not suitable for predicting TMF life of CM247LC DS based on isothermal data at the maximum temperature. Similar conclusions were drawn for the Ni-base superalloy M963 by Huang et al. [4].

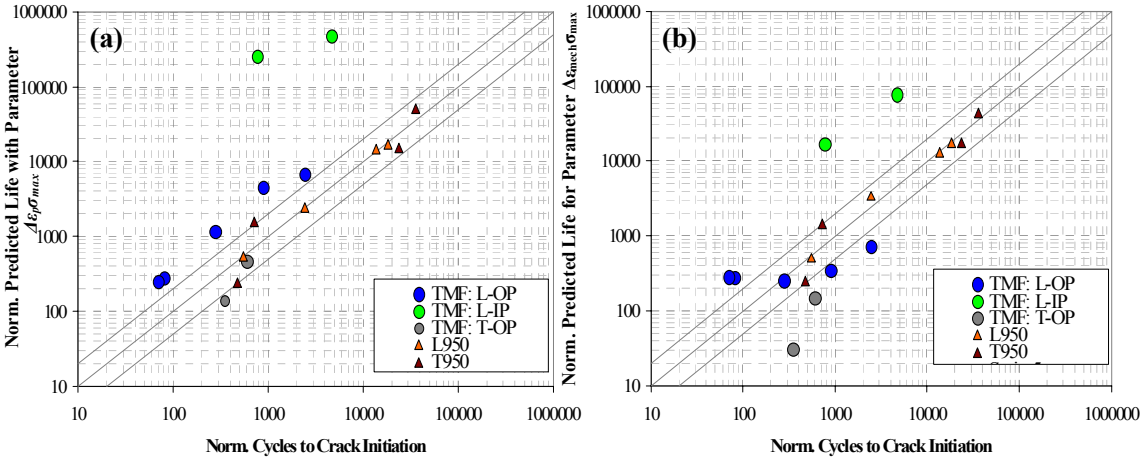

Figure 9-2: Predicted life with the Ostergren parameter correlated to isothermal LCF data at 950°C using (a) the plastic strain range and (b) the mechanical strain range versus cycles to crack initiation for isothermal LCF and TMF of CM247LC DS.

The Ostergren model was further modified for OP by Zamrik and Renauld [90] by relating the maximum tensile stresses and strains of mid-life hysteresis to the ultimate

strength and elongation to failure measured from a monotonic tensile test and the minimum temperature of the OP cycle. The equation is given as

$$N_i = A(\Delta W)^B \tag{9.4}$$

where A and B are the material constants. The new energy term, ΔW is expressed as

$$\Delta W = \frac{\sigma_{\max}\varepsilon_{ten}}{\sigma_u \varepsilon_f} \tag{9.5}$$

where $\sigma_{\max}$ and ε_{ten} are the maximum tensile stress and strain ranges of the midlife hysteresis loop, respectively, and σ_u and ε_f are the ultimate strength and elongation to failure measured under monotonic tensile loading at the minimum temperature of the OP TMF cycle.

Isothermal test data at 950°C was used to determine the constants A and B for cases where T_{min}=100°C and 500°C using values of σ_u and ε_f obtained from the literature [5]. The correlated energy function and predicted cycles to crack initiation are shown in Figure 9-3.

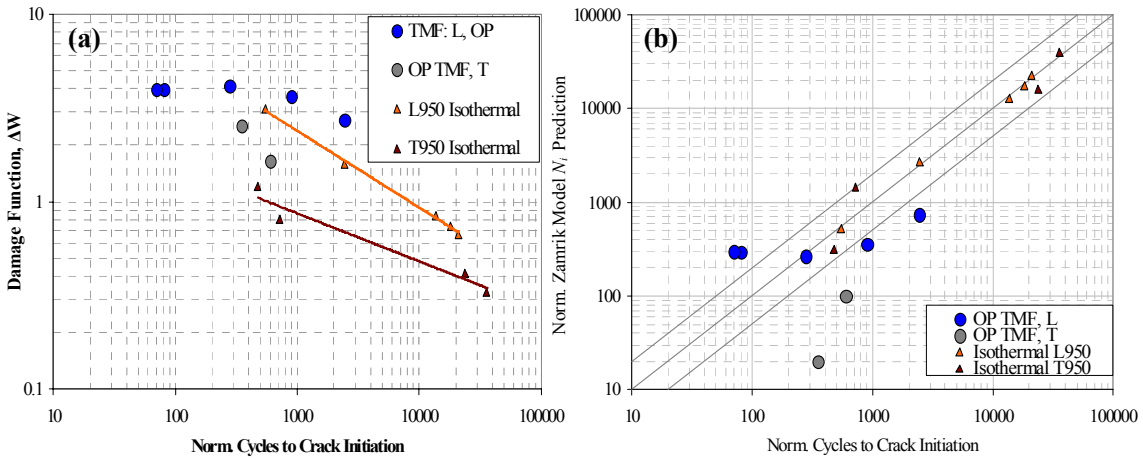

Figure 9-3: Correlation between life and (a) the Zamrik parameter and (b) the cycles to crack initiation predicted by the Zamrik model for isothermal LCF and OP TMF of CM247LC DS.

Only one TMF point is within a factor of two if the unit correlation line, indicating this model has no better capability of estimating OP TMF life than the Ostergren parameter. Additionally, a poor fit of the transverse data indicates that using transverse material properties at T_{min} may be insufficient to fully model the material anisotropy.

In general, these models are only effective over a limited range of stress and strain values. Based off of isothermal LCF data, they do not explicitly model the physics of the different damage mechanisms occurring during TMF. As such, they cannot weight a particular mode which may be dominant. The correlations achieved with these models show that a more comprehensive approach is required to account for damage occurring during TMF of CM247LC DS.

9.1.3 Linear Accumulation Damage Models

A general high temperature damage accumulation model for TMF was developed by Neu and Sehitoglu [91-93]. The model incorporated terms associated with the individual cyclic damage mechanisms of fatigue, environment (oxidation), and creep processes and summed them to obtain a composite damage per cycle, similar to Miner's Rule. Assuming that the damage summation equals one at the failure life, N_f, this can be expressed as

$$\frac{1}{N_f} = \frac{1}{N_f^{fat}} + \frac{1}{N_f^{ox}} + \frac{1}{N_f^{creep}} \tag{9.6}$$

The terms are based on the physics characterizing each damage mechanism individually. Regimes for which each damage component is known to be dominant are used to characterize and calibrate them to the response of CM247LC DS.

Fatigue Module

The fatigue damage term, N_f^{fat}, represents the nominal cyclic damage from fatigue mechanisms. The formulation is similar to the strain-life representation, where

$$\frac{\Delta\varepsilon_{mech}}{2} = C(2N_f^{fat})^d \tag{9.7}$$

in which $\Delta\varepsilon_{mech}$ is the mechanical strain range, and C and d are material constants determined experimentally from isothermal tests.

This model was further refined by Gordon et al. [2] to reflect the effect of orientation on the evolution of TMF damage in DS GTD-111. The LCF damage term defined in (2.1) was expanded to become

$$N_i^{fat} = C_{in} f_{in}(\omega)(\Delta\varepsilon_{in})^{d_{in}} \tag{9.8}$$

where C_{in} and d_{in} were constants determined from fits of longitudinally oriented (ω=0) isothermal fatigue tests, and $\Delta\varepsilon_{in}$ was obtained from corresponding numerical FE simulations. The orientation-dependence was captured using the shape function, $f_{in}(\omega)$, which was fit to results of both L and T-oriented specimens.

The uniaxial fatigue term was determined for unnotched CM247LC DS using isothermal LCF data from tests conducted at 500°C and relatively high strain rates (i.e. ≥0.1%/s) for which little or no creep or oxidation would occur. The use of this data set ensured fatigue damage was isolated. To account for the anisotropy of the material resistance, both longitudinal and transverse data was utilized. This allows the fatigue term to capture the tendency of cracks to initiate along weak planes in the microstructure, such as grain boundaries or interdendritic channels.

The temperature-dependent orientation function, $f(\omega,T)$, is determined using uniaxial data in different orientations. As Figure 3-15 demonstrates that orientation has little influence on the slope of the strain life curves, f can be a scalar. A sixth-order

polynomial is used which is referenced with respect to the L orientation (i.e. 0° is longitudinal and 90° is transverse), where

$$f(\omega,T) = f_6(T)\omega^6 + f_5(T)\omega^5 + f_4(T)\omega^4 + f_3(T)\omega^3 + f_2(T)\omega^2 + 1 \qquad (9.9)$$

where ω is in radians and T is in ° C. Figure 9-4 shows $f(\omega, 500^o C)$ used in the current analysis as determined by Moore [17]

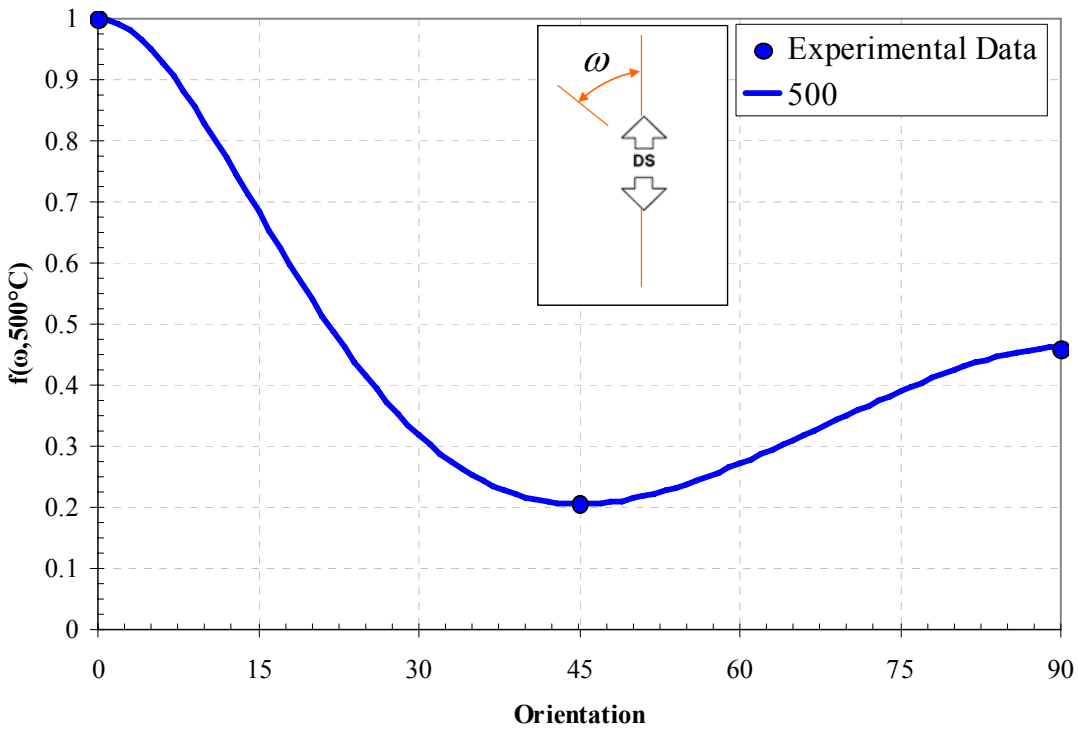

Figure 9-4: $f(\omega, 500^o C)$ for CM247LC DS compiled using experimental data [17].

The model predicts that the case where $\omega = \pi / 4$ (45°) will result in the least number of cycles to crack initiation. This is similar to results obtained in off-axis fatigue

testing of CM247LC DS by Erickson [48], as shown in Figure 3-15, and also that for the DS Ni-base superalloy Mar-M247LC by Hasabe et al. [94].

Crack initiation lives based solely on Equation (9.8) for smooth specimens in both orientations are compared with experimental results in Figure 9-5. The fatigue module yields good results for OP and IP TMF in situations where the crack initiation life is below 1000 cycles. The significant increase in the inelastic strain range which resulted from either reducing T_{min} or tensile-rafting the microstructure is fit well by this term. The crack initiation lives predicted by the fatigue module for these two tests were better than those of the plastic-strain based Ostergren parameter, indicating that the phasing of the TMF cycle (which strongly influences the σ_{max} term in the Ostergren model) is better accounted for under fatigue-dominant conditions. Similarly, a good correlation with the lower-life IP test indicates although creep damage is active for this test, as was seen in both Figure 6-7 and Figure 6-23, fatigue is the dominant mechanism. The relatively strong correlation with $\Delta\varepsilon_{pl}$ indicates low-cycle fatigue played an important role in most of the tests in this study. At longer lives, where $\Delta\varepsilon_{pl}$ is typically very small compared to $\Delta\varepsilon_{mech}$, other damage mechanisms are likely active and thus other terms need to be added for a better correlation with the N_i obtained experimentally.

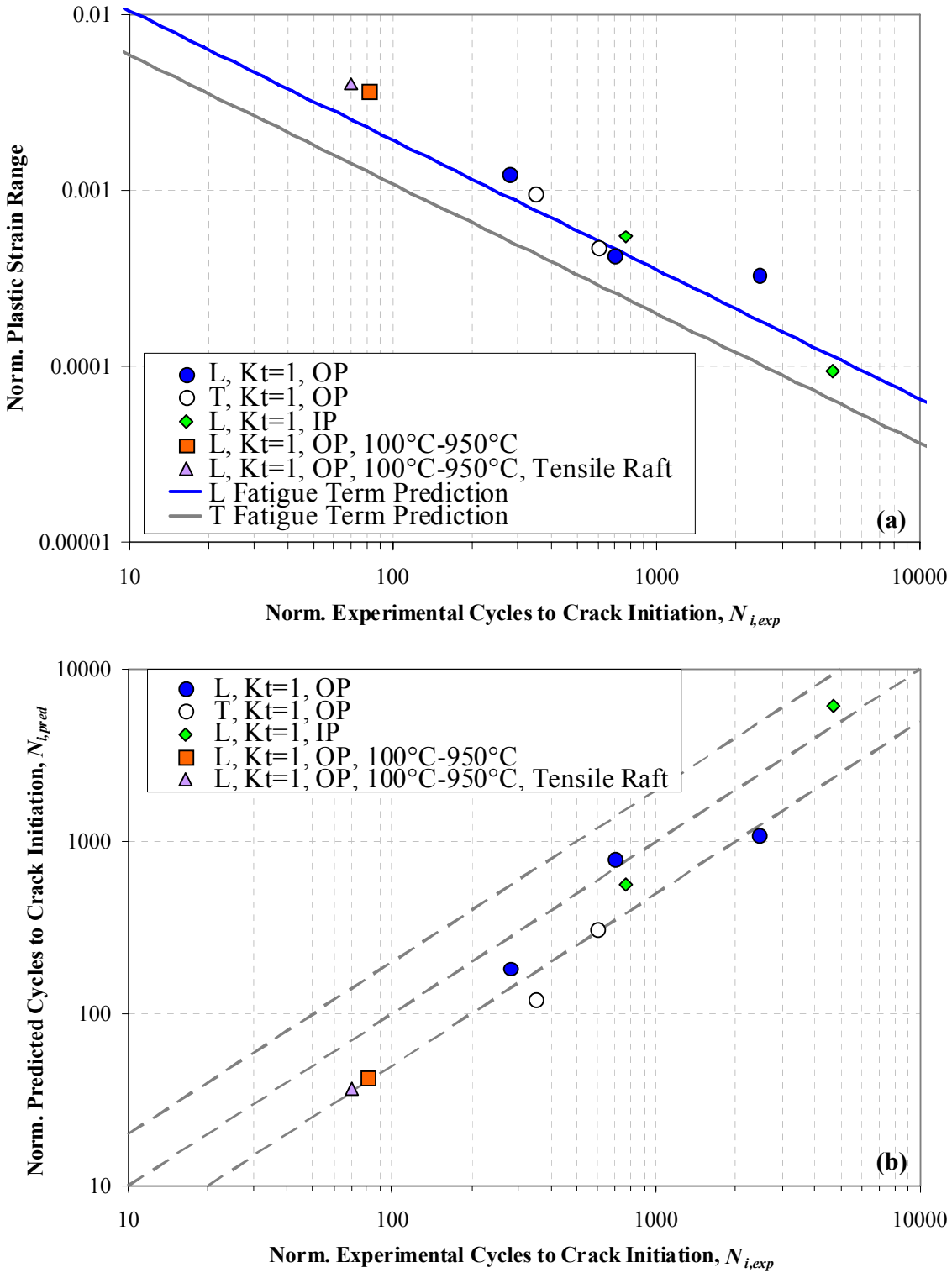

Figure 9-5: (a) Fit based on isothermal plastic strain range and (b) predictions of crack initation life for the uniaxial fatigue damage module as compared to smooth specimen experimental test results on L- and T- oriented CM247LC DS.

Creep Module

The creep damage term used by Neu and Sehitoglu [92] is a function of resolved effective and hydrostatic stresses, as well as temperature. It is expressed as

$$\frac{1}{N_i^{creep}} = \Phi^{creep} \int_0^t A e^{(-\Delta H / RT(t))} \left(\frac{\alpha_1 \bar{\sigma} + 2\alpha_2 \sigma_H}{K} \right)^m dt \tag{9.10}$$

where $\bar{\sigma}$ is the effective stress, σ_H is the hydrostatic stress, K is the drag stress, and α_1 and α_2 are factors that scale the expression to relate the relative damage occurring in tension and compression. In addition, ΔH is the activation energy for rate-controlled creep, A and m are material constants and Φ^{creep} is the time-dependent creep contribution due to phasing.

The creep term used by Gordon [2] updated the expression in Equation (9.10) utilizing some creep-rupture work conducted by Ibanez [95] for DS GTD-111. Based on the power law relationship between the Larson-Miller Parameter and stress, the modified term is given as

$$\frac{1}{N_i^{creep}} = \frac{t_{ht}}{\Theta_{creep}} \exp\left(\frac{-B'_L f_{cr} (\sigma_{tens})^{-k_L}}{RT} \right) \tag{9.11}$$

where the terms Θ_{creep}, B'_L, and k_L are determined from creep deformation and rupture experiments and the orientation function, f_{cr}, is derived from experiments comparing the

L and T orientations. In this case, f_{cr} was normalized to 1 for L-oriented ($\omega=0$) tests and equated to 0.97 for the T orientation ($\omega=\pi/2$). The term t_{ht} is used to define a tensile hold time for creep-fatigue experiments.

For CM247LC DS, the Larson-Miller parameter at rupture was determined using Equation (2.2) for creep deformation experiments provided by the sponsor and obtained from the literature [12, 96]. These were conduced in accordance with the ASTM standard E139-96. The LMP can be fit with a power law relationship with the applied stress from each creep-rupture experiment, yielding

$$\frac{T(\log t_r + C)}{1000} = B(\sigma_{tens})^{-k} \tag{9.12}$$

where the term on the left represents the expanded Larson-Miller parameter and B and k are constants determined through a regression fit of the experimental data. These constants are orientation dependent, but lack of off-axis creep data for CM247LC DS limited the orientation function, f_{cr}, to that defined by Gordon [2] using work by Ibanez [95] on DS GTD-111.

By isolating the rupture life in Equation (9.12) and replacing 1000B with B'/R, the expression becomes

$$t_r = \Theta_{cr} \exp\left(\frac{-B' f_{cr}(\sigma_{tens})^{-k}}{RT}\right) \tag{9.13}$$

In this form, the diffusion constant, Θ_{cr}, is the only unknown. For isothermal conditions, an average value for each temperature was found by dividing the rupture times for each temperature set by the exponential expressions. Correlation between model-predicted rupture lives using (9.13) for CM247LC DS and the data from experiments is shown in Figure 9-6.

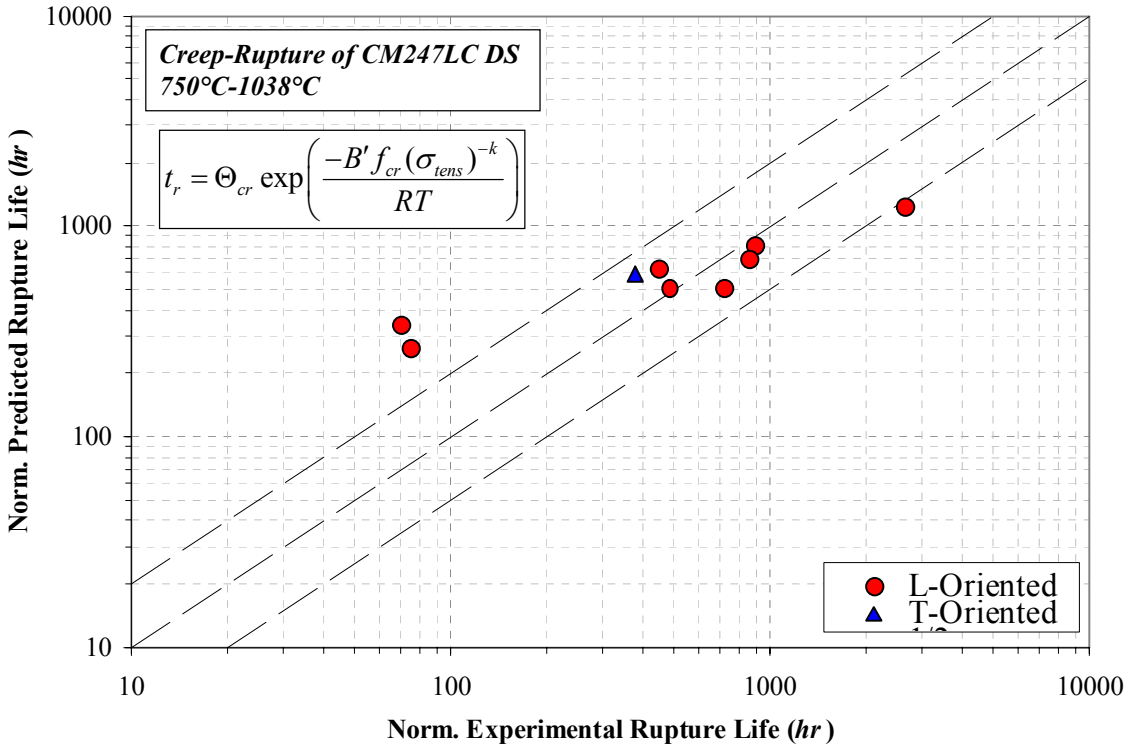

Figure 9-6: Comparison of creep-rupture experiments and creep module correlations for L- and T-oriented CM247LC DS under isothermal creep conditions between 750°C and 1038°C.

The model correlates the different data sets well, especially in the regime where rupture life was greater than 100 *hrs*. Approximately 67% of the data is within a factor of two of the predicted life.

To extend the model to TMF, the temperature-dependence of the diffusion coefficient is accounted for by integrating the Arrhenius form over the temperature waveform of the TMF cycle, i.e.,

$$\Theta_{cr}^{TMF} = \frac{1}{t_c}\int_0^{t_c} D_0 \exp\left(\frac{-Q}{RT(t)}\right)dt \tag{9.14}$$

where D_0 is a material property, t_c is the cycle time, R is the universal gas constant (8.314 *J/mol-K*), Q is the activation energy for rate-controlled creep, and *T(t)* is the instantaneous material temperature at time *t* in Kelvin which varies in time during the TMF cycle. This term averages the effect of tensile creep over the cycle, as there were no holds in the TMF experiments. The creep damage associated with TMF cycling can then be written as the ratio

$$D^{cr} = \frac{1}{N_i^{cr}} = \frac{t_c}{t_r} \tag{9.15}$$

Using this formulation, it is assumed the creep in compression is not damaging, which is consistent with observations of OP TMF tests from Chapter 6. Additionally, creep-fatigue experiments with compressive dwells conducted on DS GTD-111 revealed that at 982°C and -100 *MPa*, the longitudinal material did not reach the tertiary creep stage as at 100 *MPa* [95]. To compensate, the time-dependent term which accounts for phasing, Φ^{creep}, was introduced as

$$\Phi^{creep} = \frac{1}{t_c}\int_0^t \phi^{creep}\, dt \tag{9.16}$$

where

$$\phi^{creep} = \exp\left[-\frac{1}{2}\left(\frac{(\dot{\varepsilon}_{th}/\dot{\varepsilon}_{mech})-1}{\xi^{creep}}\right)^2\right]$$

Here, $\dot{\varepsilon}_{th}/\dot{\varepsilon}_{mech}$ is the ratio of thermal to mechanical strain rates, t_c is the cycle time, and the constant ξ^{creep} defines the sensitivity of the cyclic phasing to creep damage. Neu and Sehitoglu [92, 93] established that for isothermal fatigue, $\dot{\varepsilon}_{th}/\dot{\varepsilon}_{mech}$=0, for out-of-phase TMF $\dot{\varepsilon}_{th}/\dot{\varepsilon}_{mech}$=-1, and under in-phase TMF $\dot{\varepsilon}_{th}/\dot{\varepsilon}_{mech}$=1. Combining this term with Equation (9.13) and Equation (9.15) yields the expression

$$N_i^{cr} = \Theta_{cr}^{TMF} \exp\left(\frac{-B' f_{cr}(\sigma_{tens})^{-k}}{RT}\right)\Phi^{creep} \tag{9.17}$$

Active creep mechanisms can change depending on the conditions. Stress rupture experiments on CM247LC DS by Satyanarayana [96] showed that for low stresses at temperatures above 850°C, the primary operating creep mechanism was dislocation climb over the γ' precipitates. For higher stresses, some shearing of the precipitates was found. Microcracks initiate internally at carbide particles and the γ-γ' interface, as well as grain boundaries and pre-existing pores in the interdendritic regions. As the material constants

for the creep damage term was modeled off L- and T-oriented CM247LC DS subjected to pure creep-rupture conditions, the dependency of damage on the temperature and applied structural load for all active creep mechanisms (i.e. diffusion, dislocation climb, γ' shearing, etc.) is combined.

There are several limitations accorded with using this term to model the creep contribution to damage. If the load bearing capability had been checked at various instances throughout the creep-rupture experiments, it would have been possible to substitute the crack initiation life of the material under nominally creep conditions. As it stands, the term assumes a decoupling of creep damage from fatigue during the high temperature half-cycle, and cannot account for stress relaxation effects or a change in the material compliance under non-isothermal conditions. The latter effects are only accounted for in a more complex and time-intensive visco-plastic modeling of the material response.

Environment-Fatigue Module

The coupled environmental-fatigue damage prevalent in OP TMF is the most physically-complex of the damage modules. Chapter 6 demonstrates the this type of damage accrues in CM247LC DS when T_{max} was 950°C much the same way as in other Ni-base superalloys. As oxide spikes and the repeated rupture of oxides at the crack tip continually expose new material to oxygen ingression, the kinetics found in Chapter 8 must be applied in an iterative manner. A general model for this process per unit cycle uses the expression [9]

$$\frac{dh}{dN} = \frac{dh}{dt}\frac{dt}{dN} \tag{9.18}$$

where h is the depth of the oxide spike and dt/dN is the cycle time, t_c. After each repeated rupture, oxide and γ' depleted zone growth will follow the parabolic growth law, as expressed in Equation (2.3) and shown pictorially in Figure 9-7.

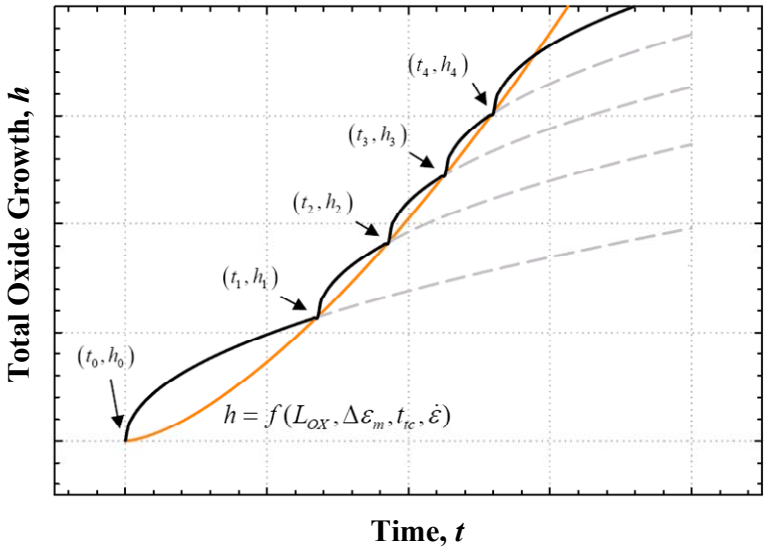

Figure 9-7: Pictorial representation of repeated oxide growth and rupture ahead of the crack tip under high temperature TMF conditions [2].

The oxidation term from the Neu-Sehitoglu model is based on the contribution of crack formation and growth in the oxide layer, and can be expressed by

$$\frac{1}{N_i^{ox}} = \left[\frac{h_{cr}\delta_0}{B\Phi^{ox}(K_{peff}^{ox} + K_{peff}^{\gamma'})}\right]^{\frac{-1}{\beta}} \frac{2(\Delta\varepsilon_{mech})^{(2/\beta)+1}}{\dot{\varepsilon}^{1-(\alpha/\beta)}} \tag{9.19}$$

where h_{cr} is the critical crack length at which damage from environmental attack trails behind the advance of the crack tip, δ_0 is the material ductility within the environmentally-affected zone, B is a coefficient, β is an exponent, and α is a constant representing the strain-rate sensitivity. All of these values are determined through experimentation.

The expression for the repeated rupture of the oxide spike tip, as depicted in Figure 9-7, involves the mechanical strain range, $\Delta\varepsilon_m$, and rate, $\dot{\varepsilon}$, was established in earlier studies [92, 93], i.e.,

$$\overline{h}_f = \frac{\delta_0}{(\Delta\varepsilon_{mech})^2 \Phi^{ox} \dot{\varepsilon}^b} \tag{9.20}$$

In order to account for the phasing of environmental damage with respect to the cycle, a phasing factor Φ^{ox} is used. This term is defined as

$$\Phi^{ox} = \frac{t}{t_c} \int_0^t \phi^{ox} dt \tag{9.21}$$

and

$$\phi^{ox} = \exp\left[-\frac{1}{2} \left(\frac{(\dot{\varepsilon}_{th} / \dot{\varepsilon}_{mech}) + 1}{\xi^{ox}} \right)^2 \right]$$

Here, ξ^{ox} is the relative magnitude of oxidation damage occurring for different thermal and mechanical strain ratios, as determined through experiments. Testing is also needed to express the ratio of the thermal to mechanical strain rates, $\dot{\varepsilon}_{th} / \dot{\varepsilon}_{mech}$. Again, this ratio is taken to be zero for isothermal conditions, -1 for OP TMF, and 1 for IP TMF. The oxidation and γ' depletion constants, K_{peff}^{ox} and $K_{peff}^{\gamma'}$, can be calculated by

$$K_{peff}^{ox} = \frac{1}{t_c}\int_0^{t_c} D_{ox} \exp\left(\frac{-Q_{ox}}{RT(t)}\right) dt \tag{9.22}$$

and

$$K_{peff}^{\gamma'} = \frac{1}{t_c}\int_0^{t_c} D_{\gamma'} \exp\left(\frac{-Q_{\gamma'}}{RT(t)}\right) dt \tag{9.23}$$

where the temperature, *T(t)*, is a function of time, t_c is the cycle period, *R* is the universal gas constant, and D_{ox} and $D_{\gamma'}$ are the diffusion coefficients for oxidation and γ' depletion. The activation energies governing the diffusion processes for oxidation and precipitate depletion are Q_{ox} and $Q_{\gamma'}$, respectively.

Gordon's environmental-fatigue damage module for damage induced through environmental exposure and oxidation was modeled by

$$\frac{1}{N_i^{env}} = B_{env}\left[f_{el}(\omega)\right]^{-1}\left[\frac{\Theta_{ox}\Phi_{cc}^{env}\dot{\varepsilon}^{\alpha-\beta}(\Delta\varepsilon_{mech})^{b+\beta}}{(h_{cr}-2h_{pre})(1+t_{hc}\delta'_{hc})}\right]^{\frac{1}{\beta}}\sqrt{\tau_{hc}t_{hc}+1} \tag{9.24}$$

where again $f_{el}(\omega)$ is the orientation function, Φ_{cc}^{env} is a term relating the thermomechanical phasing, Θ_{ox} models oxide diffusion into the surface, and h_{cr} and h_{pre} are constants defining the material surface condition. The thermomechanical phasing term from Equation (9.21) was used for Φ_{cc}^{env}. The terms t_{hc}, δ'_{hc}, and τ_{hc} are all used to model additional environmental damage from dwells at high temperature.

As the current work did not contain the proper experiments to characterize pre-exposure or dwells, Equation (9.19) was used to account for cyclic environmental damage. This module utilized and incorporated the oxidation kinetics found in Chapter 8. The constants K_{peff}^{ox} and $K_{peff}^{\gamma'}$ were found by integrating the expressions in Equations (8.2) and (8.4) over the cycle period, as shown in Equations (9.22) and (9.23). The value of h_{cr} was obtained from SEM observation of cracks in sectioned samples. The values for δ_0 and ξ^{ox} were taken as the values used by Boismier and Sehitoglu [9] for Mar-M247. The remaining constants were determined using an iterative solver.

Predictions for Total Crack Initiation Life

Predictions for the total crack initiation life for CM247LC DS were made by combining the three damage modules into one formulation, obtaining N_i through summation of active damage mechanisms using the expression introduced in Equation (9.6). In practice, experiments often show a dominant damage mechanism which governs the majority of fatigue life. In these cases, damage from one mechanism exceeds the contribution from others by an order of magnitude or more. Isolation of this mechanism led to the prediction for a dominant mechanism, i.e.,

$$\left.\frac{1}{N_i}\right|_{cum} \approx \max\left\{\frac{1}{N_i^{fat}}, \frac{1}{N_i^{cr}}, \frac{1}{N_i^{env}}\right\} \approx \left.\frac{1}{N_i}\right|_{dom} \tag{9.25}$$

In circumstances where there was a clearly dominant mechanism, predictions by both methods are approximately equivalent. In cases where damage contributions from fatigue and another mechanism were roughly equivalent, however, a linear damage summation model would tend towards a conservative prediction, as $2N_i|_{cum} \approx N_i|_{dom}$. However, the vast majority of smooth specimen experiments conducted in this work were strongly correlated to the inelastic strain range, as seen from the predictions of the isolated fatigue module in Figure 9-5. As such, this is expected to be the dominant driving force for crack initiation predicted by the cumulative model.

Examples of the effective damage formulation using the combined modules of the accumulation model are shown in Figure 9-8. The predicted damage mechanisms active in each were demonstrated through post-test metallographic analysis discussed earlier (Figure 6-6, Figure 6-14, and Figure 8-9 for the OP test and Figure 6-7 for the IP test).

- **Correlation with CM247LC DS OP TMF test:**

  ➢ Primarily fatigue and oxidation damage:

$$N_i^{fat} = C_{in} f_{in}(\omega)(\Delta\varepsilon_{in})^{d_{in}} \Rightarrow N_i^{fat} = 788$$

$$\frac{1}{N_i^{ox}} = \left[\frac{h_{cr}\delta_0}{B\Phi^{ox}(K_{peff}^{ox} + K_{peff}^{\gamma'})}\right]^{\frac{-1}{\beta}} \frac{2(\Delta\varepsilon_{mech})^{(2/\beta)+1}}{\dot{\varepsilon}^{1-(\alpha/\beta)}} \Rightarrow N_i^{ox} = 6501$$

  ➢ Terms as damage accumulation:

$$\frac{1}{N_i} = \frac{1}{N_i^{fat}} + \frac{1}{N_i^{ox}} \Rightarrow N_i = 702$$

  ➢ Terms as dominant damage mechanism:

$$\frac{1}{N_i} = \frac{1}{N_i^{fat}} \Rightarrow N_i = 788$$

(a)

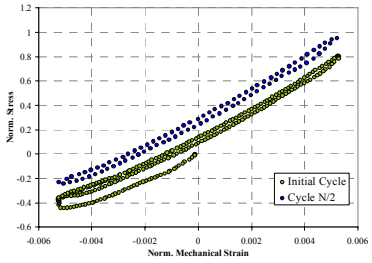

Test Details:

L, Out-of-Phase (OP)
k_t= 1
500°C ↔ 950°C
Norm. $\Delta\varepsilon_{mech}$= 1.05%
N_i= 700

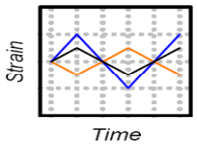

- **Correlation with CM247LC DS IP TMF test:**

  ➢ Primarily fatigue and creep damage:

$$N_i^{fat} = C_{in} f_{in}(\omega)(\Delta\varepsilon_{in})^{d_{in}} \Rightarrow N_i^{fat} = 6123$$

$$N_i^{cr} = \Theta_{cr}^{TMF} \exp\left(\frac{-B' f_{cr}(\sigma_{tens})^{-k}}{RT}\right)\Phi^{creep} \Rightarrow N_i^{cr} = 7763$$

  ➢ Terms as damage accumulation:

$$\frac{1}{N_i} = \frac{1}{N_i^{fat}} + \frac{1}{N_i^{cr}} \Rightarrow N_i = 3423$$

  ➢ Terms as dominant damage mechanism:

$$\frac{1}{N_i} = \frac{1}{N_i^{fat}} \Rightarrow N_i = 6123$$

(b)

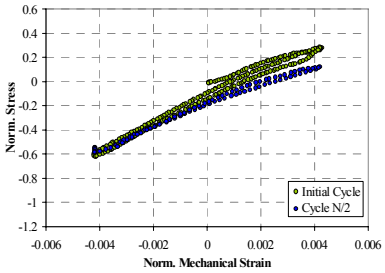

Test Details:

L, In-Phase (IP)
k_t= 1
500°C ↔ 950°C
Norm. $\Delta\varepsilon_{mech}$= 0.84%
Norm. N_i= 4698

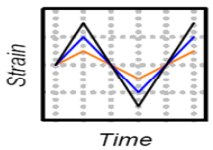

Figure 9-8: Representative results of linear damage accumulation model for smooth specimen TMF of CM247LC DS subjected to (a) OP and (b) IP cycling.

Predicted contributions of the different mechanisms to the crack initiation life of each smooth specimen TMF test based on the damage accumulation model are tabulated in Table 9-1. Correlations using the cumulative damage accumulation model for CM247LC DS subjected to OP and IP TMF are shown in Figure 9-9. Reasonable predicts are obtained for the lives of both L- and T-oriented specimens for the variety of conditions tested. For all phases, fatigue damage was dominant for the range of $\Delta\varepsilon_{mech}$ used. The contributions of oxidation and depletion of the γ' strengthening particles near the surface in OP increased with a decreasing mechanical strain range. Similarly, the amount of creep as a fraction of total damage for IP rose under the same conditions. Conservative predictions were obtained for all but one test point. For all strain ranges, the predicted fatigue lives of longitudinal samples were longer than those of transverse oriented CM247LC DS. In general, L-oriented data was closer to the line where $N_{i,exp}$=$N_{i,corr}$, indicating the model performs slightly better for the longitudinal material.

Table 9-1: Summary of contributions predicted by the damage accumulation model for smooth specimen TMF of CM247LC DS.

Test Parameters						***Damage Accumulation Model Predictions***					
Orien.	IP/OP	T_{min} (°C)	T_{max} (°C)	Norm. Mech. Strain Range, $\Delta\varepsilon_{mech}$ (%)	Exp. N_i	Predicted Fatigue Contribution, N_i^{fat}	Predicted Creep Contribution, N_i^{cr}	Predicted Oxidation Contribution, N_i^{ox}	Cumulative Damage Prediction, N_{icum}	Dominant Damage Prediction, $N_{i,dom}$	Dominant Mechanism
L	OP	500	950	1.26	279	183	∞	3435	174	183	Fatigue
L	OP	500	950	1.05	700	788	∞	6501	702	788	Fatigue
L	OP	500	950	0.84	2460	1089	∞	14197	1012	1089	Fatigue
L	OP	100	950	1.26	81	42	∞	10555	42	42	Fatigue
L	OP	100	950	1.26	70	37	∞	10555	37	37	Fatigue
T	OP	500	950	0.84	350	120	∞	14197	119	120	Fatigue
T	OP	500	950	0.47	601	310	∞	106354	309	310	Fatigue
L	IP	500	950	1.05	779	558	2367	∞	452	558	Fatigue
L	IP	500	950	0.84	4698	6123	7763	∞	3423	6123	Fatigue

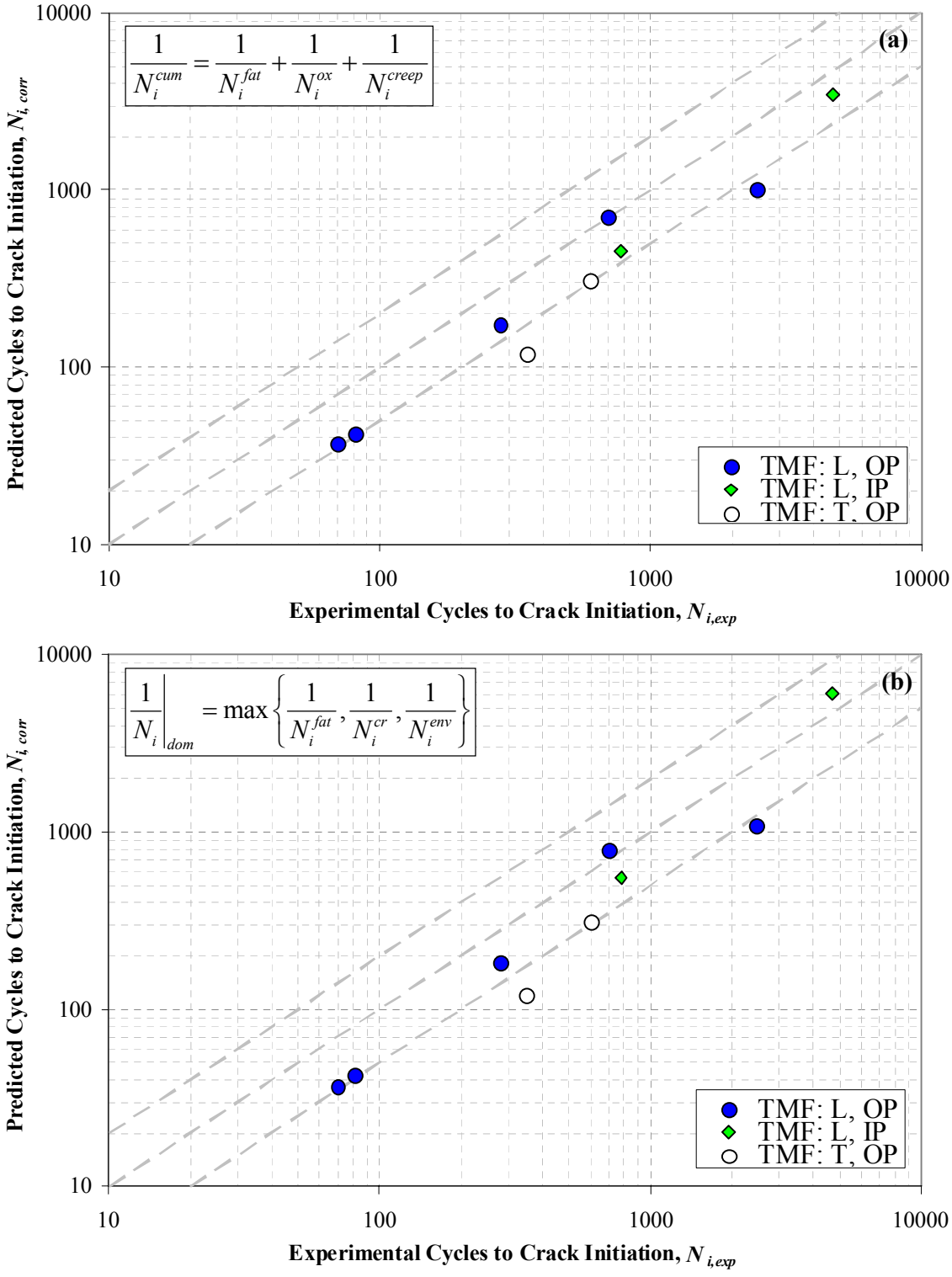

Figure 9-9: Predictions for total crack initiation life of L- and T-oriented CM247LC DS based on the cumulative damage model for (a) summation and (b) dominant damage.

9.2 Influence of Geometric Discontinuities

9.2.1 Background of Stress Concentration Analysis

Most classic procedures of life cycle analysis of notched components are based on either comparing the component's local stress and strain amplitude to cyclic tests or relating the theoretical linear-elastic stress and strain to a fatigue sensitivity concept [65, 71, 97-101]. These approaches have the limitations which often limit their large-scale applicability to engineering design and analysis under varying conditions. The local approach excessively conservative when large stress-strain gradients are encountered, while the notch sensitivity concept requires knowledge of classical notch factors and accurate characterization of the net section stress.

One of the most common approaches, known as Neuber's Rule, was first proposed by Neuber [99] in 1961. Neuber derived a relation for the non-linear material behavior at the notch root, where the product of the elastic-plastic stress and strain (σ and ε, respectively) is equivalent to the product of the linear elastic stress and strain (σ^* and ε^*, respectively). That is to say

$$\sigma\varepsilon = \sigma^*\varepsilon^* \tag{9.26}$$

Neuber showed that the theoretical elastic stress concentration factor (k_t) is equivalent to the geometric mean of the stress and strain concentration factors (k_σ and k_ε, respectively), thereby relating the local stress and strain at the notch to those of the fully-elastic bulk surrounding it by

$$k_t = \sqrt{k_\sigma k_\varepsilon} \tag{9.27}$$

The stress and strain concentration factors can be written in terms of local (σ and ε) and nominal (S and e) stress and strain components

$$k_\sigma = \frac{\sigma}{S} \qquad k_\varepsilon = \frac{\varepsilon}{e} \tag{9.28}$$

This concept is illustrated graphically in Figure 9-10.

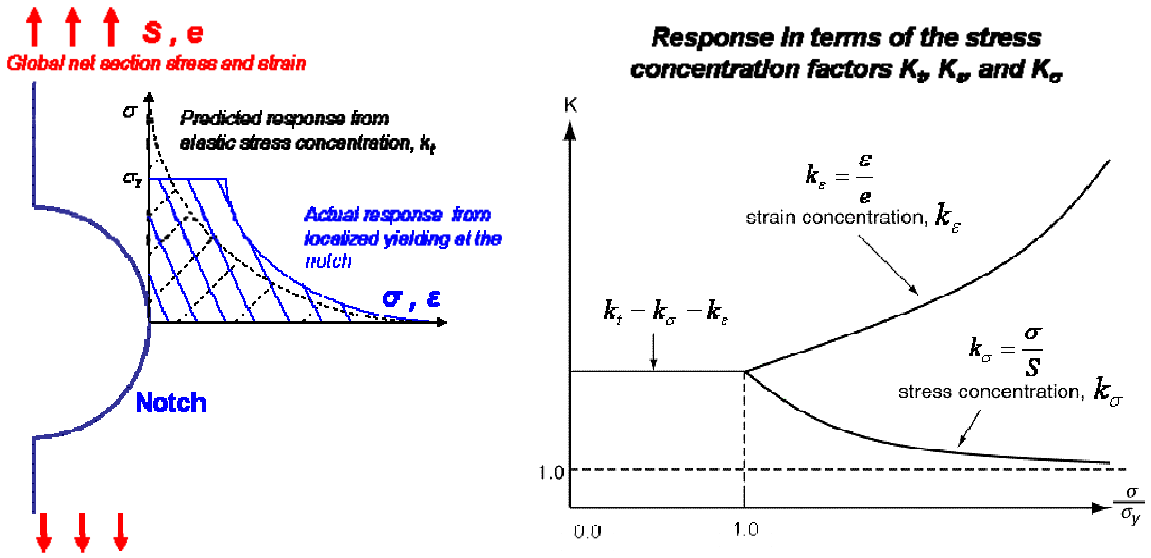

Figure 9-10: Decomposition of stress concentration factors for analyzing notches using Neuber's Rule [102].

Simplifying (9.27) and (9.28), Neuber's rule can be written as

$$\sigma\varepsilon = \frac{k_t^2 S^2}{E} \tag{9.29}$$

For fatigue analysis of notched components, Topper et al. [103] demonstrated it was possible to extend Neuber's rule by incorporating stabilized cyclic parameters (strength coefficient *K'* and strain hardening exponent *n'*) through the Ramberg-Osgood stress-strain relation. In addition, the fatigue notch factor k_f is used to account for material properties in the stabilized hysteresis and avoid design situations where using k_t would yield a grossly conservative response. Topper's relation results in

$$\frac{k_f^2 \Delta S^2}{2E} = \frac{\Delta\sigma^2}{2E} + \Delta\sigma\left(\frac{\Delta\sigma}{2K'}\right)^{1/n'} \tag{9.30}$$

which is a relation with only one local component unknown.

The equivalent strain energy density (ESED) rule was an alternate method proposed by Molski and Glinka [104]. The strain energy density, quantified as the total area beneath the stress-strain response, is used to calculate the local stress-strain state at the notch. This method leads to a more accurate, though less conservative, fatigue analysis. Assuming plane-stress conditions (i.e. a uniaxial state of stress at the notch), this method, known as Glinka's Rule, yields a similar expression to (9.30),

$$\frac{k_f^2 \Delta S^2}{4E} = \frac{\Delta\sigma^2}{4E} + \frac{\Delta\sigma}{n'+1}\left(\frac{\Delta\sigma}{2K'}\right)^{1/n'} \tag{9.31}$$

Methods such as Neuber and Glinka are capable of predicting the local response accurate to an extremely small region within the notch; as a result, predicting component life using these load conditions in a traditional fatigue analysis yields very conservative results. There is also no set method for expanding these methods to handle non-isothermal situations. An approach using a modulus weighted towards the high temperature regime similar to that proposed by Gordon et al. [105] was shown to give reasonable correlations between the analytical and elastic-plastic notch root stresses and strains only if TMF damage and deformation were weighted towards the high temperature half-cycle.

9.2.2 Non-local Computational Analysis

Computational methods which utilized FEA are often a more efficient and repeatable means of obtaining the local response at the notch. The local stress and strain states are then either correlated with experimental data or averaged over a localized region using a critical distance-type approach. Simple elastic or elastic-plastic simulations are ideal for system level design, where results can be rapidly fed into metamodels which set constraints on system performance or aid in down-selecting conceptual designs. These methods typically do not account for more complex, time-dependent deformation or anisotropic material behavior, and as a result are less suitable to detailed design.

Non-local methods utilizing an effective distance are often used to capture the effect of a fatigued area or volume of material by averaging the elastic stress over a particular region. Taylor [106] summarized a collection of such methods known as the theory of critical distances (TCD). The length scale, L, would be incorporated into further

fatigue analysis by using the crack propagation threshold (K_{th}) and fatigue limit (σ_0) defined at the same load ratio, R. Symbolically:

$$L = \frac{1}{\pi}\left(\frac{K_{th}}{\sigma_0}\right)^2 \tag{9.32}$$

This expression can be expanded to relate to features of the microstructure, such as grain size.

When multiaxial, constant-amplitude fatigue loading exists, a critical plane can be identified which contains the maximum shear strain. Approaches using such a parameter involve identifying the critical site and orientation of the plane within the material for the onset of damage and then estimating the cycles to fatigue crack initiation based on some criterion. Socie [107, 108], in particular, has done extensive work documenting the pronounced effect of the progression of damage and cracking on the critical plane, and has developed several such approaches. A good summary of common critical plane parameters is provided by Moore [17].

Műcke and Kiewel [109] developed a non-local approach for fatigue life prediction of notched components where stress and strain gradients were explicitly taken into account in addition to the local magnitudes of stress, strain, and temperature. A linear relationship (on a log-log scale) was found between life and the local strain amplitude (from FE simulations) for notches of differing radii. This suggested an empirical relation which was a function of the notch radius and therefore the local strain gradient. Material constants which related the local FE response and notch geometry to life were determined from the fatigue tests on multiple notch geometries. This relation fit

well for both 1.5%CrNiMo rotor steel and the Ni-base superalloy MAR-M247. Component tests performed with a realistic turbine blade-rotor interface affirmed the reliability of the prediction method.

Similarly, a model for notched isothermal LCF life prediction which utilized an Integrated Local Energy Density (ILED) approach was proposed by Domas and Antolovich [110, 111]. This coupled the results from an elastic-plastic FEA analysis with an active damage zone "volume" and hysteresis loop energy density parameter. In this way it is similar to an Ostergren-type parameter, where the energy of the half-life stabilized hysteresis loop is taken as a measure of the energy used in failing the specimen. The plastic strain and stress range data at the notch root predicted by the FEM model was fit to the expression

$$\Delta\sigma = A(\Delta\varepsilon_p)^{n'} \tag{9.33}$$

where A is the strength coefficient and n' is the strain hardening exponent. For the notch, an average strain energy density, W_A, is determined over an appropriate process volume

$$W_A = \frac{\sum_{i=1}^{N} w_i v_i}{\sum_{i=1}^{N} v_i} \tag{9.34}$$

where w_i is the strain energy density in element i, v_i is the volume of element i, and N is the number of elements contained in the process volume. A power-law correlation relating the maximum axial stress at the notch root to the depth of oxidation spikes was

used to account for damage through oxidation. This, combined with the strain energy density parameter, provided a good correlation to experimental data from round bar notched specimens of k_t=2.22 and k_t=3.49 conducted at 871°C and 982°C. At test temperatures at and below 760°C, a significant reduction in the interaction between damage parameters prevented a direct application of the model.

Using these models as a foundation, empirical fitting of the local response or averaging over a process volume could be done for any damage parameter with a suitable elastic-plastic FEA model. Similar to the Ostergren and Zamrik models, this leaves them primarily suited for the conceptual design stage. To extend either of these models to non-isothermal situations would require all the parameters and most of the constants to take on a temperature-dependence. Additionally, stress redistribution and creep during the high temperature half-cycle would significantly alter the local notch response, which would require a relatively accurate and more complex visco-plastic FE analysis to effectively capture.

The model developed by Moore [17] for notched, high temperature LCF of CM247LC DS utilized a multiaxial Neuber approach to notches. A cyclic Ramberg-Osgood relationship using Neuber's rule was used to determine the cyclic local 3D stress-strain response at the stress concentration. Anisotropic-elastic finite element simulations provided the inputs for this relationship. The driving force for fatigue crack initiation was taken to be a function of the Smith-Watson-Topper (SWT) parameter, i.e.

$$SWT = \sigma_{\max} \varepsilon_a \tag{9.35}$$

where $\sigma_{\max}$ and ε_a are the maximum normal stress and total strain amplitude, respectively, resolved on the critical plane. The critical value of *SWT*, SWT_{crit}, captures the anisotropy of the material resistance. The size of both the k_t=2 and k_t=3 notches was successfully accounted for using the non-local critical distance (point method) approach. In the same way, a larger length scale was incorporated into this approach to account for the reduced notch effect seen in transverse experimental results.

Damage was quantified using a Coffin-Manson type power law relationship fit to uniaxial data, i.e.,

$$SWT_{crit}(\omega,T) = f(\omega)A(T)(2N_i)^{b(T)} \tag{9.36}$$

where *A* and *b* are the material constants. The expression $f(\omega)$ is a shape function, of the same form introduced in Equation (9.9), to model the orientation dependence. Dwells were incorporated as continuous but rate-dependent loading. This allowed the model to effectively capture the mean stress effect without explicitly considering creep.

This model utilized the same notch geometry as used in the current TMF experiments. As the model incorporated many material parameters specific to CM247LC DS over a range of temperatures used in the current TMF experiments (i.e. 500°C, 750°C, 850°C, and 950°C), it is useful to compare the predictions obtained using the values from an anisotropic, non-isothermal finite element analysis. Such an exercise will demonstrate if isothermal notched results can predict TMF without explicit modeling of the damage mechanisms. The maximum Hill's stress and normal stress based on these simulations was obtained from the high temperature half-cycle. This was used because

isothermal results more closely resembled those of TMF at T_{max} (Figure 6-1 and Figure 6-27), and also because the model parameters at 500°C were based on an isothermal cycle, and thus would yield extremely non-conservative results.

Multiaxial Neuber Model (MNM) predictions for the longitudinal orientation are shown in Figure 9-11. Interestingly, for the range considered, the OP curves for both notches lie very close to the MNM prediction for k_t=2. Model predictions for k_t=3 fell well below those of k_t=2 and were thus extremely conservative.

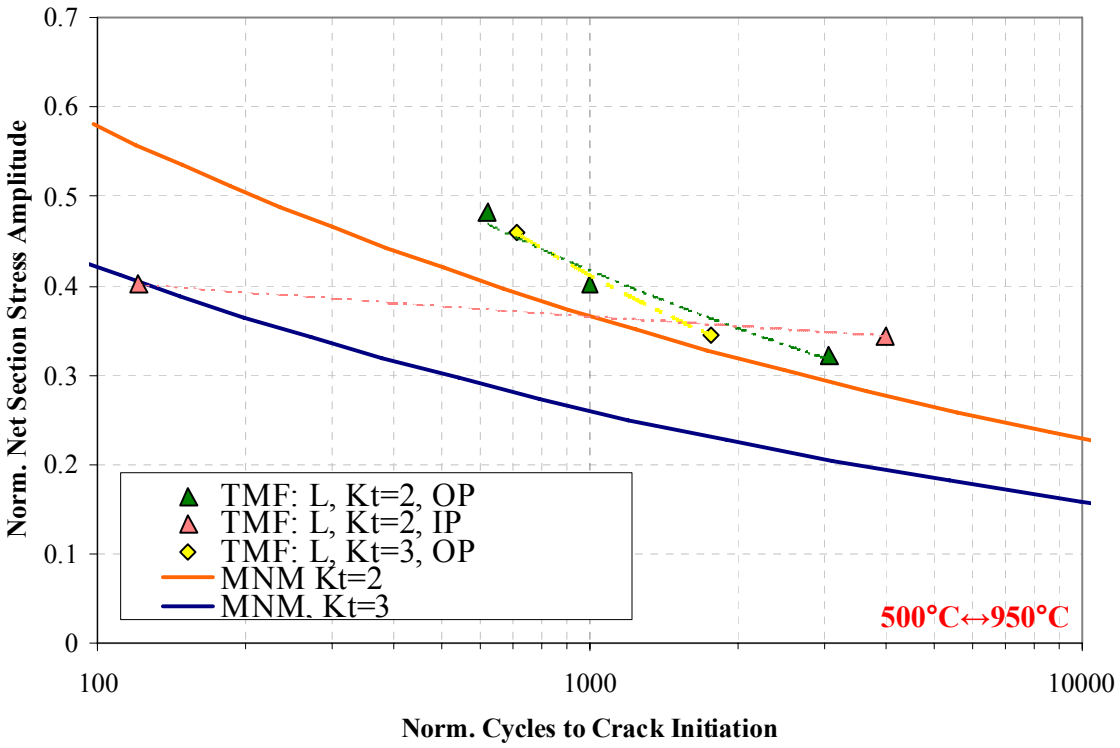

Figure 9-11: Normalized Multiaxial Neuber Model predictions for longitudinal CM247LC DS as compared to experimental data for.

This result indicates the simplified methods used by Moore's model account for time-dependent deformation and predict crack initiation life do not reflect the mechanisms influencing the TMF tests. As expected from the SWT approach, the IP TMF results fit

quite poorly with the model predictions. This is likely due to the fact that the model does not explicitly account for creep damage, but only the mean stress and strain behavior resulting from a dwell. This was similar to the results obtained when trying to correlate the Ostergren parameter to IP TMF of CM247LC DS, as seen from Figure 9-1. For these reasons, predictions for the transverse orientation with the model were not attempted.

To fully expand such a model to anisothermal conditions, more explicit account for the individual damage mechanisms would likely be needed. This is a simplified formulation, so contributions from the environment are not included, even though the mechanism was active for several of the dwell tests at 950°C (Figure 6-19). As it stands, the mean stress and rate effects are effectively modeled, but their interactions with creep and stress relaxation are not accounted for. The triaxiality of the stress state at the notch contributes considerably to the complexity of these mechanisms. Other authors [112] have also noted the problems with modeling stress relaxation effects in notched specimens under high tensile loads at elevated temperature.

9.2.3 Notched Modeling Summary

As a result of the observations associated with the models presented, a more comprehensive and physically-complex model would be needed for accurate life prediction of notched thermomechanical fatigue. Without predicting the visco-plastic response, an elastic or elastic-plastic FE structural analysis is only suitable for analytical modeling of TMF at the preliminary design stage.

For a more advanced, detailed design analysis, the macroscopic constitutive response of notched TMF requires a detailed FE analysis incorporating the influence of

the underlying microstructure. Follow-on work could incorporate the approach proposed by Tjiptowidjojo [41] for the microstructure-sensitive notch analysis of CM247LC DS. This would provide the framework for useful design tools such as heat treatment optimization, geometric spacing of blade cooling holes, and the visco-plastic response for life modeling.

CHAPTER 10. CONCLUSIONS

Key findings of this research are as follows:

10.1 Smooth Specimen TMF Behavior

Performed experiments which highlight the high temperature thermomechanical fatigue behavior of CM247LC DS. Tests were used to simulate the material behavior under a wide variety of conditions. Experiments characterize the effects of orientation, temperature, and microstructural morphology on the TMF life of CM247LC DS. Key observations include:

- TMF testing results in a reduction in life when compared to isothermal tests at T_{max} with the same applied mechanical strain ranges.
- IP cycling is significantly less damaging than OP for low mechanical strain ranges, where N_i increased by a factor of two for a normalized $\Delta\varepsilon_{mech}$ of 0.84%.
- OP testing in the transverse orientation resulted in an increase in plastic strain by a factor of nearly three and a reduction in crack initiation life by seven times compared to a longitudinal test with the same mechanical strain range. This was due to weak points in the microstructure which were favorable locations for crack initiation.
- Reducing T_{min} from 500°C to 100°C resulted in a nearly three-fold increase in inelastic strain for the same mechanical strain range and a

reduction in life by a factor of 3.4. This was primarily driven by the change in elastic modulus as a function of temperature.

10.2 Notched Specimen TMF Behavior

Determined the effect of notches on crack initiation on the alloy under TMF. Tests with notched specimens are used to account for geometric stress concentrations in blades. The reduction in fatigue life as a result of a stress concentration was characterized. Additionally, geometric influences on the location and preliminary growth of cracks in the notched region were defined.

- Regardless of orientation or T_{max}, k_t=2 and k_t=3 notches follow the same stress life curve.
- TMF in the transverse orientation is less sensitive to notches, most likely due to microstructural inhomogeneities.
- Notched testing with a reduced T_{max} of 750°C resulted in substantially greater fatigue resistance due to the exclusion of creep and oxidation mechanisms. An increase in applied force of approximately 50% was required to yield the same N_i as the baseline.
- Global creep ratcheting occurred in all notched tests with T_{max}=950°C. The effect of ratcheting was especially severe in IP tests, which were quite sensitive to the applied net section stress amplitude.

10.3 TMF Damage Mechanisms as a Function of Test Conditions

Identified the dominant active damage mechanisms as a function of test conditions. A variety of variables were altered to define when fatigue, environmental-fatigue, or creep would be most damaging and lead to crack initiation. Active damage mechanisms are identified through extensive post-test microscopy of failed fatigue specimens.

- Evidence of creep and oxidation damage was observed extensively during microscopy of both smooth and notched specimens subjected to TMF with T_{max}=950°C. During IP cycling, creep manifested as internal voids forming at weak points in the microstructure, such as carbides, grain boundaries, and the interdendritic region. Under OP loading, environmental damage occurred when cracking of the brittle surface oxide layers resulted in crack initiation through oxide spiking.
- Under both OP and IP cycling, longitudinal samples exhibited primarily transgranular cracking, while loading in the transverse orientation resulted in intergranular cracking along grain boundaries and the eutectic γ' in the interdendritic regions.
- The oxidation kinetics of CM247LC DS followed the parabolic growth law. Arrhenius forms involving the activation energies for the oxidation and γ' depletion processes correlated well with measurements from stress-free oxidation experiments.
- Microstructure morphology in the form of γ' precipitate rafting was observed as a result of thermomechanical cycling with T_{max}=950°C,

indicating this is above the threshold temperature needed to catalyze thermodynamic process.

Evolution of microstructure morphology and its effect on the mechanical properties and TMF behavior. Comparison of baseline samples to those which had undergone pre-exposure to raft the microstructure revealed that pre-exposure influenced the material properties and the number of cycles necessary for crack initiation.

- At 950°C, 144 *hrs* under a load of ± 112.5 *MPa* was required to raft the microstructure of previously untested samples.
- Compared to virgin samples, specimens whose γ-γ' microstructure had been rafted normal to the stress axis exhibited an increased yield strength by a factor of 1.2 at temperatures below 500°C and a reduced strength above. The opposite effect was observed for rafts lying parallel to the stress axis.
- Despite an appreciable increase in the plastic strain range over the virgin microstructure, the OP TMF life of a tensile-rafted sample was not appreciably affected for T=100°C↔950°C and norm. $\Delta\varepsilon_{mech}$=1.26%.
- Localized rafting occurred around cracks in many short-duration tests, indicating that at high temperatures the microstructure is sensitive to localized stress concentrations.

10.4 Crystal Visco-plasticity Finite Element Simulations

Characterized the material and notch response using computational simulations. Single-crystal crystal visco-plastic simulations demonstrated the time- and temperature-dependent deformation response of smooth and notched specimens.

- All notched tests resulted in cracking at the location of the maximum effective (either Hill's equivalent or Von Mises) stress. This location is offset (approximately 350 μm and 150 μm for k_t=2 and k_t=3, respectively) on either side of the notch root.
- The local notch response is in a combination of force- and displacement-control.
- Simulations predicted creep ratcheting for all notched tests with T_{max}=950°C, which was observed in experiments.

10.5 Life Modeling Implications

Various models were used to correlate the response of CM247LC DS to TMF loading. Such models are useful at different stages of conceptual and detailed design.

- Simple smooth specimen damage function correlations based on isothermal LCF data at T_{max} such as the Ostergren parameter were capable of predicting the trends of OP TMF, but could not accurately capture a change in cycle phasing (IP TMF) or grain orientation.
- A strong correlation was observed with the plastic strain range, indicating fatigue was the dominant mechanism influencing life over the range of conditions tested.

- A physics-based approach accounting explicitly for the contributions from fatigue, creep, and environmental damage was effective in predicting the crack initiation life of smooth specimens.
- Existing isothermal notched models do not explicitly account for the damage mechanisms and deformation response occurring during thermomechanical cycling. For a more advanced, detailed design analysis, the macroscopic constitutive response of notched TMF requires a detailed FE analysis incorporating the influence of the underlying microstructure.

CHAPTER 11. RECOMMENDATIONS

While a considerable amount of work has been done to characterize the response of smooth and notched CM247LC DS to thermomechanical fatigue, many of observations were new and unique. Others were simply outside the scope of the current study. As a result, there is ample opportunity for future work to gain further insight into various aspects of the material behavior and thus advance the understanding of crack initiation. These future objectives would also contribute to better develop and calibrate the mechanistic approaches to life prediction introduced herein.

11.1 Experimentation

- *Exploration of notched behavior with a smaller k_t.*

  Experiments demonstrated that for out-of-phase loading, k_t=2 and k_t=3 notches followed the same stress-life curve. This trend was consistent for both the baseline temperature range and for cycling between 500°C and 750°C. Isothermal LCF data showed considerable difference in life between the same notches at both 750°C and 950°C. As microscopy demonstrated the same fatigue and environmental damage mechanisms found in smooth specimen tests, testing with $1 \leq k_t \leq 2$ would help explain this anomaly by differentiating between notch effects and active TMF mechanisms.

- *Determine the extent to which strain rate affects the baseline temperature range from 500°C to 950°C.*

  All thermomechanical fatigue tests in the baseline temperature range were conducted using the same 180 *s* cycle time. As such, the influence of applied strain rate was negligible between these experiments. Conducting similar tests with a considerably slower rate, such as that used for experiments where T_{min}=100°C, would decouple any rate effects and isolate their influence on TMF life.

- *Further evaluate the physics of the microstructure morphology process.*

  Further experiments are necessary to capture the time-dependent thermodynamic instability of the γ' precipitates. An expanded understanding of the kinetics of this process would allow designers to take into account the evolution from virgin to partially-rafted to fully-rafted microstructures and their impact on the service capabilities of the material. Additionally, the factors which influence the rate of this process could be determined; i.e., the extent to which an increase in temperature or load results in a shorter time period to a completely rafted structure.

- *Isolate the effects of ageing and precipitate rafting on the mechanical properties of Ni-base superalloys.*

  Interesting phenomena, such as the difference in cyclic stability and strength between tests whose microstructure had been pre-rafted in tension and compression, indicates there may be other effects at work. Thermal ageing will

cause the secondary precipitates to dissolve in the matrix and the primary particles to coarsen. The effects of this process on the material response can be isolated by conducting tests with a prior ageing treatment.

- *Thermomechanical fatigue with superimposed dwells as a creep-fatigue and microstructure-morphing mechanism.*

  Determine the effects of holds at peak temperature in tension and compression on the thermomechanical fatigue life, creep properties, and microstructure of the alloy. These conditions simulate extended baseload operation which occurs between engine start-up and shut-down or trip transients.

- *Measure the rate of crack growth in and around the notch stress concentration.*

  The extensive circumferential cracking in all high temperature notched experiments is indicative of retarded crack growth outside of the notch stress concentration. As a result, multiple small cracks could nucleate and grow before the defined initiation was detected. Additional crack growth testing to determine the rate of propagation as cracks transition between the notch and net section stress fields would be valuable for future geometric design considerations of blades.

- *Determined off-axis thermomechanical fatigue behavior of DS Ni-base superalloys.*

  Though many of the models presented in this work are capable of accounting for any grain orientation of a DS material, validation data for off-axis (e.g. 30°, 45°, and 60°) is extremely scarce. Due to resources, experiments in the

current work were performed in the L and T orientations only. Future off-axis work would allow full calibration of the orientation-dependence captured by the models.

11.2 Computational Modeling

- *Update the CVP FEA model constants to reflect the behavior of CM247LC DS.*

  Currently, the crystal visco-plastic computational model contains the material constants found for the DS Ni-base superalloy GTD-111. As such, only the trends in the deformation response of CM247LC DS could be modeled. Calibration and optimization of the necessary material constants requires more time and deformation data than was available for the current work. A future update of the model to reflect the exact behavior of CM247LC DS would allow for the validation of more comprehensive analytical notched models. Complete documentation of the consistent procedure to determine the appropriate constants would create a methodology for a more rapid expansion the framework to other DS and single crystal Ni-base superalloys.

- *Develop formulation for damage extraction from constitutive FE models.*

  Once the accurate, visco-plastic response of the material is determined for a wide range of geometries and test conditions, a methodology for quantifying material damage based on the different mechanisms contributing to the deformation response needs development.

11.3 Analytical Modeling

- *Enhance existing models to better reflect notch sensitivity under thermomechanical fatigue conditions.*

  None of the notched models explored could capture the similar behavior between the k_t=2 and k_t=3 notches under out-of-phase loading. Developing this capability is a critical step in expanding existing isothermal notched models to include TMF predictions.

- *Incorporate the influence of a rafted or partially-rafted precipitates into existing microstructurally-sensitive constitutive models to improve their functionality.*

  Including the evolution of mechanical properties due to rafting over the lifetime of a service blade is critical for defining service and inspection intervals for an engine contract. Better predictive capabilities of the time- and temperature-dependent material degradation would allow a more accurate outage schedule to reflect component capability over its service life.

- *Investigate methods for expanding Neuber or Glinka analysis to TMF.*

  For IP and OP TMF, there is no widely-accepted method for correlating remotely applied loads with the local stress and strain responses. Methods to incorporate temperature-dependence into these formulations could be used to expand and improve existing isothermal notched models.

REFERENCES

1. Knop, M., R. Jones, L. Molent, and C. Wang, *On the Glinka and Neuber methods for calculating notch tip strains under cyclic load spectra.* International Journal of Fatigue, 2000. **22**(9): p. 743-755.

2. Gordon, A.P., *Crack Initiation Modeling of a Directionally-Solidified Nickel-Base Superalloy*, in *Woodruff School of Mechanical Engineering*. 2006, Georgia Institute of Technology: Atlanta.

3. (DLR), G.A.C. *Gas Turbine*. [JPEG Image] 2009 [cited 1/26/09]; Available from: http://www.dlr.de/en/Portaldata/1/Resources/portal_news/newsarchivstuttgart/kraftwerke_030306/AcrD.jpg.

4. Huang, Z.W., Z.G. Wang, S.J. Zhu, F.H. Yuan, and F.G. Wang, *Thermomechanical fatigue behavior and life prediction of a cast nickel-based superalloy.* Materials Science and Engineering A, 2006. **432**(1-2): p. 308-316.

5. Erickson, G.L., K. Harris, and R.E. Schwer. *Directionally Solidified DS CM 247 LC - Optimized Mechanical Properties Resulting From Extensive Gamma Prime Solutioning*. 1985. Houston, TX, USA: ASME, New York, NY, USA.

6. Shenoy, M.M., A.P. Gordon, D.L. McDowell, and R.W. Neu, *Thermomechanical fatigue behavior of a directionally solidified Ni-base superalloy.* Journal of Engineering Materials and Technology, Transactions of the ASME, 2005. **127**(3): p. 325-336.

7. Esser, W. *Directional Solidification of Blades for Industrial Gas Turbines*. 1994. Liege, Belg: Kluwer Academic Publishers.

8. Padture and e. al., *Illustration of a DS blade casting*. 2002, Science, p. 280-284.

9. Sehitoglu, H. and D.A. Boismier, *Thermo-mechanical fatigue of Mar-M247. II. Life prediction.* Transactions of the ASME. Journal of Engineering Materials and Technology, 1990. **112**(1): p. 80-9.

10. Okazaki, M. and M. Sakaguchi, *Thermo-mechanical Fatigue Failure of a Single Crystal Ni-based Superalloy.* International Journal of Fatigue, 2008. **30**(2): p. 318-323.

11. Esmaeili, S., C.C. Engler-Pinto, B. Ilschner, and F. Rézaï-Aria, *Interaction between oxidation and thermo-mechanical fatigue in IN738LC superalloy -- I.* Scripta Metallurgica et Materialia, 1995. **32**(11): p. 1777-1781.

12. Engler-Pinto, C.C., Jr., C. Noseda, M.Y. Nazmy, and F. Rezai-Aria. *Interaction Between Creep and Thermo-mechanical Fatigue of CM247LC-DS*. in *Superalloys 1996; Proceedings of the Eighth International Symposium on Superalloys*. 1996. Champion, PA: The Minerals, Metals & Materials Society.

13. Boismier, D.A. and S. Huseyin, *Thermo-mechanical fatigue of Mar-M247. I. Experiments.* Transactions of the ASME. Journal of Engineering Materials and Technology, 1990. **112**(1): p. 68-79.

14. Antolovich, S.D., S. Liu, and R. Baur, *Low cycle fatigue behavior of Rene 80 at elevated temperature.* Metallurgical Transactions A (Physical Metallurgy and Materials Science), 1981. **12A**(3): p. 473-81.

15. Mazza, E., M. Hollenstein, S. Holdsworth, and R.P. Skelton, *Notched specimens thermo-mechanical fatigue of a 1CrMoV turbine steel.* Nuclear Engineering and Design, 2004. **234**(1-3): p. 11-24.

16. Suresh, S., *Fatigue of Materials*. Cambridge Solid State Science Series. 1991, New York, NY: Cambridge University Press. 617.

17. Moore, Z.J., *Life Modeling of Notched CM247LC DS Nickel-Base Superalloy*, in *George W. Woodruff School of Mechanical Engineering*. 2008, Georgia Institute of Technology: Atlanta, GA.

18. Viswanathan, R., *Damage Mechanisms and Life Assessment of High-Temperature Components*, ed. A. International. 1989, New York, NY: Carnes Publication Services, Inc.

19. Cai, C., P.K. Liaw, M. Ye, and J. Yu, *Recent Developments in the Thermomechanical Fatigue Life Prediction of Superalloys.* JOM, 1999. **51**(4).

20. Boyce, M.P., *The Gas Turbine Engineering Handbook*. Chemical, Petrochemical & Process. 2006: Gulf Professional Publishing. 1-955.

21. Reger, M. and L. Remy, *High temperature, low cycle fatigue of IN-100 superalloy I: Influence of temperature on the low cycle fatigue behaviour.* Materials Science and Engineering, 1988. **101**: p. 47-54.

22. Bernstein, H.L. and J.M. Allen, *Analysis of cracked gas turbine blades.* Journal of Engineering for Gas Turbines and Power, Transactions of the ASME, 1992. **114**(2): p. 293-301.

23. Reger, M. and L. Remy, *Fatigue oxidation interaction in IN 100 superalloy.* Metallurgical Transactions A (Physical Metallurgy and Materials Science), 1988. **19A**(9): p. 2259-68.

24. Duquette, D.J. and M. Gell, *The effects of environment on the elevated temperature fatigue behavior of nickel-base superalloy single crystals.* Metallurgical Transactions A (Physical Metallurgy and Materials Science), 1972. **3**(7): p. 1899-905.

25. Sehitoglu, H. and D.A. Boismier, *Thermo-mechanical fatigue of Mar-M247. Part 2. Life prediction.* Journal of Engineering Materials and Technology, Transactions of the ASME, 1990. **112**(1): p. 80-89.

26. McDowell, D.L., S.D. Antolovich, and R.L.T. Oehmke, *Mechanistic considerations for TMF life prediction of nickel-base superalloys.* Nuclear Engineering and Design, 1992. **133**(3): p. 383-399.

27. Valerio, P., M. Gao, and R.P. Wei, *Environmental enhancement of creep crack growth in Inconel 718 by oxygen and water vapor.* Scripta Metallurgica et Materialia, 1994. **30**(10): p. 1269-1274.

28. Gordon, A.P., R.W. Neu, and D.L. McDowell, *Effect of pre-exposure on crack initiation life of a directionally solidified Ni-base superalloy.* International Journal of Fatigue, 2009. **31**(2): p. 393-401.

29. Gordon, A.P., M.D. Trexler, R.W. Neu, J.T.J. Sanders, and D.L. McDowell, *Corrosion kinetics of a directionally solidified Ni-base superalloy.* Acta Materialia, 2007. **55**(10): p. 3375-3385.

30. Corporation, T. *Gas Turbine Control Cycle*. 2000 [cited 2008; Transient Engine Sequence].

31. Loche, D., T. Beck, and K.-H. Lang. *Important Aspects of Cyclic Deformation, Damage, and Lifetime Behavior in Thermo-mechanical Fatigue of Engineering Alloys*. in *Fifth International Conference on Low Cycle Fatigue*. 2004. Berlin.

32. Embley, G.T. and E.S. Russell, *Thermal-mechanical Fatigue of Gas Turbine Bucket Alloys*. 1984, Gas Turbine Division, General Electric Company: Schenectady, NY. p. 8.

33. Bartsch, M., B. Baufeld, S. Dalkilic, L. Chernova, and M. Heinzelmann, *Fatigue Cracks in a Thermal Barrier Coating System on a Superalloy in Multiaxial Thermomechanical Testing.* International Journal of Fatigue, 2008. **30**(2): p. 211-218.

34. Sourmail, T. *Illustration of Coated Gas Turbine Blade*. Coatings for Turbine Blades [cited 2009 2/2]; Available from: www.msm.cam.ac.uk/.../coatings/index.html.

35. Padture, *Illustration of DS blade casting*. 2002, Science, p. 280-284.

36. Birks, N., G. Meier, and F. Pettit, *Introduction to the High-Temperature Oxidation of Metals*. 2nd ed. 2006, New York: Cambridge University Press. 338.

37. Kowalewski, R. and H. Mughrabi. *Thermo-mechanical and Isothermal Fatigue of a Coated Columnar-Grained Directionally Solidified Nickel-Base Superalloy*. 2000. Norfolk, VA, USA: ASTM, Conshohocken, PA, USA.

38. Bartsch M. , B.B., Heinzelmann M., Karlsson A. M., Dalkilic S., Chernova L., *Multiaxial Thermo-mechanical Fatigue on Material Systems for Gas Turbines.* Materialwissenschaft und Werkstofftechnik, 2007. **38**(9): p. 712-719.

39. Colombo, F., E. Mazza, S.R. Holdsworth, and R.P. Skelton, *Thermo-mechanical fatigue tests on uniaxial and component-like 1CrMoV rotor steel specimens.* International Journal of Fatigue, 2008. **30**(2): p. 241-248.

40. Colombo, F., B. Masserey, E. Mazza, and S.R. Holdsworth, *Simple modelling of the constitutive behaviour of a 1%CrMoV rotor steel in service-like thermo-mechanical fatigue tests.* Materials at High Temperatures, 2002. **19**(4): p. 225-233.

41. Tjiptowidjojo, Y., C. Przybyla, M.M. Shenoy, and D.L. McDowell, *Microstructure-Sensitive Notch Root Analysis for Ni-base Superalloys*, in *Fourth International Conference on Very High Cycle Fatigue*, J. Allison, et al., Editors. 2007, The Minerals, Metals & Materials Society.

42. Shenoy, M., Y. Tjiptowidjojo, and D. McDowell, *Microstructure-sensitive modeling of polycrystalline IN 100.* International Journal of Plasticity, 2008. **24**(10): p. 1694-1730.

43. Reppich, B., *A microstructural model of high-temperature strength and rupture life time for second phase particle hardened alloys.* Zeitschrift fur Metallkunde, 1982. **73**(11): p. 697-705.

44. Heilmaier, M., U. Leetz, and B. Reppich. *Order strengthening in the cast nickel-based superalloy IN 100 at room temperature*. 2001. Switzerland: Elsevier.

45. Shenoy, M.M., R.S. Kumar, and D.L. McDowell, *Modeling Effects of Nonmetallic Inclusions on LCF in DS Nickel-base Superalloys.* International Journal of Fatigue, 2005. **27**(2): p. 113-127.

46. McDowell, D.L., *Simulation-based Strategies for Microstructure-sensitive Fatigue Modeling.* Materials Science and Engineering A, 2007. **468-470**(SPEC ISS): p. 4-14.

47. Harris, K., *High Ductility Nickel Alloy Directional Casting of Parts for High Temperature and Stress Operation*. 1984, Cannon-Muskegon Corporation: United States.

48. Erickson, G.L. and K. Harris. *DS and SX Superalloys for Industrial Gas Turbines*. 1994. Liege, Belg: Kluwer Academic Publishers.

49. Sims, C., N. Stoloff, and W. Hagel, *Superalloys II*. 1987, New York: John Wiley & Sons.

50. Okada, M., M. Tsutsumi, T. Kitamura, and R. HOhtani, *Initiation and Growth of Small Cracks in Directionally Solidified MAR-M247 under Creep-Fatigue. Part I: Effect of Microstructure.* Fatigue and Fracture of Engineering Material and Structures, 1998. **21**: p. 741-750.

51. Kurz, W. and D.J. Fisher, *Fundamentals of Solidification*. 1998, Switzerland: Trans Tech Publications.

52. Komazaki, S. and T. Shoji, *Formation of the Al-rich phase on grain boundary and the creep damage mechanism in directionally solidified Ni-base superalloy.* Metallurgical and Materials Transactions A: Physical Metallurgy and Materials Science, 1997. **28A**(9): p. 1945-1949.

53. Davis, J., *Heat-Resistant Materials*. 1997: ASM International.

54. Shenoy, M., *Constitutive Modeling and Life Prediction in Ni-base Superalloys*, in *George W. Woodruff School of Mechanical Engineering*. 2006, Georgia Institute of Technology: Atlanta, GA. p. 318.

55. Reed, R., *The Superalloys: Fundamentals and Applications*. 2006, Ney York: Cambridge University Press. 372.

56. Marchionni, M., G.A. Osinkolu, and M. Maldini, *High Temperature Cyclic Deformation of a Directionally Solidified Ni-base Superalloy.* Fatigue and Fracture of Engineering Materials & Structures, 1996. **19**(8): p. 955-962.

57. Blumm, M., C. Engler-Pinto, F. Meyer-Olbersleben, and F. Rezai-Aria. *Grain Orientation and Size Effects on Thermal Fatigue Behavior of CM247 LC DS*. 1994. Liege, Belg: Kluwer Academic Publishers.

58. Vasseur, E. and L. Remy, *High Temperature Low Cycle Fatigue and Thermal-mechanical Fatigue Behaviour of an Oxide-dispersion-strengthened Nickel-base Superalloy.* Materials Science & Engineering A (Structural Materials: Properties, Microstructure and Processing), 1994. **A184**(1): p. 1-15.

59. Nazmy, M.Y. and R.F. Singer, *High Cycle Fatigue and Fatigue Crack Growth of the Oxide Dispersion Strengthened Alloy MA 754.* Metallurgical Transactions A (Physical Metallurgy and Materials Science), 1985. **16A**(8): p. 1437-44.

60. Calderon, H.A., M. Benyoucef, N. Clement, A. Coujou, and P. Caron (2005) *Characterization of γ- γ' Interfaces in Ni Base Superalloys Subject to Creep Deformation by Conventional TEM and HREM*. Microsc Microanal **Volume**, 1670-1671

61. Hasselqvist, M. and J. Moverare. *Constitutive behaviour of IN738LC under TMF cycling with and without intermediate ageing*. in *Proceedings of the ASME Turbo Expo 2007*. 2007. Montreal, Que., Canada: ASME, New York, NY.

62. Arrell, D., M. Hasselqvist, C. Sommer, and J. Moverare, *On TMF damage, degradation effects, and the associated TMin influence on TMF test results in γ/γ'alloys*, S. 2004, Editor. 2004, Minerals, Metals and Materials Society, Warrendale, PA 15086: Champion, PA. p. 291-294.

63. Jung-Seob, H., S. Gee-Wook, and L. Young-Shin, *Thermo-mechanical fatigue of the nickel base superalloy IN738LC for gas turbine blades.* Key Engineering Materials, 2006. **321-323**: p. 509-12.

64. ABAQUS, *ABAQUS v6.7*. 2007, Dassault Systèmes: Providence, RI.

65. Mucke, R. and O. Bernhardi, *A Constitutive Model for Anisotropic Materials based on Neuber's Rule.* Computer methods in applied mechanics and engineering, 2003. **192**(2003): p. 4237-4255.

66. Kuhn, H.-A. and H.-G. Sockel, *Elastic properties of textured and directionally solidified nickel-based superalloys between 25 and 1200°C.* Materials Science and Engineering A, 1989. **112**: p. 117-126.

67. Hasebe, T., M. Sakane, and M. Ohnami, *Elastic Anisotropy of Directionally Solidified Superalloy.* Journal of Engineering Materials and Technology, Transactions of the ASME, 1992. **114**(2): p. 141-146.

68. Shenoy, M.M., *Constitutive Modeling and Life Prediction in Ni-Base Superalloys*, in *Woodruff School of Mechanical Engineering*. 2006, Georgia Institute of Technology: Atlanta.

69. Boger, R.K., *Non-Monotonic Strain Hardening and its Formulations*, in *Materials Science and Engineering*. 2006, Ohio State University: Columbus, OH.

70. Liu, F., Y.C. Wang, H. Zhang, S.H. Ai, and Z.G. Wang, *Evolutionary stress cycle behaviour and damage mechanisms in nickel based superalloy under thermomechanical fatigue.* Materials Science & Technology, 2003. **19**(7): p. 853-858.

71. Carpinteri, A., M. De Freitas, and A. Spagnoli, *Biaxial / Multiaxial Fatigue and Fracture*. Materials & Mechanical. 2003: Elsevier. 1-503.

72. Ziebs, J., J. Meersmann, H.-J. Kuehn, and H. Klinglehoeffer. *Multiaxial Thermo-mechanical Deformation Behavior of IN 738 LC and SC 16*. 2000. Norfolk, VA, USA: ASTM, Conshohocken, PA, USA.

73. Rie, K.-T. and P.D. Portella, *Low Cycle Fatigue and Elasto-Plastic Behaviour of Materials*. 1rst ed. 1998, New York: Elsevier Science Ltd. 890.

74. Moore, Z.J., R.A. Kupkovits, and R.W. Neu. *Creep-fatigue of a Notched Directionally-Solidified Ni-base Superalloy*. in *SEM XI International Congress & Exposition on Experimental and Applied Mechanics*. 2008. Orlando, FL.

75. Lu, Z., F. Pyczak, H. Biermann, and H. Mughrabi, *CBED study of local strain distribution in γ and γ' phases of a crept Ni base superalloy.* Acta Metallurgica Sinica, 2006. **42**(7): p. 694-8.

76. Feng, H., H. Biermann, and H. Mughrabi, *Computer simulation of the initial rafting process of a nickel-base single-crystal superalloy.* Metallurgical and Materials Transactions A (Physical Metallurgy and Materials Science), 2000. **31A**(3): p. 585-97.

77. Biermann, H., U. Tetzlaff, B. von Grossmann, H. Mughrabi, and V. Schulze, *Rafting in monocrystalline nickel-base superalloys induced by shot peening.* Scripta Materialia, 2000. **43**(9): p. 807-812.

78. Aghaie-Khafri, M. and M. Hajjavady, *The effect of thermal exposure on the properties of a Ni-base superalloy.* Materials Science and Engineering: A, 2008. **487**(1-2): p. 388-393.

79. Ott, M. and H. Mughrabi, *Dependence of the high-temperature low-cycle fatigue behaviour of the monocrystalline nickel-base superalloys CMSX-4 and CMSX-6 on the γ/γ'-morphology.* Materials Science and Engineering A, 1999. **272**(1): p. 24-30.

80. Mughrabi, H. and U. Tetzlaff, *Microstructure and high-temperature strength of monocrystalline nickel-base superalloys.* Advanced Engineering Materials, 2000. **2**(6): p. 319-26.

81. Kraft, S.A. and H. Mughrabi. *Thermo-mechanical fatigue of the monocrystalline nickel-base superalloy CMSX-6*. 1996. Phoenix, AZ: ASTM, Conshohocken, PA, USA.

82. Neuner, F.C., U. Tetzlaff, and H. Mughrabi. *Enhancement of Thermomechanical Fatigue Resistance of a Monocrystalline Nickel-base Superalloy by Pre-rafting*. 2003. Dallas, TX: American Society for Testing and Materials, West Conshohocken, PA

83. Pessah-Simonetti, M., P. Caron, and T. Khan, *Effect of a Long-Term Prior Aging on the Tensile Behaviour of a High-Performance Single Crystal Superalloy*. 1998.

84. Hasselqvist, M., *Reference for OP TMF test minimum temperature*, R.A. Kupkovits, Editor. 2008: Atlanta. p. 1.

85. Reuchet, J. and L. Remy, *High temperature low cycle fatigue of MAR-M 509 superalloy. II. The influence of oxidation at high temperatures.* Material Science and Engineering, 1983. **58**(1): p. 33-42.

86. Geng, L., Z.-Z. Zheng, Y.-S. Na, and N.-K. Park, *Effect of thermal exposure on precipitation behavior and hardness of alloy 718.* Transactions of the Nonferrous Metals Society of China, 2000. **10**(3): p. 340-4.

87. Das, D.K., V. Singh, and S.V. Joshi, *High temperature oxidation behaviour of directionally solidified nickel base superalloy CM - 247LC.* Materials Science and Technology, 2003. **19**(6): p. 695-708.

88. Coffin, L.F., *A Study of the Effect of Cyclic Thermal Stresses on a Ductile Metal*. 1953, American Society of Mechanical Engineers: New York.

89. Ostergren, W.J., *Damage Function and Associated Failure Equations for Predicting Hold Time and Frequency Effects in Elevated Temperature, Low Cycle Fatigue.* Journal of Testing & Evaluation, 1976. **4**(5): p. 327-339.

90. Zamrik, S.Y. and M.L. Renauld. *Thermo-mechanical out-of-phase fatigue life of overlay coated IN-738LC gas turbine material*. 2000. Norfolk, VA, USA: ASTM, Conshohocken, PA, USA.

91. Sehitoglu, H. *Thermo-mechanical fatigue life prediction methods*. 1992. San Francisco, CA, USA: Publ by ASTM, Philadelphia, PA, USA.

92. Neu, R.W. and H. Sehitoglu, *Thermomechanical fatigue, oxidation and creep. II. Life prediction.* Metallurgical Transactions A (Physical Metallurgy and Materials Science), 1989. **20A**(9): p. 1769-83.

93. Neu, R.W. and H. Sehitoglu, *Thermomechanical fatigue, oxidation, and creep. I. Damage mechanisms.* Metallurgical Transactions A (Physical Metallurgy and Materials Science), 1989. **20A**(9): p. 1755-67.

94. Hasebe, T., M. Sakane, and M. Ohnami, *High Temperature Low Cycle Fatigue and Cyclic Constitutive Relation of MAR-M247 Directionally Solidified Superalloy.* Journal of Engineering Materials and Technology, Transactions of the ASME, 1992. **114**(2): p. 162-167.

95. Ibanez, A.R., V.S. Srinivasan, and A. Ashok Saxena, *Creep Deformation and Rupture Behaviour of Directionally Solidified GTD 111 Superalloy.* Fatigue and Fracture of Engineering Material and Structures, 2006. **29**(12): p. 1010-20.

96. Satyanarayana, D.V.V., C.M. Omprakash, B. Jagadeesan, and N. Das, *Effect of section thickness on creep and stress rupture behavior of DS CM247 nickel base superalloy.* Materials at High Temperatures, 2008. **25**(1): p. 17-26.

97. Sehitoglu, H., *Constraint Effect In Thermo-Mechanical Fatigue.* Journal of Engineering Materials and Technology, Transactions of the ASME, 1985. **107**(3): p. 221-226.

98. Pilkey, W.D., *Peterson's Stress Concentration Factors*. 2nd ed. 1997, New York: John Wiley & Sons, Inc.

99. Neuber, H., *Theory of notch stresses: principles for exact calculation of strength with reference to strutural form and material*. 2 ed. 1958, Berlin: Springer Verlag.

100. Moftakhar, A., A. Buczynski, and G. Glinka, *Calculation of elasto-plastic strains and stresses in notches under multiaxial loading.* International Journal of Fracture, 1994. **70**(4): p. 357-73.

101. Davies, C.M., N.P. O'Dowd, K.M. Nikbin, G.A. Webster, and F. Biglari, *Comparison of methods for obtaining crack-tip stress distributions in an elastic-plastic material.* Journal of Strain Analysis for Engineering Design, 2005. **40**(5): p. 431-50.

102. Bannantine, J.A., J.J. Comer, and J.L. Handrock, *Fundamentals of Metal Fatigue Analysis*. 1990, Upper Saddle River, NJ: Prentice-Hall, Inc. 271.

103. Topper, T.H., R.M. Wetzel, and J. Morrow, *Neuber's rule applied to fatigue of notched specimens.* Journal of Materials, 1969. **4**(1): p. 200-209.

104. Molski, K. and G. Glinka, *A method of elastic-plastic stress and strain calculation at a notch root.* Materials Science and Engineering, 1981. **50**(1): p. 93-100.

105. Gordon, A.P., M. Schulist, and E.P. Williams. *Applicability of Neuber's Rule to Thermomechanical Fatigue*. in *Proceedings of the ASME Turbo Expo 2008: Power for Land, Sea, and Air*. 2008. Berlin, Germany: ASME.

106. Taylor, D. *The theory of critical distances*. in *Proceedings of the 16th European Conference on Fracture (ECF16)*. 2006. Alexandroupolis, Greece.

107. Socie, D. *An evaluation of methods for estimating fatigue lives under multiaxial nonproportional variable amplitude loading*. 1998. Amsterdam, Netherlands: Elsevier.

108. Fatemi, A. and D.F. Socie, *A critical plane approach to multiaxial fatigue damage including out-of-phase loading.* Fatigue & Fracture of Engineering Materials & Structures, 1988. **11**(3): p. 149-65.

109. Mucke, R. and H. Kiewel. *Non-Local Cyclic Life Prediction for Gas Turbine Components with Sharply Notched Geometries*. 2007. Montreal, Que., Canada: American Society of Mechanical Engineers, New York, NY 10016-5990, United States.

110. Domas, P.A. and S.D. Antolovich, *An integrated local energy density approach to notch low cycle fatigue life prediction.* Engineering Fracture Mechanics, 1985. **21**(1): p. 187-202.

111. Domas, P.A. and S.D. Antolovich, *A mechanistically based model for high temperature notched LCF of rené 80.* Engineering Fracture Mechanics, 1985. **21**(1): p. 203-214.

112. Hurley, P.J., M.T. Whittaker, S.J. Williams, and W.J. Evans, *Prediction of fatigue initiation lives in notched Ti 6246 specimens.* International Journal of Fatigue, 2008. **30**(4): p. 623-634.